USING LIGHT EMITTED CLUSTERS AS A PROBE OF THE SYMMETRY ENERGY IN
THE NUCLEAR EQUATION OF STATE

By

Michael David Youngs

A DISSERTATION

Submitted to
Michigan State University
in partial fulfillment of the requirements
for the degree of

Physics - Doctor of Philosophy

2013

ABSTRACT

USING LIGHT EMITTED CLUSTERS AS A PROBE OF THE SYMMETRY ENERGY IN THE NUCLEAR EQUATION OF STATE

By

Michael David Youngs

The symmetry energy, and more specifically its density dependence, has been studied for quite some time from both a theoretical and experimental approach. In order to sufficiently constrain the symmetry energy, we need to experimentally measure observables sensitive to the symmetry energy within a reasonable uncertainty and compare those results to those of simulations of the same nuclear reactions. This dissertation aims to achieve both experimental measurements and compare them to the results of studies using the pBUU transport code.

These studies using pBUU aim to find the sensitivity of different observables to different transport variables as well as the symmetry energy itself. Some of the predominant variables that have been investigated in this dissertation are the in-medium cross section between nucleons as well as the effect of cluster production. The specific observables upon which we report are the center of mass spectra of protons, neutrons, deuterons, tritons and finally ^{3}He. In addition we investigate the n/p and t/^{3}He single and double ratios which have been suggested as being sensitive to the symmetry energy. As an added check we also study the coalescence invariant n/p spectra and ratios.

We also include a study of spectra for all charged particles up through mass A=4 emitted from reactions of ^{112}Sn+^{112}Sn and ^{124}Sn+^{124}Sn at both 50 and 120 MeV/A. The experiment to measure these reactions used the Large Area Silicon Strip Array to detect the charged particles and the MSU Miniball to detect charge particle multiplicity in order

to select central collisions. Neutrons were also measured in this experiment using the Large Area Neutron Array along with two thin scintillators used as a start timer for the neutron walls and a charge particle veto to discern contamination in the neutron walls. The neutron analyses are not extensively reported in this dissertation as they were the focus of the dissertation of Daniel Coupland [1]. Finally, another scintillator was used to measure the beam rate.

We compare the new experimental data with previous data. We have achieved higher statistical precision and measured up to higher emission energies. The 50 MeV/A data shows reasonable agreement with previous measurements. There are no prior measurements of the 120 MeV/A Sn+Sn reactions. Simulated results suggest a sensitivity to the density dependence of the symmetry energy, nevertheless there are still significant differences between the experimental data and simulated results. We present evidence that this is partly due to clustering effects in both the experiment and simulations. More theoretical work will need to be completed in order for the theory to be more accurately compared to the experimental results.

TABLE OF CONTENTS

LIST OF TABLES

LIST OF FIGURES

xv

Chapter 1

Introduction

1.1   Introduction to the Symmetry Energy

Nuclear physics is often times discretized into several different fields: reactions, structure and astrophysics. The Nuclear Equation of State (EoS) is of particular importance to all three fields. An Equation of State is a thermodynamic equation that relates different state variables under a given set of physical conditions. Classical and quantum liquids as well as a wide variety of solid state systems have their own EoS. One of the most basic and well known EoS is that of an ideal gas,

$$P = \rho k T, \tag{1.1}$$

which relates the pressure, P, density, ρ, and temperature, T. A similar equation involving the energy, E,

$$E/V = (3/2)\rho k T, \tag{1.2}$$

is another EoS. The EoS of nuclear matter has been studied for many years and has been reasonably constrained for symmetric matter, that which consists of nearly identical proton and neutron densities. This EoS has been useful in describing both bulk properties as well as thermodynamic properties of macroscopic nuclear matter for these symmetric systems, however it is does not describe these properties when the matter has unequal proton and neutron densities [9].

In order to compensate for this, a correction to the EoS is made which includes the isospin asymmetry. The form of this equation is,

$$\frac{E}{A}(\rho,\delta) = \frac{E}{A}(\rho,0) + E_{\text{sym}}(\rho)\delta^2 + O(\rho)\delta^4 \ldots, \tag{1.3}$$

where $E/A(\rho,0)$ is the EoS for symmetric matter, ρ is the density and δ is the isospin asymmetry defined by,

$$\delta = \frac{\rho_n - \rho_p}{\rho_n + \rho_p}. \tag{1.4}$$

In the case of a single nucleus at uniform density, δ would reduce to (N-Z)/A. In Equation 1.3, there is also a term, E_{sym}, which has become known as the symmetry energy. The significance of the symmetry energy can be plainly seen in Figure 1.1 which shows the difference between the energy density of the system from symmetric matter to pure neutron matter.

The symmetry energy has been theorized using many different forms. In this work, the form used will be,

$$E_{\text{sym}} = S_{\text{kin}}(\rho/\rho_0)^{2/3} + S_{\text{int}}(\rho/\rho_0)^{\gamma}. \tag{1.5}$$

This form contains two distinct parts, the first of which is derived from Fermi motion,

2
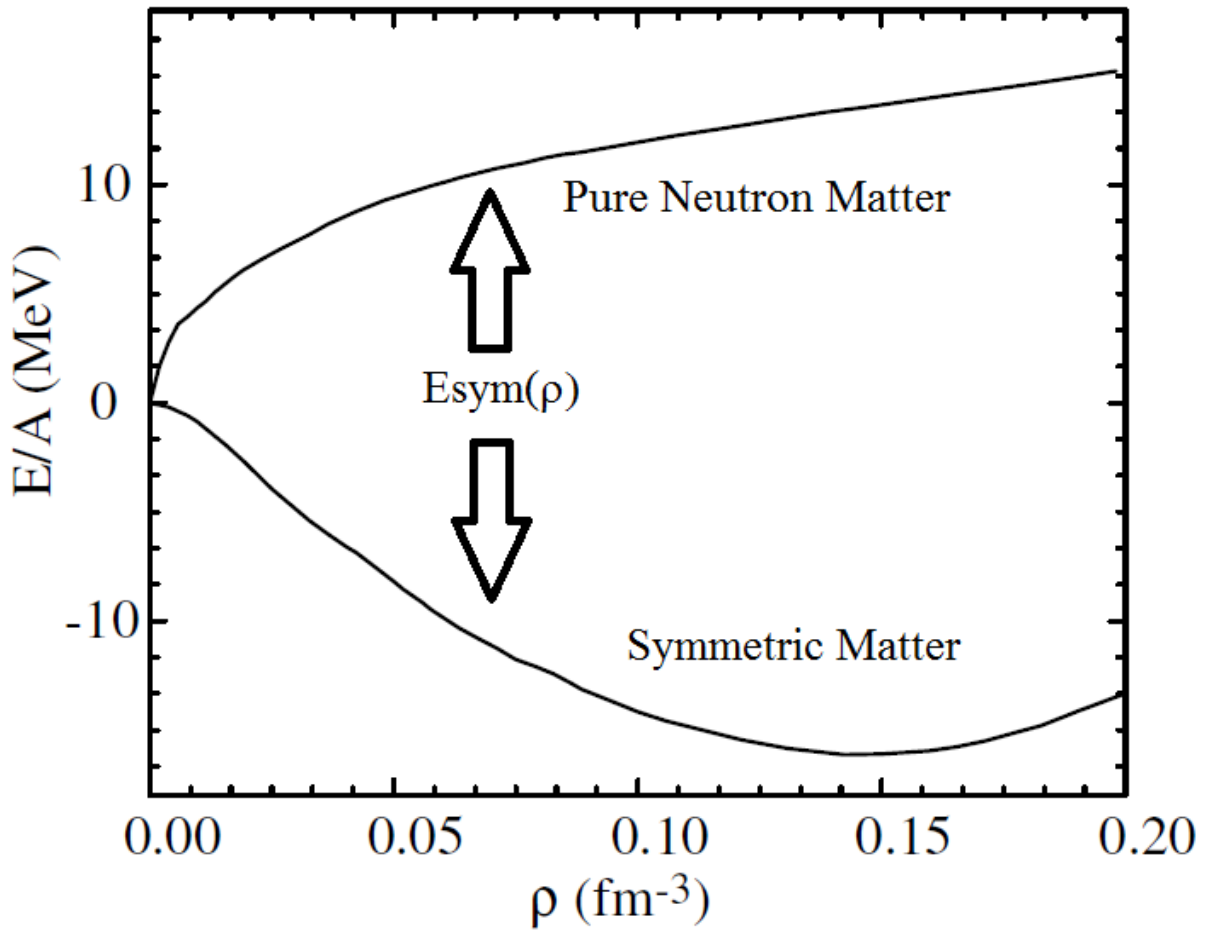
Figure 1.1: This figure (modified from [2]) provides an illustrative example of the Equation of State for both pure neutron and symmetric matter. The difference between the two is symmetry energy.
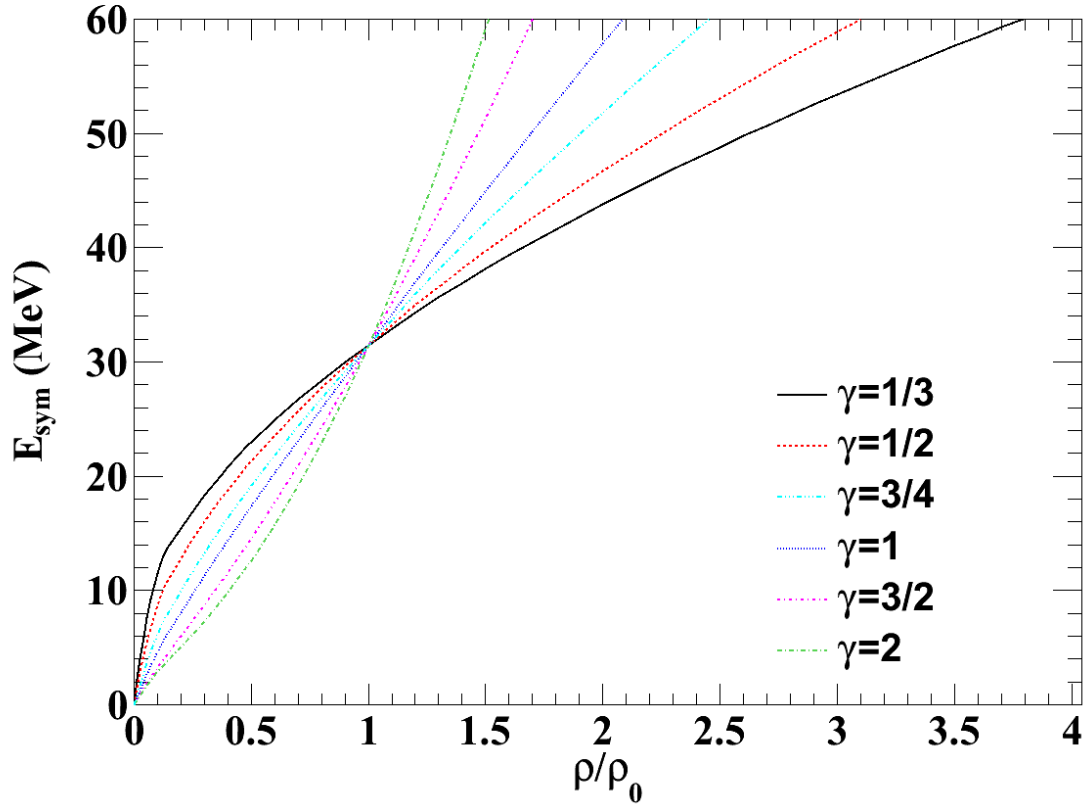
Figure 1.2: Several examples of the symmetry energy from Equation 1.5 as a function of density with different possible values for γ. For interpretation of the references to color in this and all other figures, the reader is referred to the electronic version of this dissertation.

giving S_{kin} a value of about 12.5 MeV. The value of the symmetry energy at saturation density, ρ_0, has been constrained to a value around 31 MeV with some uncertainty. As such, S_{int} is assumed to be a value near 19 MeV. The value of γ is the least constrained parameter in this equation. Theoretical constraints provide a super-stiff value of 2 and a super-soft value of 1/3 for the most extreme values of γ. Figure 1.2 shows the symmetry energy as a function of density for different possible values of γ.

The final term in Equation 1.3 also indicates correction terms that are higher order in δ are possible. Most theoretical estimates, however, indicate orders higher than δ^2

are small and may even be negligible compared to the current experimental uncertainties. Reference [10] provides some evidence for the inclusion of these terms for supersaturation densities, however the remainder of this work will prioritize subsaturation densities and will therefore only assume the form of the EoS to be quadratic in δ.

The symmetry snergy has been approached from many different avenues over the last 15 years and has many far reaching consequences. In nuclear structure, the symmetry energy contributes significantly to the binding energies, neutron skin thicknesses [4], isobaric analog states [11], and giant dipole and monopole [12] resonances. To this day there is still debate over whether the symmetry energy can be constrained by pygmy dipole resonance measurements [13–15]. In astrophysics, the symmetry energy has been shown to strongly affect a neutron star's maximum mass [16], mass-radius relationship [17], cooling rates [10,17,18], even crustal vibration frequencies [19]. Nuclear reactions have used numerous probes to constrain the symmetry energy including isoscaling [20,21], isospin diffusion [22,23], n/p ratios [24], n/p flow [25], π^+/π^- ratios and flow [26,27], t/^{3}He and ^{7}Li/^{7}Be ratios [28–32].

An example of the current constraints placed on the symmetry energy can be seen in Figure 1.3. These constraints come from a variety of sources including heavy ion collisions, neutron skin thicknesses, isobaric analog states and pygmy dipole resonances. This figure parameterizes the symmetry energy in another analogous way where,

$$E_{\text{sym}}(\rho) = S_0 + \frac{L}{3}\left(\frac{\rho - \rho_0}{\rho_0}\right) + \frac{K_{\text{sym}}}{18}\left(\frac{\rho - \rho_0}{\rho_0}\right)^2 + \dots \qquad (1.6)$$

This equation is a Taylor expansion of the symmetry energy around saturation density. Here S_0 is the value of the symmetry energy, L is the slope and K_{sym} is the curvature all

5

at saturation density. The slope can also be related to the pressure of the system, P_{sym}, through,

$$L = 3\rho_0 \frac{\partial E_{\text{sym}}}{\partial \rho}\bigg|_{\rho=\rho_0} = \frac{3}{\rho_0} P_{\text{sym}}. \qquad (1.7)$$

It is the goal of this dissertation to add additional constraints to the symmetry energy by comparing simulated results to new experimental heavy ion collision data.

1.2   The BUU transport model

Boltzmann-Uehling-Uhlenbeck, or BUU, models have been used to simulate heavy ion reactions in nuclear physics ever since Bertsch and Kruse in Ref [33] where it was initially used for relativistic heavy ions. Since then, quite a few different models have been developed based on the same basic principle. The model used throughout this dissertation is a BUU model developed by Danielewicz and collaborators that I will refer to as pBUU [34–36]. This pBUU code has been tested previously and compared to certain experimental data such as single particle distributions [34, 35], elliptic flow [37], and stopping observables [36]. Bertsch and das Gupta provide a review of many transport models including BUU in Ref [38].

BUU models require solving the modified Boltzmann Equation,

$$\frac{\partial f}{\partial t} + \frac{\partial \epsilon_{\mathbf{p}}}{\partial \mathbf{p}} \frac{\partial f}{\partial \mathbf{r}} - \frac{\partial \epsilon_{\mathbf{p}}}{\partial \mathbf{r}} \frac{\partial f}{\partial \mathbf{p}} = \int d\mathbf{p}_2 \int d\Omega' v_{12} \frac{d\sigma}{d\Omega'}((1 \mp f_1)(1 \mp f_2)f_1'f_2' - (1 \mp f_1')(1 \mp f_2')f_1 f_2), \quad (1.8)$$

self-consistently in heavy ion collisions for fermions (-) and bosons (+). The right side of the equation describes the changes to the one particle density matrix, f, due to collisions between particles, Pauli-blocking and scattering between momentum states while the
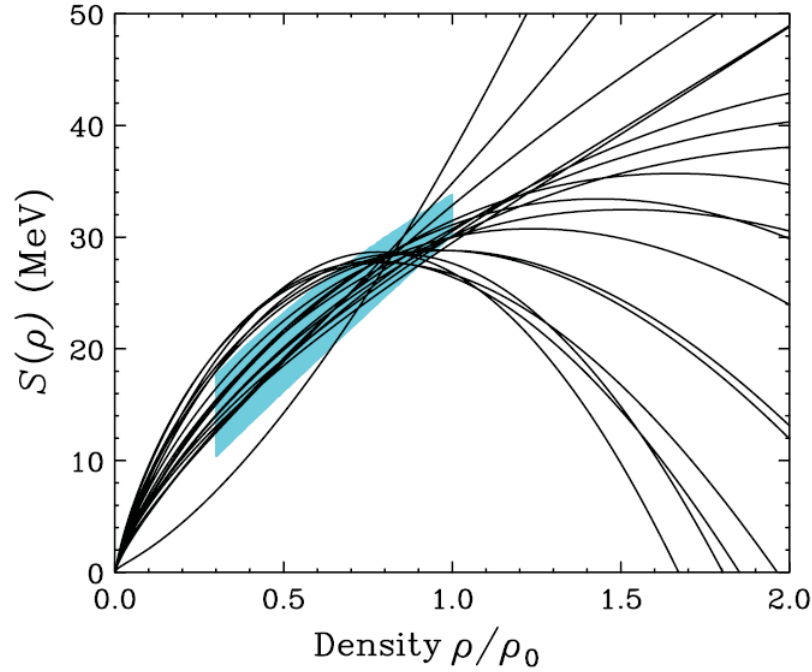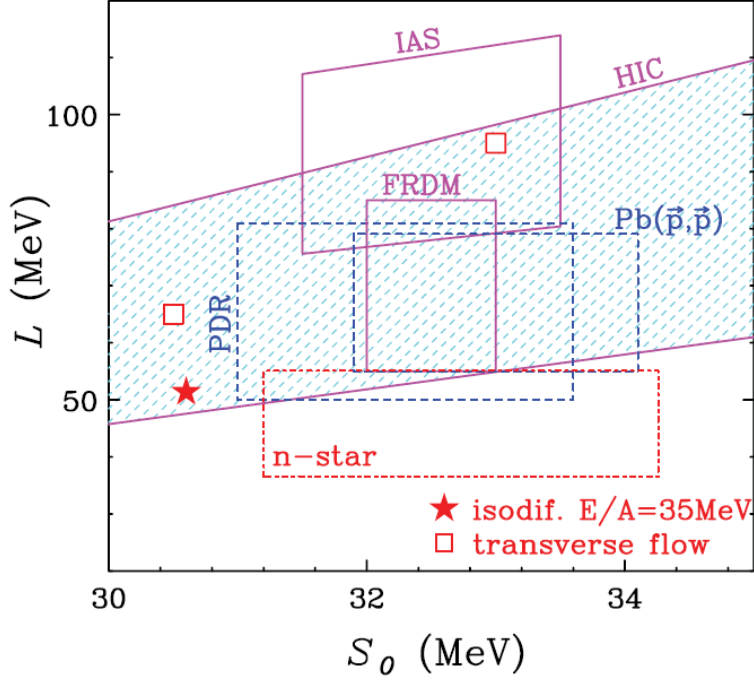
Figure 1.3: The top plot displays current constraints presented in Ref [3] on the first two terms, S_0 and L of the Taylor expansion of the symmetry energy in Equation 1.6. The contributing constraints are obtained from Heavy Ion Collisions (HIC), neutron skin thicknesses from Sn isotopes, Isobaric Analog States (IAS) and the possible constraints from Pygmy Dipole Resonances (PDR). In the bottom plot, constraints from HIC indicated by the blue box are compared to several Skyrme parameterizations for the symmetry energy. The chosen Skyrme interactions are those used in [4].

left side describes changes in the Wigner transform of f due to motion of particles in the mean field. In this equation the mean field is calculated self-consistently using the Wigner transorm, f, from all particles and ϵ is the single particle energy for a particle with momentum **p**, in the mean field.

In general, Equation 1.8, can be derived as a semi-classical limit of the Hartree-Fock equation. Regardless of its derivation, its form is identical to the classical Boltzmann equation. If one assumes f to be positive and definite, it can be solved by breaking up each proton and neutron into a number of test particles. By using a sufficient number of test particles, a physically realistic mean field and phase space density required for a proper treatment of Pauli blocking can be achieved. A study on the dependence of test particles is described in chapter 4.

This BUU model has two different options for calculating the mean field potential. The first, an oversimplified momentum independent model, with the second being a more complete, albeit more complex, momentum dependent model. At low momentum, this dependent model can be approximated by replacing the mass of nucleons with an effective mass. It is still uncertain on whether the proton or neutron effective mass is larger, however they are both in the vicinity of $m^* = 0.7m$ and are set to be equal in this code. While the momentum dependent model is more physically correct, it is also more computationally expensive. Both options are studied in this dissertation, however, most studies on the effect of individual variables other than the momentum dependence of the mean field use the momentum independent model for the improved computational time.

Pauli blocking and other higher order effects cause the nucleon-nucleon cross section to be modified. This pBUU code provides three possibilities for the reduced cross section.

The free cross section is provided in the code as an initial starting point. These cross sections were parameterizations of experimental data. An energy dependent reduced cross section, which is referred throughout this dissertation as the Rostock cross section, is obtained from fits to Brueckner-Hartree-Fock calculations. This parameterization has the form,

$$\sigma(\rho) = \sigma_{\text{free}} \exp\left(-0.6\frac{\rho}{\rho_0}\frac{1}{1 + (\text{KE}_{\text{CM}}/150\text{MeV})^2}\right). \tag{1.9}$$

A more strongly density dependent reduction which is referred to as the Screened cross section is based on a more geometric approach with the form,

$$\sigma = \sigma_0 \tanh(\sigma_{\text{free}}/\sigma_0) \quad \text{where} \tag{1.10}$$

$$\sigma_0 = y\rho^{-2/3}, \quad y = 0.85. \tag{1.11}$$

This is another interesting case where the Rostock reduction may be more physically correct however, the Screened reduction has shown slightly better reproduction of stopping data. Neither the Rostock or Screened reductions were able to fully describe the data, but both were large improvements over the Free cross section. The effects of the three cross sections will be explored in Chapter 4.

For this work, free hydrogen and helium isotopes as well as neutrons that are emitted from the colliding nuclei are important. In order to determine which of these particles are free particles and not bound within a larger residue, a local density cut is placed on the particles. If the particles have a local density less than $0.01\rho_0$ at the end of the simulation, or when the particle leaves the grid of calculation, it is considered a free particle and taken into consideration in the data. Here, ρ_0 is the nuclear saturation density with a value of

$0.16~\text{fm}^{-3}$. The grid of calculation is another aspect of this code that can be modified and possibly effect the calculation. This study is also included in chapter 4.

The pBUU code is unique amongst other BUU formulations because it has the ability to produce light clusters up through mass A=3. The premise behind the cluster formation in this code is that the breakup cross section for a deuteron by a proton is proportional to the formation probability of a deuteron where either a neutron or a proton are scattered by a third nucleon into the phase space volume of a deuteron as described in [35]. In a similar fashion tritons and ^{3}He can be created using collisions involving four nucleons, three of which end up as the final triton or ^{3}He.

1.3   Organization of Dissertation

This dissertation will be organized the following way; Chapter 2 will describe the experimental setup and detectors used for an experiment to parameterize the symmetry energy, Chapter 3 will describe the calibration used for the detectors needed for the observables of interest for this dissertation, Chapter 4 will describe a systematic study of different pBUU transport variables and how they influence the observables of interest in this experiment, and Chapter 5 will provide experimental results and comparison to simulated data. Finally, Chapter 6 will provide several conclusions and suggestions for future experiments.

Chapter 2

Experimental Setup

2.1 Reaction Systems

In this dissertation we measured two systems, ^{112}Sn+^{112}Sn and ^{124}Sn+^{124}Sn at the beam energies of E/A = 50 and 120 MeV. These systems were chosen to give the largest range of asymmetry possible for stable Sn isotopes. In addition, we aimed to confirm the calibration of the Large Area Silicon Strip Array (LASSA) by bombarding a CH$_2$ target with a ^{16}O beam at E/A = 16.8 and 29.4 MeV. The protons in the polyethylene target were elastically back-scattered into the LASSA array. This was intended to provide at least one extra calibration point as described in Section 3.3.

2.2 Experimental Layout

We used six different detector systems in this experiment. LASSA was used to detect all isotopes of hydrogen and helium, as well as some isotopes of lithium and beryllium. The Minball array was used to select the magnitude of the impact parameter via gates on

the charged particle multiplicity as well as to measure the transverse energy. It can also provide information about the orientation of the reaction plane. The Large Area Neutron Array (LANA) was used to detect the neutrons emitted over a similar angular range as LASSA. The neutron energy was determined via time of flight measurement, using the Neutron Walls as a stop timer. A Forward Array consisting of plastic scintillators was used as a start timer. A complication with the Neutron Walls is that high energy hydrogen isotopes that punch through the walls must be distinguished from neutrons. For this purpose, Proton Veto scintillator paddles were constructed and used in order to detect and veto those charged particles. Finally, a scintillator was used downstream of the reaction target to calibrate the beam intensity. In this chapter, we discuss the placement and properties of these detectors. The details of the calibration and analysis of all of the detectors can be found in Chapter 3. Figure 2.1 shows a three dimensional design drawing of the S2 experimental vault at the NSCL where the experiment took place. This drawing gives relative locations of the Miniball, LASSA and the Neutrons Walls. Figure 2.2 shows a picture of the vault from the entrance, directly before the experiment began.

2.3   LASSA: The Large Area Silicon Strip Array

LASSA is an array of charged particle detecting telescopes each consisting of two separate silicon strip detectors followed by a set of four thallium-doped cesium iodide (CsI(Tl)) crystals which are read out using a photodiode. The total array consists of nine telescopes that can be arranged into differing geometries depending on the needs of particular experiments. In the case of this experiment, only six telescopes were used. Each telescope is capable of precisely measuring the energy, charge and mass of particles emitted from a
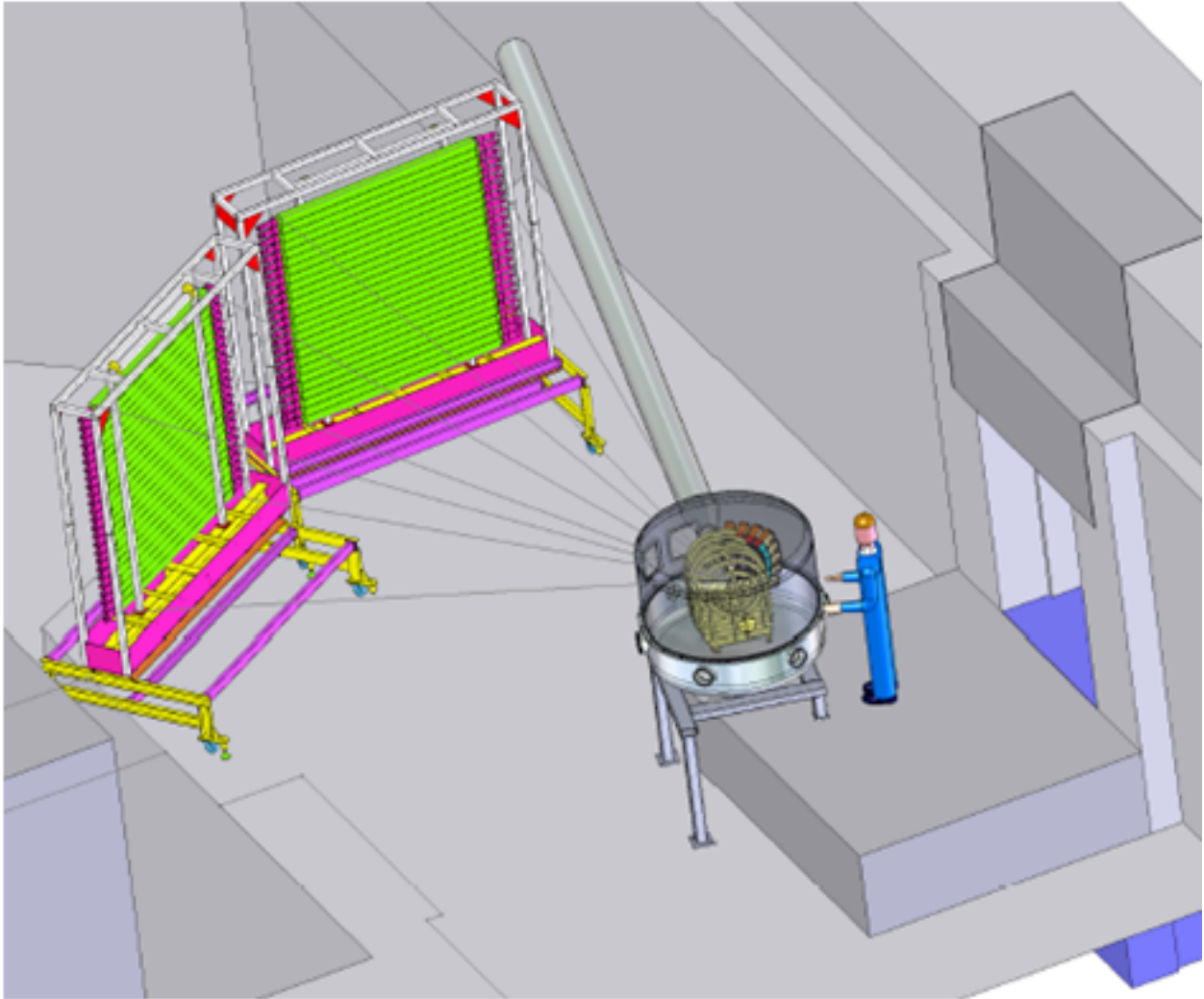
Figure 2.1: Three dimensional drawing of the layout of the experimental vault.
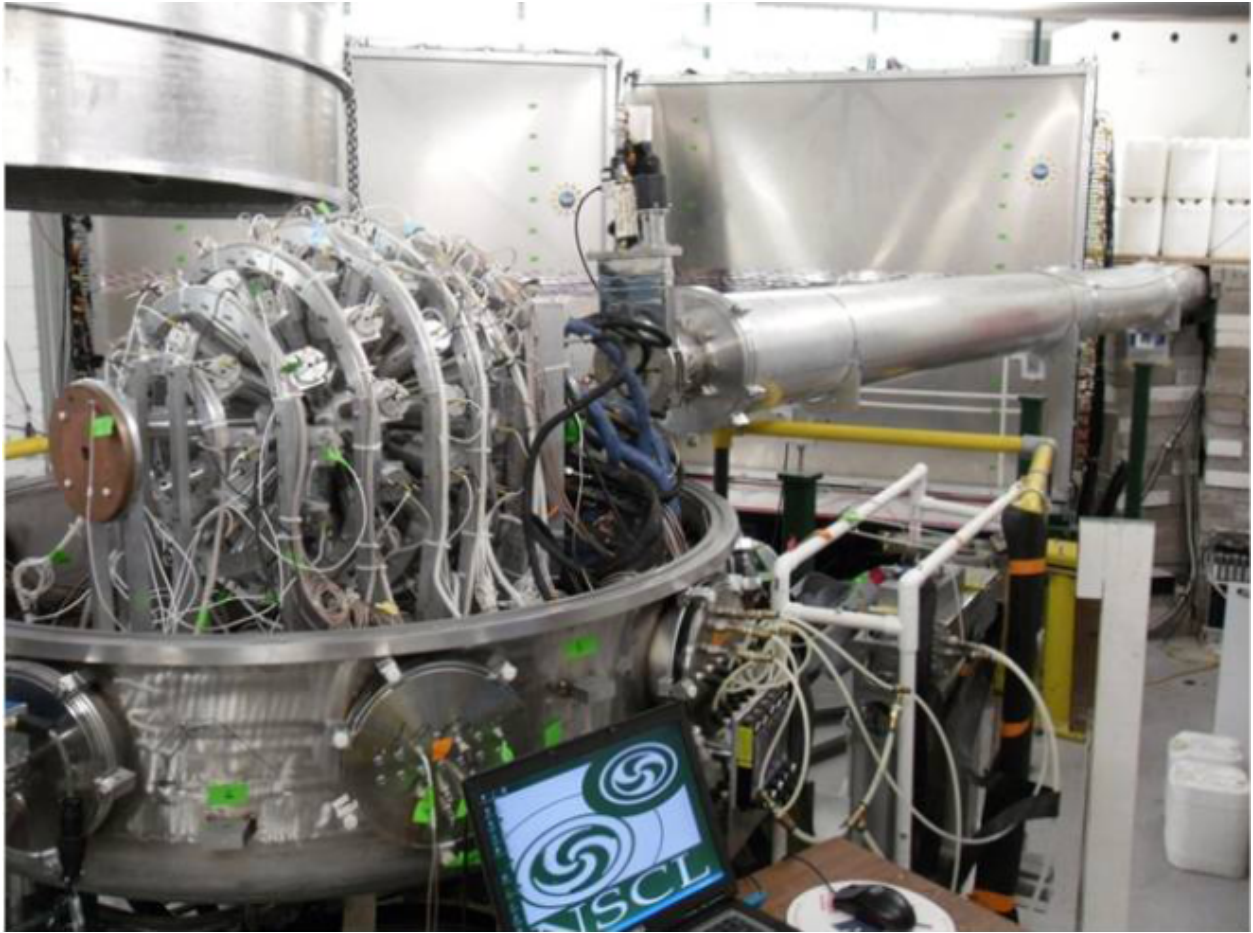
Figure 2.2: A picture of the vault in running condition with the top of the chamber removed showing (from this angle) the Miniball inside the scattering chamber and the Neutron Walls in the back of the vault.
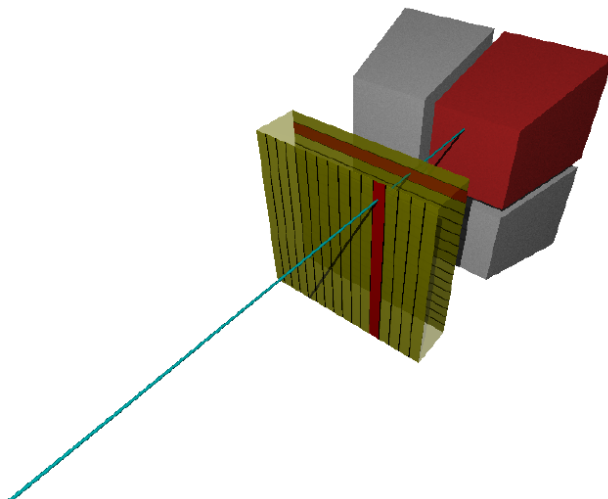
Figure 2.3: A schematic of the inside of a LASSA telescope. The first piece is a 500 μm thick double sided silicon all backed by four 6 cm CsI(Tl) telescopic shaped crystals.

reaction.

2.3.1 The Silicon Detectors

The first of the three physical detectors in a full LASSA telescope is a 65 μm thin, dE (or

ΔE) silicon strip detector. The face of the silicon is split into 16 strips each 3 mm wide with

a 100 μm interstrip gap to get some angular distribution information out of each hit. As

will be described in more detail to follow, by plotting the energy loss in the dE detector

versus the energy deposited in the E detector (for a particle that stops in the E) one is able

to obtain particle identification (mass and charge). Since particles that stop in the thick

silicon are too low in energy to be interesting in this experiment, the dE detectors were

left out of the telescopes.

The next detector in the telescope is a 0.5 mm thick, E silicon strip detector. The thick

silicon has the front half of the face segmented horizontally and the back half segmented

vertically, each with 16 channels as can be seen in Figure 2.3. Each strip, like the dE, has a

15
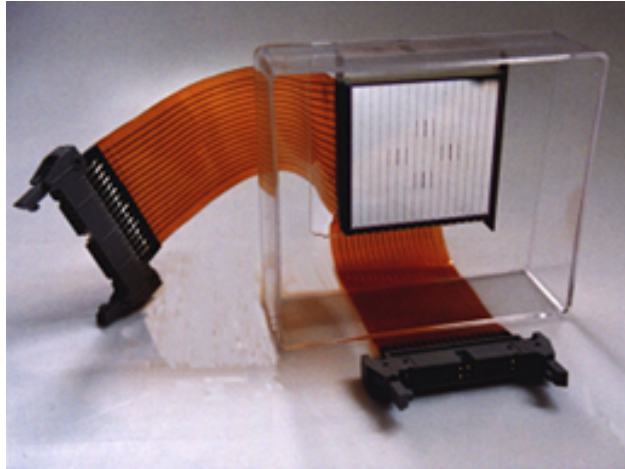
Figure 2.4: A picture of a thick LASSA double sided silicon.

3 mm pitch with a 100 μm interstrip gap. A picture of a thick silicon detector can be seen in Figure 2.4. In order to keep the solid angle coverage the same at the front of the CsI crystals as at the back, the front face of the silicon detector must be 20 cm from the target. At this distance, the 3 mm strip width corresponds to a width of 0.86°in angular coverage. In this experiment, the detectors were arranged in a way to cover polar angles, θ, from approximately 16°to 58°and azimuthal angles, ϕ, ranging from -45°to 45°. The coverage in the lab can be found in Figure 2.5. Each point in the figure corresponds to the location of the center of a 3 mm by 3 mm pixel defined by the combinations of different front and back strips.

2.3.2   The CsI(Tl) Crystals

CsI(Tl) crystals are incredibly beneficial in detecting charged particles in a range of E/A=30-200 MeV. The crystals are far cheaper than silicon detectors, they are less hygroscopic than their sodium iodide (NaI) counterparts and they can be made into a wide variety of shapes and geometries. CsI(Tl) crystals have been used in many experiments that require
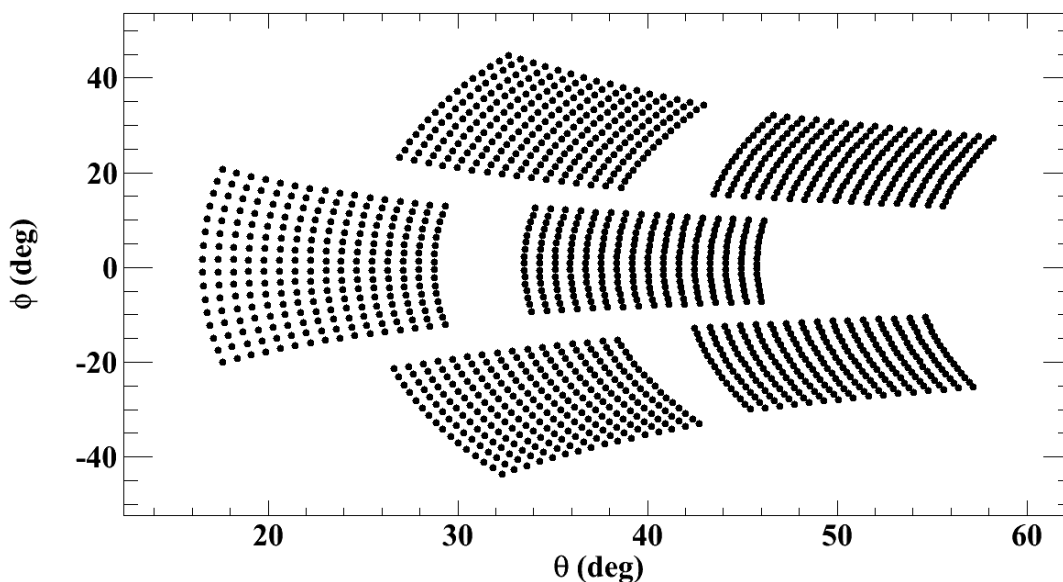
Figure 2.5: A plot of the LASSA coverage in the lab.

energetic charged particle detection over a large solid angle and continue to be a cost effective choice for such purposes.

In the case of LASSA, four crystals were tapered at the front to allow for a telescopic shape and to maintain the same solid angle throughout the full length of the crystal. Each crystal has a front face of 2.5x2.5 cm^2, a back face of 3.5x3.5 cm^2 and is 6 cm in length. At this length, each crystal is capable of stopping up to 150 MeV protons and 580 MeV alpha particles. The crystals can be seen in Figure 2.6 where two of the sides of a LASSA telescope have been removed.

Each crystal is backed by a transparent acrylic light guide which is in turn optically connected to a 2x2 cm^2 photodiode. Each side was then wrapped with teflon in order to ensure maximum uniform light collection. The front surface and the two inner sides of each crystal were covered with an aluminized mylar foil for two reasons. The mylar at the front is essential to providing maximum light collection with minimal energy loss.

17
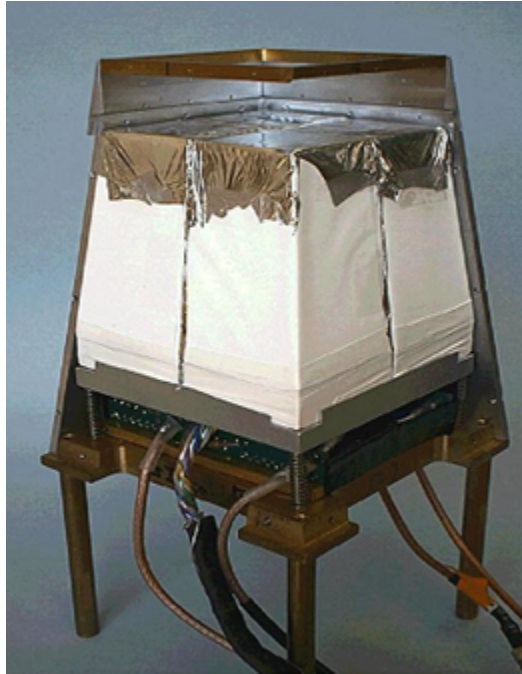
Figure 2.6: A picture of the inside of a LASSA telescope without the silicon included.

The mylar between the crystals is pivotal in preventing light produced in one crystal from entering its neighbor.

More detail about the construction of the LASSA detectors can be found in Ref. [39].

2.3.3 Particle Identification

One of LASSA's primary functions is to identify the particles that come out of the reactions. LASSA uses a ΔE vs E technique for PID. In the case of this experiment, the thick E detector is the ΔE and the CsI is the E measurement. The energy loss of an energetic ion through a material can be described by the Bethe formula given in Equation 2.1. The relationship of the energy loss in the silicon to the remaining energy measured in the CsI provides particle identification curves that can be seen in Figure 2.7.
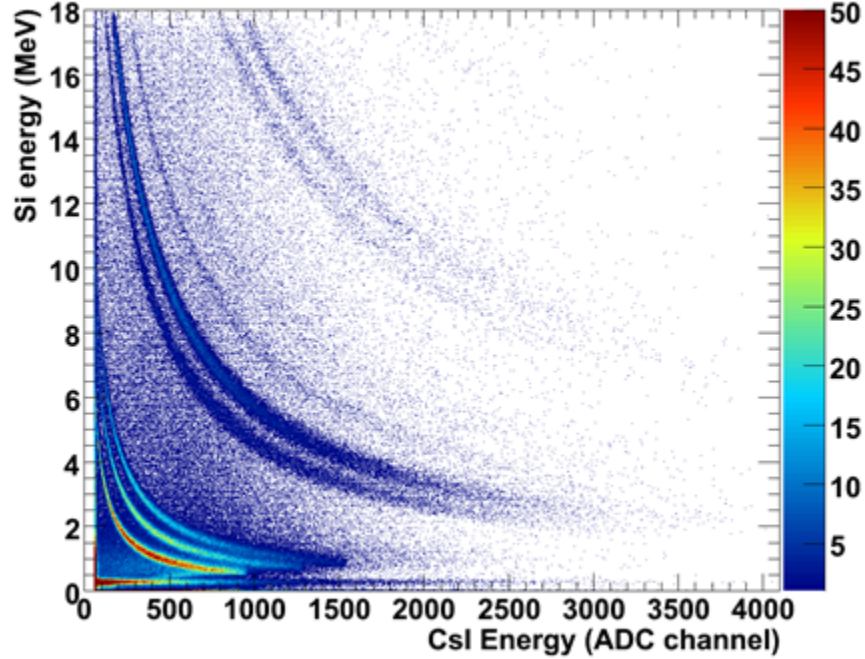
Figure 2.7: An example of the LASSA particle identification clearly displaying protons, deuterons and tritons (lowest set of three bands), helium isotopes and lithium isotopes. Increasing mass moves from lower left to upper right. Given more statistics a set of beryllium bands would also be seen.

$$-\frac{dE}{dx} = \frac{4\pi}{m_e c^2}\frac{nz^2}{\beta^2}\Big(\frac{e^2}{4\pi\varepsilon_0}\Big)^2\Big[\ln\Big(\frac{2m_e c^2\beta^2}{I(1-\beta^2)}\Big)-\beta^2\Big] \tag{2.1}$$

2.4   The MSU Miniball 4π Array

The Miniball Array in its entirety is comprised of 11 rings arranged coaxially around the beam axis. The detectors on an individual ring are all identical, however, since the solid angle of detection increases with an increase in lab angle, each ring has crystals with different shapes. The geometry of the detectors in each ring is described in Ref [5]. Table 2.1 contains information on how many detectors are in each ring as well as the solid angle for detectors in each ring.

Ring	Detector	$\Delta\Omega$	θ	$\Delta\theta$	$\Delta\phi$	d
		(msr)	(deg)	(deg)	(deg)	(mm)
5	15(24)	30.8	45	10	15	140
6	14(20)	64.8	57.5	15	18	90
7	19(20)	74.0	72.5	15	18	90
8	16(18)	113.3	90	20	20	70
9	13(14)	135.1	110	20	25.7	70
10	11(12)	128.3	130	20	30	70
11	8(8)	125.7	150	20	45	70

Table 2.1: A table of each ring of the Miniball with the amount of telescopes used in each ring (out of the full complement), the polar angle of each ring, with it's polar and azimuthal angular spans as well as the distance from the target to the front face of each crystal.

Each Miniball detector is a phoswich style detector with a thin 40 μm plastic scintillating foil made from Bicron BC-498X followed by a 2 cm CsI(Tl) crystal. Two UVT light guides and a 10-stage Burle C830622E PMT are glued to the back of the crystal using the optical cement BC-600. A picture of an individual Miniball element can be seen in Figure 2.8. Similar to the PMTs for the Neutrons Walls, the cylindrical light guide and the PMT are enclosed by a μ-metal magnetic shield in order to prevent stray cosmic rays and magnetic fields to alter the measurement of particles of interest. Each crystal is fronted by a layer of aluminized mylar to improve light collection and two layers of SnPbSb foil to keep secondary electrons from entering the scintillator. A schematic can be seen in Figure 2.9. More details about the construction of the Miniball can be seen in Ref [5].

For this particular experiment, only Rings 5-11 were used. The forward angles needed to be kept clear so that neutrons could fly straight to the Neutron Walls without the possibility of scattering from the Miniball and so that light charged particles could be detected by LASSA.

The Miniball's primary purpose in this experiment is to select the impact parameter

Figure 2.8: A picture of an individual Miniball element.
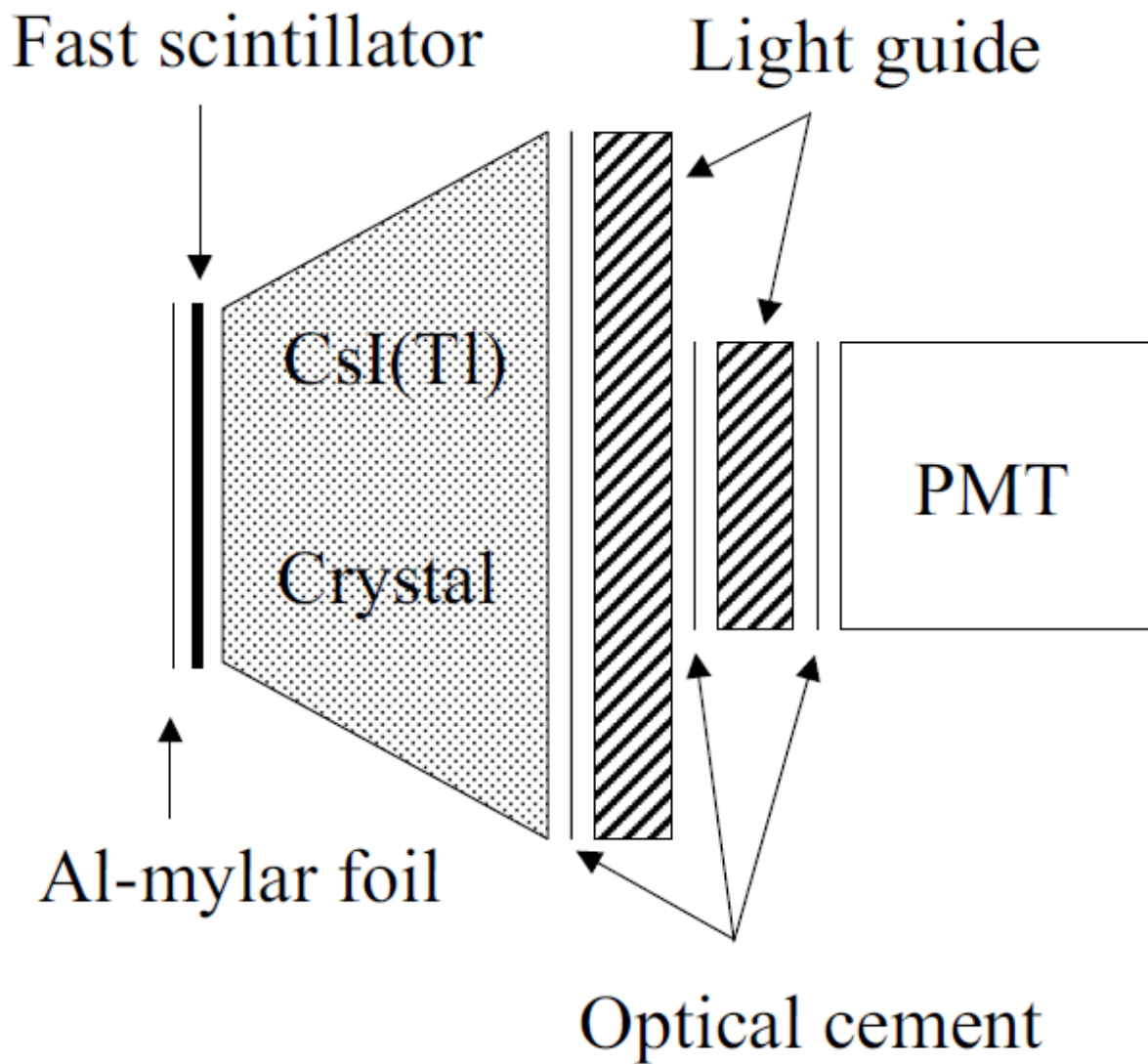
Figure 2.9: A schematic of an individual Miniball element. [5]

of an event. The observables for this experiment are mainly sensitive to the symmetry energy in central collisions with very low impact parameters. This can be achieved by measuring the charged particle multiplicity in the Miniball. The secondary purpose is to measure transverse energies of particles over the angles covered by the Miniball. In order to measure transverse energy, proper particle identification is required. This can be achieved using the stacked scintillators in a phoswich method. As shown in Figure 2.10, the Miniball phoswich detector's signal is divided into three distinct regions designated fast, slow and tail. The shape of this curve is due to the difference in light output between thin fast plastic scintillator and the slower CsI crystal. Using a pulse shape discrimination technique, we can identify different particles that are detected by the Miniball. This process will be described in more detail in Chapter 3.

Many modifications to the Miniball array had to be made for this experiment. Telescopes had to be removed to allow particles to be detected in the Forward Array, LASSA, and the Neutron Walls. Two telescopes also had to be removed to be replaced by the target drive and a camera used for beam alignment. Experimental pictures can be seen in Figures 2.11 , 2.12.

2.4.1 The Downstream Scintillator

As already discussed, the Miniball is the detector used to measure the centrality of a collision. It does this by measuring the number, or energies, of particles that enter any of the Miniball tubes in a given event. The multiplicity of the Miniball can be directly related to the cross section of a reaction and as such, be directly related to the impact parameter. In order to accurately determine the cross section, an accurate determination of the beam

0 33ns 180ns 540ns   1.5μs   3μs

Time

Fast   Slow   Tail
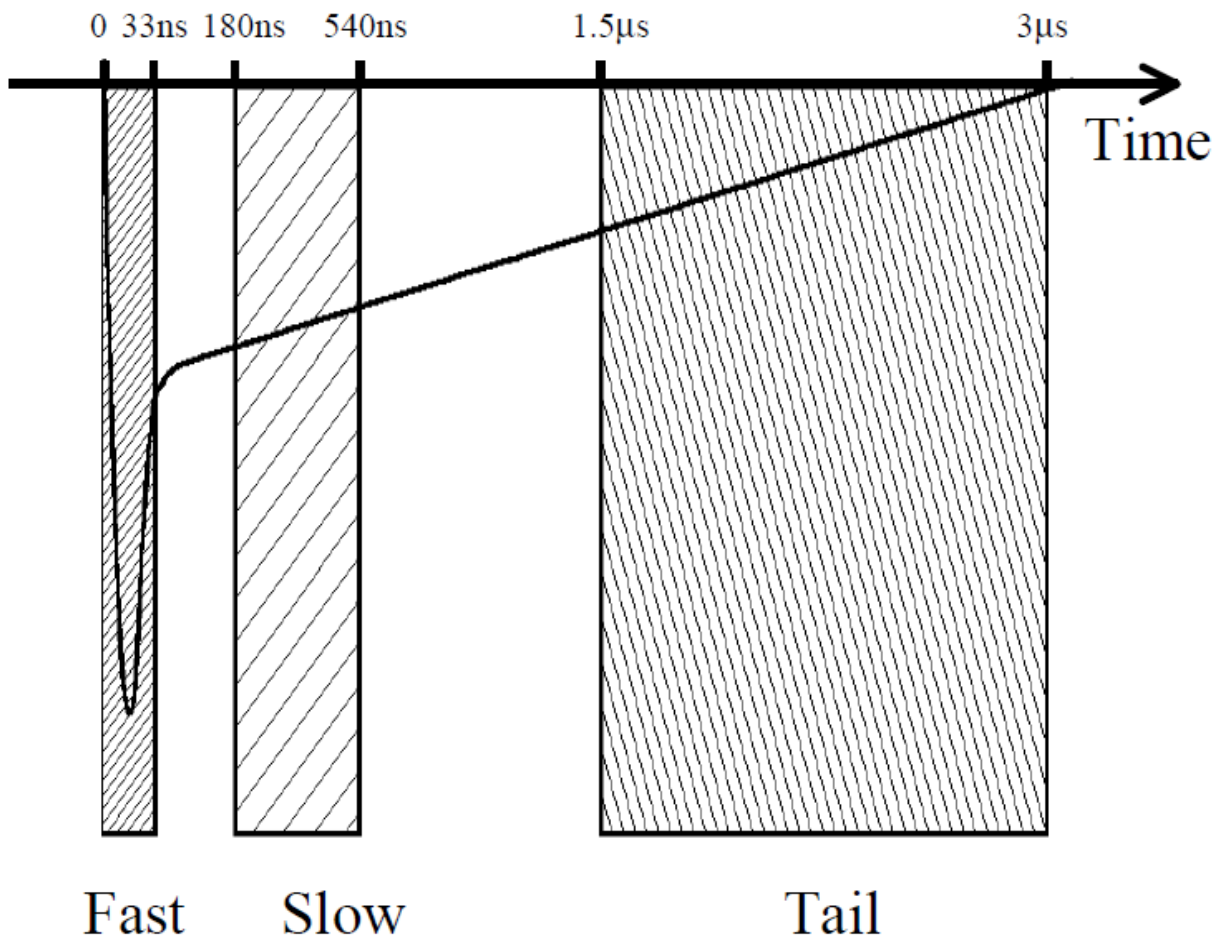
Figure 2.10: An example of the time signal seen through the phoswich method. [5]
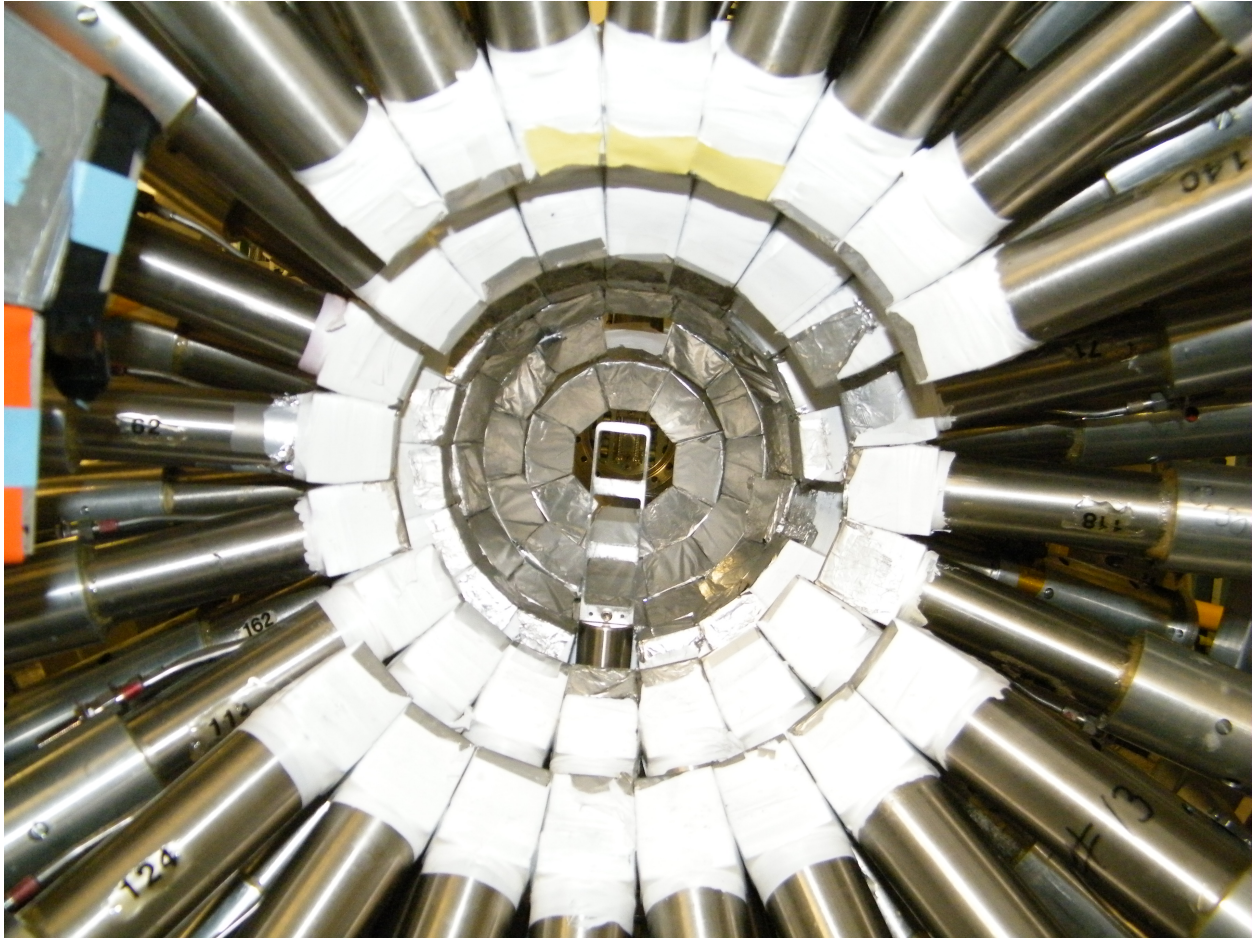
Figure 2.11: A picture of the inside of the Miniball looking upstream with the target ladder in place.
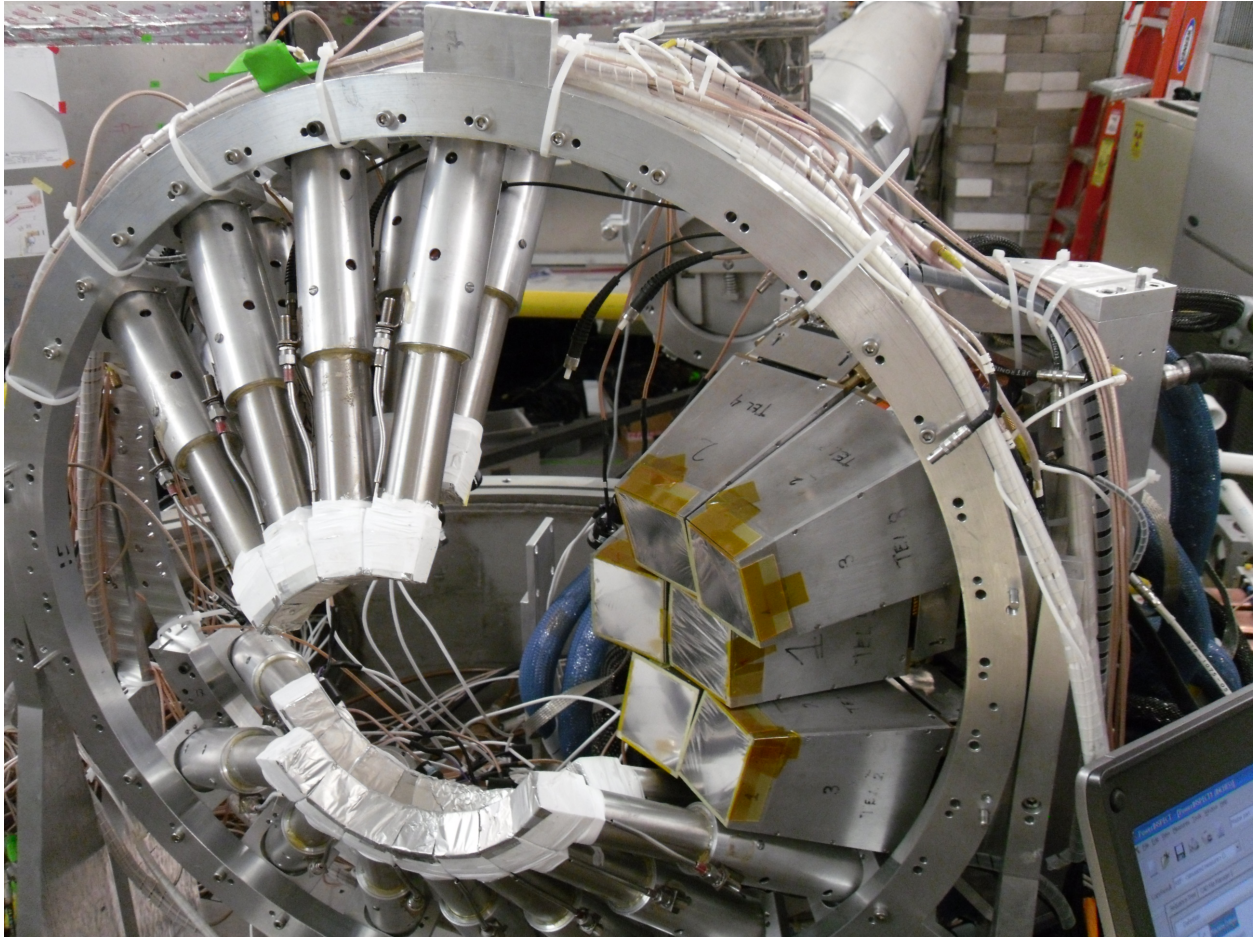
Figure 2.12: A picture showing LASSA's positioning in relation to rings 5 and 6 in the Miniball.

rate is needed.

This is achieved by what was called the Downstream Scintillator, a 3.5 inch by 3.5 inch square piece of 0.125 inch thick Bicron BC-404 Scintillator. The scintillator was optically coupled to a piece of Ultraviolet Transmitting (UVT) light guide which was then glued to a 4.8 cm in diameter piece of UVT light guide with Tra-Bond F113 Optical Epoxy. This light guide was coupled to a Thorn EMI 4011 PMT using Dow Corning Q2-3067 optical grease. This scintillator was lowered into the beamline just downstream of the Miniball to get an accurate value for the beam rate. The full construction as mounted in the experimental chamber is shown in Figure 2.13.

2.5 LANA: The Large Area Neutron Array

The neutron detectors used for this experiment are called the Large Area Neutron Array, also called LANA or the Neutron Walls. Each of the two walls in the array contains a stack of 25 hollow Pyrex bars. For this experiment each wall only used 24 bars due to limited availability of electronics channels for the data readout. Each Pyrex bar is 2 meters long, 7.62 cm tall and 6.35 cm thick and is filled with approximately 10 L of the liquid, organic scintillator NE-213. Each bar is tapered at each end to a 3 inch diameter circle so that it can be coupled to a photomultiplier tube which collects the light from interactions in the bar. A detailed description of the construction of the walls can be found in Ref [6]. A picture of the inside of one of the walls can be seen in Figure 2.14. In experimental running conditions a cover is in place to prevent light contamination in the scintillator. The two walls were arranged normal to the target with the center of the wall covering forward angles at 6 m from the target and the backward wall at 5 m from the target. The
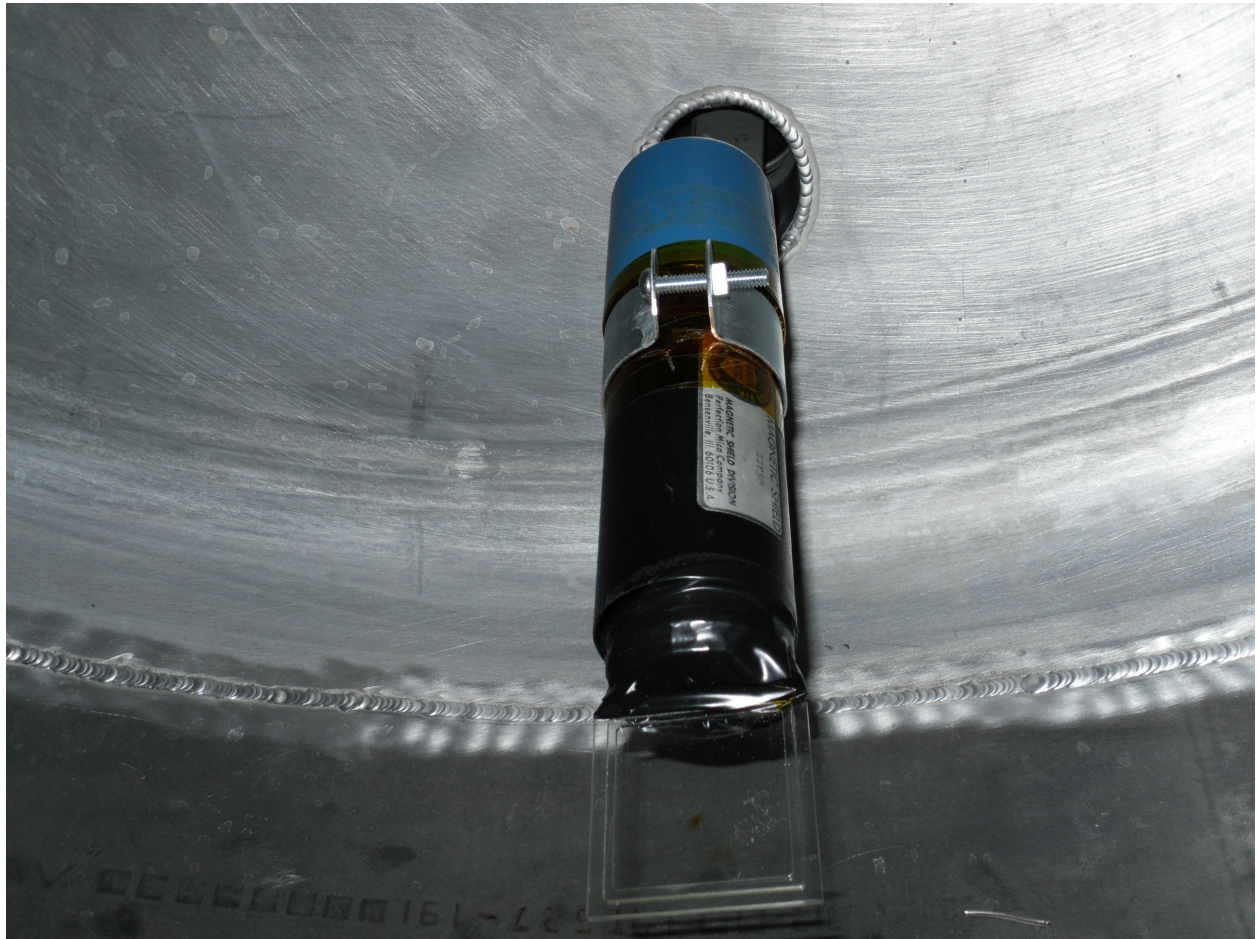
Figure 2.13: The full Downstream Scintillator as mounted in the chimney of the experimental chamber.

angular coverage of the active area of walls is seen in Figure 2.15.

This particular array was chosen as the neutron detector because of the liquid scintil-lator. Ionizing particles have two components in their scintillation process, a fast, prompt light generation and a slower, delayed light generation. The time constant for the prompt generation is on the order of nanoseconds where the delayed constant is on the order of hundreds of nanoseconds. For the same total light generation, different particles will have different proportions of light generated in the two regions. For example, cosmic rays or electrons that have been Compton scattered from γ rays, produce most of their light in the prompt region. Protons that have been scattered by a neutron, however ionize the system much more strongly and produce more of their light in the delayed region. An example of this concept can be seen in Figure 2.16.

This concept is the basis for a process called Pulse Shape Discrimination which lets us selectively omit cosmic and γ ray contamination. Figure 2.17 shows an example of this where we plot the charge collected in the fast gate versus the charge collected in the total gate. The fast and total gates correspond to approximately the first 30 and 300 ns after a detected hit, respectively. This figure shows a calibration run using an americium-beryllium source. This source is a neutron and γ emitter which follows the process in Equation 2.3. The separation between the two bands allows a gate to be drawn around the reactions coming from strongly ionizing particles.

$$^{241}\text{Am} \rightarrow ^{237}\text{Np} + \alpha + \gamma \tag{2.2}$$

$$\alpha + ^{9}\text{Be} \rightarrow ^{12}\text{C} + n + \gamma_{4.4\text{MeV}} \tag{2.3}$$

Figure 2.14: A picture of the inside of the Neutron Walls.
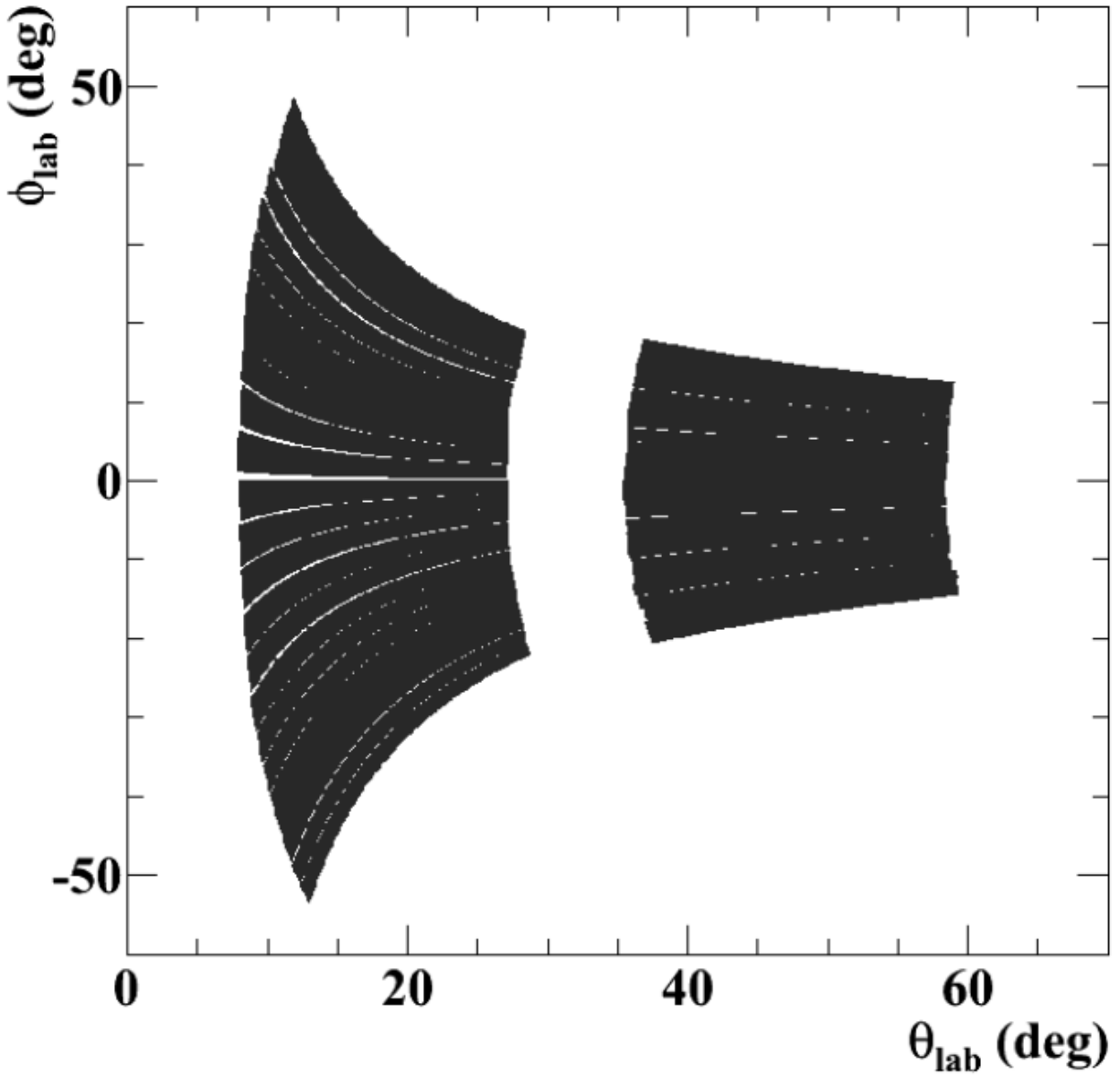
Figure 2.15: A plot of the Neutron Wall coverage in the lab.
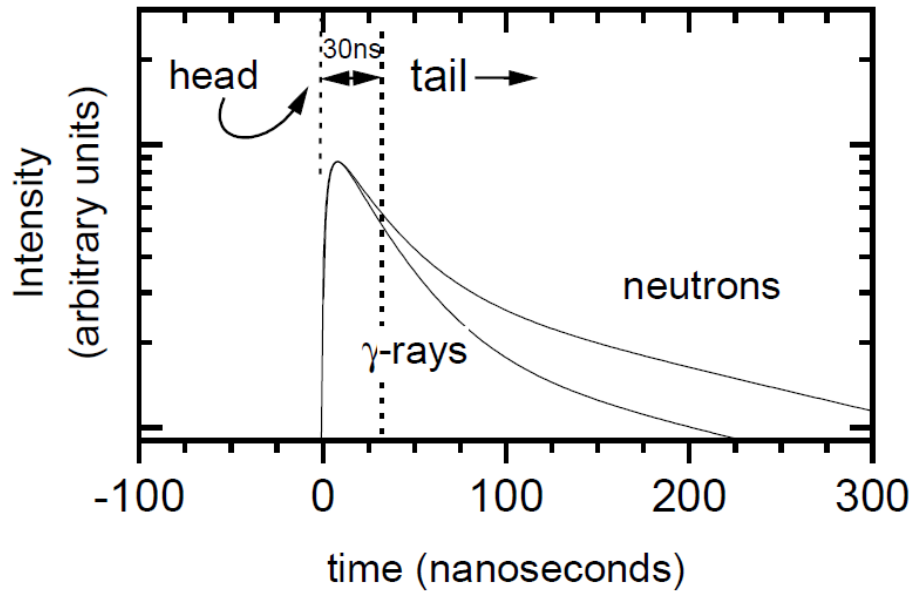
Figure 2.16: An example of the intensity versus time for different particles in the NE-213 in the Neutron Walls. [6]

One difficulty with neutron detection is that neutrons will almost never deposit all of their energy in just one collision. They will deposit some energy and scatter off at another angle. Due to this, a significant amount of neutrons detected by the neutron walls can come from scattering off of other materials in the experimental vault.

In an attempt to determine the contamination from background scattering, a set of 30 cm x 6.8 cm x 7.5 cm solid brass shadowbars were used to block all direct particles coming from the target on their path to the neutron walls. The shadowbars were centered just under 2.5 m from the target. A picture of one of the shadowbars can be seen in Figure 2.18 as well as an example of their use during experiment in Figure 2.19. The bars were situated such that they would have enough solid angle coverage to fully shadow the height of at least one bar in the Neutron Wall. By comparing the number of neutrons detected in the shadowed region to the spectra across the rest of the bar, one can determine the fraction of events that are background.
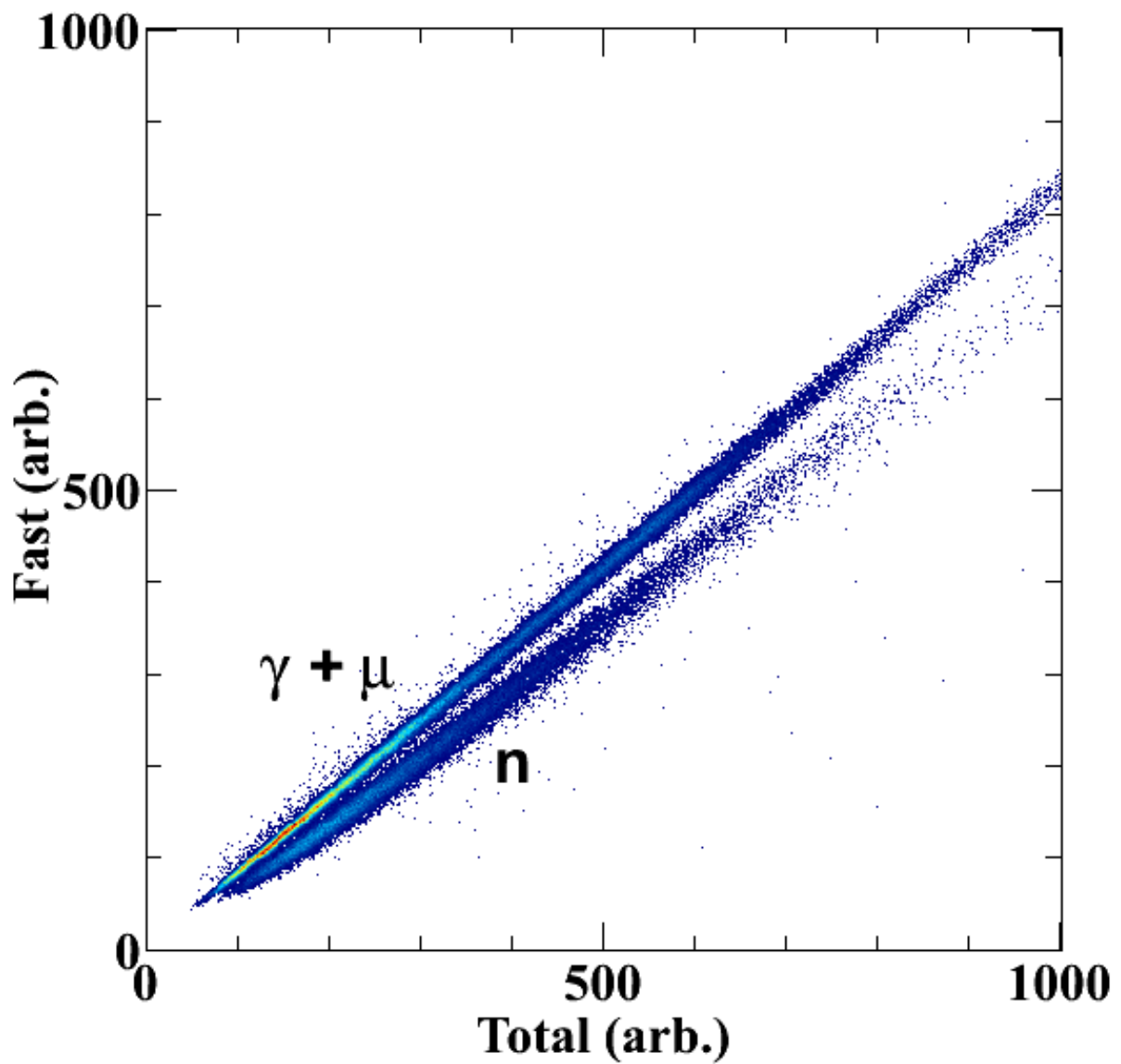
Figure 2.17: An example of the pulse shape discrimination in the Neutron Walls from an AmBe source. The gamma (and any cosmic) rays are in the upper band with the neutrons (and in an experiment hydrogens) in the lower band.
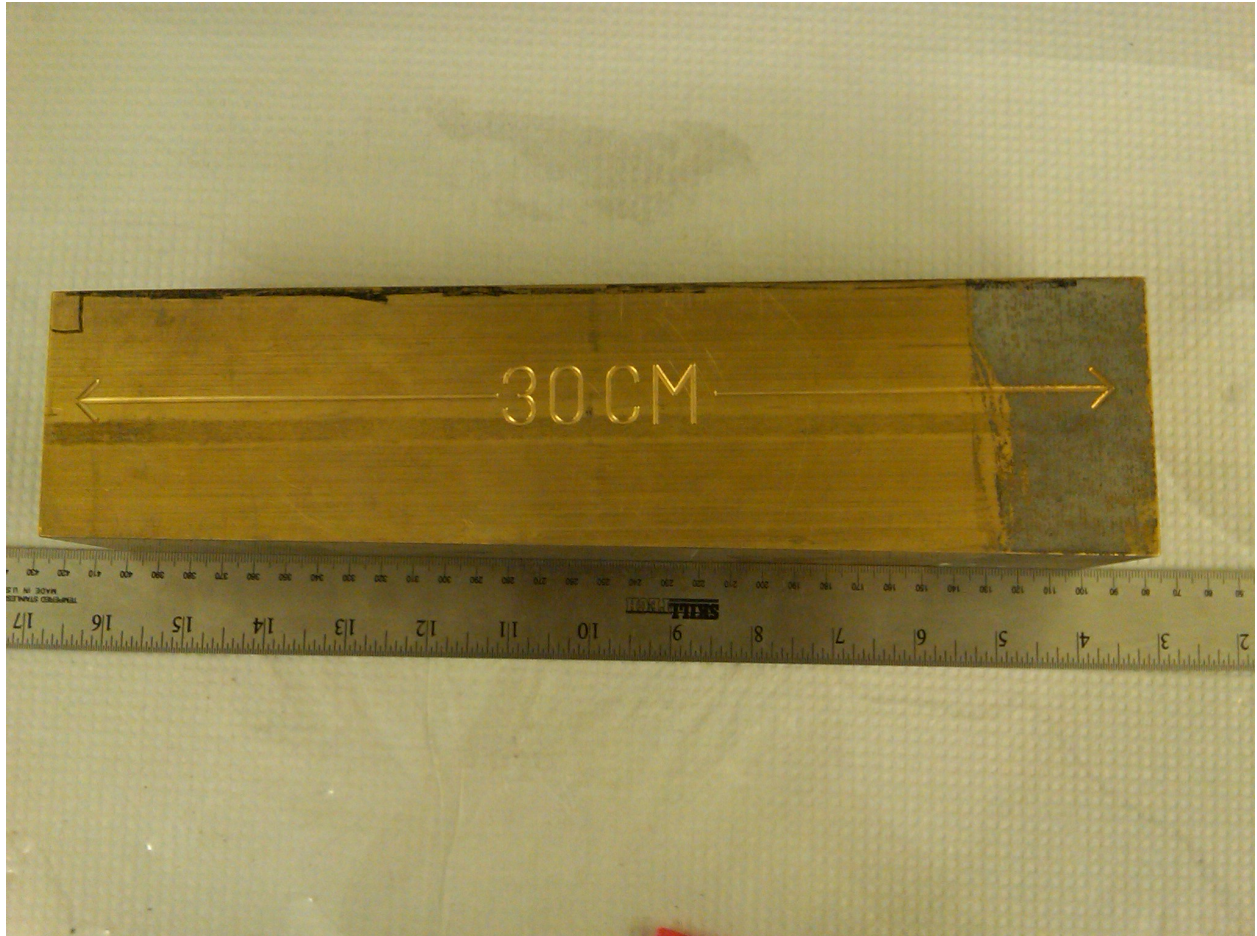
Figure 2.18: A picture of one of the four shadowbars.

Figure 2.19: A picture of the shadowbars in the mount blocking certain areas of the backward wall.

2.5.1 The Forward Array Start Timer

The Forward Array is a new timing detector array of 16 scintillating pieces built specifically for this experiment and for two directly preceding it. It replaced a timing array consisting of 5 scintillating pieces used previously. The Forward Array was constructed and tested in the early Spring of 2009.

The Forward Array consists of an aluminum plate constructed at Western Michigan University with modifications made at Michigan State University. The plate is circular with a 4.5 inch diameter and a 72°gap in azimuthal angle about the beam axis. The plate has a one inch diameter hole cut in the center to allow passage of the beam. The plate is aligned normal to the beam axis with the center being about 11 cm from the center of the target.

Sixteen roughly equal sized, plastic NE-110 scintillators are arranged on the face of the plate. All faces of each scintillator were painted with Bicron BC-620 reflective paint and wrapped in aluminized mylar foil in order to keep as much light as possible from escaping the scintillator or entering the next. Only the back face was left unpainted and unwrapped where it is coupled to a very small Hamamatsu R5600U photomultiplier tube with an E5780 base. The tubes are held in place using Tra-Bond F113 Optical Epoxy. This epoxy was designed to have good optical conducting properties especially for contacts with glass and plastic which made this epoxy a good option for this task. The reflective paint and aluminzied mylar create a nearly undetectable cross talk between scintillators. Figure 2.20 shows the construction of the Forward Array.

In order to measure the energy of neutrons from a beam on target reaction, one must use time of flight techniques. Time of flight techniques require both a start trigger provided
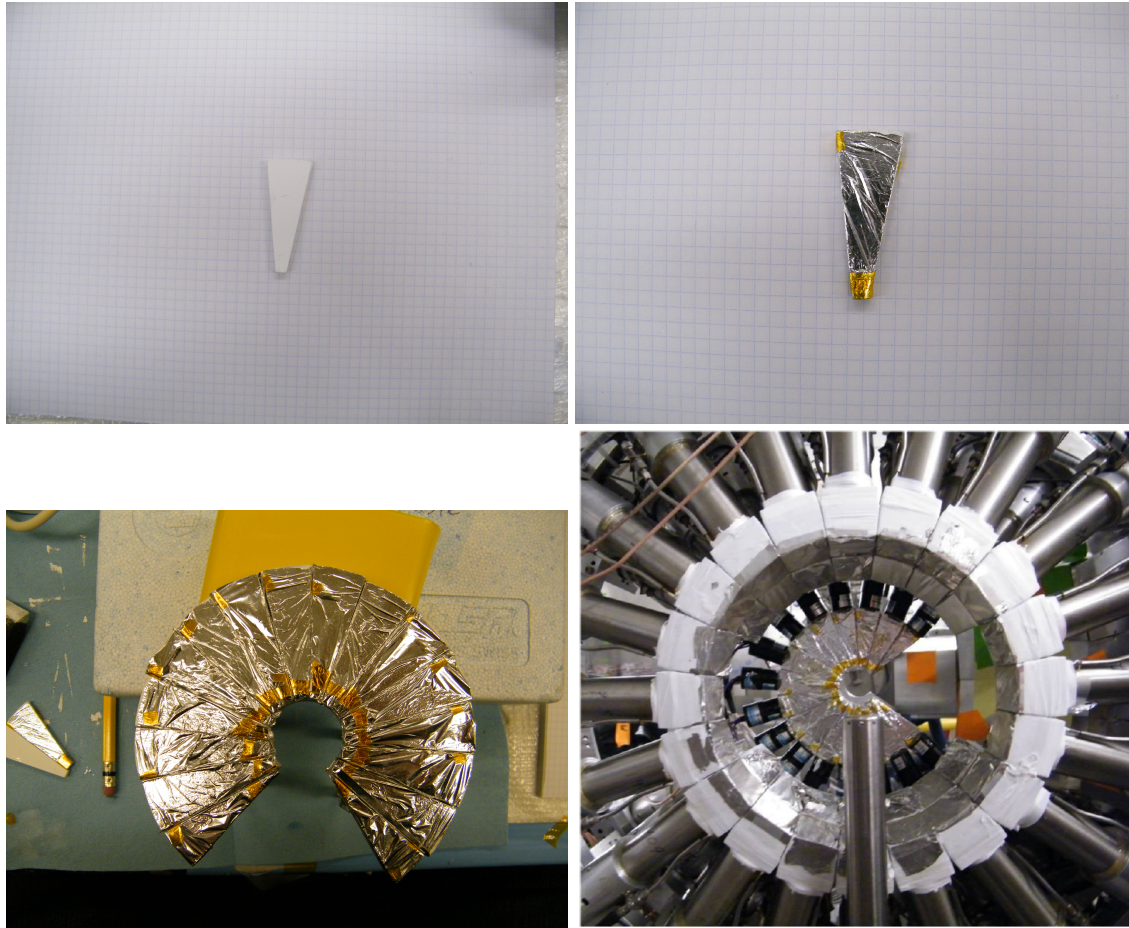
Figure 2.20: (upper left) A single element after painted with reflective paint. (upper right) A single element after wrapped with aluminized mylar. (lower left) All elements glued to the plate. (lower right) The Forward Array with the all of the PMTs glued and the Array put in place in the experimental setup.
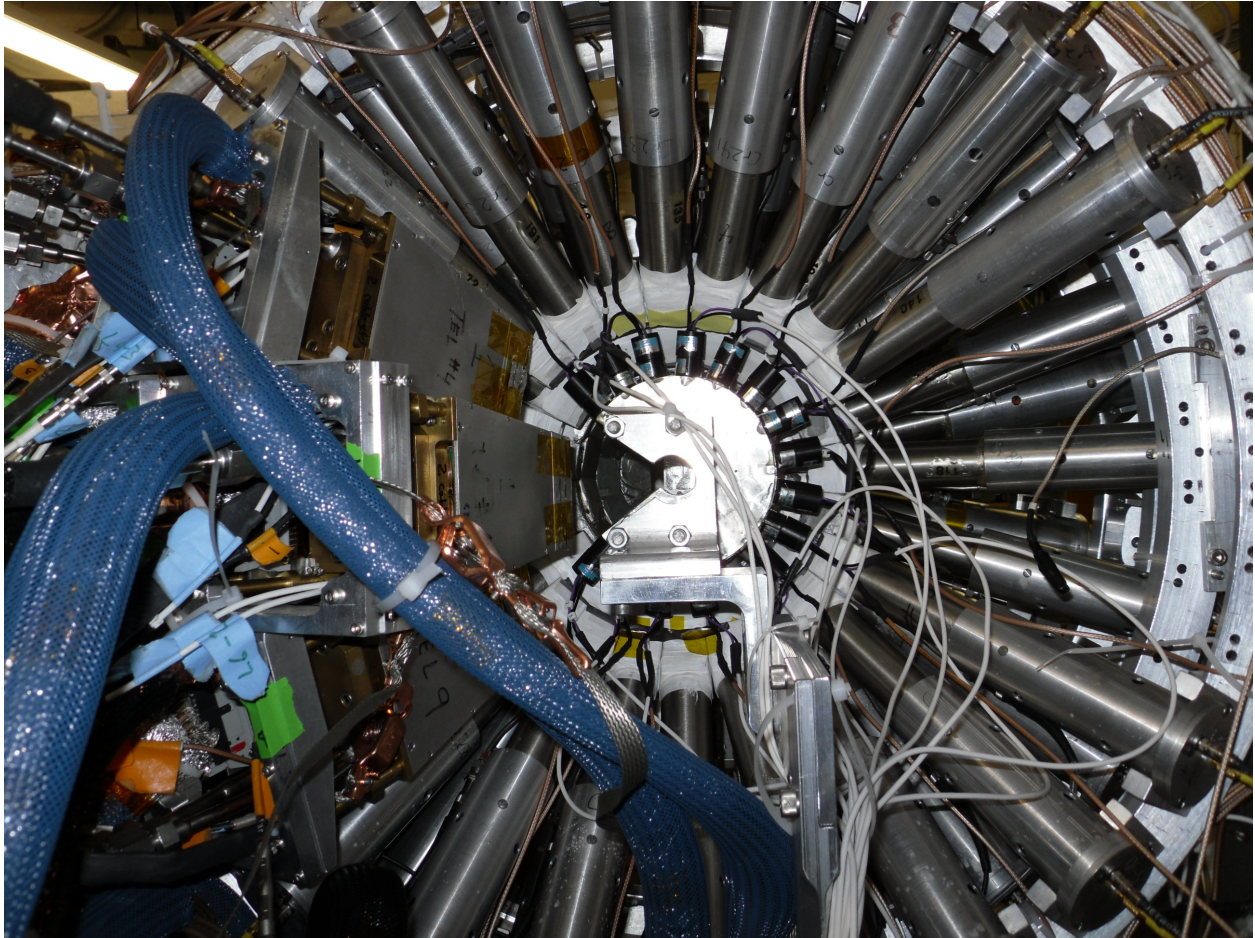
Figure 2.21: An picture taken just prior to the experiment with LASSA, the Forward Array and the Miniball all in final position.

from a detector and a stop trigger from another. In this experiment the Neutron Walls act as the stop trigger and the Forward Array acts as the start trigger. The neutron detected by the neutron wall is not the particle that acts as the start trigger, instead, the start comes from the shower of charged particles entering the Forward Array from a reaction in the target. With the small distance from target to Forward Array, the mean time that the shower of particles hits the Forward Array can be extrapolated back to the target to obtain a start time for the neutron time of flight. An example of the position of the Forward Array in relation to LASSA and the Miniball can be seen in Figure 2.21.

2.5.2 The Proton Vetoes

Neutron detectors, such as the Neutron Walls, use the scintillation from a recoil proton to measure the interaction of a neutron. In the case of very high energy protons, the Neutron Walls will detect the protons that interact in a similar way as the recoiled protons making it impossible to differentiate between neutrons and protons without additional information. This is the reason the Proton Vetoes were used. For each event, particles will pass through the Proton Vetoes which are thin enough that there is less than a 1% probability of interaction for neutrons. Unlike neutrons, protons and other charged particles will always deposit some energy in the vetoes on their flight path to the Wall. In these cases, software gates can usually be used to identify any charged particle contamination in the neutron spectra and determine which particles are charged and which are not.

Two different designs of Proton Veto scintillators were used in this experiment. One design, designated as the paddle design, is made from Bicron BC-408 scintillator and shaped into squares of 16 cm in length and 3/8 inch in thickness. On two adjoining sides of the scintillator is a wavelength shifting light guide. The junction of these light gudes is glued to a 1 inch diameter cylinder of UVT light guide which is coupled to a PMT with Dow Corning Q2-3067 optical grease. These paddles were sufficient for the low multiplicity of charged particles in previous experiments, however, in this experiment the high multiplicity of charged particles means that there could be an unacceptably high accidental coincidence rate between the charged particles and neutrons in the same region of the neutron wall. As such a finer granularity than the paddles can achieve was required.

For this reason, a set of 13 Proton Veto bars was made. Each bar was made out of the same plastic scintillating material as the paddles but are 12 mm thick by 24 mm wide

and 274 mm in length. Each bar was polished, wrapped in a white reflective paper, then wrapped in aluminized mylar and finally wrapped in a black plastic, all to avoid light loss and light contamination as well as to prevent optical cross talk. For this experiment, these bars were used to cover the angles of the forward wall and four paddles were used to cover the angles of the backward wall. A picture of their mount location on the outside of the thin walled chamber can be seen in the last picture of Figure 2.22.

2.6 Electronics

This experiment required extensive amounts of electronics. Over this section I will describe the electronics of each section as individually as possible. To begin I will start with the master trigger and then proceed to move through each individual system's submaster.

2.6.1 Master Trigger

During the course of the experiment, several different trigger conditions were used, primarily for different calibration purposes. During standard data runs, a coincidence between the Forward Array and Miniball submasters was required to generate a trigger. All the other systems operated in a slave condition. These two systems were chosen for the trigger requiring that the Miniball have a minimum multiplicity in order to reject peripheral events that were not the focus of this experiment and so that the Forward Array would ensure a time component for every event. If need be, any logic signal in the dashed box in Figure 2.23 could be used as the trigger for different purposes by switching one cable. This allowed rapid trigger changes between calibration runs.

Due to efficiency issues in the silicon, a trigger for the 2 Hz LASSA pulser is also

Figure 2.22: (From top to bottom) The Veto bars after they have been polished and partially wrapped. The complete array of the Proton Veto bars in their mount. All Proton Veto bars and paddles in experimental setup.

implemented separate from the rest of the system submasters. The "OR" trigger from the Pulser trigger and the submaster trigger provided the Master trigger signal. The output from this "OR" gate was set to a 20 μs length to avoid any retriggering. If an event causes the Master trigger to fire, this 20 μs gate is sent to each of the submaster systems. At this time the master also begins a latch, providing a computer busy signal. In the instance of a pulser trigger the computer trigger is delayed an additional 786 μs to provide enough time for the signal digitization in the ASIC electronics. Once triggered, data was acquired through the NSCL DAQ system. Once the DAQ is finished with an event, a signal from the I/O module clears the computer busy latch and the LASSA internal busy latch, readying the electronics for another event.
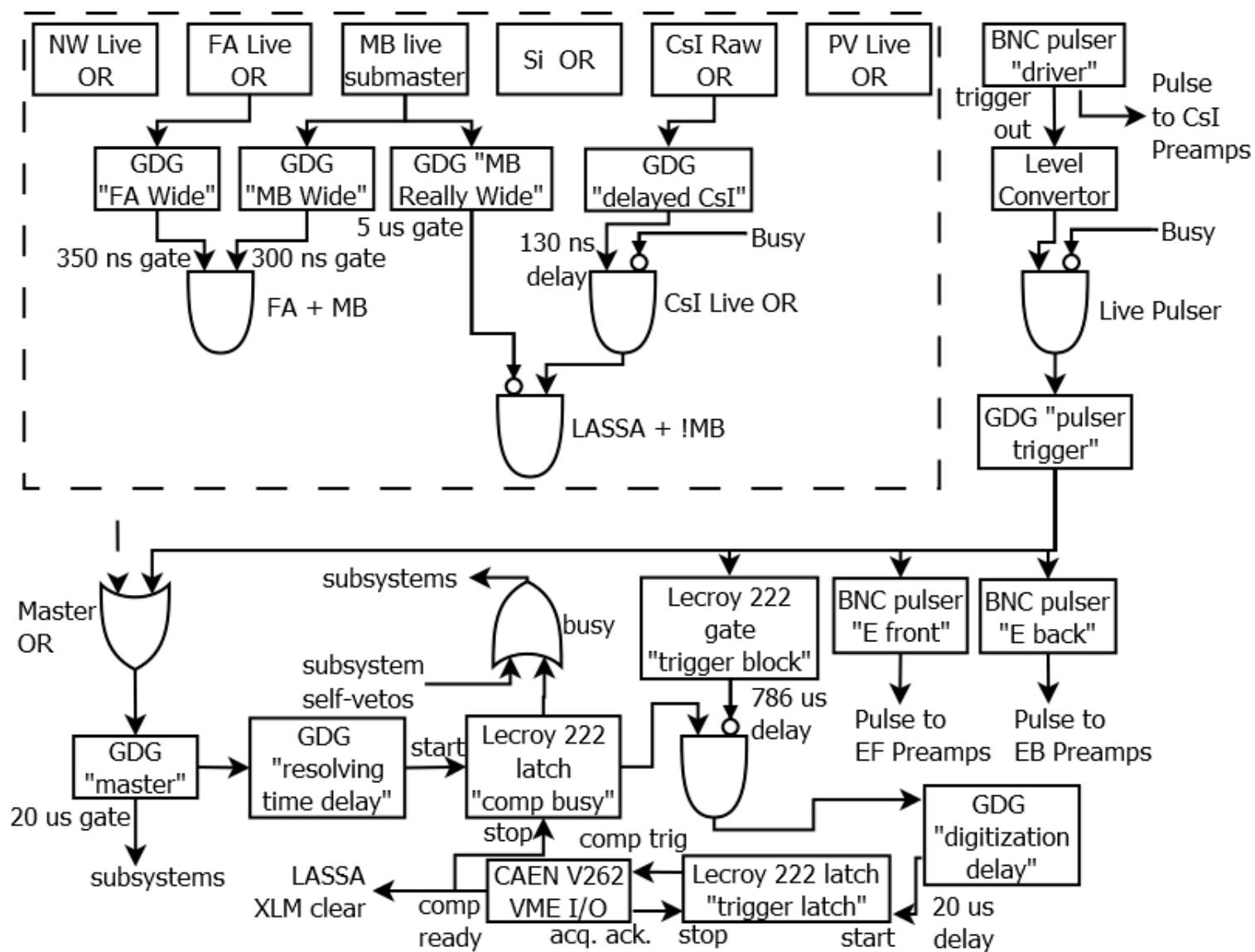
Figure 2.23: This is a schematic diagram of the Master trigger logic for this experiment. The individual subsystems will follow.
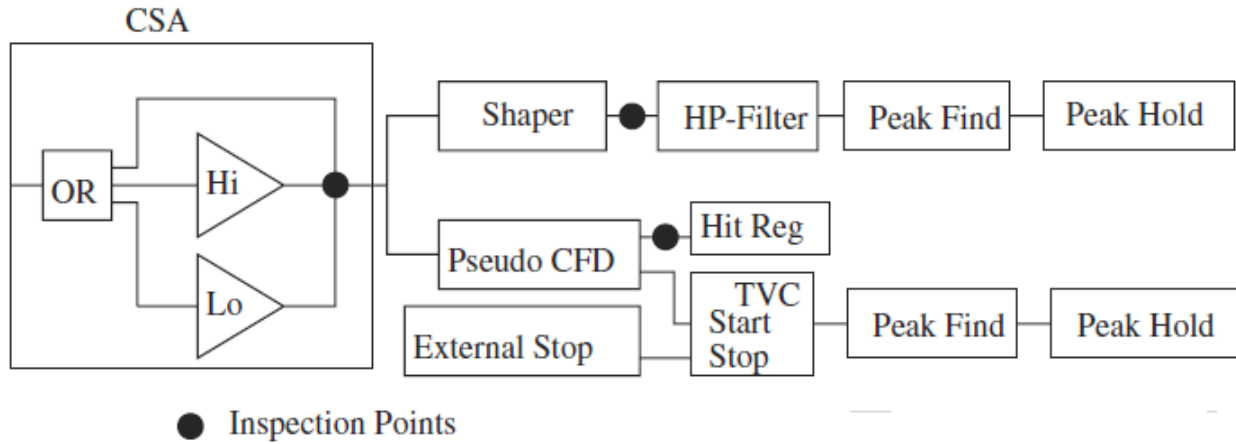
Figure 2.24: A block diagram of the ASIC electronics logic. [7]

2.6.2 LASSA submaster

The silicon strips and the CsI crystals are read out using very different systems. The silicon uses an Application Specific Integrated Circuit (ASIC) while the CsI uses conventional electronics. The ASIC's were designed to be used with the HiRA array, a similar telescope like detector to that of LASSA. The descriptions of the H1NP16C chip can be seen in [7]. In general, the electronic processing which is shown in 2.24 is not that different than any of the other detector systems.

The signal from a silicon strip can be directed through a high gain or low gain charge sensitive amplifier (CSA), depending on the constraints of the experiment. Instead, we chose to use external preamps to maximize the gain. The signal is then divided to a constant fraction discriminator (CFD) that determines if a particle hit that strip and then on to a time to voltage converter (TVC). The other part of the signal is shaped in a time of about 1 μs. The time and energy of each strip is stored for readout until a trigger tells it to be read out. If the trigger is not provided in a given amount of time, the values are cleared. This is the same concept as the Neutron Wall and Miniball subsystems except the

44
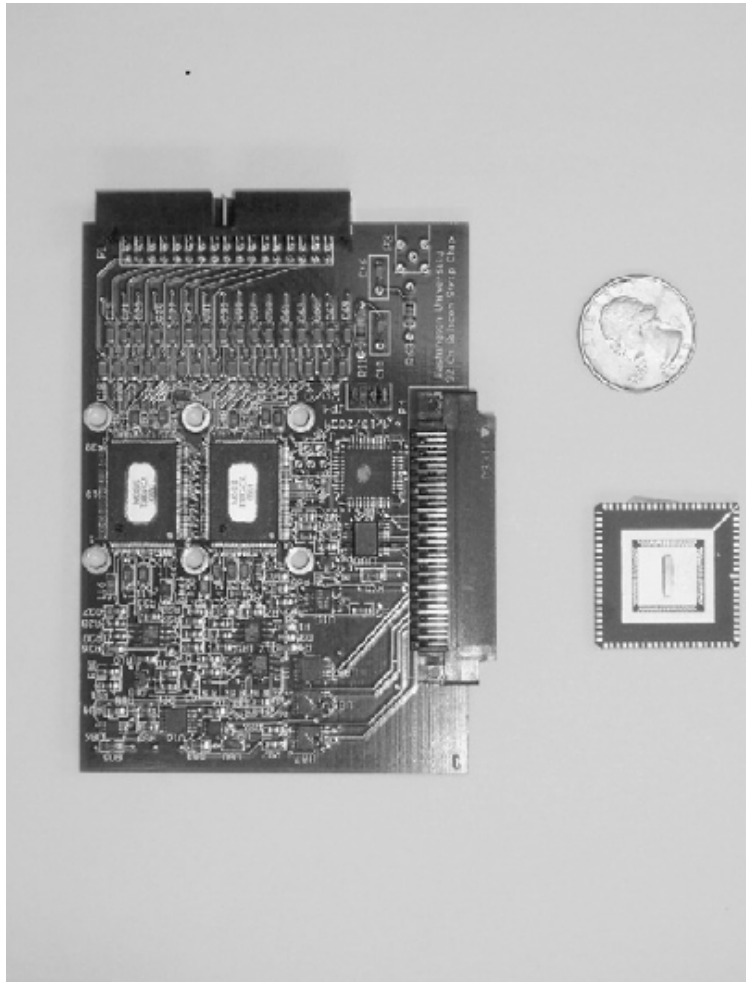
Figure 2.25: An example of a chipboard with a prototype chip. The quarter is used for a size reference.

ASIC's do it on a channel by channel basis. The biggest difference between the ASIC's and conventional electronics is the scale of the space, size and cost difference. Each chip processes 16 channels individually, with two chips comprising one chipboard. A chipboard is shown in Figure 2.25 with a prototype chip and a quarter for a size reference. Another benefit of the ASIC's is that they have several inspection points, shown by the large black circles in Figure 2.24, which can be monitored on a channel by channel basis remotely. The chipboards also contain the electronics to distribute the bias voltage to the silicon strips.
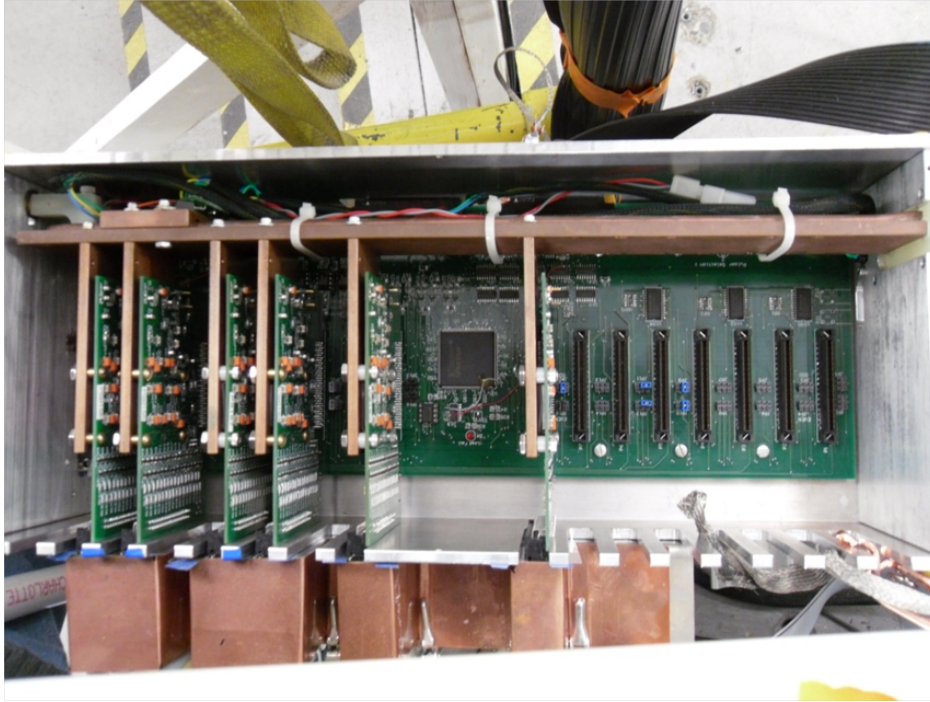
Figure 2.26: A picture of the HiRA motherboard used for this experiment with six chip-boards contained within.

A maximum of 16 chipboards can be used in one motherboard. A motherboard with six chipboards that were used in this experiment can be seen in Figure 2.26. Each motherboard contains a field programmable gate array (FPGA) in order to handle the communication between the chips and the DAQ system. The energy and time from the ASIC are sent to a SIS3301 flash ADC. A JTEC XLM universal logic module manages the communication between the silicon subsystem and the master logic. This is the module that accepts the master trigger and tells the computer when the silicon data has been digitized. In general this system is optimized for sparse readout, which is the reason that there is the long 786 μs delay for the 2 Hz pulser trigger. The system is not optimized to read out that many channels.

Since the ASIC chips treat each channel individually, particularly noisy strips or electronics channels will not cause a backup on the whole system so long as those strips are
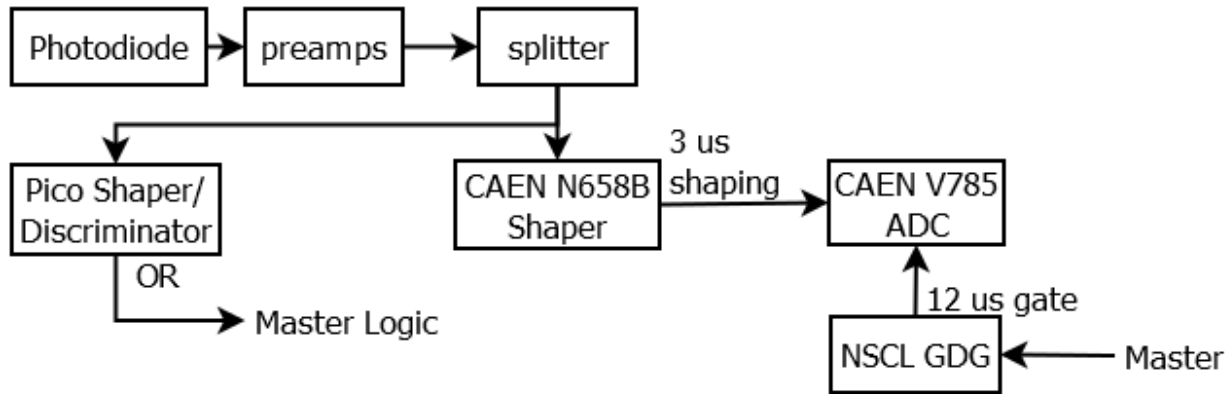
Figure 2.27: A schematic diagram of the CsI Subsytem.

not part of the trigger. The down side to this is that the dead time of individual channels is impossible to measure through scalers. The 2 Hz pulser was designed to measure this and the treatment and analysis of such is described in 5.1.2.

The CsI subsystem is much simpler than the other systems since there are much fewer channels than most of the other detectors, and the times are not digitized. In an event, the light generated in the crystal is collected by a photodiode and amplified by preamplifiers contained within the LASSA telescope. The signal is split into a time path which creates a raw "OR" signal that is passed to the master logic while an energy path is shaped and digitized in an ADC. The time length of a signal from the CsI is sufficiently long that a subsystem busy and fast clear are not required, instead the master trigger simply starts the ADC gate. The electronic diagram for the CsI subsystem is shown in Figure 2.27

2.6.3 Miniball Subsystem

Signals from the photomultiplier tubes in the Miniball are treated two different ways. For telescopes in rings 7 and forward, their signals are sent directly to custom made Miniball splitters. For the backward rings, their signals are first amplified before being sent to

the splitters. The splitters passively split each signal into four paths. A portion of the signal is amplified and sent to a modified Phillips 7106 discriminator which provides time information and the basis of the Miniball logic. Modifications were made to the discriminators in order to prevent any retriggering within 1.5 μs. The remaining signal is split into the other three paths, designated fast, slow and tail. This split is done passively at 92% for the fast and 4% each for the slow and tail. This causes the integrated charge between all three time regions to be reasonably similar.

Due to the Pulse Shape Discrimination timing, the Miniball subsystem would be triggered before the master logic would produce a master trigger. To rectify this, a fast clear circuit was created that would abort digitization and close the QDC gates if a master trigger is not received within 500 ns of the subsystem trigger. A Miniball subsystem busy gate was sent to the global busy so that triggering on another event was impossible during this fast clear window. The Miniball busy was set to be 1.5 μs long so to account for the fast clear time as well as the QDC internal busy to flush the aborted data that was digitized.

The Miniball subsystem was typically triggered on a minimum multiplicity in order to concentrate on central collisions. To achieve this, the analog SUM outputs from each discriminator were added in a summer/amplifier module. Each discriminator provided a 50 mV/hit signal. The discriminator settings for the trigger were then set to correspond to a multiplicity in the Miniball chosen for each beam isotope and energy combination. Since our data collection was limited by data rate and not beam rate, we adopted two different multiplicity triggers. This increased statistics for the largest multiplicity events while still allowing for collection data from more peripheral collisions. Both discriminators were blocked by the global busy to avoid triggering while the system was busy. The high
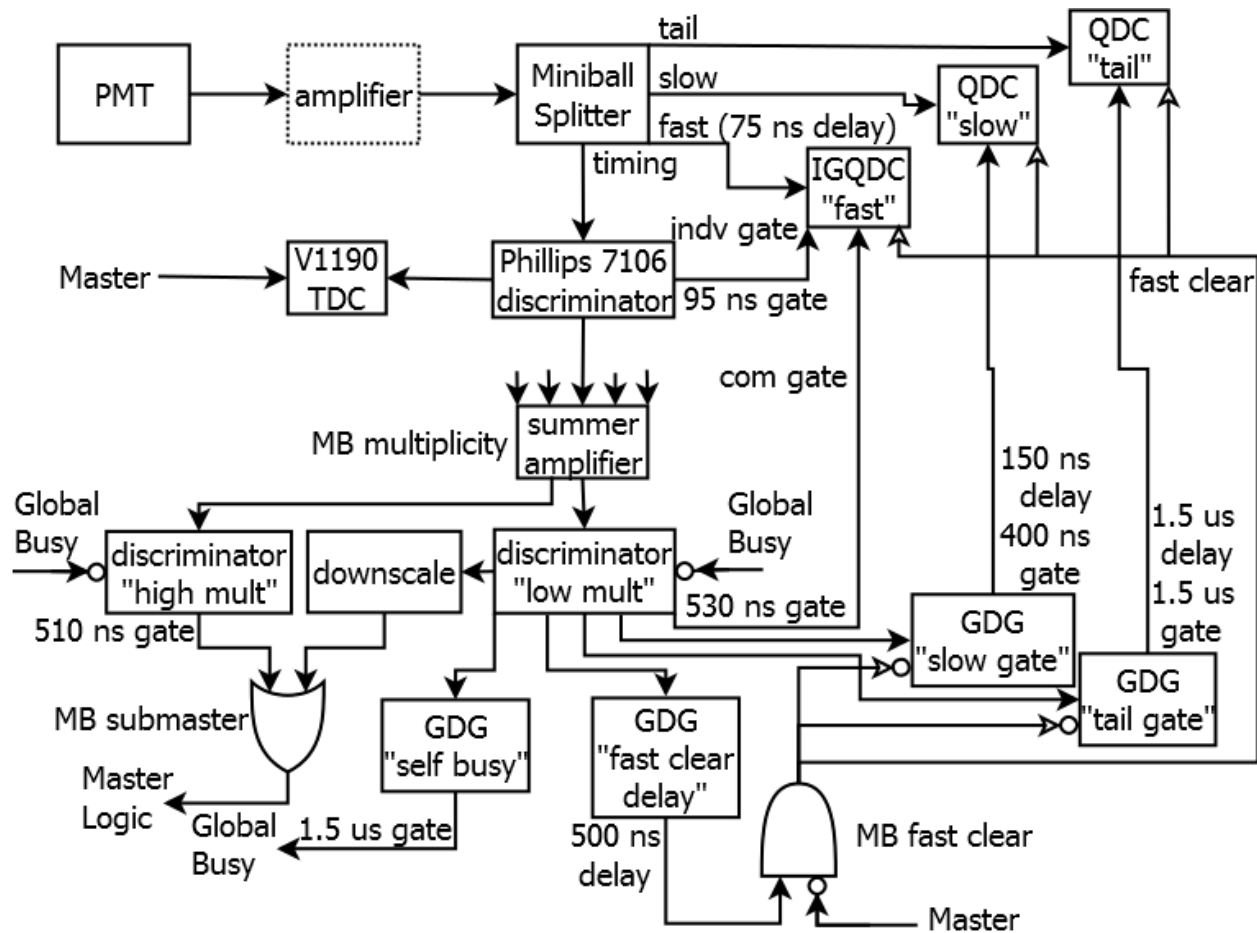
Figure 2.28: A schematic diagram of the Miniball Subsystem.

multiplicity trigger was run in an "OR" condition with a downscaled low multiplicity trigger. This "OR" signal created the Miniball submaster trigger which was then sent to the global trigger logic. For better Pulse Shape Discrimination, the fast QDC was triggered by the low multiplicity trigger instead of the submaster. The Miniball subsystem as a whole is shown in Figure 2.28

2.6.4   Neutron Wall Subsystem

In order for the Pulse Shape Discrimination techniques used in the Neutron Wall, the anode signal from the photomultiplier tubes are passively split to a common gated QDC and an

individually gated QDC (IGDQC). The common gated QDCs integrate the collected charge for approximately 300 ns while the IGQDC capture integrated charge for the first 30 ns of signal. The dynode signal from the PMT is sent to a constant fraction discriminator for timing purposes and to start the subsystem logic. All channels in a given QDC are "OR"ed together to provide the start logic for the common gate, while the individual discriminator signals from the dynodes start a 60 ns long signal for the IGQDC. The common gates are vetoed by a local self veto, which prevents refiring, and by the global busy so that the Neutron Walls stay inactive while another subsystem or data acquisition process was busy. Three common gated QDC's were needed to accomodate all the electronics channels. An "OR" signal between these three QDC's comprises the Neutron Wall submaster. In a similar way to the Miniball, the QDC's must begin integration of charge before the global master can start. To counter this, a fast clear circuit was again created when the submaster fired. If a master trigger was not received in time, the data was flushed. The full Neutron Wall subsystem is shown in 2.29.
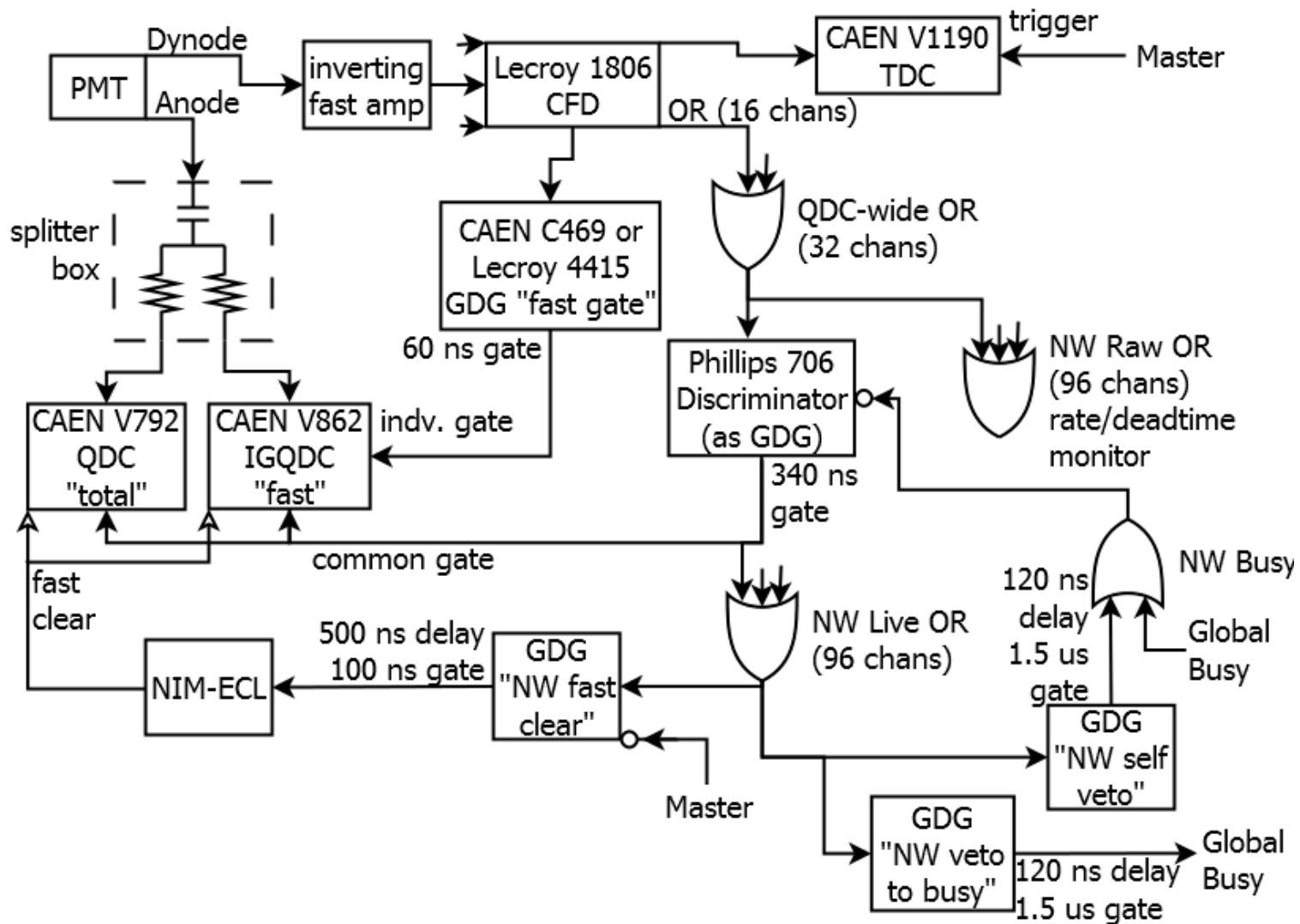
Figure 2.29: A schematic diagram of the Neutron Wall Subsystem.

2.6.5 Forward Array, Proton Veto and Downstream Scintillator Subsystem

The Forward Array trigger logic is very similar to the CsI subsystem with an addition of time processing. The subsystem is shown in Figure 2.30. A TDC was set to common stop mode so that a fast clear circuit was needless. Since the Forward Array TDC was self timing the "OR" from the Forward Array provides the common stop. Since the Forward Array is meant as the start time for the system, the "OR" is also sent to the Neutron Wall and Miniball TDCs to provide a time reference.

The same TDC and ADC used for the Forward Array was also used for the Proton Veto time and pulse heights. Figure 2.31 shows the similarity of the electronics from the Forward Array to the Proton Vetoes.

The signal from the photomultiplier in the Downstream Scintillator was simply discriminated and counted in a CAEN V830 scaler. This was sufficient information for the purpose of this experiment and as such the energy and time was not read out for this system.
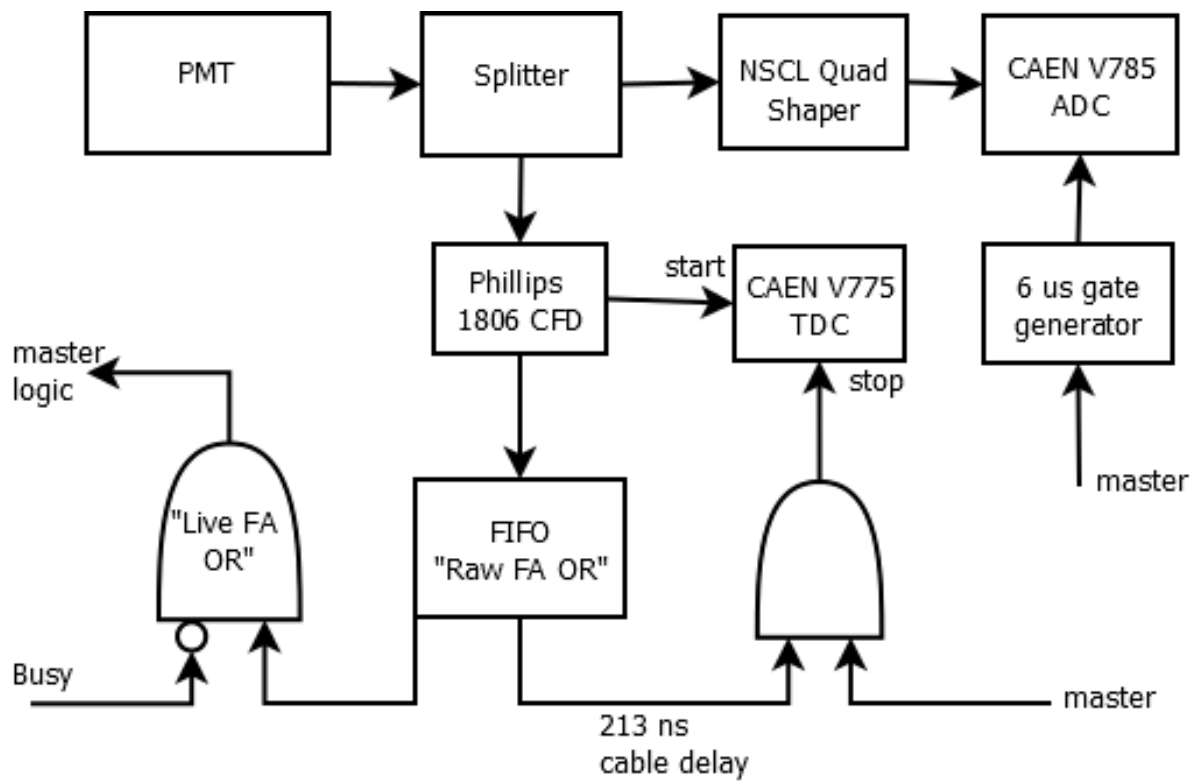
Figure 2.30: A schematic diagram of the Forward Array Subsytem.
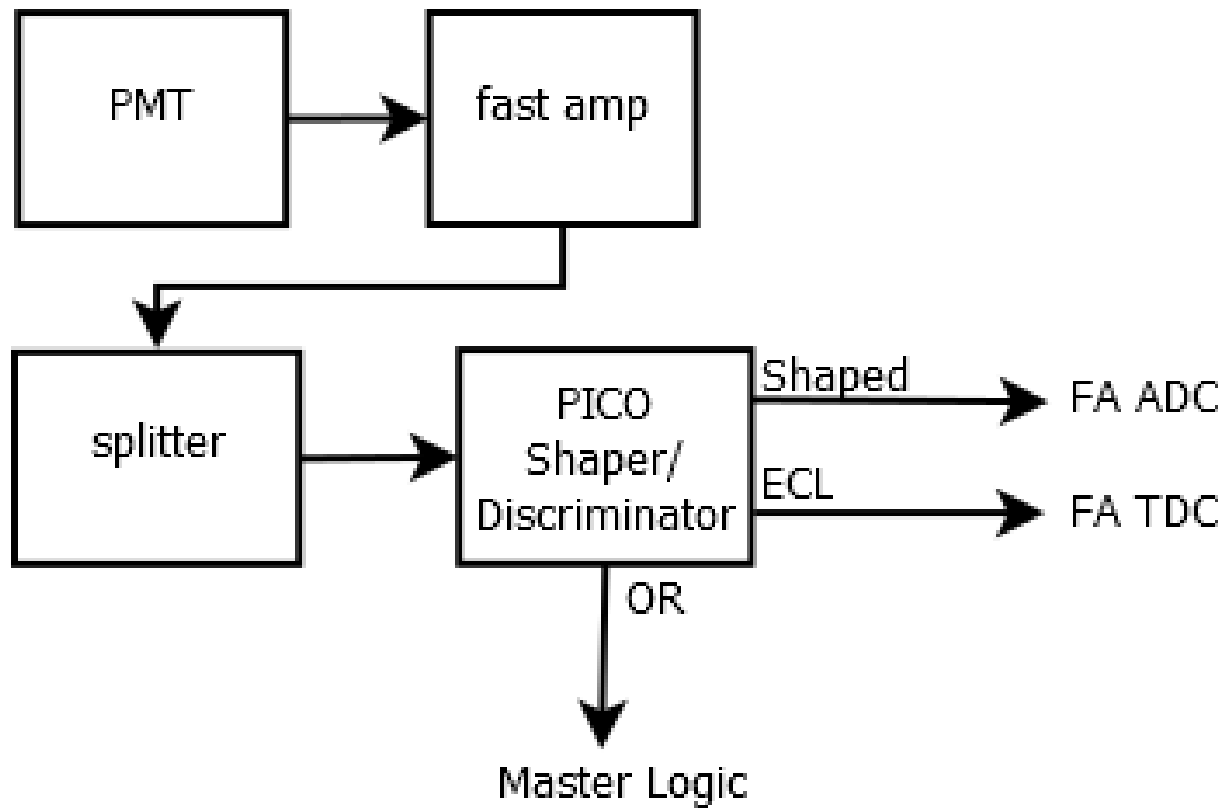
Figure 2.31: A schematic diagram of the Proton Veto Subsystem.

Chapter 3

Data Calibration

3.1   LASSA Calibration

The calibration of the LASSA telescope consists of three steps; a precise energy calibration of the silicon detectors using an α emitting ^{228}Th source, a pulser calibration to test for any nonlinear responses in the electronics and finally an energy calibration of the CsI(Tl) crystals.

3.1.1   Silicon

3.1.1.1   Thorium Source Calibration

For this experiment a ^{228}Th source was used to calibrate the silicon detectors. This source has a decay chain with five strongly populated energies separated by at least 200 keV making it ideal for our uses. To greater benefit, the decay chain includes the 8.78486 MeV decay from ^{212}Po to ^{208}Pb which is a largest energy that one can obtain in a commercially available source.

At Emission	After Losses
5.42315	5.0509
5.68537	5.3268
6.28808	5.9532
6.77830	6.4616
8.78486	8.5210

Table 3.1: A list of the α energies (in MeV) used for calibrating the Silicon. The right column shows the value after the energy losses are taken into account.

There are several issues that need to be addressed in our calibration. The source is sealed with a 50 μg/cm^2 gold window through which the α particles must pass in order to reach the detector. Each LASSA telescope also has a 1.9 micron thick aluminized mylar foil in front of the silicon in order to prevent the interference of electrons in the detector and to effectively create a Faraday cage around it, minimizing electronic noise contamination. This foil provides the largest contribution to the energy loss of the alpha particles. We must also correct for the dead layer of the silicon. Each silicon detector has a region approximately one micron thick that does not actually contribute to the active volume of the detector. In this dissertation the total energy loss for the particles to pass through each layer was calculated with the spectrometer simulation code LISE++ which bases its calculations in the Bethe equation, i.e. Equation 2.1. Table 3.1 gives the energies of the thorium source before and after losses from the foils and the dead layer.

Using the ^{228}Th source we can get a very accurate calibration of energy as a function of electronic channel. Using an equation of the form,

$$E(\text{MeV}) = A_0 + A_1 * \text{ch} \tag{3.1}$$

where A_0 and A_1 are calibration constants, a simple calibration formula can be fit. Figure

3.1 shows the result of a program written for the HiRA array to automatically fit the alpha energies of each strip of the silicon detectors. The automatic fitting is useful since it avoids having to calibrate all 192 strips of the LASSA array by hand. The program is designed to fit a gaussian to the five strong peaks as seen in the top of Figure 3.1. The locations of those peaks are then fit to match with the energies from Table 3.1. The fit result for the alpha energy as a function of channel can be seen on the bottom of the figure.

3.1.1.2 Pulser Calibration

In previous experiments with these electronics, a nonlinear response was noted in certain voltage regions. To paramaterize this dependence, we use a well tested, linear PB-5 pulser developed by Berkeley Nucleonics Corp. During the experiment a series of pulser ramps were completed both for the preamps used for the silicon and for the preamps used for the CsI.

In the case of the silicon preamplifiers, it was found that at low voltage, the voltage of the peak processed by the electronics became slightly nonlinear as a function of the output voltage of the pulse. During the experiment we ramped the pulser two different ways. The first ramp used 18 pulses from 0 to 9 V. The second was a very fine ramp using over 20 pulses from 0 to 1 V. The two ramps overlap from 535 mV to 1.035 V. Figure 3.2 displays all the pulses from both ramps as well as a linear fit for all points greater than 535 mV in a typical strip. The lower plot zooms in to display the nonlinearity of the electronics at low voltages.

One benefit of silicon detectors is that the charge ionized by light particles depends linearly on the energy deposited by a charged particle. If this charge is amplified by a charge sensitive premaplifier the output voltage of the preamplifier will also depend
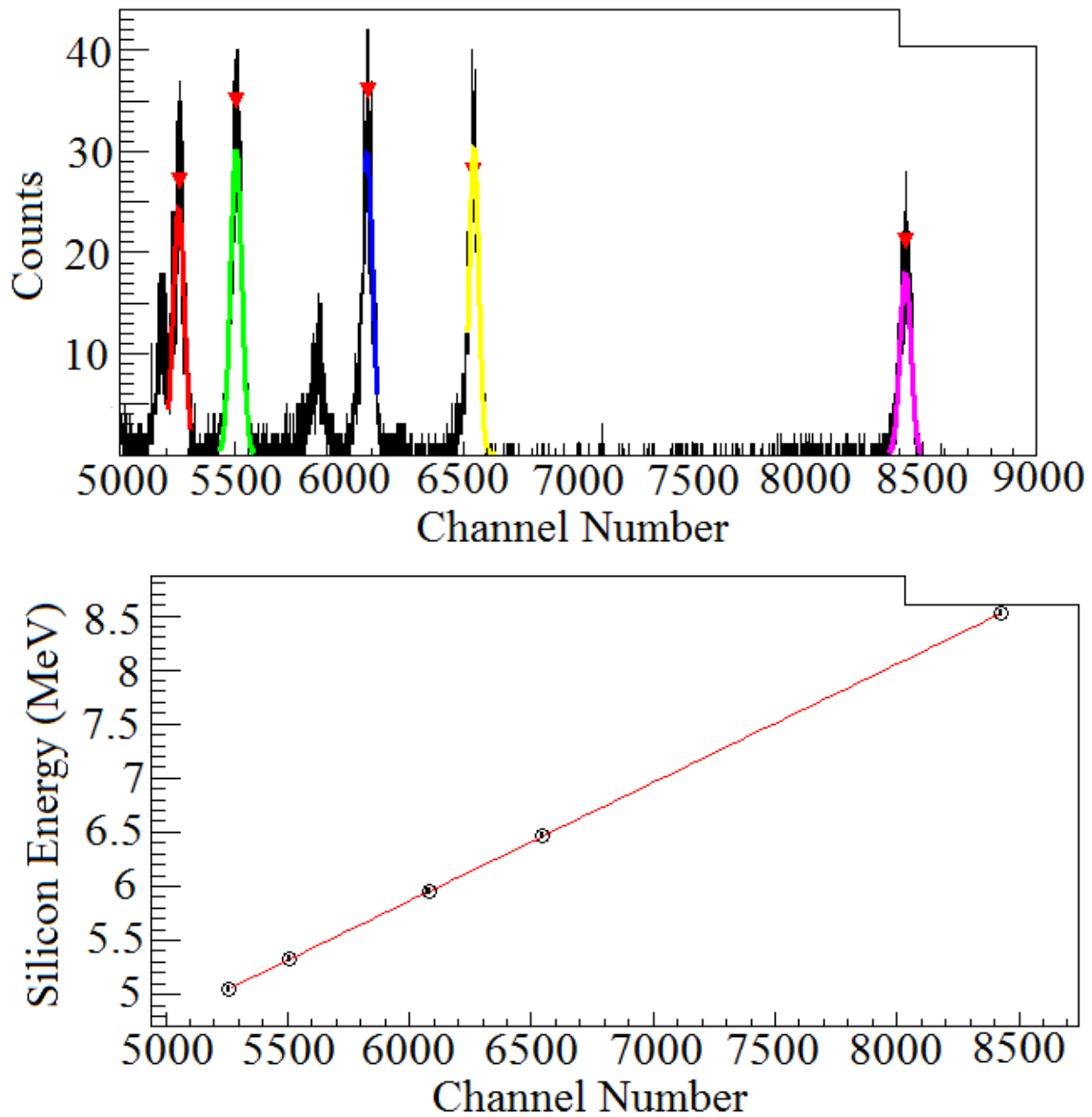
Figure 3.1: Using a fitting program we can automatically generate peak locations(top) and energy vs channel relation (bottom).
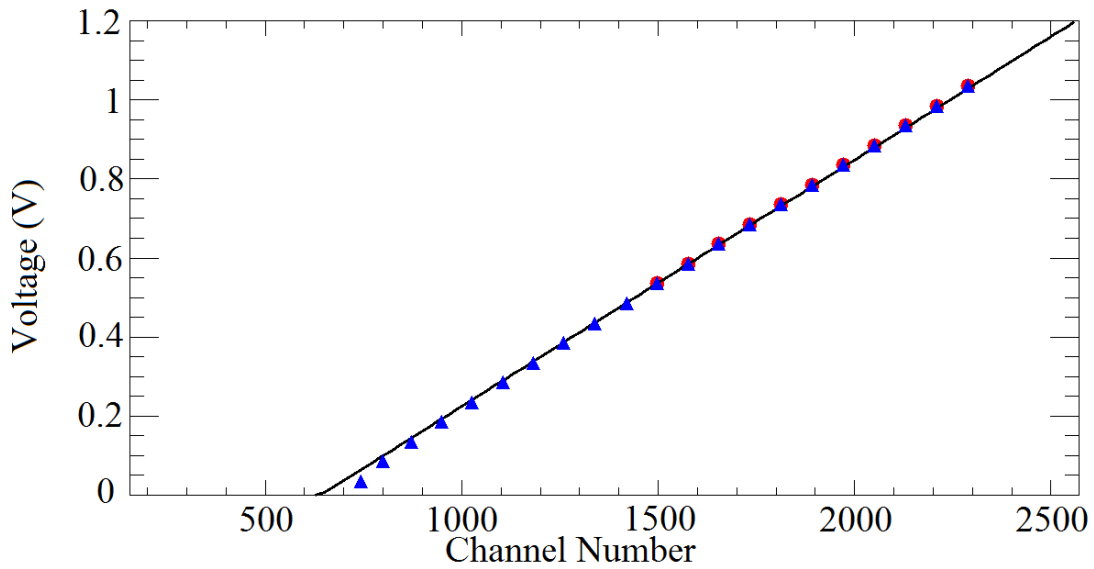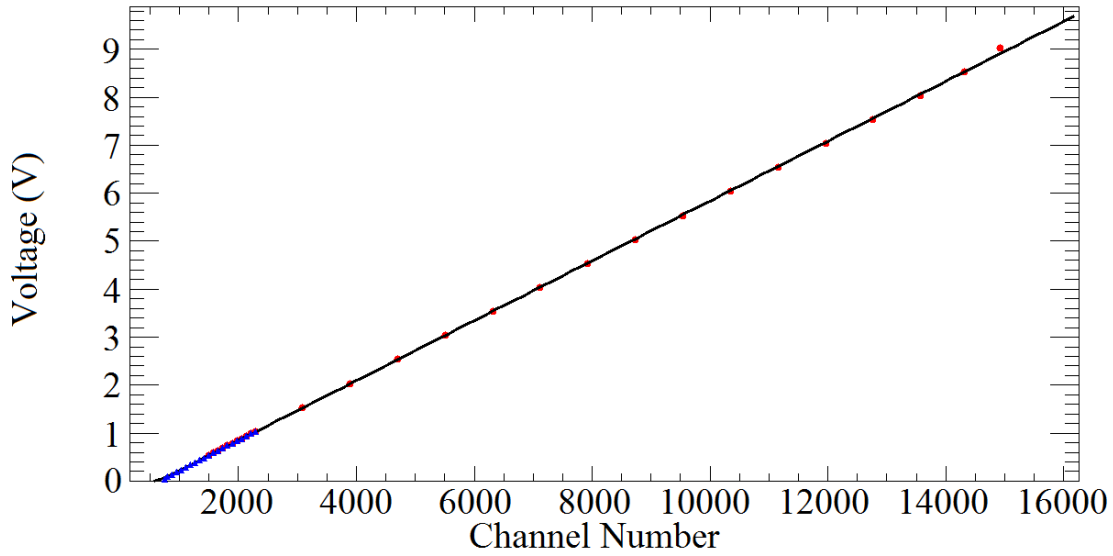
Figure 3.2: An example of the pulser ramps over the different regions of one strip of a silicon. The red circles correspond to pulses greater than 535 mV and the blue triangles are less than 1.035 V. The plot on the bottom is zoomed in on the low region to demonstrate the nonlinearity and offset.

linearly on the energy of the charged particle. In the region where the response of the electronics is linear the following equations can be used to relate the pulser voltage to the channel number obtained when the electronics signal is digitized.

$$V = l_0 + l_1 \text{ch} \quad \text{for} V \geq 535\text{mV} \tag{3.2}$$

$$\text{ch} = \frac{V - l_0}{l_1} \tag{3.3}$$

Here, V is the output voltage of the pulser, ch is the digitized channel number, and finally l_0 and l_1 are linear fitting parameters. This formula is valid above 535 mV where the response is linear. Since the alpha calibration provided a relationship between the energy and the channel as shown in 3.1, a linear relation between energy and voltage can be described by,

$$E = A_0 - \frac{A_1 * l_0}{l_1} + \frac{A_1}{l_1} V. \tag{3.4}$$

In the region where the electronic response is linear, the function used for the voltage, V, is obviously given by the linear fit from the pulser, causing the energy equation to reduce to exactly the same as the alpha fit. In the region where the electronic response is nonlinear, all pulses less than 1.035 V were fit with a fourth order polynomial and this fit is used. In order to avoid a discontinuity in the energy calibration due to a discrete switch from the nonlinear to linear regions, a blending was done in the region of overlap from 535 mV to 1.035 V. The energy calibration for this region has the form

$$E = E_{\text{poly}} \frac{c_{\text{lin}} - x}{c_{\text{lin}} - c_{\text{poly}}} + E_{\text{lin}} \frac{x - c_{\text{poly}}}{c_{\text{lin}} - c_{\text{poly}}}. \tag{3.5}$$

Here, E_{poly} represents the energy from the calibration equation in the nonlinear response

region and c_{poly} represents the channel corresponding to 535 mV. Similarly, E_{lin} represents the energy from the calibration equation in the linear response region and c_{lin} represents the channel corresponding to 1.035 V.

3.1.2 Cesium Iodide

The CsI energy calibration has two components, like the silicon. As with the silicon calibrations, the first is to calibrate the ADC values to a linear function of the charge at the input of the preamplifier which reads the photodiode signal. In the case of the CsI shapers there is a nonlinearity at the high channel end of the spectrum beginning near channel 3800 out of 4096 across all crystals. Using a procedure similar to that of the silicon calibrations , all pulses below channel 3800 are fit linearly. For the region above 3800, a fitting procedure using the formula,

$$V = l_0 + l_1 * \text{ch} + n * (\text{ch} - 3800)^2 \tag{3.6}$$

where l_0 and l_1 are fixed values from the linear fit and n is the only variable being fit for this region.

The point of the pulser calibration is to simulate the light output collected by the photodiode. Hydrogen isotopes produce a light output that is linearly proportional to the energy deposited in the crystal. The second step of the calibration is to calibrate the signal corresponding to the energy deposited in the CsI based on the corresponding energy deposited in the silicon. Using the LISE++ program developed at the NSCL, we are able to calculate the energy an isotope would deposit in both the silicon and the CsI. For protons that stop in the CsI and for a particular thickness of silicon, the relationship

E(CsI)=f(E(Si)) is valid for a first order calibration, where f is a fifth order polynomial. A program was written to make this process more streamlined. Displayed in Figure 3.3 is an example of a typical CsI crystal.

This program takes two inputs, a plot of the calibrated silicon energy versus the CsI channel number from the ADC and a hand drawn gate around the protons at silicon energies larger than 2 MeV as shown in the top half of the figure. The program already knows the relationship between energy deposited in the silicon and energy deposited for particles that are stopped by the CsI crystal for the given thickness of silicon. The program then finds the profile, or average, value of silicon energy for a given ADC channel number and calculates the CsI energy corresponding to the same silicon energy. By performing the calibration for each channel number within the gate the program can generate a linear relationship from CsI ADC channel number (in the linear region of the electronics) to CsI energy. An example of this calibration is shown by the red line in the bottom half of the figure.

The limiting factor in the calibration of the CsI is that the fit becomes less trustworthy if you include silicon energies below about 2 MeV since high energy protons deposit a slowly decreasing amount of energy ($\propto (1/E)$) in the silicon. If those energies are included in the fit, the weak dependence on silicon energy can cause fluctuations in the extracted values leading to a less reasonable fit. Thus, only the low energy region is initially calibrated by this method. In order to extend the calibration to higher energies, the punch through points are used. Protons with sufficient energy will penetrate through the CsI, i.e. "punch through". In this case the particles will not deposit all of their energy in the CsI. The minimum energy required for a proton to punch through the CsI crystal is
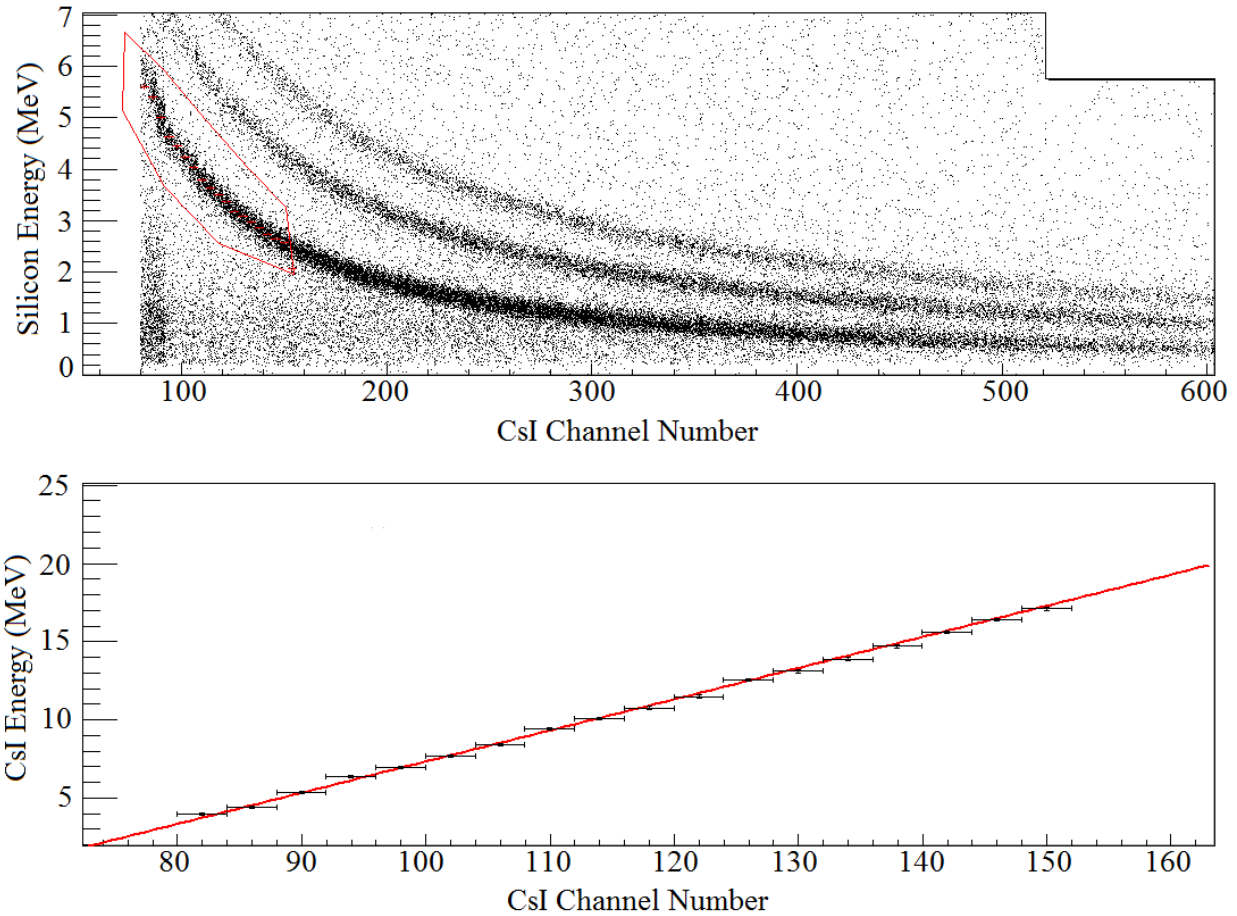
Figure 3.3: An example of the first step calibration of the CsI for a crystal in LASSA.

0.51 + 146.8 = 147.31 MeV where 0.51 MeV is deposited in the silicon and the 146.8 MeV is deposited in the CsI. After the first step calibration from the CsI fitter program the punch through point is typically between 5 and 10 percent off from where it should be. To fix this, a gate is drawn around the end of the calibrated spectra for protons. A one-dimensional plot of the CsI energy spectra from within this gate can then be plotted as shown in Figure 3.4.

The red fit line in Figure 3.4, is made using the formula:

$$\text{Counts} = \frac{ax + b}{1 + e^{(x-c)/d}} + fx + g \tag{3.7}$$
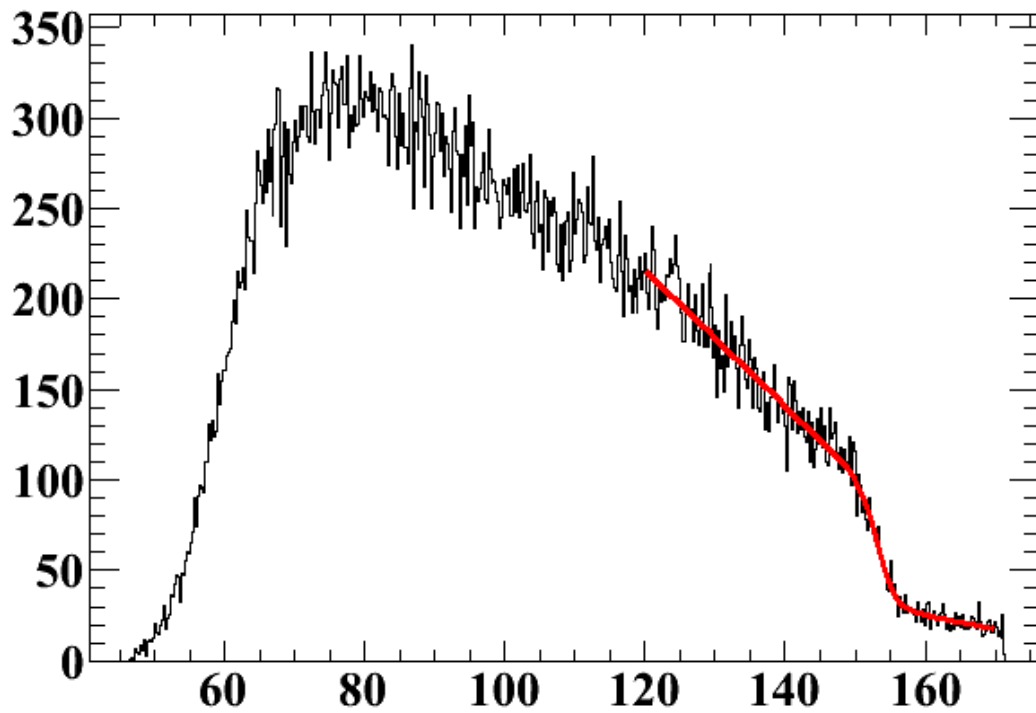
Figure 3.4: An example of the CsI energy gated on protons only. The punch through is represented by the halfway point of the sharp falloff. The initial calibration of the CsI is then adjusted by the punch through found through a fitting procedure.

where a, b, c, d, f and g are parameters fit independently for each crystal. The parameter c, represents the halfway point of the Fermi function-like falloff. This value, c, represents the punch through energy value in the CsI from the first order fit. Since we know the punch through energy in the CsI is 146.8 MeV, we can scale the first order CsI energy by the ratio $146.8/c$ in order to correct the energy calibration at these higher energies. Deuterons and tritons have a light output that is linearly proportional to energy deposition as well and as such, we repeat this procedure to correct the energy calibration independently for these two isotopes.

When charged particles enter the CsI they ionize the particles along their path. Some of the atoms that get ionized are the thallium atoms that were used to dope the crystals. The thallium particles have several excited levels that decay through photoemission. Hydrogen isotopes do not deposit enough energy to saturate these levels and as such have a linear light output as a function of deposited energy. Particles with higher Z, such as ^{3}He and ^{4}He have enough ionizing power that the response is no longer linear and so another method must be used to correct their calibrated CsI energy.

3.1.3 Ionization Correction

Up until this point the CsI calibration procedure has been valid only for hydrogen isotopes. It is well known that higher Z particles, and even deuterons and tritons, have a light output per MeV of deposited energy that differs from that of protons. In the case of deuterons and tritons, the light output depends linearly on energy and is treated the in the same manner as the protons.

In a previous experiment, a set of equations had been developed for LASSA to correct

for this effect for higher Z particles. Since we use the same crystals for this experiment, we can assume that the same relationship between energy deposition and light output between different isotopes is still valid. Under this assumption, the proton calibration parameters can be used to obtain a formula for the light output,

$$L = \frac{E_p - b}{a} \tag{3.8}$$

where E_p is the current energy calibration based on protons and L is the light output. The formula for L can then be substituted in the other equations,

$$E = aL + bA^c(1 - e^{dL}) \qquad\qquad Z = 2 \tag{3.9}$$

$$E = a\sqrt{AZ^2}L + b(1 + cAZ^2)L^{1 - dZ\sqrt{A}} \qquad\qquad Z = 3 \tag{3.10}$$

$$E = aAZ^2L + b(1 + cAZ^2)L^{1 - dZ\sqrt{A}} \qquad\qquad Z = 4 \tag{3.11}$$

to correctly account for the ionization differences. In all of these equations, E is the new corrected energy, L is the light generated by the particle as it passes through the CsI, Z is the charge of the particle and A is the mass number of the isotope. The other variables are parameters for each isotope and can be found in Table 3.2. The determination of these factors can be found in [40]. The calibration for some of the heavier isotopes have been cross-checked against the energy loss in both the silicon and CsI.

3.2   LASSA Pixelation Routine

The data for this experiment is analyzed using ROOT [41], a C++ scripting framework meant to handle and perform calculations on large amounts of data in an organized

Z	a	b	c	d
1	0.2010	-0.9587		
2	0.1696	4.575	0.3380	-0.05772
3	0.01783	0.2456	0.09743	0.06358
4	0.0006680	0.4493	0.01015	0.02616

Table 3.2: Table providing the fitting parameters used in order to correct for the reactions different isotopes have on the light output in the CsI.

format. At the beginning of the analysis process, the data files from the experiment are converted into a ROOT file that has the raw channel values for different properties of each of the detectors. The calibration processes described thus far in this chapter are used to create a new calibrated ROOT file with information strictly about LASSA. This calibrated ROOT file contains only calibrated energy for the silicon and CsI for each strip and crystal in each telescope. Much of the energy calibration has already been detailed in this chapter, except for two details; pedestal determination and effects of interstrip hits and overflow.

In this experiment, there was a large amount of pickup noise coming from the high voltage supply used for the Miniball. In order to avoid an unreasonable efficiency for high energy protons we ran the electronic thresholds for the LASSA ASIC's very near the noise level. We then ran the LASSA electronics as a slave system to avoid triggering the experiment on that noise. With the structure of the readout for LASSA, the noise signals are still read into the LASSA data when a master trigger is fired. To counteract this, we find the noise pedestal by looking at the raw spectra for each silicon channel. This spectra shows a large peak around a pedestal channel. This peak is fit with a gaussian and a pedestal threshold value is designated to be the peak position plus two standard deviations. During the calibration routine, only values that lie above this threshold are filled into the calibrated ROOT file.

During the calibration routine, once values have been assigned for each strip in a

telescope another loop through the strips is initiated. In roughly 3% of events a particle will pass through the gap between two strips. When this happens the particle deposits energy in both strips and so both strips would have an energy less than the actual value measured by the opposite face of the detector. This last loop compares neighboring strips to try to correct this situation. If a strip has a neighbor that has an energy measurement in the range of $0.03E < E_{\text{neighbor}} < E$, the neighboring strip's energy is added to the strip of reference. The neighboring strip's energy then assigned a value of zero energy. This process is called the gluing procedure.

The structure of the calibrated ROOT file makes it difficult to quickly determine real, identifiable particles in LASSA from unidentifiable ones and do physics calculations at the same time. To counteract this problem, we create a new ROOT file which we call a primary file through a routine that we call pixelation. The pixelation routine selects true charged particle hits in LASSA while filtering out "phantom hits" due to noise. The routine contains several steps and begins only after the calibrated ROOT has been created. A step by step walkthrough will be explained next.

There are three basic steps to the pixelation routine. I will describe the procedure for one telescope since each telescope is independent from each other in this regard. This routine is run on an event by event basis. The first step is to create a list of all CsI crystals in the telescope that measure a real energy (above threshold). The second step is to create a list of all combinations of front and back strips that measure energy deposition within

the tolerance of,

$$\left| E_{\text{front}} - E_{\text{back}} \right| < 0.4 \qquad \text{for} E_{\text{back}} < 3\text{MeV, or} \qquad (3.12)$$

$$\left| \frac{E_{\text{front}} - E_{\text{back}}}{E_{\text{back}}} \right| < 0.1 \qquad \text{for} E_{\text{back}} \geq 3\text{MeV.} \qquad (3.13)$$

In principle, a particle that passes through a pixel should have the energy deposition measured the same by the front and back strip. The third and final step is to eliminate any of the pixel locations from step two that are not backed one of the CsI crystals listed in step one. All pixels that pass this third step are added into the primary file. During this process, we also include other information about the particle such as the vector from the center of the target to the center of the pixel, laboratory angles, total lab energy (with corrections described in later in this chapter), transverse energy and momentum, center of mass kinetic energy and angle, and identification of which isotope the particle is (PID).

This relatively simple sounding routine eliminates many issues that arise from high level noise and multiple hits in the same telescope, if not necessarily the same crystal. The rest of this section will describe how this occurs.

Let us begin with the logic behind the simplest case, that of one real particle in LASSA. In this case, we would expect one front strip, one back strip and one CsI crystal all to detect the particle with a given energy and that the front and back strips would measure the same deposited energy within tolerance. Following through the three steps, step one lists only the one CsI that was hit, step two lists the one pixel location corresponding to the two strips that measured energy, and step three would do nothing in this case since the pixel is in front of a CsI that measured energy.

Moving to the next most complicated situation where two particles hit different CsI

crystals, hit separate front and back strips and leave vastly different energies in the silicon. If this assumption holds true, then the number of pixel locations for N real particles that measure energy (not necessarily matched within tolerance) is N^2. In this case there would be four possible locations. For this situation, step one would create a list of the two crystals. Step two would create only the two possible pixel locations where the front and back energies match. The other two possible pixel locations would never be considered because the front and back energies would be out of tolerance of each other. Step three again does nothing. This process would hold true for three and four real particles that all hit different crystals and different strips.

Continuing in complication, assume two particles deposit the same energy in the Silicon and enter opposite crystals. Step one would create a list of the two crystal locations. Step two would then create four possible pixel locations by matching each front strip with two back strips and vice versa. In this case, step three would then eliminate two of the false hits because there was no CsI struck behind those pixels.

In the previous case the particles entering opposite crystals allows for filtration of the phantom hits. If the particles enter adjacent crystals however, this is not possible. All four possible pixels would be created and advance onto the primary file. Later in the chapter other techniques will be described that help to filter these false hits out.

The examples just described can be continued and expanded upon for more particles and more complications, but the premise is the same in these cases. A series of checks were completed to determine the stability of this procedure. In theory the procedure is sound, however, noise in the silicon, neutron contamination, bad strips and particles that stop in the silicon require more consideration. Several examples of checks follow from

		Crystal 0				Crystal 1			
		M 1	M 2	M 3	M 4	M 1	M 2	M 3	M 4
1	Total Events	89844	19016	1542	87	58543	14346	1392	87
2	0-0 Events	21210	2210	123	34	13712	1916	113	34
3	0-x/x-0 Events	5147	3117	263	14	6275	2569	285	14
4	1-1 Events	59449	8002	509	14	34494	6096	452	15
5	Other Events	4038	5687	647	25	4062	3765	542	24
6	0 Pixels	26357	5327	386	48	19987	4485	398	48
7	1 Pixel	59449	8002	509	14	34494	6096	542	15
8	>1 Pixel	4038	5687	647	25	4062	3765	542	24
9	0 Matched Pixels	29332	8708	827	68	24070	7063	804	75
10	1 Matched Pixel	59199	9497	634	15	33949	6830	526	12
11	>1 Matched Pixels	1313	811	81	4	524	453	62	0
12	Matched Pixels w/o CsI	1834	534	36	N/A	2498	693	58	N/A
13	1-1 Match to 1 Pixel	57780	5228	240	7	33066	4384	209	3
14	1-1 Match to 0 Pixels	1669	2774	269	7	1428	1712	243	12
15	>1 Pixels to 1 Matched	1419	4269	394	8	883	2446	317	9
16	>1 Pixels to >1 Matched	1313	811	81	4	524	453	62	0

Table 3.3: A table representing different situations for two sample crystals in the pixelation routine.

here for a telescope that had only one bad strip on the front, none on the back, had all good CsI crystals and was not shadowed by any apparati. The checks that were completed use two crystals in this telescope, one with all good strips in front (crystal 0) and one with one bad strip in front (crystal 1). We complete these checks for one data run from the ^{112}Sn data at 50 MeV/A.

Table 3.3 contains much of the information for these checks for crystal 0 on the left and crystal 1 on the right. Each column for the respective crystals represents the multiplicity of crystals measuring energy in the telescope when that particular crystal measured a particle. For example, when two crystals measure a particle, crystal 0 was one of the hits

in 19,000 events and crystal 1 (the more backward crystal) in 14,300 events. Each row below that will specify how many of those events fit the criteria of the row.

Row 2, labelled 0-0, shows events in which the crystal was hit but no front strip or back strip in front of the crystal measured a particle. These events mainly occur when a neutral particle (almost exclusively neutrons) interacts with the CsI and thus deposits no energy in the silicon. The following row (3) labelled 0-x/x-0 Events, have several possible sources. For crystal 1 where there is a bad strip in front this would be a relatively common occurance (about 1/8 of events). Other possible sources are a neutron interacting with a CsI while a neighboring CsI was hit by a charged particle. Another option is when a particle stops in the Silicon in front of a neighboring CsI. It is possible that some of these events come from the inefficiency of the Silicon caused by noise in a strip as discussed later in 5.1.2 however this is a nearly negligible effect (1%) in this data run. Row 4, labelled 1-1 Events, indicates events with only one front strip and one back strip in front of the crystal that fired, with Row 5 measuring any other combination.

Continuing down the table, the next three rows (6-8) provide the number of pixels, that is, combinations of front and back strips in front of the crystal, where both measure energy, without any consideration for energy matching. The next three rows (9-11) provide the number of pixels in front of the crystal where the energy between the front and back is within tolerance provided by equation 3.12.

The next row (12) is different than all the others. In this row we are describing the multiplicity of fired CsI when this crystal did not measure a particle (all the others show only events where that crystal did measure a particle). Moreover, these are the events that contain the number of pixels that are energy matched when this occurs. This type of event

is generally dominated by particles that stop in the silicon detector or mylar foil in front of the CsI and never make it to the CsI crystal. This row provides an interesting check on Row 3. In this particular telescope, the front and back strips have an inefficiency of about 1%. This implies that about 2% of Row 4 (1200 events) would fall into this category. We can assume a comparable amount would stop over the crystal directly beneath it. Combine this from the stopped particles over its neighbor, crystal 1, as well as the 1200 events from the inefficiency and we might expect something around 5500 events in Row 3 for the multiplicity 1. These calculations are relatively back of the envelope and in many cases it is difficult to verify just how many counts fall into what category, this at least provides a reason for the relatively large amount of counts in Row 3 for a crystal with all good strips in front.

The last four rows are more complicated. Row 13 provides the number of events in Row 4 that were energy matched, while Row 14 provides the number of events in Row 4 that were not within the energy tolerance. This is quite expected, suggesting that over 97% of events that have only one possible front and back that correspond to a measured energy in the CsI are matched in energy. It should be noticed as well that the sum of Rows 13 and 15 add up to Row 10 as they should. Rows 15 and 16 provide the number of events from row five that give exactly 1 matched pixel (15) or more than 1 (16).

The events in Row 16 are some events that cause issue. In general we cannot tell which of the pixels in these events are the ones to keep. In principle, if one particle were to stop in the silicon and the other pass into the CsI we would be able to measure those. If two particles were to both penetrate into the CsI however, it would be impossible to accurately distinguish them, even though the combination would likely have an artificially

high enough energy in the CsI to push each other out of a particle identification curve. This is one option for filtering out these particles.

The first check on the pixelation routine is to confirm that the number of pixels in the newly made primary file for events where there is only one combination of pixels in front of a particular crystal matches the prediction. In this case, for crystal 0, the number of pixels found in the primary file is 69345. This matches the sum of the values of row ten in the table as anticipated. All of the events in the last row create, in the example of this crystal, around 4500 more pixels. There are a myriad of explanations for what types of events these can be. Two or more particles could hit the same CsI, or they could hit neighboring crystals and deposit a similar amount of energy in the Silicon. A study of how many of these pixels get filtered out will be described later in this chapter.

One of the issues that arises is when there are bad strips. One would assume that the fraction of events lacking a pixel in front of the crystal would increase by the fraction of nonusable pixels. For example, 29.07 % of events in crystal 0 are part of row six. Crystal 1 has one bad strip and so we might expect an increase of 12.5 % of that rate, with a slight tolerance for a lower particle hit rate in that crystal. Crystal 1 has 33.5 % of events in row six, consistent with $29.06 * 1.125 = 32.70\%$.

At this point, one should be concerned about the number of events in which there are more than one possible pixel that are energy matched represented in row eleven. In the next section as well as in Chapter 5 I will detail what contribution those particles make into the final spectra.

3.2.1 Particle Identification

Particles in LASSA are usually identified using the measured ΔE and E energies from the silicon and CsI, respectively. These curves provide good separation as illustrated in Figure 2.7. Typically this is enough to allow gates to be drawn minimizing the contamination of wrongly identified particles. However, in high energy cases it becomes difficult to determine the particle type due to punch through effects. For example, the tritons that punch through the CsI deposit less energy in both the silicon and CsI detectors than those that stop in the CsI. When this happens the triton curve stops and crosses back across the deuteron and proton lines. In addition, the separation between ^{3}He and ^{4}He requires better resolution than can be achieved through this form. For this purpose, a new *PID* variable is created of the form,

$$PID = b * \text{Ln}(300) - \text{Ln}(b * \Delta E) - (b - 1)\text{Ln}(E + 0.5 * \Delta E) \qquad (3.14)$$

$$b = 1.825 - 0.18 * \frac{\Delta E}{25} \qquad (3.15)$$

This PID variable allows for a better utilization of the good resolution in the silicon and CsI to identify the isotopes of the particles measured in LASSA. Figure 3.5 illustrates the CsI energy versus *PID* to identify hydrogen and helium isotopes while Figure 3.6 displays the Si energy versus *PID* to identify the small range of lithium and beryllium isotopes.

In general, not every particle that enters the telescope will be visualized within these curves. There are some small effects that cause some background as seen in Figure 2.7. It is helpful to know how many particles are being detected that are part of this background. The primary effects that cause this to happen are when two particles enter the same strip
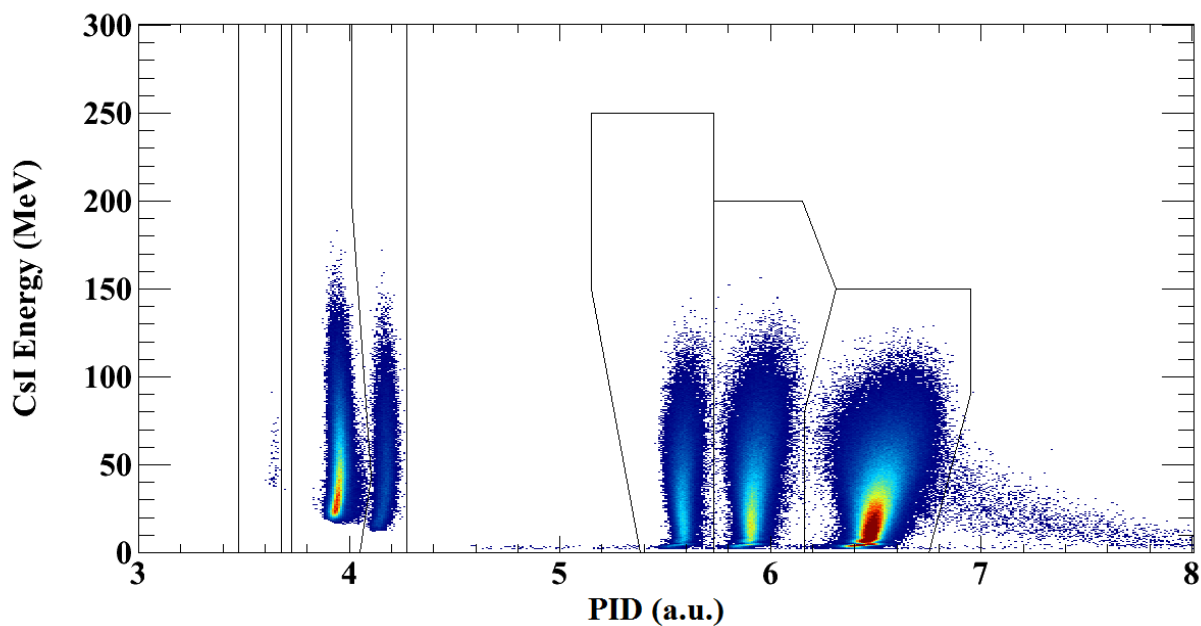
Figure 3.5: A plot showing an example of the gates used for hydrogen and helium isotopes. Each crystal has an individual set of gates drawn. Hydrogen isotopes are the cluster on the right, with helium on the left, with increasing mass moving from right to left.
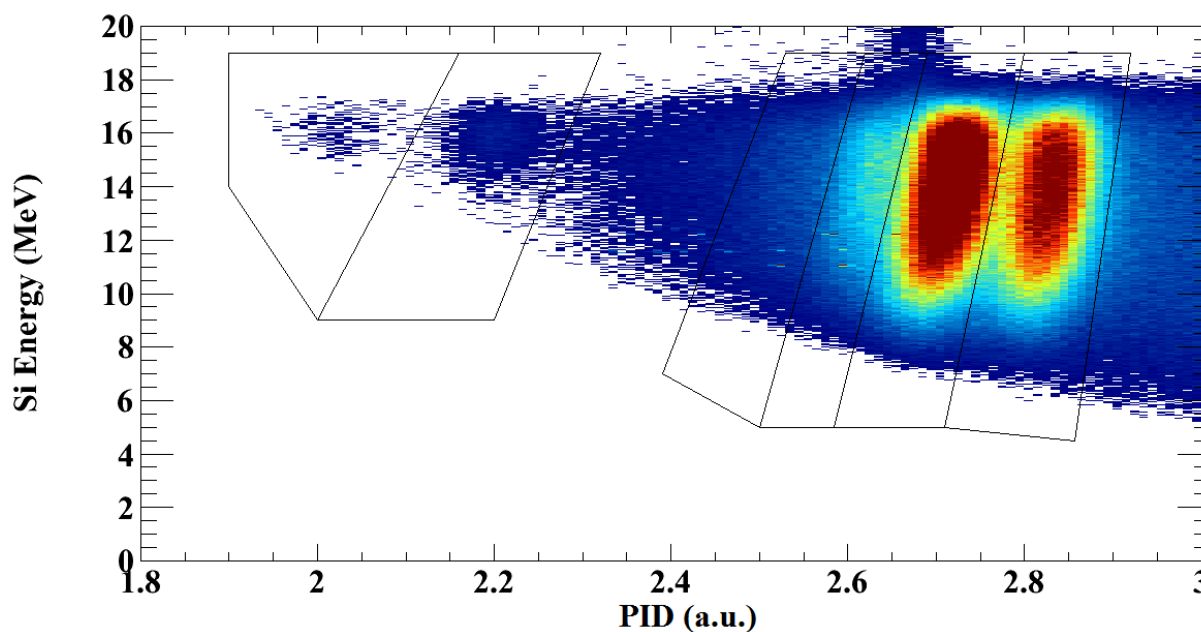
Figure 3.6: A plot showing an example of the gates used for lithium and beryllium isotopes. Each crystal has an individual set of gates drawn. Again increasing mass moves from right to the left with lithium on the right and beryllium on the left.

		Crystal 0	Crystal 1
1	1 Matched Pixel	69345	41292
2	1 Matched Pixel in a PID line	66735	39636
3	Fraction of Pixel in a PID line to Pixels	0.962	0.960
4	Events with >1 Matched Pixel	2209	1039
5	Pixels from >1 Matched Pixel	4931	2257
6	Pixels in PID lines	3419	1717
7	Fraction of >1 in PID line to exactly 1 in a PID	0.0512	0.0433

Table 3.4: A table comparing the respective contributions of created pixels from events with only one possible energy matched combination and many combinations.

or same CsI crystal. If two particles hit the same strip, the silicon energy will be shifted up and in the same crystal the CsI energy will be shifted up as well. We use this process to filter out some of the events that have more than one possible matched pixel in front of a CsI. Table 3.4 displays some of the information for the same two test crystals as in 3.3 from the pixelation routine verification.

This table provides several pieces of important information. Row 1 shows the number of events in which there was only one possible energy matched combination of pixels, the sum of the four columns in Table 3.3. This is very important in confirming that the routine is correctly producing all of the pixels that we expected. The next row (2) shows the number of those pixels fall within the particle identification gates. The third row then shows the fraction of events that get identified. The next three lines show the contribution of events that produced more than one matched pixel. Rows 4 and 5 provide the number of events and produced pixels from those events, respectively. Row 6 provides the number of those matched pixels in Row 5 that fall within a particle identification gate. Finally, Row 7 shows the that in this crystal about 5% of pixels created from the routine are from events that contain more than one possible matched pixel in from of a crystal.

In general a 5% contribution from these types of events is probably acceptable. It is

important to remember however, that this telescope is at relatively backward angles where the amount of multiple hits and particle bombardment is not very high. At the forward angles this contribution increases. In the 120 MeV/Areaction this proportion increases even more, up to a 35% effect in the forward angles. In Section 5.1.2 we attempt to compensate for multiple hits in the CsI and so we therefore choose to omit any pixels that have more than one possible matched pixel in front of the same crystal.

While a relatively small effect, it is possible that two neighboring crystals each have only one matched pixel in front of it, with those matched pixels sharing either the front or back strip with the other pixel. Since the gates across the silicon energy are relatively broad, these types of events are not as likely to boost each other out of a particle identification gate and so we choose to elminate these types of events as well.

3.2.2   Foil Correction

There are a number of thin foils at different locations along the flight path to the silicon and CsI detectors. These foils cause a slight amount of energy loss for charged particles passing through them. We describe the energy loss as proceeding through 7 steps: the energy loss in (1) half the thickness of the target, (2) in a set of SnPbSb foils, (3) in a layer of aluminized mylar foil, (4) in the dead layer of the Si, (5) in the active Si detector, (6) in another layer of aluminized mylar and finally, (7) in the CsI. In Table 3.5 is a list of the foil thicknesses. These thicknesses were input in LISE in order to generate a correction. This correction moves through the following path. Using the energy in the CsI, the energy lost in the mylar foil can be calculated. The energy in the CsI is added to the energy lost in the silicon and the mylar to calculate the energy lost in the dead layer of the silicon. This

Material	Thickness(mg/cm^2)
Half ^{112}Sn target	2.785
Half ^{124}Sn target	2.65
SnPbSb	16.69284
Al	0.02
Mylar	0.24543
Si Deadlayer	0.2321

Table 3.5: Thickness of all the components of the foils in the experiment.

running sum is then used to calculate the energy lost in the first mylar foil. This process continues back to the target. The target's thickness must be adjusted slightly to account for the target being aligned normal to the beam axis and not normal to the front of the detectors. As such, the thickness used for the target is $t/(2\cos\theta)$ where t is the thickness and θ is the laboratory angle of the center of the pixel the particle was detected in. This thickness is chosen under the assumption that collision takes place at the exact center of the target.

3.3   Elastic Scattering

A series of data runs were completed using a beam of ^{16}O at E/A = 29.4 and 16.8 MeV on a 9.2 mg/cm^2 CH$_2$ target. These data runs were intended to measure elastically backscattered protons in LASSA. The scattering should have a very precise energy deposition in the CsI based on the laboratory angle. If possible, inelastic scattering peaks would have also been used. During the experiment a mistake in the FPGA firmware programming caused data to only be read out when there were at least 3 strips in the LASSA system with data. This glitch would make it look like data was being measured but not actually being read out to the DAQ. This issue was not fully understood until the calibration beamtime had run out and so the low statistics during these data runs made it difficult to use for

extra calibration purposes. We were fortunate that the rest of the experiment was focused on high multiplicity, central events, as those data runs were unaffected by this glitch. This is especially true considering the normal LASSA data was run as a slave system with thresholds near the level of the noise. The elastic scattering trigger used a much higher threshold for event detection.

3.4 Miniball Calibration

3.4.1 Energy Calibration

The energy calibrations of the Miniball were completed for the tail and slow components only. The fast component had a significant amount of electronics channels that were not functioning properly and so they were omitted from calibration. By looking at the raw tail versus raw slow signal we can find the punch through of each of the hydrogen isotopes for both signals which can be seen in Figure 3.7. Using LISE++, we can calculate what the punchthrough energy should be in the 2 cm crystal. By assuming a linear relationship between energy deposition and ADC channel for the three hydrogen isotopes, the pedestal channel and three punchthrough channels can be linearly fit for both the slow and tail components. This must be done by hand on a telescope by telescope basis. In this experiment, we choose the calibrated energy from the slow signal to be the energy in the lab. We use the slow signals because they are the most reliably measured signals in the Miniball over the course of the experiment.
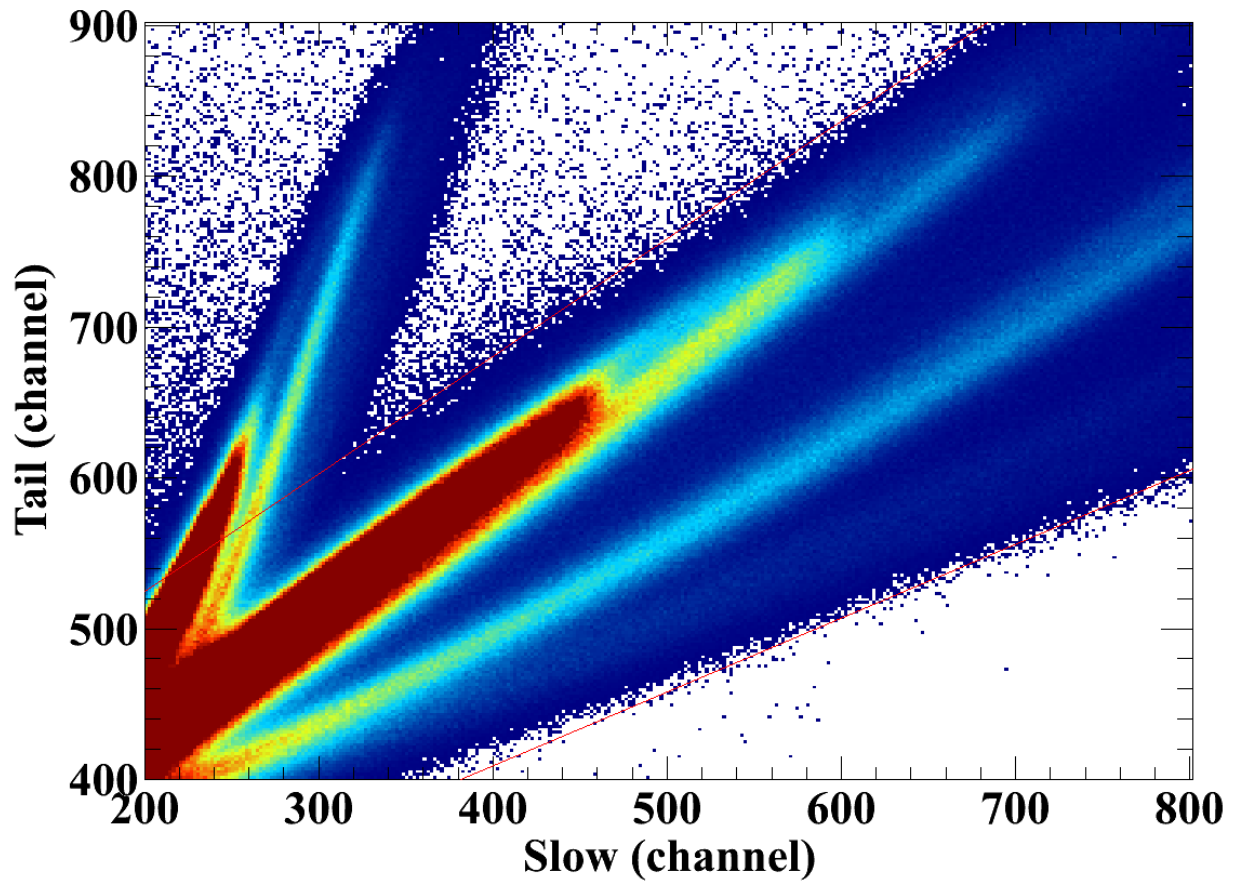
Figure 3.7: The raw tail versus raw slow signal zoomed around the hydrogen punch throughs. Here the proton punch through is near channel 460 in the slow and channel 625 in the tail.

3.4.2   Particle Identification

As mentioned previously, each Miniball element is composed of a phoswich detector read out by a photodiode. Figure 2.10 showed an example of the pulse shape generated by a particle in a Miniball telescope. The shape is defined by three distinct parts. The fast part comes from the light generation in the fast plastic scintillator which has a signal that extends from 2-30 ns. The slow and tail parts come from the CsI crystal with time constants on the order of 100 ns and 1.5 μs respectively.

We can take advantage of the difference in pulse shapes in a variety of ways. The relationship between the fast signal and the slow signal is sensitive to the charge of the particle being detected. By plotting the charge collected in the fast gate versus the charge collected in the slow gate as shown for an example telescope in Figure 3.8 which displays the various elements detected by the Miniball with gates drawn around each. In the figure, hydrogens are the lowest gate moving counterclockwise until aluminum in the case of this detector. This example comes from a forward detector. As you move backwards in rings fewer elements can be seen.

The relationship between slow and tail signals are sensitive not only to charge but also to mass. Figure 3.9 shows an example of a plot of the tail signal versus the slow signal in a Miniball telescope. If you were to zoom in on different regions, you would be able to see different isotopes in the Figure, however, drawing gates around each one is difficult to do cleanly. For this, a variable called PDT is created where,

$$PDT = \text{Tail} + \frac{m_1 * \text{Slow} + b_1}{(m_1 - m_2) * \text{Slow} + (b_1 - b_2)}, \tag{3.16}$$
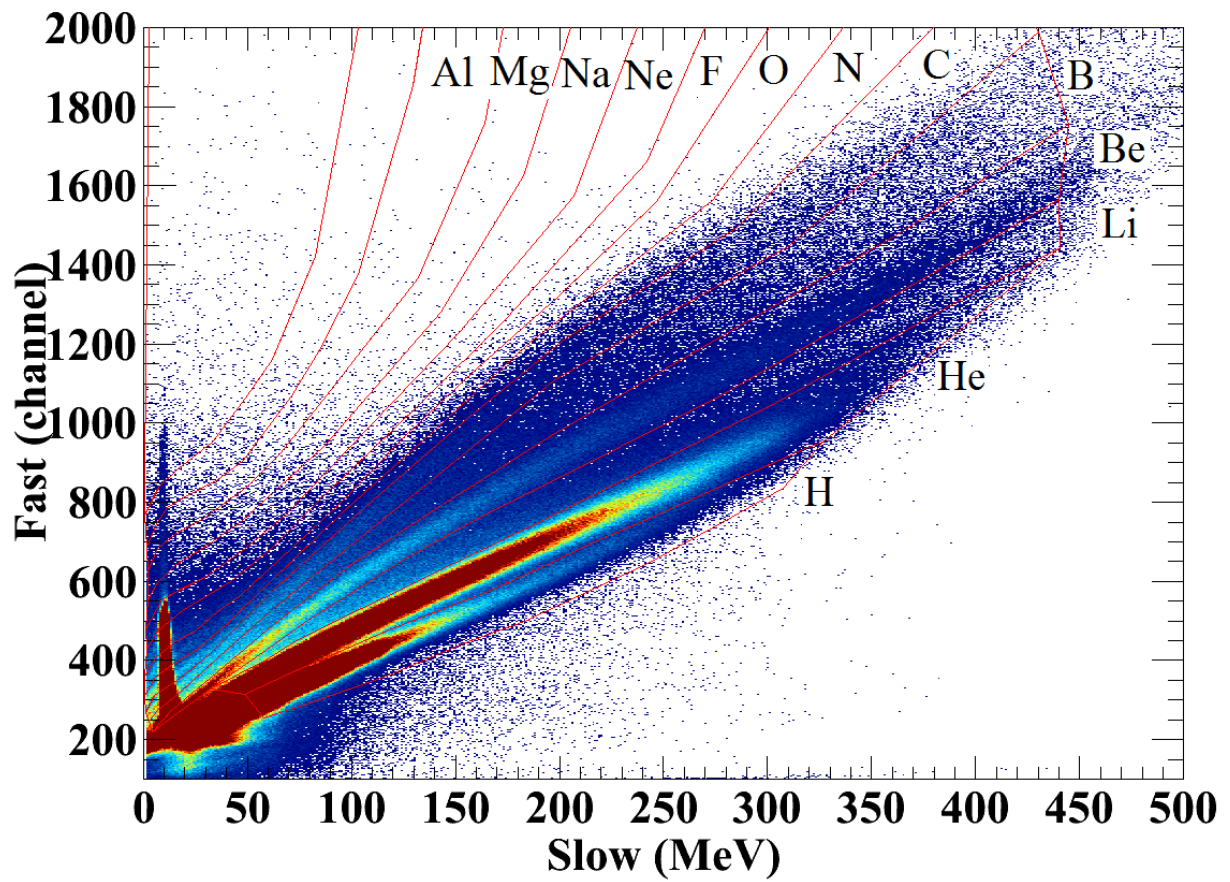
Figure 3.8: A plot of the raw fast signal versus the calibrated slow signal. Gates representing different elements.
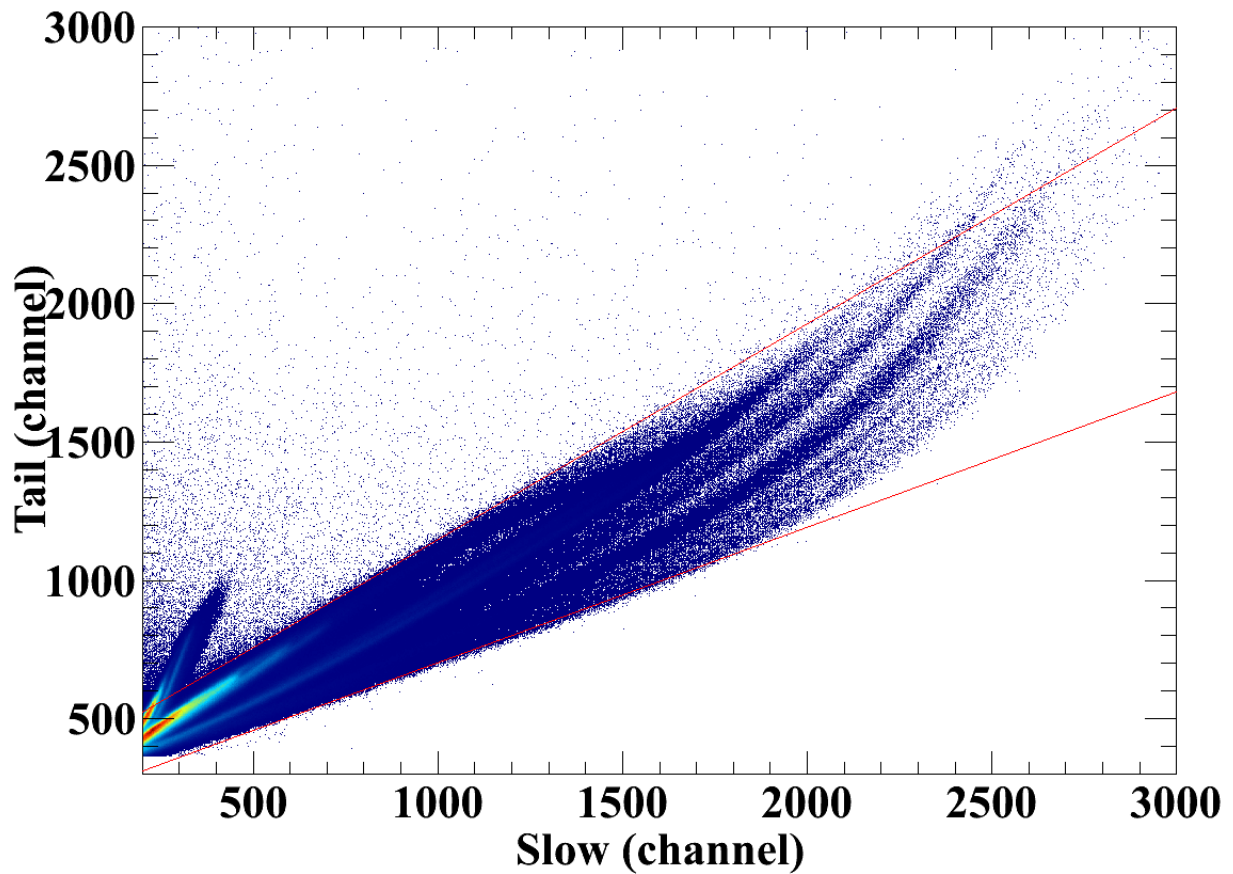
Figure 3.9: A plot of the raw tail signal versus the raw slow signal. The lines drawn represent the lines used in order to create the PDT variable in Equation 3.16.

where $m_{1(2)}$ and $b_{1(2)}$ are the slope and offset from the upper(lower) red lines in the Figure. If we instead plot the *PDT* value versus the slow signal as shown in Figure 3.10, the different isotopes are easier to identify and gate. For this particular telescope, different hydrogen and helium isotopes are identified. In both elemental and isotopic selection, the gates are drawn individually for each telescope in the Miniball.
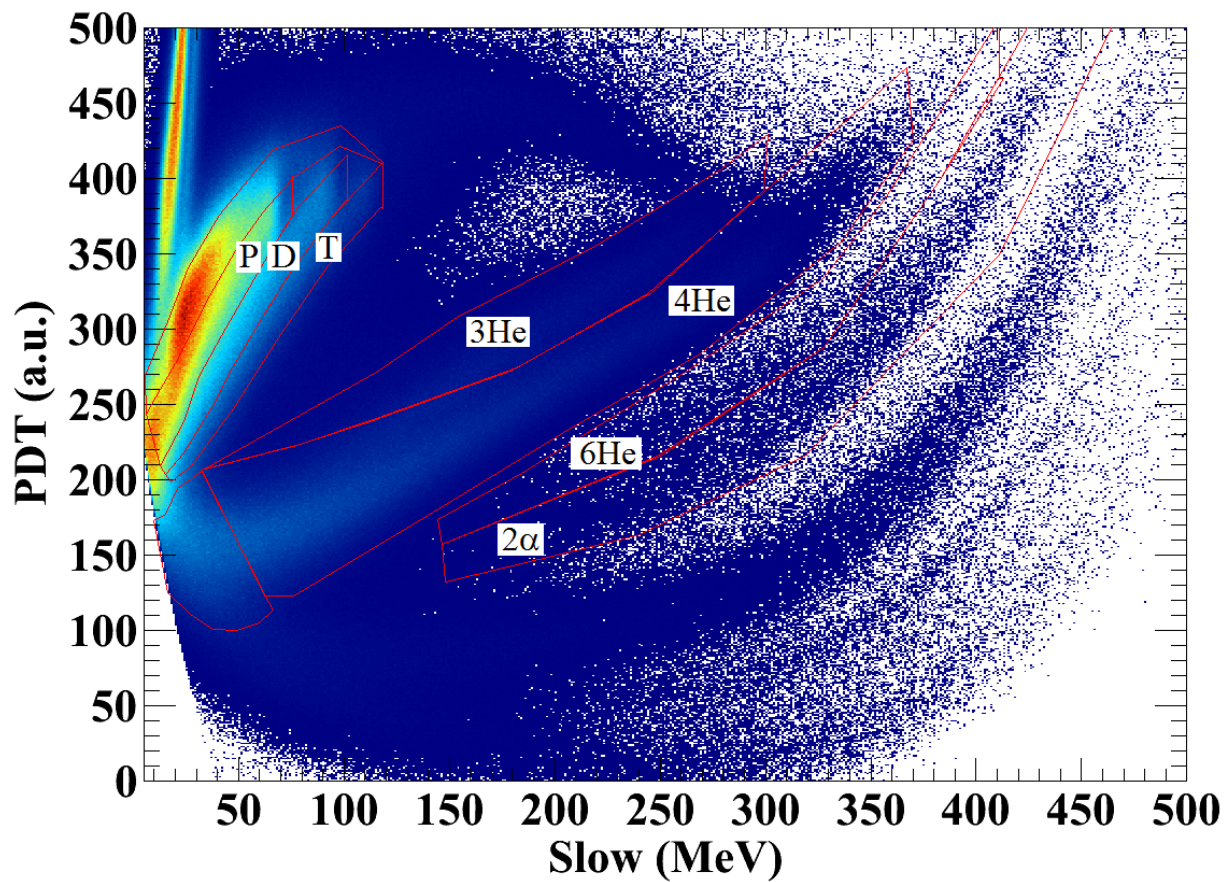
Figure 3.10: A plot of PDT versus the calibrated slow signal. Gates are drawn for hydrogen and helium isotopes. The 2α gate represents two α particles coming from the instantaneous decay of ^{8}Be

3.5   Cross Section and Impact Parameter

Like most experiments a measurement of the reaction cross section is important. In this experiment we measure the cross section for a range of multiplicities in the Miniball and use that to assign impact parameters to values of Miniball multiplicity. While the Miniball measures the charged particle multiplicity the Downstream Scintillator measures the amount of incident beam particles.

For each combination of beam energy and target a series of minimum bias runs were completed. In general the trigger for data runs required a minimum number of hits in the Miniball. For these minimum bias runs only one Miniball hit was required to trigger the system. The series consisted of all four combinations of Downstream Scintillator in place and out with the target in and out.

The run with the combination of scintillator in and target out provides a background measurement for the run with the combination of scintillator in and target in. Both data sets were taken for the same amount of time so the background spectrum was subtracted from that of the data. This same process took place for the combinations with scintillator out. In all cases there was a nonphysical peak at multiplicity equal to one likely due to the effect of noise. It is unclear where this data is coming from and as such only data using multiplicity of at least two is used for the remaining procedures.

The measurement with the Downstream Scintillator out and target in mimicks the running conditions of the normal data runs. In this setup however, it is impossible to measure the number of incident beam particles, so data was taken using the scintillator in and target in. This configuration has a limitation that the beam rate cannot be as high as a standard running configuration because of the possibility of flooding the scintillator's PMT

and damaging it. Also, the scintillator contributes some low multiplicity contamination in the Miniball through backscattering, however the high multiplicity region of the spectrum is unaffected.

Using this concept, the integrated number of counts for multiplicities in the Miniball of at least 7 are compared from the background corrected spectra between the scintillator in and scintillator out runs. Equation 3.17 shows how the beam rate for the scintillator out run is calculated from the scintillator in run.

$$I_{\text{out}} = I_{\text{in}} \frac{\sum\limits_{N_C \geq 7} \text{counts}_{\text{out}}}{\sum\limits_{N_C \geq 7} \text{counts}_{\text{in}}} \tag{3.17}$$

In this equation, out represents the value from the scintillator out data set and in represents the value from the scintillator in data. By using the calculated number of incident beam particles we have everything needed to calculate the cross section. The cross section for a given value of N_C is then calculated using the formula,

$$\sigma(N_c) = \frac{\sum\limits_{N_c}^{\infty} \text{events}}{I_i \times t}. \tag{3.18}$$

Here the I_i is the number of incident particles calculated in Equation 3.17 and t is the thickness of the target in particles/cm^2 which can be found in Table 3.5. From the cross section, an impact parameter can be determined. The formula for the impact parameter,

$$\sigma(N_c) = \pi b^2, \tag{3.19}$$

uses the concept of a geometric probability to calculate b. Instead of using the raw impact

87
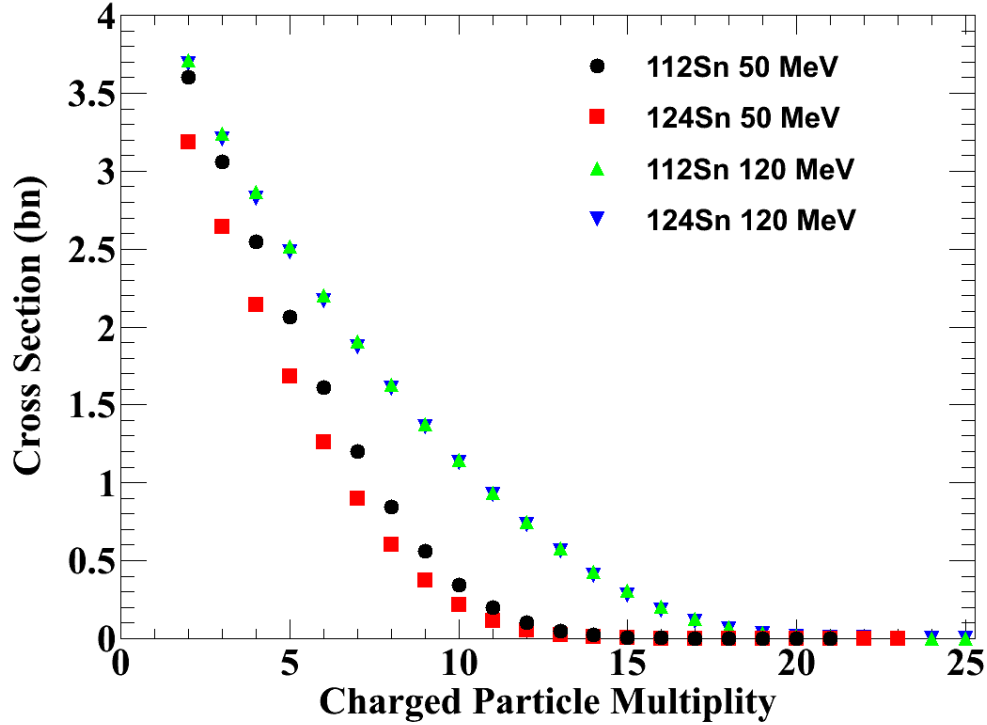
Figure 3.11: The cross section for all four beam and energy systems as a function of charged particle multiplicity in the Miniball. In this plot, the cross section is not the cross section of a given N_C but for all N_C of at least that amount.

parameter alone to make selections on the data, one can also compare data using a reduced impact parameter, $\hat{b}$. This allows a more direct comparison between central collisions in systems of different size. The reduced impact parameter is calculated using,

$$\hat{b} = \frac{b}{b_{\max}}, \qquad (3.20)$$

where $b_{\max}$ is the value of the impact parameter at $N_c = 2$. Figures 3.11 and 3.12 show the dependence of the cross section, impact parameter and reduced impact parameter on the charged particle multiplicity.

The exact same treatment can be explored using the total transverse energy measured
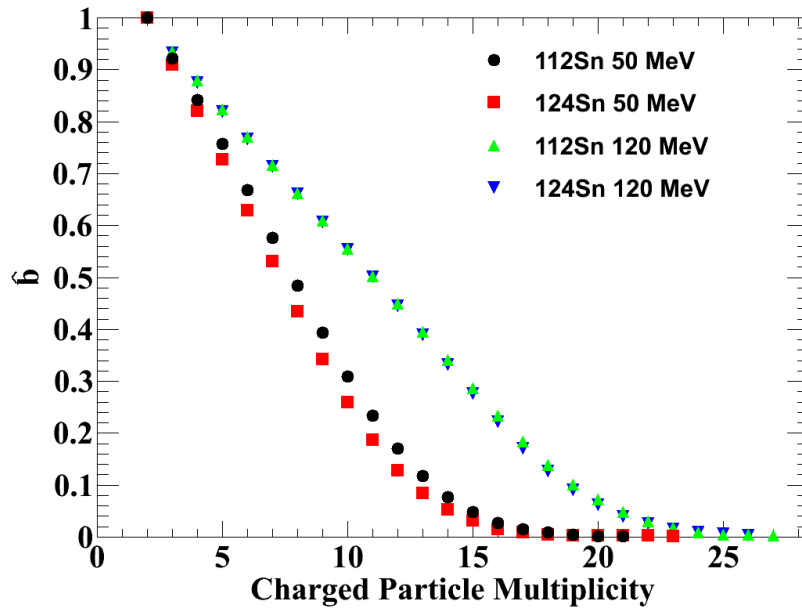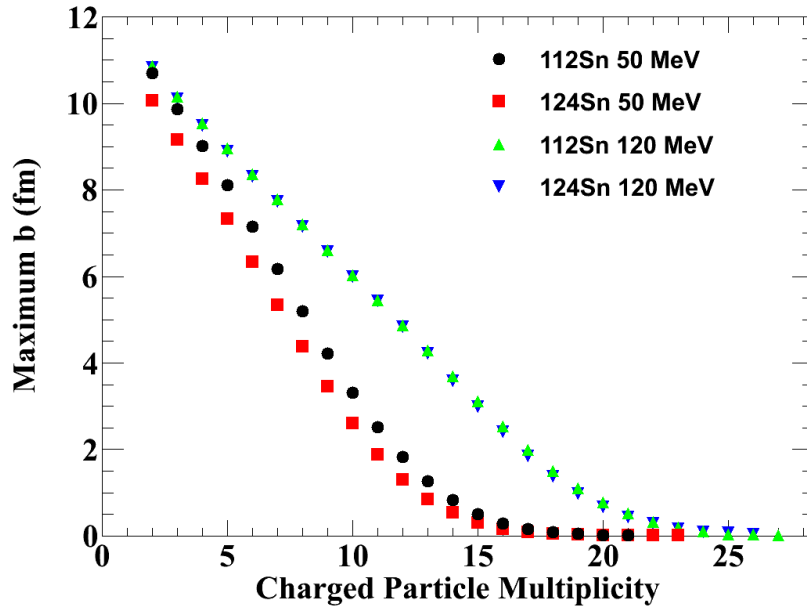
Figure 3.12: The impact parameter and reduced impact parameters for all four beam and energy systems as a function of charged particle multiplicity in the Miniball. Here the impact parameter at a given N_C is the maximum impact parameter given that multiplicity.

in the Miniball instead of the charged particle multiplicity. Those results can be seen in

Figure 3.13.
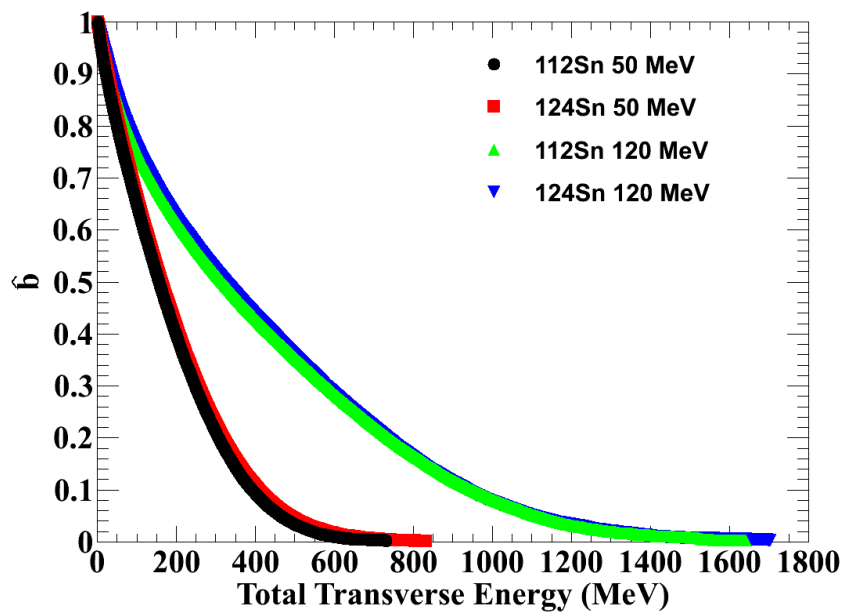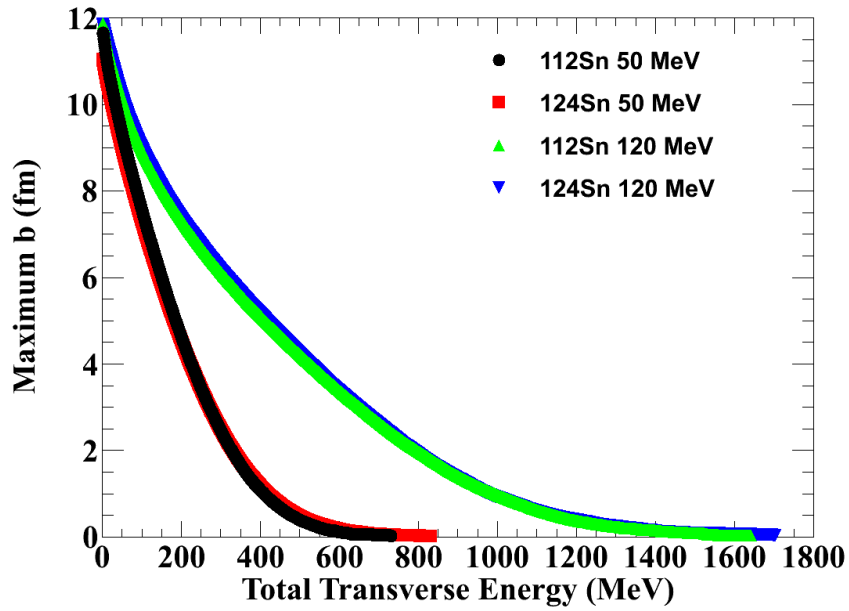
Figure 3.13: The impact parameter and reduced impact parameters for all four beam and energy systems as a function of total transverse energy in the Miniball.

Chapter 4

pBUU analysis

4.1 Introduction

As introduced previously, pBUU is a transport simulation code that uses a large amount of parameters in order to simulate a collision between two nuclei. Many of these parameters are physical in nature, such as the impact parameter, mean field compressibility, in-medium cross section, incident energy, and symmetry energy parameters to name a few. Others are purely computational such as grid size, length of time of the simulation, and the number of test particles.

It is imperative that the code should produce results insensitive to the computational parameters as long as certain conditions are met as the variables are changed. For instance, as long as the large residues from a collision remain on the grid, the size of the grid should also not affect the observable. As long as the large residues have finished interacting with the rest of the system, the observable should not be too sensitive to the increase in time of calculation since secondary decay time scales tend to be very long. Finally, there should be enough test particles used in the simulation so that increases in the number of test

partcles do not change the physical conclusions.

4.2 Computational Parameters

Several simple tests were completed using the pBUU code at the beginning of this study. To begin all simulations were run with an incident energy of 50 MeV/A. The first check was to verify that the grid size is large enough. Figure 4.1 shows an example pBUU simulation without cluster production using a grid size of 45.08 fm along the positive beam axis and 18.4 fm in both positive transverse directions. The simulation progresses over time and by around 300 fm/c the large residues have stopped interacting and are still on the grid. It would be expected then that if the grid size were changed, the results would not. Figure 4.2 shows the spectra of protons and neutrons that were emitted from the central source in the range of $70 \leq \theta_{C.M.} \leq 110$ degrees as indicated schematically by the lines in the bottom right part of Figure 4.1. It is important to note that the angular range is in momentum space, not coordinate space. All four spectra are nearly identical, indicating that as long as the main residue stays on the grid, the grid size does not have an effect on the results. This also confirms that all grid sizes are large enough for this system.

A similar set of calculations was done with 120 MeV/Acollisions. Since the residues are certainly not going to leave the grid in the transverse direction, only the two different longitudinal lengths were compared. Figure 4.3 shows that in a higher energy system, the large residues leave the grid. In an unexpected result, the spectra for the standard grid and expanded grid are nearly indistinguishable. This is a consequence of the fact that the particles of interest, especially at high energy, come from the participant region of the interaction. Once the two residues have passed through each other very few free
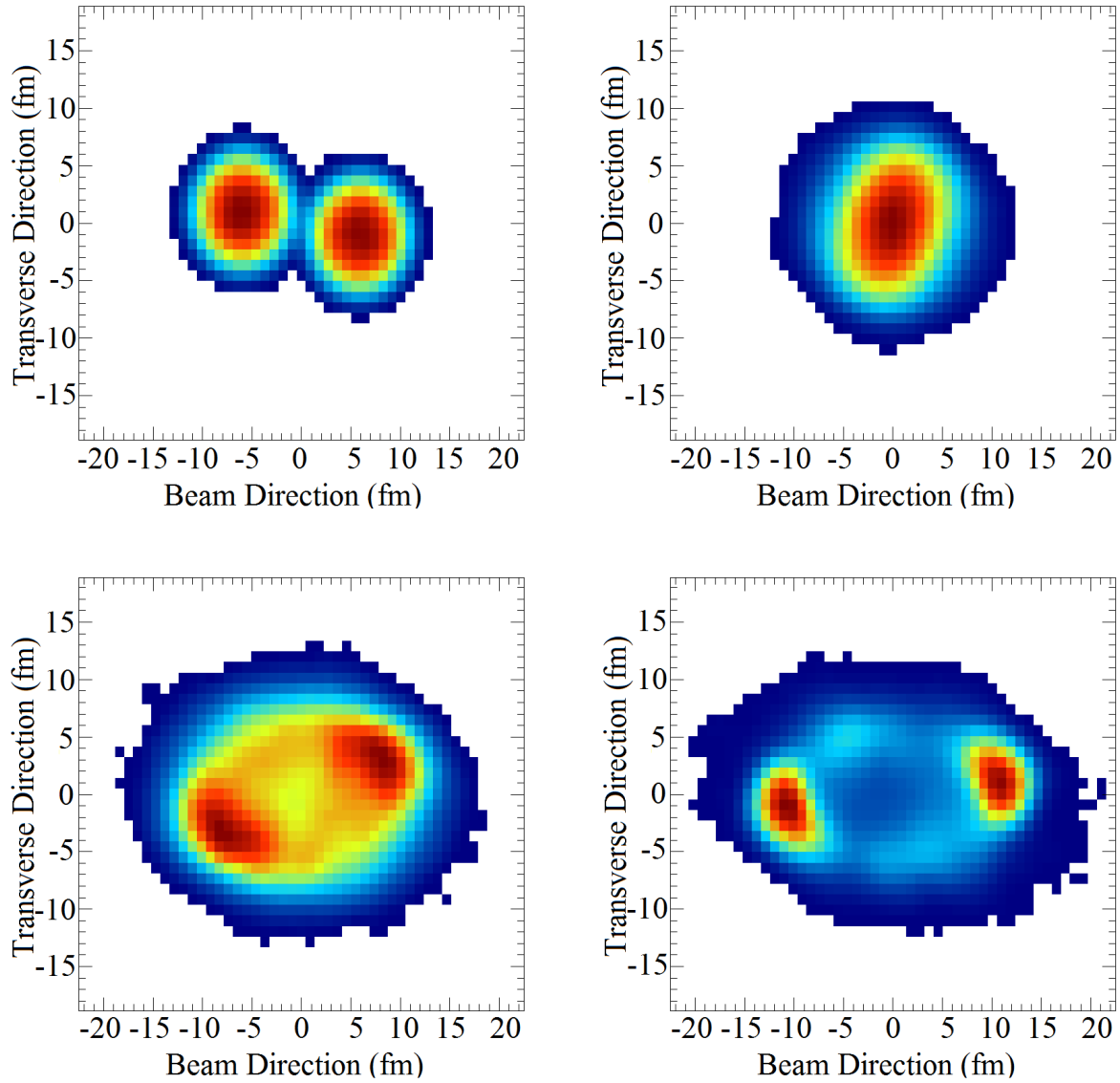
Figure 4.1: An example of the collision of two ^{112}Sn nuclei from a 50 MeV/Areaction with an impact parameter of 2 fm. The time of each panel is 0 (upper left), 54 (upper right), 108 (lower left) and 162 (lower right) fm/c.
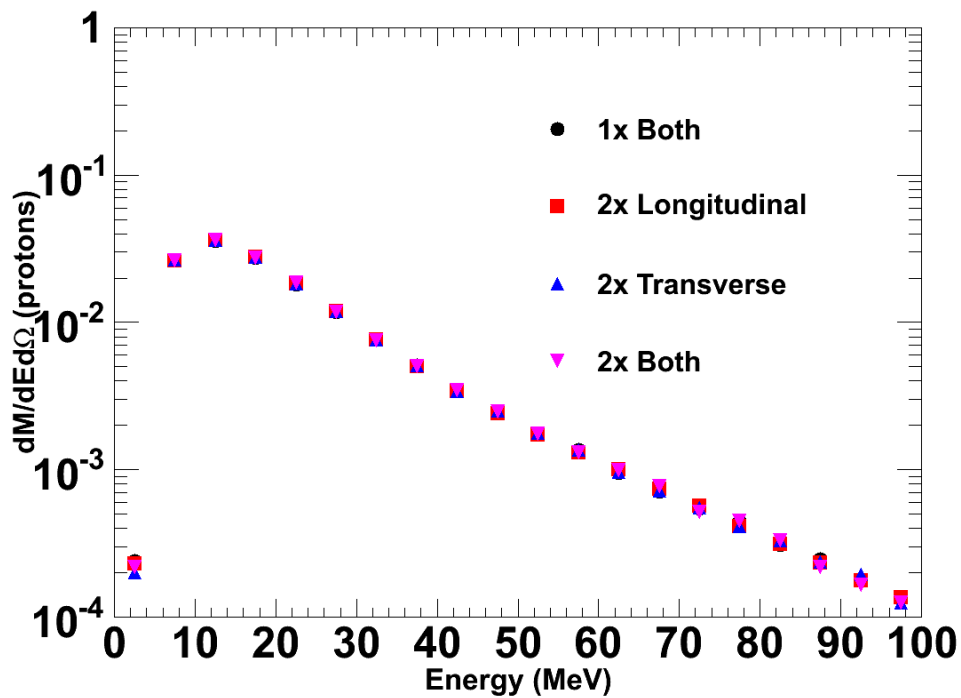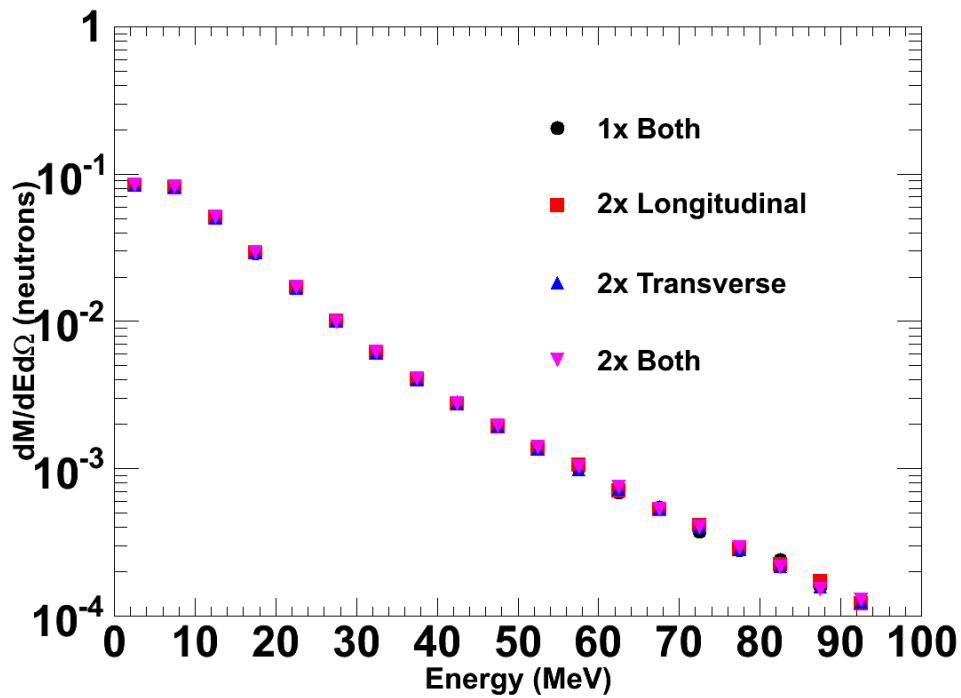
Figure 4.2: An example of the neutron (top) and proton (bottom) spectra for varying grid sizes. 2x longitudinal indicates that the grid was doubled in size for the beam axis, 2x transverse indicates that both the transverse axes were doubled in size and 2x both indicates that all three axes were doubled.

particles will contribute to the spectra in the angles of interest. This indicates that as long as the grid is large enough to finish the main collision, the grid is large enough for the observables of interest to this work.

Next, the simulation was run for varying lengths of time for a 50 MeV/Areaction. The code proceeds through the simulation in time steps of 0.36 fm/c. Five different calculations were completed out to 416, 624, 832, 1040 and 1248 time steps which correspond to 150, 225, 300, 375 and 450 fm/c. Figure 4.1 shows that at the two earlier times the residues are not completely done interacting. Even at 300 fm/c the residues are still connected by a neck region but are very weakly interacting. Figure 4.4 shows the spectra for each time length. At the very low energies, less than 20 MeV, the different times show very different results. At the higher energies however, the spectra are very similar. The higher energy particles are emitted at the earliest times of collision where the interactions are strongest and most numerous. As such we are confident that the effects of probing the dense, central source can be seen through the emission of particles at energies larger than 20 MeV and in simulations run to anytime after the residues have stopped their primary interaction. From this result we are confident in simulations run out to 300 fm/c, for all incident energies.

Finally, a series of calculations were completed with different amounts of test particles. For the duration of this dissertation when the number of test particles is given, it implies the number of test particles per nucleon. Simulations were run with 50, 100, 200, 400, 600, 800, 1200 and 1600 test particles. It is anticipated that the results would depend on the amount of test particles until a certain amount where pBUU can accurately represent the phase space and the results converge. Figure 4.5 shows the spectra for several of
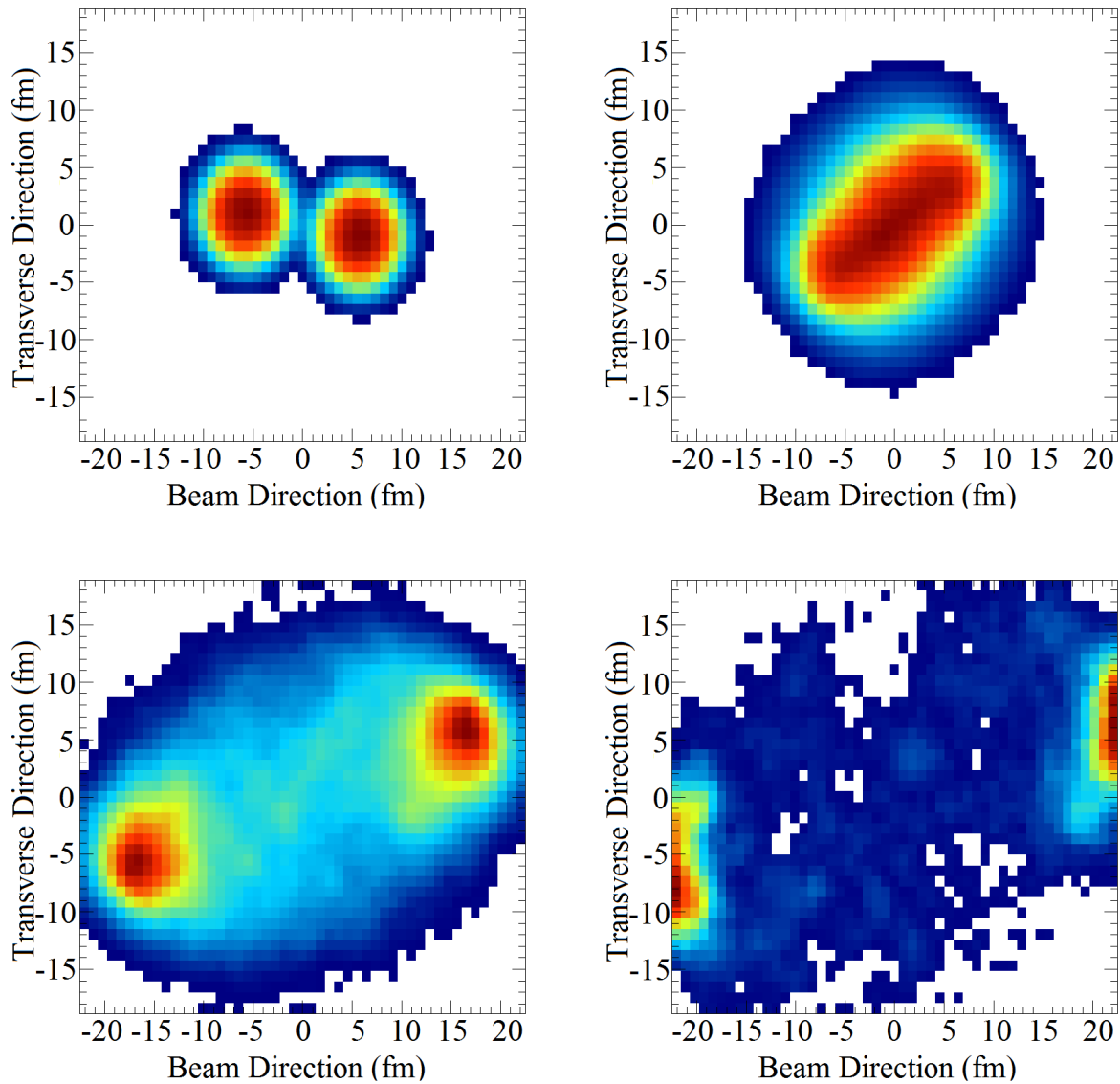
Figure 4.3: An example of the collision of two ^{112}Sn nuclei from a 120 MeV/A reaction at an impact parameter of 2 fm. In the case of the higher energy system, the main residues leave the grid when it has a length of 45.08 fm. The time of each panel is 0 (upper left), 54 (upper right), 108 (lower left) and 162 (lower right) fm/c.
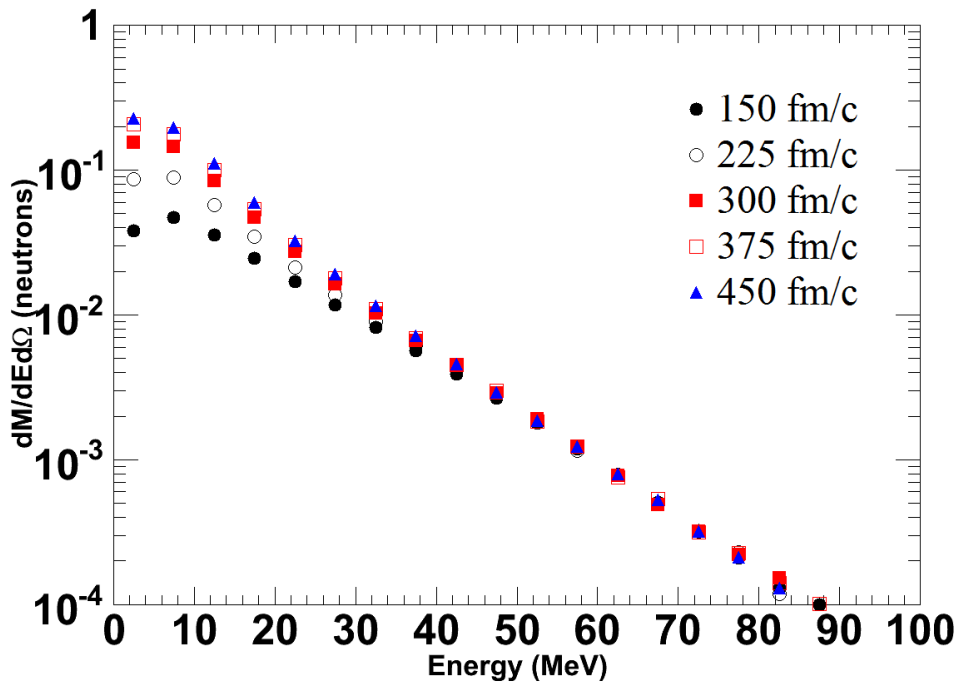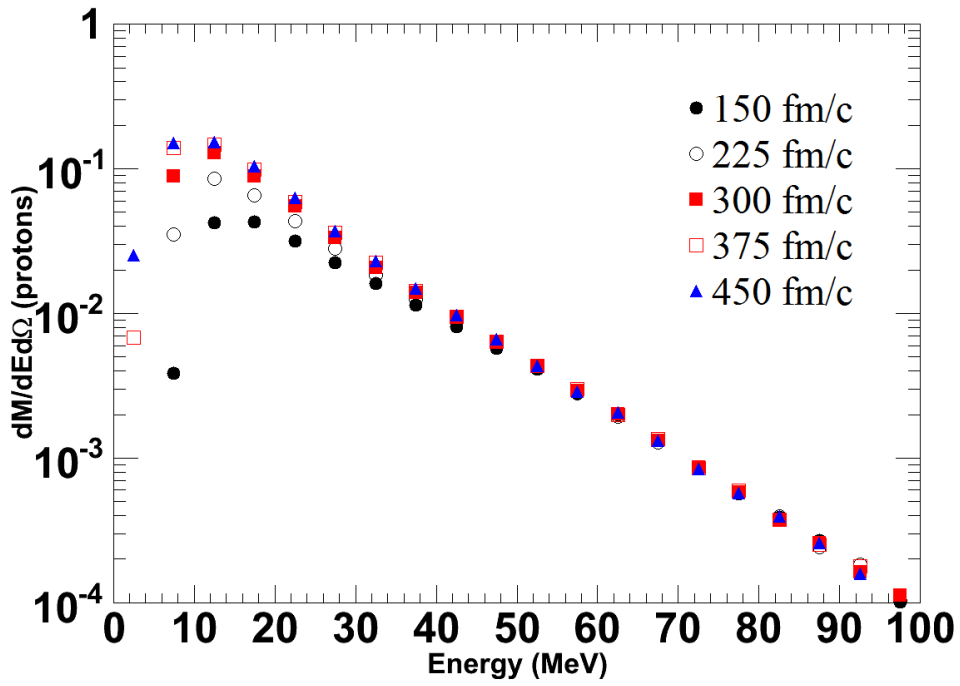
Figure 4.4: An example of the spectra for protons (top) and neutrons (bottom) with the simulation run out to different lengths of time.

the different calculations. As predicted the spectra continue to change, and in particular

decrease, until 600-800 test particles where all simulations with more test particles give a

consistent result. With this understanding, a value of 800 test particles was chosen to be

the standard for which all further calculations would be completed.

4.3   Mean Field

This BUU model uses two separate options for calculating the mean field potential, a

momentum dependent and momentum independent model. The momentum dependent

model utilizes more proper treatments of nucleon effective mass and mean field inter-

actions, however requires much more time consuming simulations. In addition to the

momentum dependence, the code allows for the variance of the isoscaler mean field com-

pressibility, commonly defined as K. In this treatment, the two values for K that are used

are a soft compressibility, 210 MeV, and a stiff compressibility, 380 MeV.

Figure 4.6 shows the double ratio for all four combinations of compressibility and

momentum dependence. As with all spectra in this chapter unless otherwise stated, the

angular range of the particles in question are from $70 \leq \theta_{C.M.} \leq 110$ degrees. The spectra

from the momentum dependent calculations show a slight increase in particle production

in the region above 40 AMeV, while lesser production below that level. Above 10 AMeV,

the stiff mean field also causes an increase in particle production. The effects are all

reasonably similar for neutrons and protons however, as the double ratio does not show

significant changes with these variations as shown in Figure 4.6. Unless otherwise stated,

for the remainder of this treatment, momentum independent calculations will be used

with compressibility of 210 MeV. This compressibility is reasonably similar to an accepted
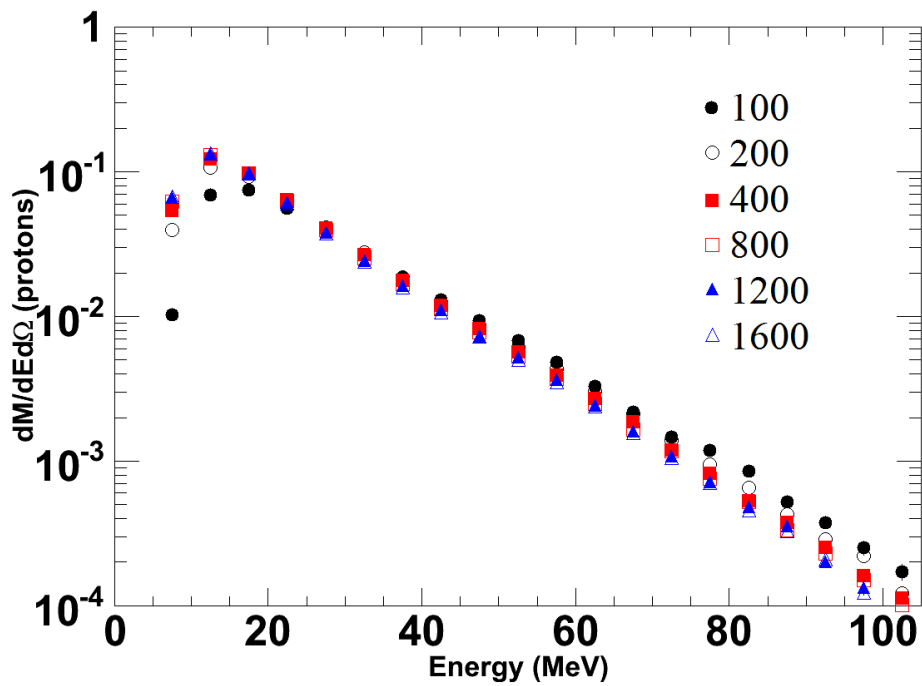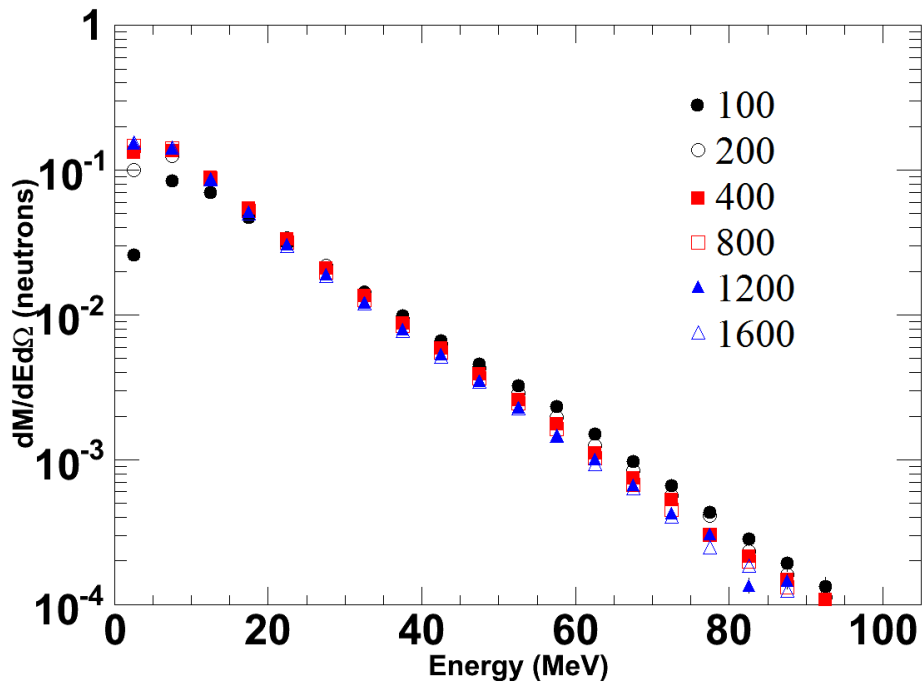
Figure 4.5: The spectra for neutrons (top) and protons (bottom) for varying numbers of test particles. As the number of test particles increases the spectra converge to a consistent value. Around 600-800 test particles the spectra are all consistent to within the variance of different random seeds.
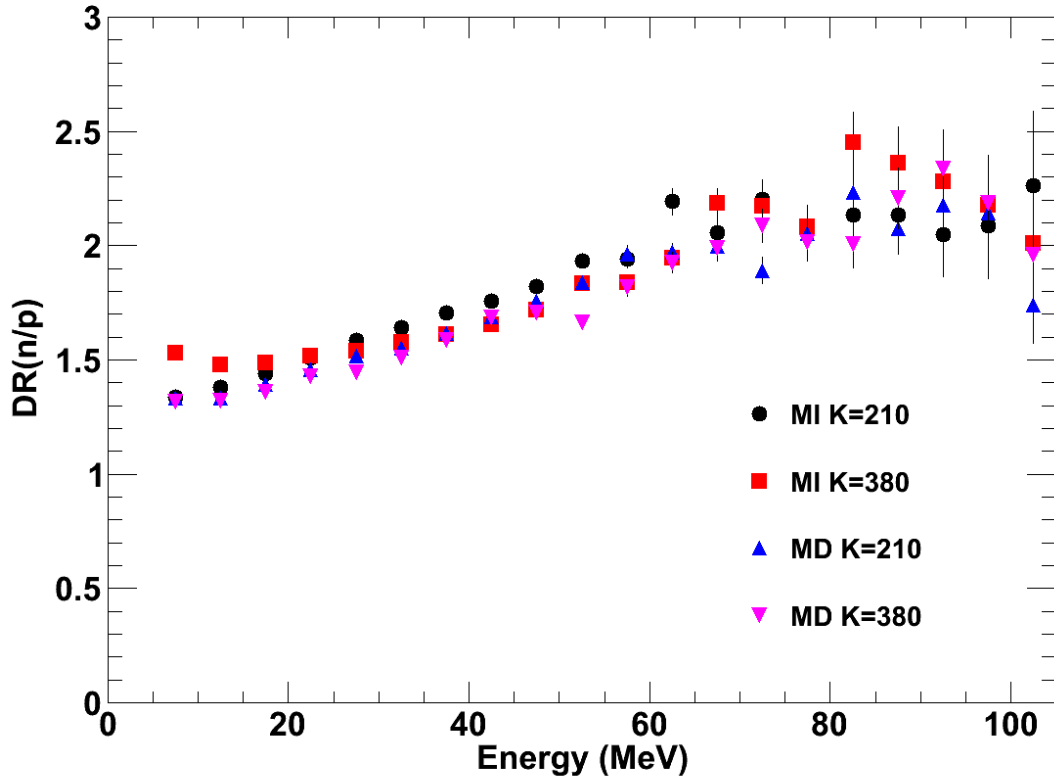
Figure 4.6: An example of the double ratio as the momentum dependence and mean field compressibility are varied. These double ratios show little sensitivity to these variables.

value of 231 ± 5 MeV [42]. The use of momentum independent calculations is to account for the faster calculation time.

4.4 Physical Parameters

Once the main computational parameters were chosen, a long campaign of simulations was completed to learn how different physical parameters affect certain observables, primarily spectra as well as single and double spectral ratios. Since this work is going to be used primarily for comparing to experimental results, the first parameter that was investigated was the dependence on γ from Equation 1.5. One of the simplest cases was

Parameter	Value
Momentum Dependence	Independent
Beam Energy	50
Cluster Production	Off
Compressibility	K=210 MeV
Impact Parameter	2 fm
In-Medium Cross Section	Screened
S_{int}	19
Angular Range	$70 \leq \theta_{C.M.} \leq 110$

Table 4.1: A table of typical values for transport variables in pBUU simulations. Unless otherwise stated, studies throughout this treatment will use these specifications.

chosen as the starting point. The parameters used in the simulation are contained in Table 4.1.

The particles that are chosen for these particular observables are ones that are emitted between 70 and 110 degrees in the center of mass. Figure 4.7 shows the spectra of protons (top) and neutrons (bottom) as a function of angle from a ^{112}Sn reaction at 50 MeV. Each set of data contains all particles in a 10 degree range centered on the labeled value. As can be seen, the spectra shows almost zero sensitivity to emission angle as might be expected from the most central collisions. Figure 4.8 shows the same information for a simulation at 4 fm impact parameter. This figure shows that the particles are emitted symmetrically about 90 degrees as well as with an increase in magnitude the farther from 90 degrees the particles get. The largest enhancement occurs near $\theta = 0$ and 180 degrees, which corresponds to the region of projectile/target like fragments (PLF/TLF). However, in the region from 70 to 110 degrees the spectra are reasonably isotropic. This gives confidence that particles the PLF and TLF are being minimized in this range. Naturally there will be a slight contribution from later collisions but this is negligible at energies above 20 MeV.

Once the selection of data was determined to be valid, a comparison of the spectra as a function of γ was made. Since the effect of the symmetry energy is very small, it is not
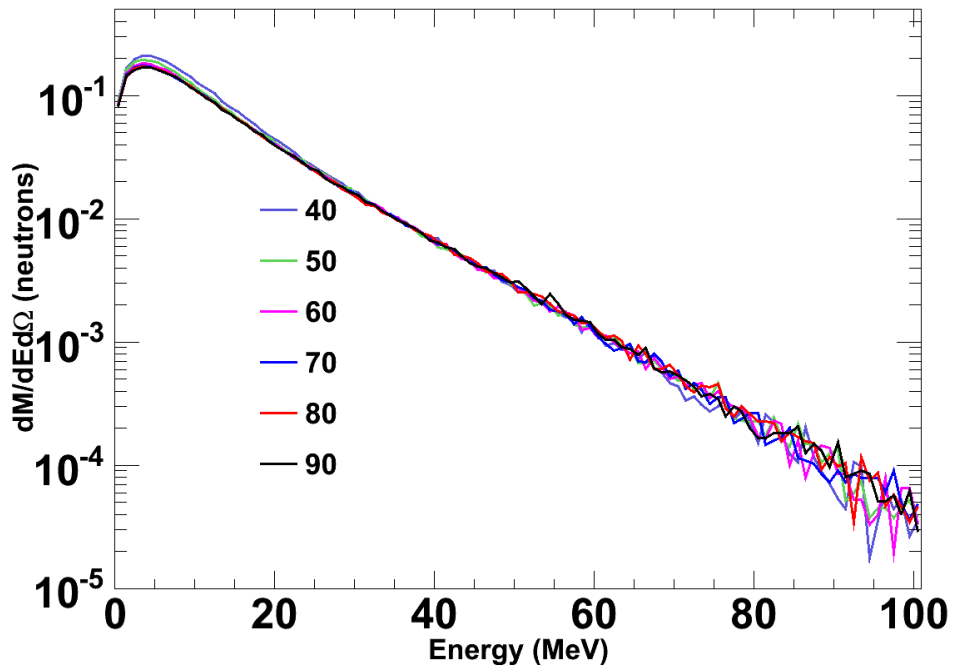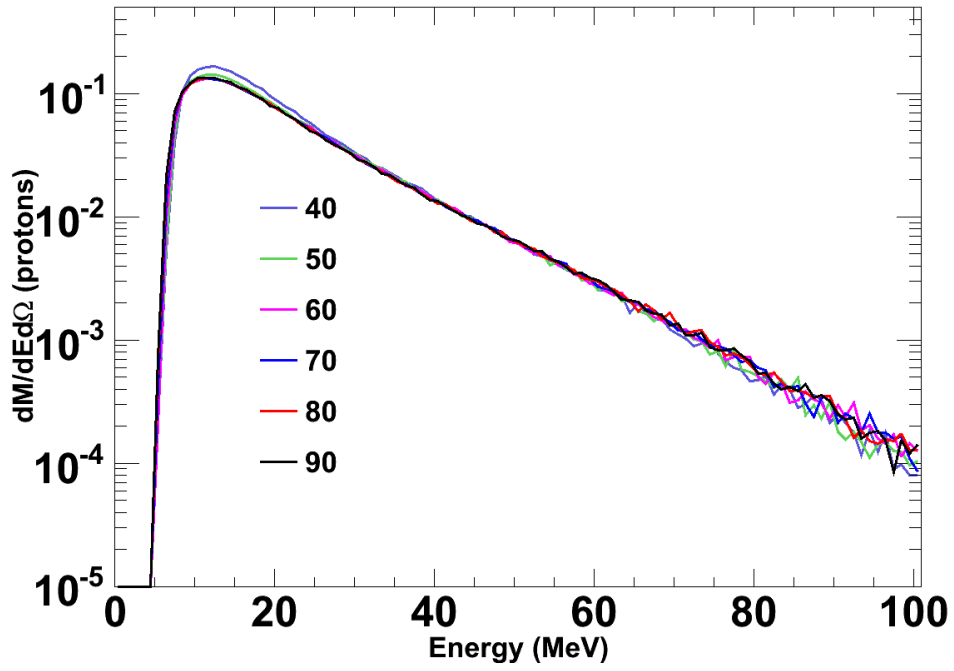
Figure 4.7: Spectra of protons (top) and neutrons (bottom) of a ^{112}Sn reaction at a 0.1 fm impact parameter and $\gamma = 1$ gated every ten degrees.
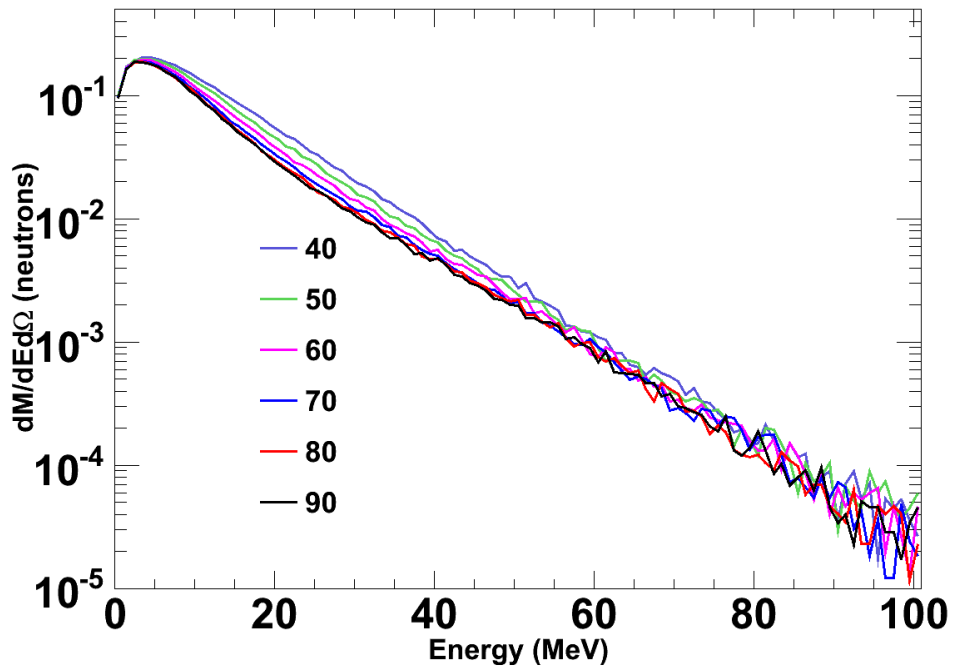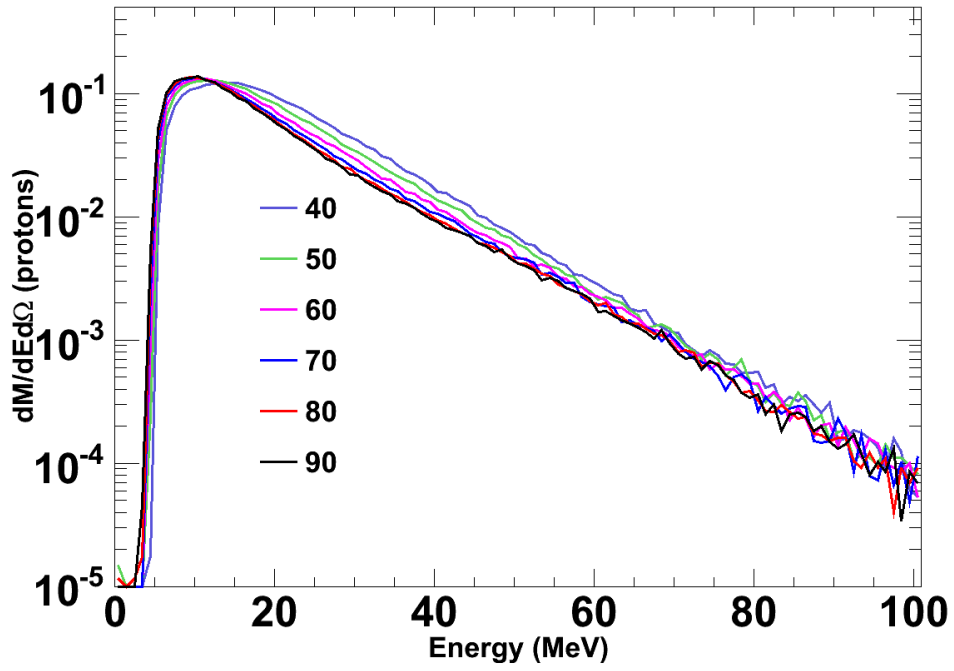
Figure 4.8: Spectra of protons (top) and neutrons (bottom) of a ^{112}Sn reaction at a 4 fm impact parameter gated every ten degrees.

expected that a clear difference would be seen in just the spectra. Instead, the spectral ratio of neutrons to protons is expected to show a difference. Figure 4.9 shows the single ratios,

$$\frac{dM(n)}{d(E_{\text{C.M.}}/A)d\Omega} \bigg/ \frac{dM(p)}{d(E_{\text{C.M.}}/A)d\Omega}, \qquad (4.1)$$

for both ^{112}Sn (left) and ^{124}Sn (right) as a function of γ. The force from the symmetry energy ejects neutrons from the system with a stronger symmetry energy encouraging a larger n/p ratio. Since this energy range probes densities at subsaturation energy, the larger γ gets, the smaller the force from the symmetry energy. This figure clearly shows this effect with $\gamma=1/3$ producing the largest value of a spectral ratio and $\gamma=2$ producing the lowest with a continual trend in between. Also included on each plot is a line representing the n/p ratio of the system pre-collision. If there was no sensitivity to the symmetry energy one would anticipate a flat distribution even with this line. The ^{112}Sn collision, having a much smaller value of δ, shows the expected result of being less sensitive to γ.

One surprising result is that the ratio is almost completely less than one. On first thought, it would be expected that since this collision is neutron rich, the ratio would be greater than one. The Coulomb force effects the protons such that the lowest energy bins are actually vacated of most protons so the n/p ratio is very large. A simpler but less informative ratio where the sum of all emitted neutrons to protons in the area of interest is indeed greater than one. Table 4.2 contains the ratio of integrated neutrons to integrated protons for different values of γ.

The biggest issue behind measuring an n/p ratio experimentally is that accurately determining the neutron detection efficiency to a necessary confidence level is difficult. There are also other issues such as determining the Coulomb effects in these ratios. An-
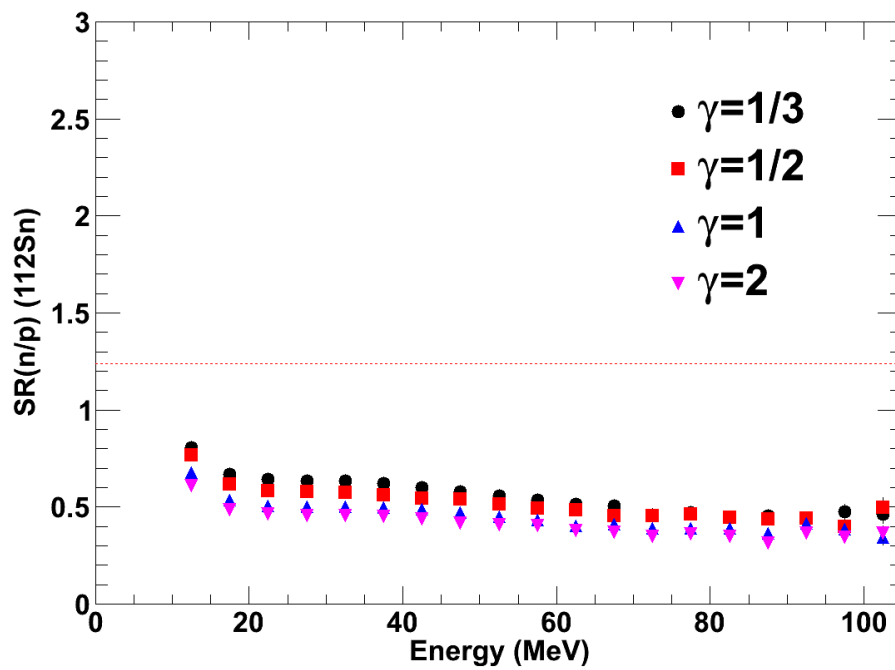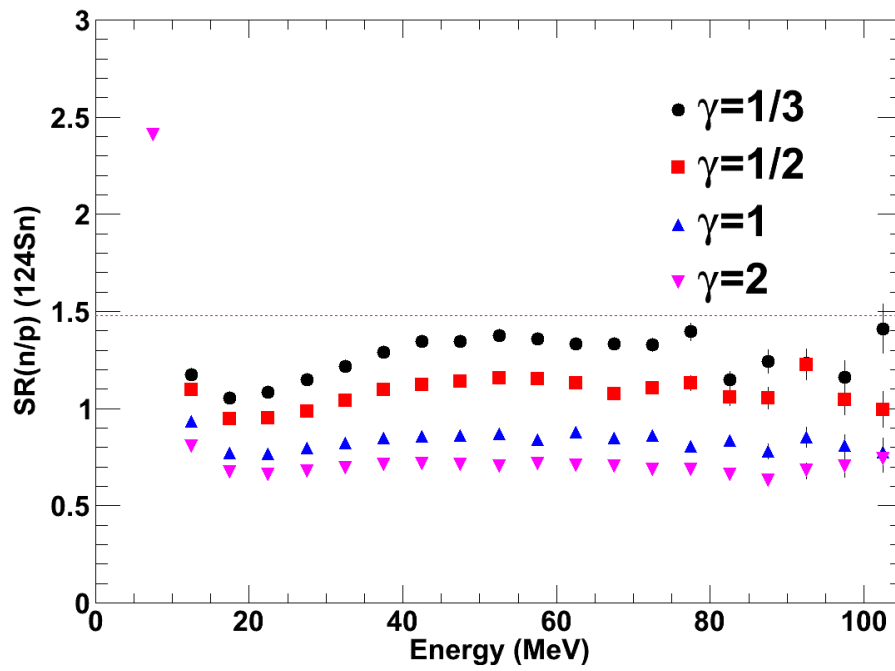
Figure 4.9: The n/p single ratios for ^{124}Sn (top) and ^{112}Sn (bottom).

γ	n/p ^{112}Sn	n/p ^{124}Sn
1/3	1.29784	1.83995
1/2	1.27808	1.79859
1	1.21812	1.67046
3/2	1.16072	1.56517
2	1.12473	1.49398

Table 4.2: The integrated neutron to integrated proton ratios for five different values of γ. As expected, the ratio continues to decrease with increasing γ.

other possible observable that would be able to rid the effects of efficiency is to develop an n/n or p/p ratio where the spectra from the ^{124}Sn collision is compared to the ^{112}Sn spectra. Figure 4.10 shows these independent particle ratios with several interesting qualities. As can be expected, the p/p ratio shows very little sensitivity to the symmetry energy since the amount of initial protons in both collisions is similar. What residual sensitivity there is reflects that the chemical potential for protons is higher in the ^{112}Sn system than the ^{124}Sn system. The n/n ratio shows much more sensitivity due to the large change in the number of neutrons between the system.

These ratios are not necessarily a better option than the single ratios. While there is sensitivity, it would not necessarily instill much confidence to measure simply these observables since the symmetry energy is related to the difference between proton and neutron densities. Instead, if the benefits of both sets of ratios are combined and a double ratio is created of the form,

$$DR_{n/p} = \frac{SR_{124}(n/p)}{SR_{112}(n/p)},$$

(4.2)

a new observable is provided, which is displayed in Figure 4.11.

Based on the single ratios one can expect the trend of a stronger symmetry energy resulting in a larger value of the double ratio, that is, having a stronger effect of pushing
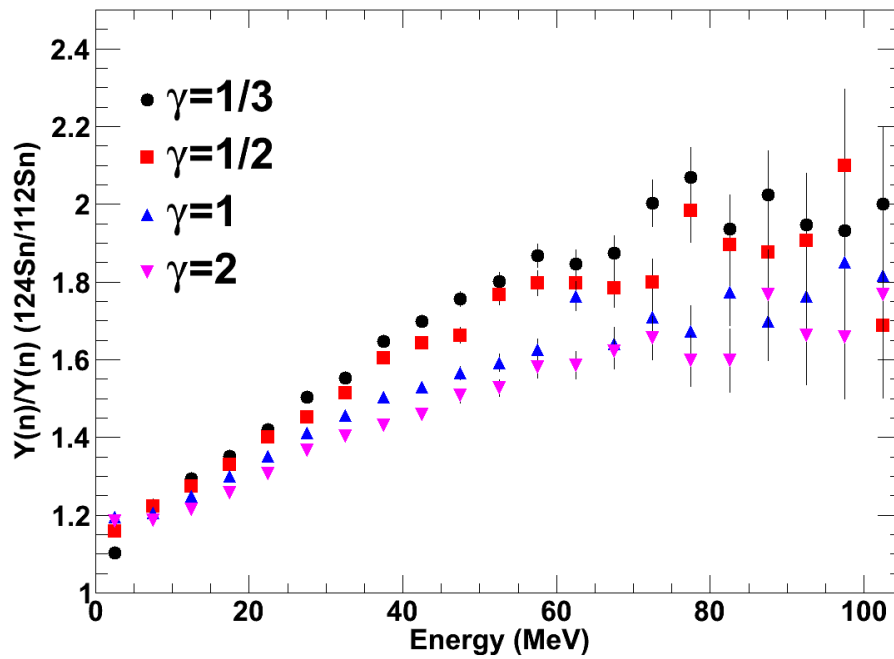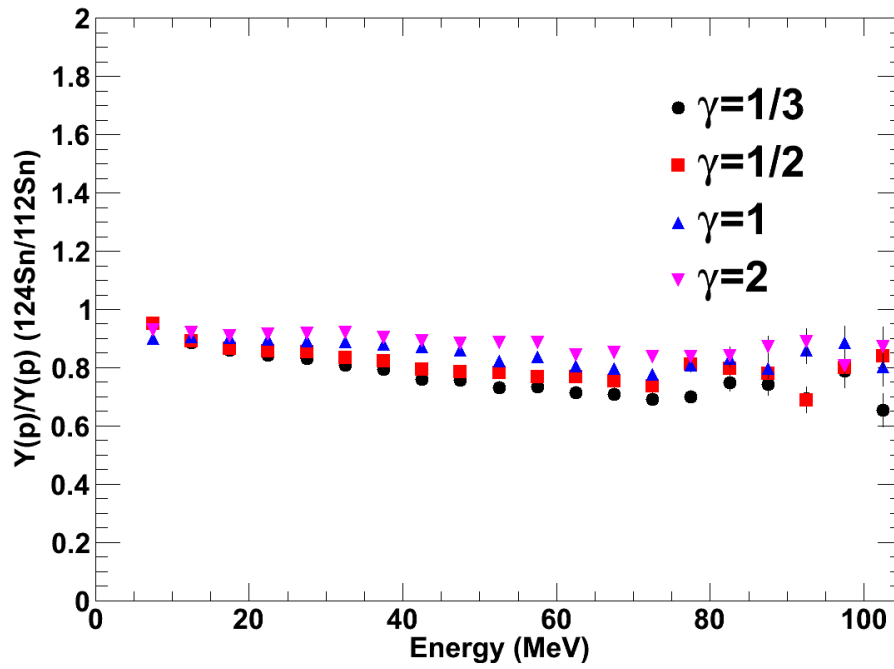
Figure 4.10: The ratio of protons from the ^{124}Sn system to that of the ^{112}Sn system are displayed on top as a function of γ. The corresponding neutrons are on the bottom.
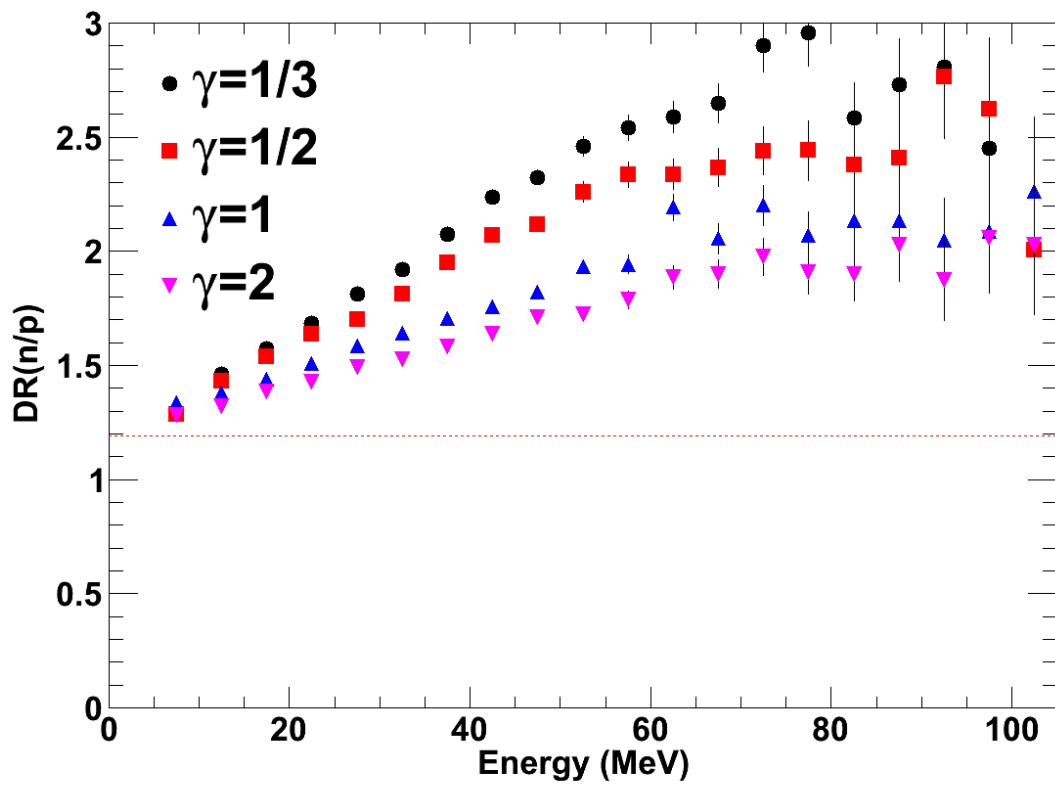
Figure 4.11: The n/p double ratio as a function of γ.

out the neutrons instead of protons in the ^{124}Sn system over the ^{112}Sn system. It would be expected then, that if the coefficient S_{int} were modified (changing the value of the symmetry energy at saturation density), a similar effect would occur. In this case however, the double ratio should increase with increasing value of S_{int}. Figure 4.12 shows examples of the dependence on S_{int} while leaving all other properties constant.

A number of interesting effects are immediately noticeable in Figure 4.12. The first of which is the confirmation of the prediction that a larger S_{int} produces a larger double ratio. The second is that as γ is increased, the sensitivity to S_{int} decreases. Simple calculations will show that when using a sample density of $0.6\rho_0$ (the density region around which we are probing), the difference in the value of the symmetry energy from $S_{int}=15$ to $S_{int}=24$ is almost 8 MeV when $\gamma=1/3$ yet only 3 MeV when $\gamma=2$, explaining the difference in sensitivity. A similar study shows that when S_{int} increases the sensitivity to γ also increases as one would anticipate.

There are three different cross sections that are introduced in pBUU, free, screened and Rostock, each of which was described in Section 1.2. The free cross section should have the largest amount of collisions, with the Rostock slightly less and the screened much lower. Figure 4.13 shows the proton and neutron spectra for the three different cross sections. Despite the differences in the shape of the spectra from the different cross sections the double ratio for all three cross sections is almost identical as displayed in Figure 4.14. This occurs since the shape change in the proton spectra is similar to the shape change in the neutron spectra.
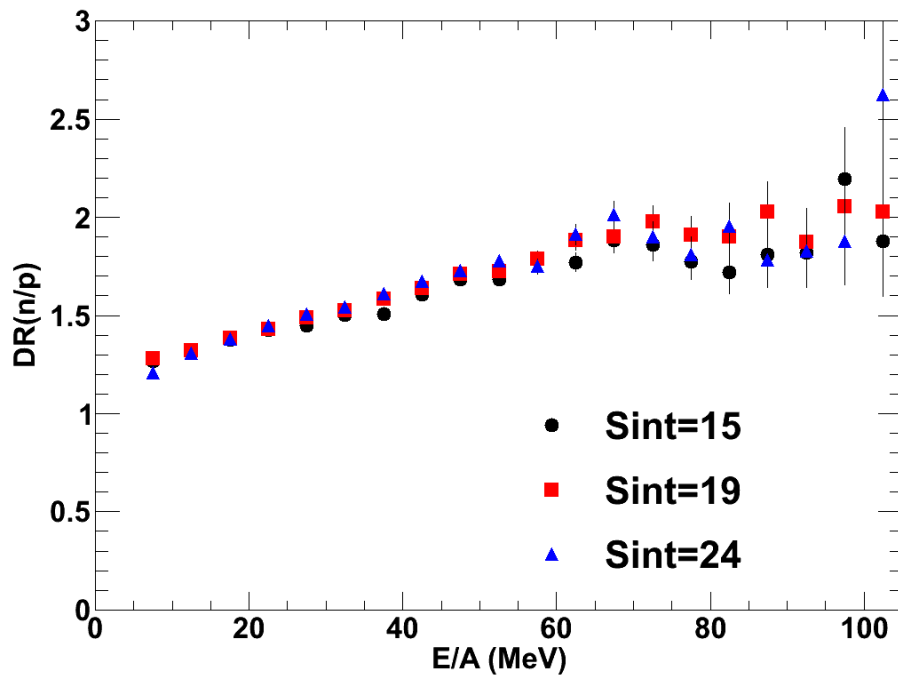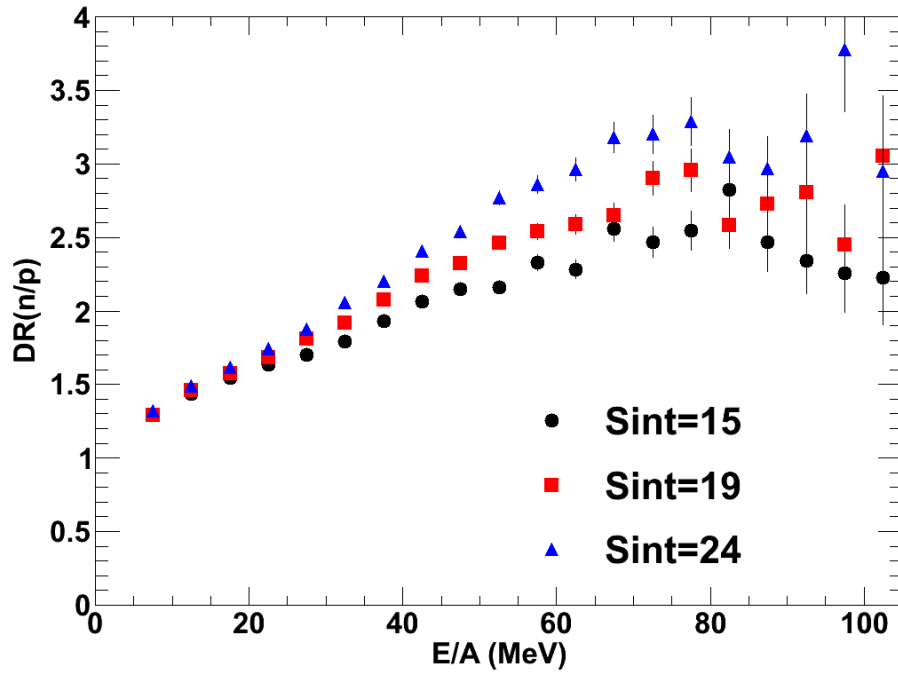
Figure 4.12: The n/p double ratio as a function of S_{int}. The top plot has simulations where $\gamma=1/3$ and the bottom with $\gamma=2$.
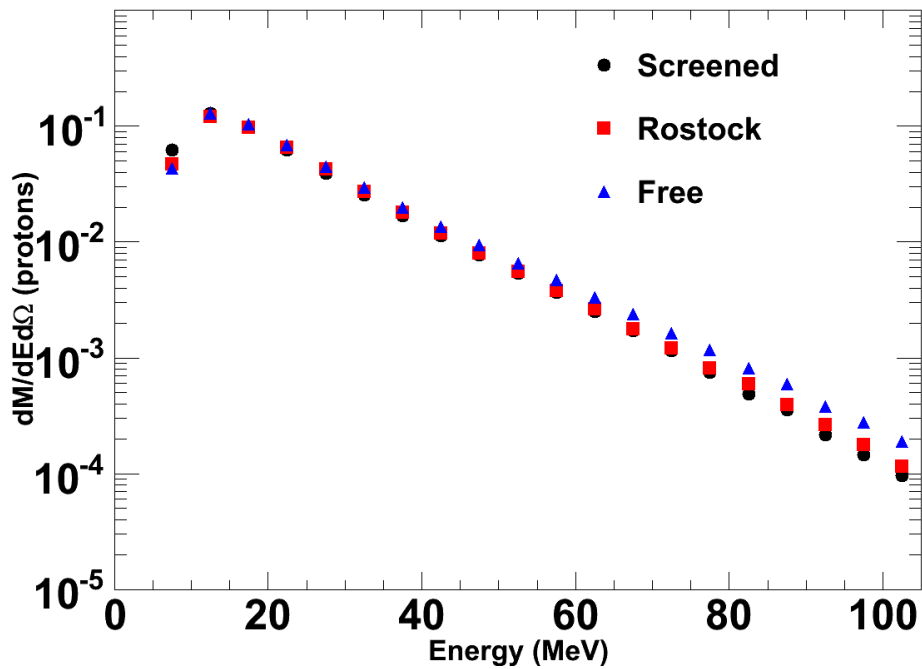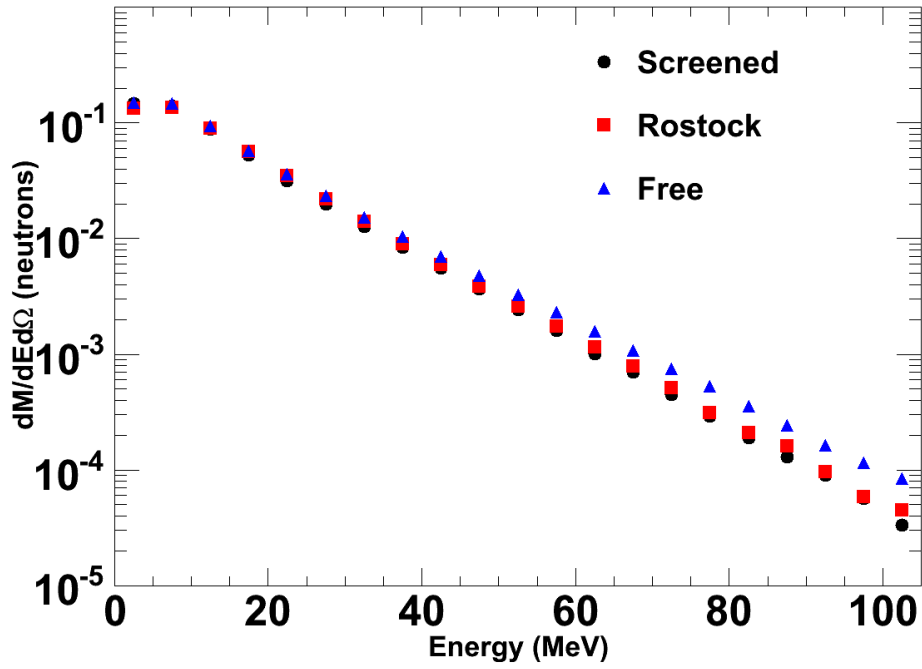
Figure 4.13: The neutron (top) and proton (bottom) spectra for the three different cross sections available in pBUU for a ^{112}Sn reaction. Contrary to what is expected, the screened produces more particles than Rostock.
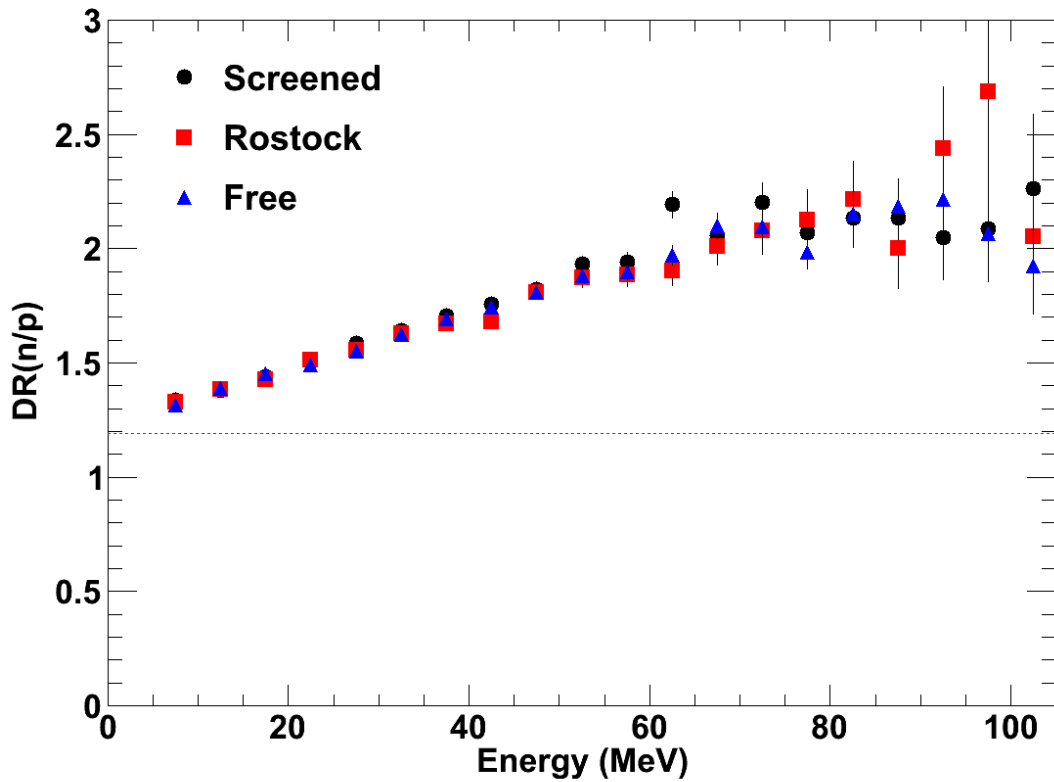
Figure 4.14: The double ratio for the three different cross sections available in pBUU. Despite the difference in the behavior, the double ratios are rather similar showing that the choice of in medium cross section does not have a strong influence on the results.
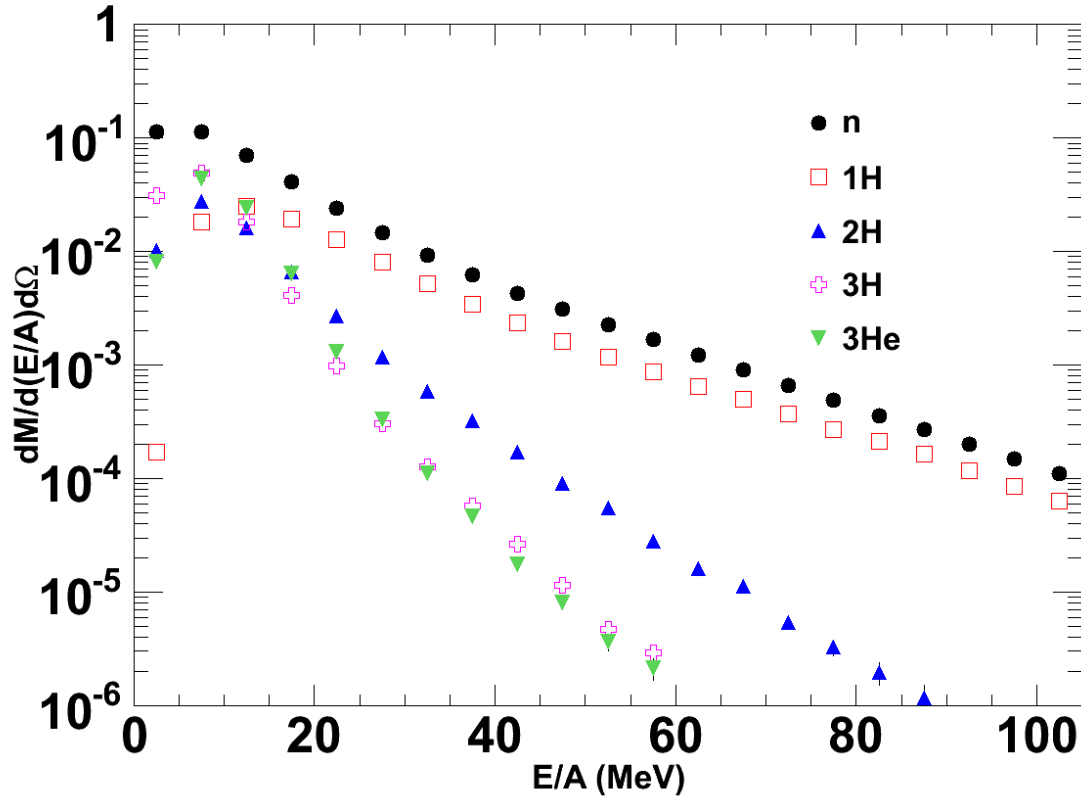
Figure 4.15: Example spectra of all five light particles that are created in the BUU when the cluster production option is activated.

4.5 Cluster Production

As discussed in Section 1.2, the unique aspect of this particular BUU code is the ability to create light clusters, which one would expect to have an impact on the dynamics and results of the spectra as well as other observables. An example of the spectra for all five produced particles is included in Figure 4.15.

Figure 4.16 shows the spectra for neutrons and protons for an example comparison. The plot shows three different results, all of which use the same parameters except that cluster production is not included in one set and is in the other two. The two results

with clusters are formed two different ways. The first is simply taking the free neutrons and protons from the reaction. The second way, described as coalescence invariant, sums up the neutrons and protons from all free particles. In this model, a deuteron would be counted as both a neutron and proton, a triton would be a proton and two neutrons, and so on. One would obviously expect a decrease in the number of free protons and neutrons when clusters are included since many of those free particles would be taken up by the clusters, which is certainly what is observed in this figure. The coalescence invariant would then be closer to what was predicted by the simulation without cluster production.

However, one may expect some difference between the two calculations resulting from the energetics of cluster formation. Cluster formation takes into account the binding energies of the clusters, which upon creation heats up the rest of the source. This causes the resulting spectra to display an increase in temperature at energies greater than 40 MeV/A, which can be seen in Figure 4.16.

Some evidence for the utility of the coalescence invariant spectra and ratios comes from the independent particle ratios. Figure 4.17 shows the independent particle ratios for protons, neutrons, tritons and ^{3}He. These ratios show a trend where the neutrons behave similar to the neutron-like tritons and the protons behave like the proton-like ^{3}He at larger emission energies. While the trend agrees reasonably, the magnitudes do not agree until above E/A=35 MeV. In contrast, we will see in Chapter 5 that the measured independent particle ratios will agree across the entire energy range instead of only at large energies. One should at this point wonder what the result would be if the simulation did not truncate at mass A=3 and included heavier particles. Chapter 5 will attempt to address this.
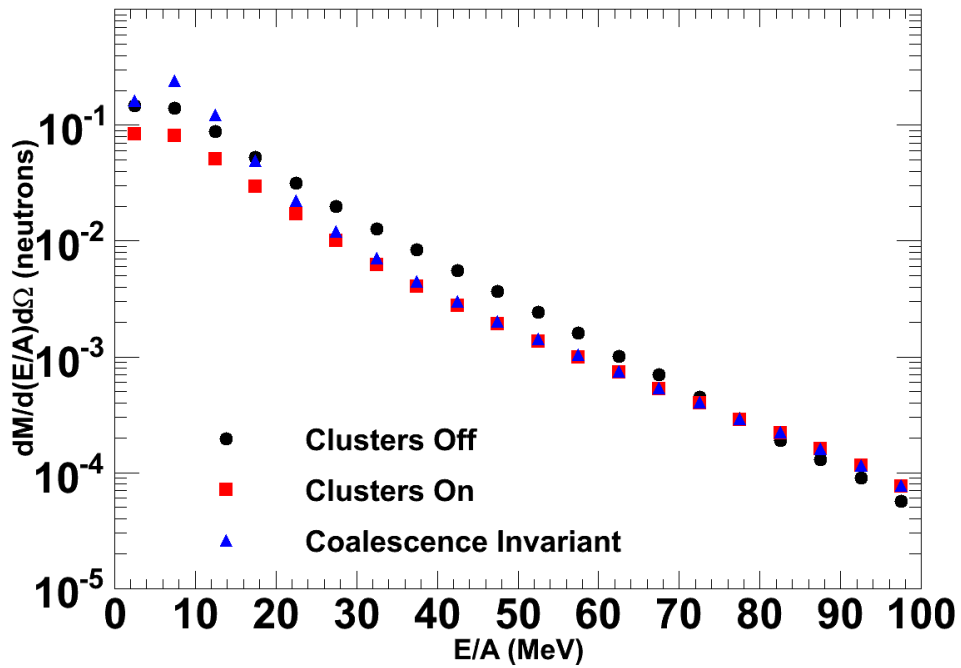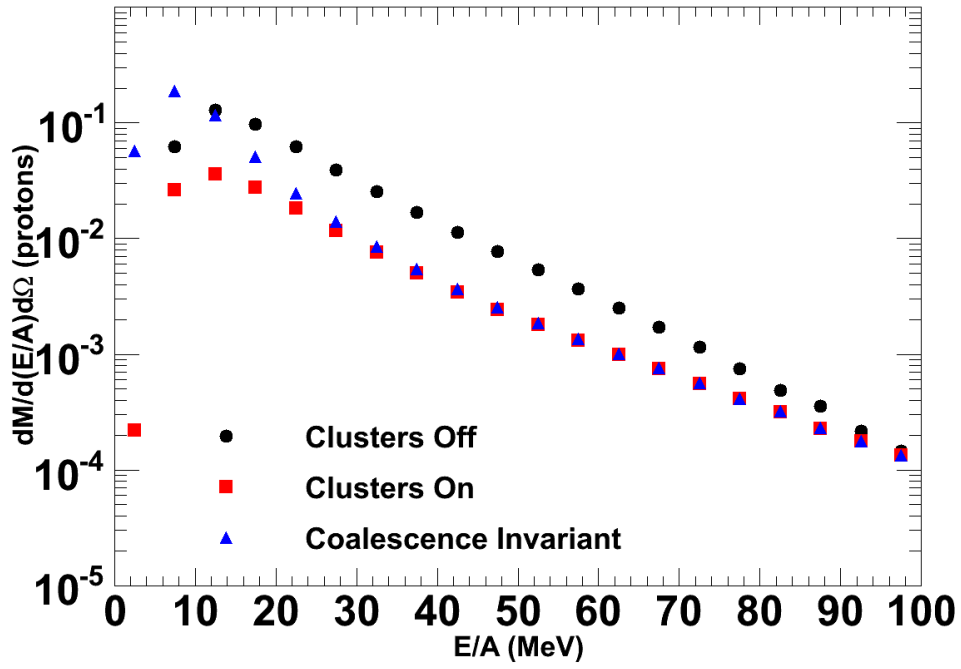
Figure 4.16: A comparison of the spectra for a non cluster producing, cluster producing and coalescence invariant spectra for protons (top) and neutrons (bottom).
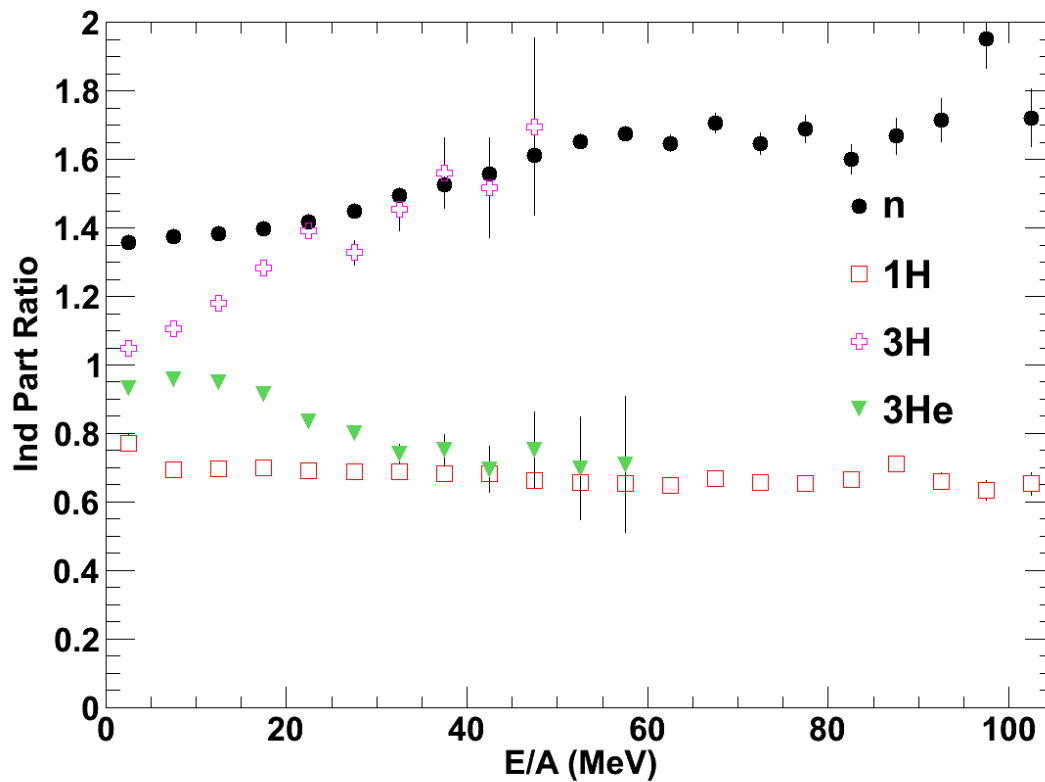
Figure 4.17: The independent particle ratios showing coalescence between proton-like and neutron-like particles in 50 MeV/Areactions.

Figure 4.18 shows a similar comparison for the single ratios for ^{112}Sn and ^{124}Sn reactions with $\gamma = 1$. After around E/A=80 MeV the coalescence invariant and the standard cluster producing n/p ratios are identical since deuterons are negligibly produced at that energy. From E/A=60 MeV to 80 MeV the deuterons lower the ratio closer to a value of one, but due to their lower production numbers, their effect is not large. Below 60 AMeV, the tritons and ^{3}He particles have a much larger effect. Both cluster producing simulations provide an n/p ratio that is increased closer to what would be initially expected, that is larger than 1 and larger than the N/Z ratio of the system. This arises partly from the neutron and proton number conservation. The A=2 and A=3 clusters are more symmetric than the protons and neutrons. As such, if a large number of clusters are produced the asymmetry of the rest of the system must increase in order to conserve mass and charge. The double ratio shows a similar increase in effect as shown in Figure 4.19.

The single and double ratios vary with γ in a similar way to the simulations without clusters. In simulations with a smaller γ which result in a stronger the symmetry energy, the larger the n/p ratio for an asymmetric system. The free n/p double ratio even shows a similar sensitivity to γ. The coalescence invariant model shows a decrease in sensitivity below around E/A=30 MeV, but in general is similar in sensitivity at higher energy to previous calculations as shown in Figure 4.20

Multiple sources have suggested that instead of simply looking at the n/p ratio which is difficult to measure, the ratio of any two particles that are mirror nuclei and are a beta decay separated from each other, can also be investigated, such as t/^{3}He or ^{7}Li/^{7}Be. The lithium and beryllium are outside the scope of this code, but the t/^{3}He ratio is an interesting option. One might expect that comparing measured and calculated t/^{3}He
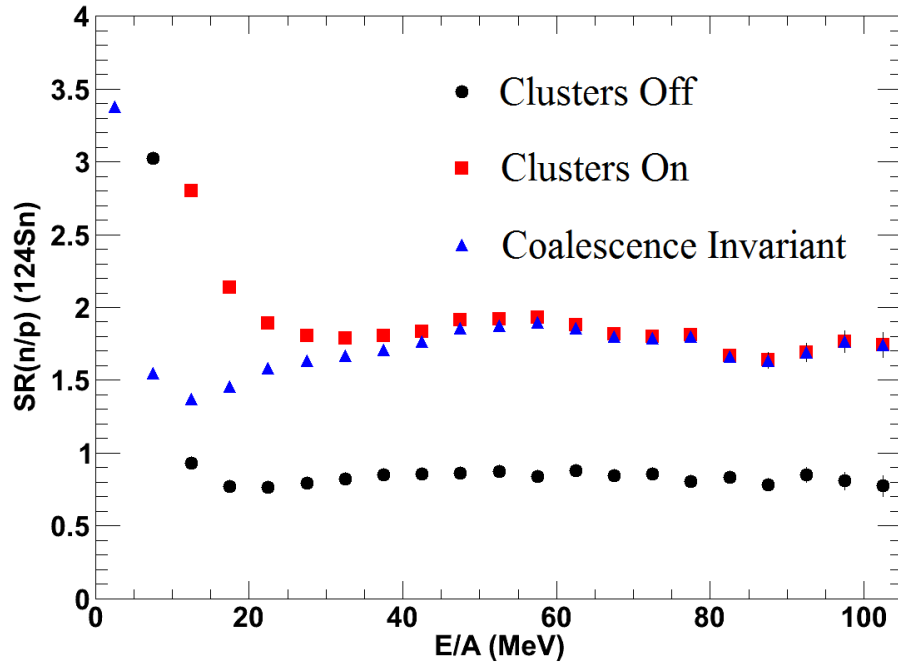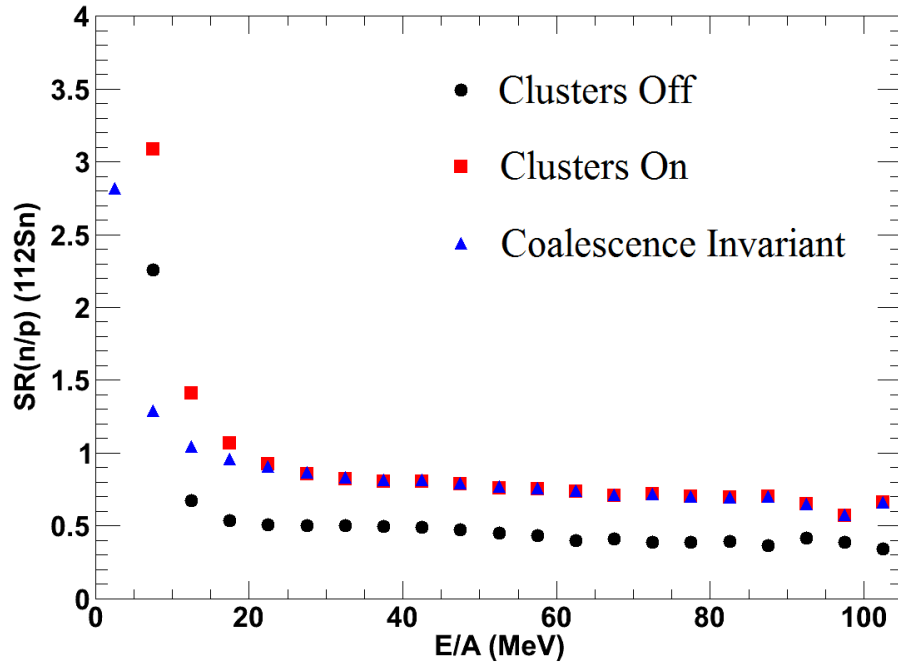
Figure 4.18: The single ratios from $\gamma = 1$ with and without cluster production as well as the coalescence invariant model. ^{112}Sn is on top with ^{124}Sn on the bottom.
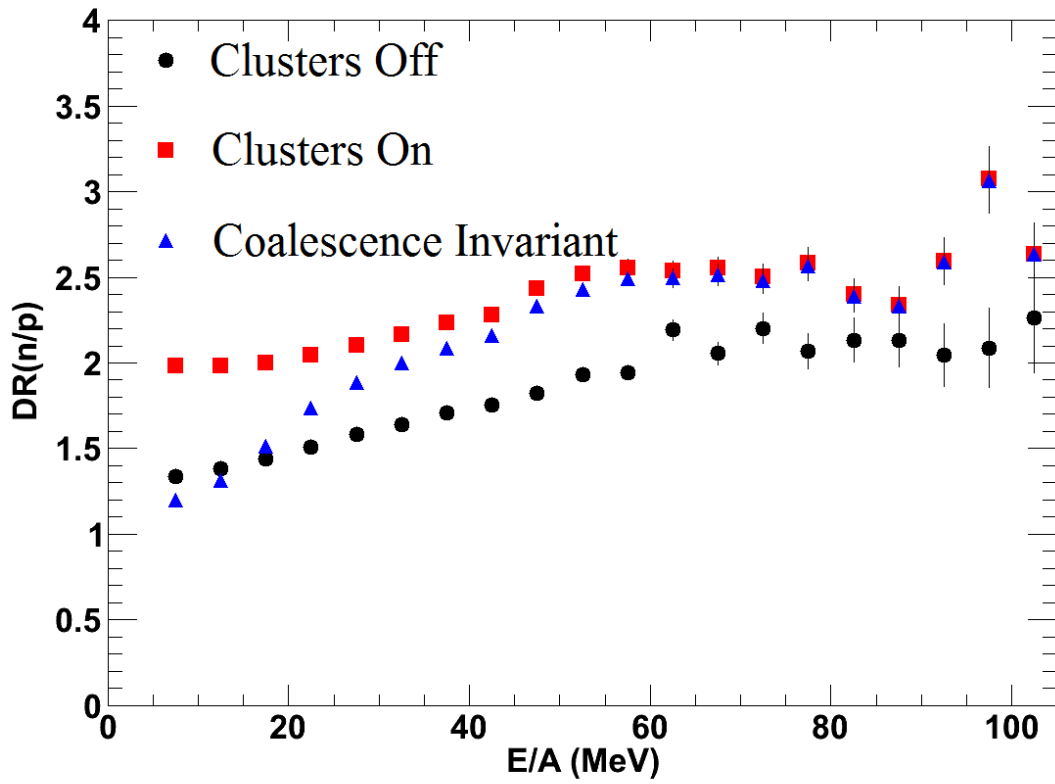
Figure 4.19: The double ratios from $\gamma = 1$ with and without cluster production as well as the coalescence invariant model.
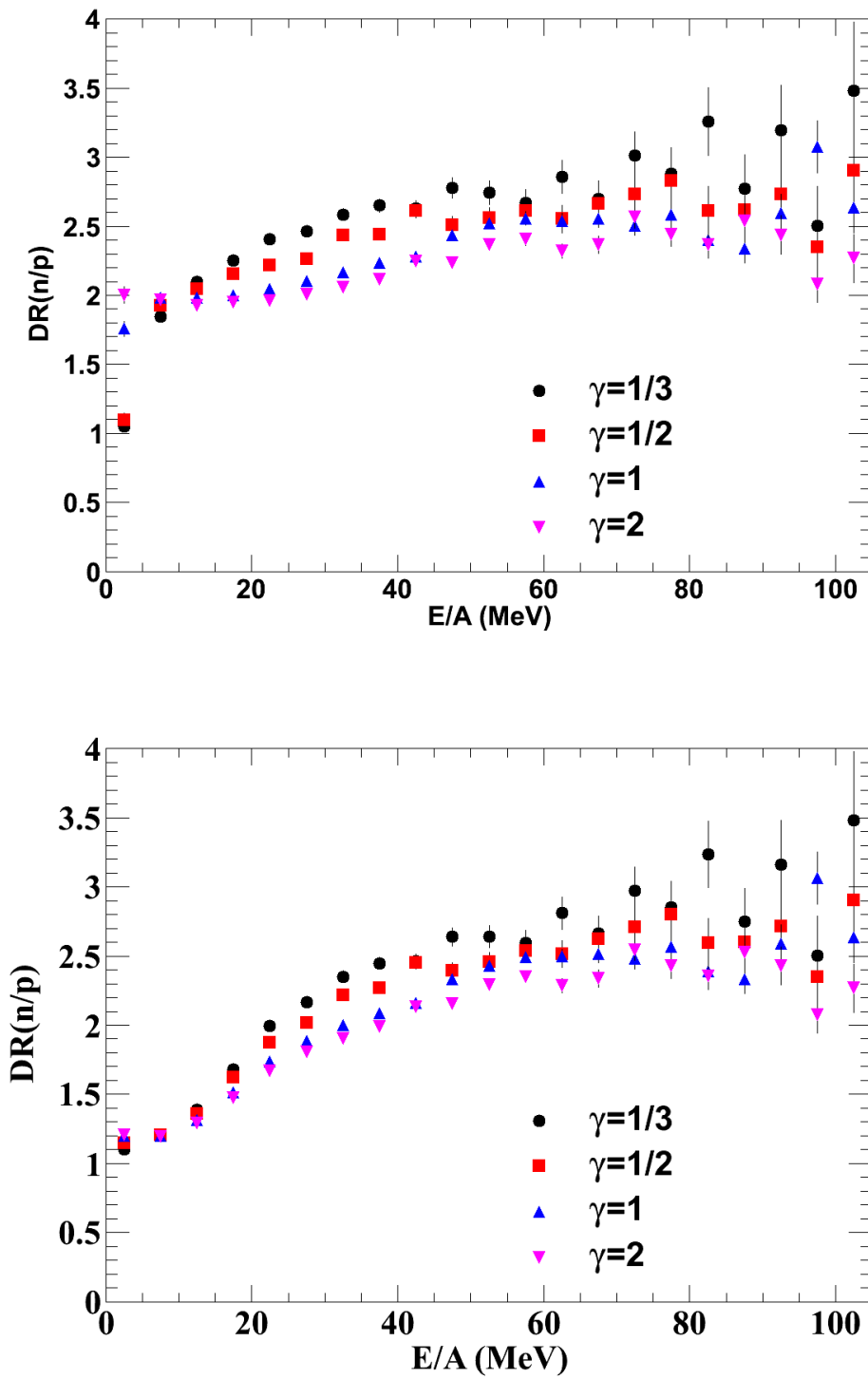
Figure 4.20: The double ratio as a function of γ in a cluster producing (top) and coalescence invariant (bottom) model. The behavior of the coalescence invariant calculation is very similar to that of the non cluster producing simulation.
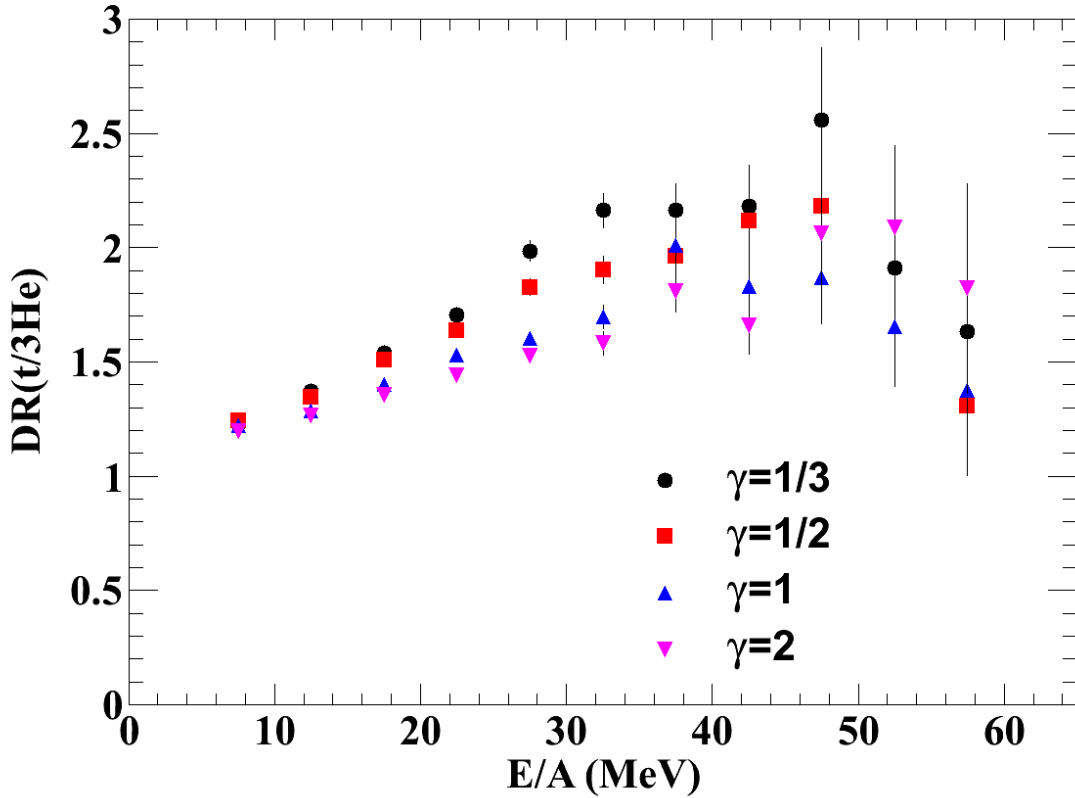
Figure 4.21: The dependence of the t/^{3}He double ratio on γ. Due to the small range of energies that this ratio is measured, it is difficult to get a large amount of statistics at above 45 AMeV.

ratios would explore some of the important questions of the clusters in simulations. One such investigation is whether tritons behave as neutron-like particles and ^{3}He as proton-like particles. If so, this ratio should then be sensitive to the symmetry energy like the n/p ratio is. Figure 4.21 shows the sensitivity to γ for the double t/^{3}He ratios. At this point in the investigation, we are statistically limited above 40 MeV, however have enough to show that there is sensitivity to the symmetry energy. A more statistically significant calculation is shown in Chapter 5 in order to compare to experimental data.

4.6 Higher Energy Range

So far I have only shown simulations using collisions at 50 MeV/A. This energy provides a range of densities in the subsaturation region. A brief study was also conducted to see the effects of the symmetry energy on the single, double and independent particle ratios at higher energies. This study consisted of simulations using the superstiff and supersoft limits of γ =2 and 1/3, respectively, at the energies of 120 and 200 MeV/A. At these energies we probe density regions around saturation density for the 120 MeV/Areaction and at supersaturation density for the 200 MeV/Areaction.

Figure 4.22 shows a comparison of the n/p double ratios in cluster forming simulations for the extrema of γ for the 50 and 120 MeV/Areactions. In the range around saturations density, the variance in the strength of the symmetry energy from γ = 1/3 to γ = 2 is much smaller than it is in subsaturation densities. As such, it might be expected that in the 120 MeV/Areaction the n/p double ratio would have a reduced sensitivity to γ than in the 50 MeV/A. Another effect that might be anticipated is that in the 120 MeV/Areactions, the collision will take place much faster, allowing the mean field (and subsequently the symmetry energy) less time to have an effect. This would lead to a double ratio closer to the 1.19 N/Z limit of the system. Both of these effects are indeed observed in Figure 4.22.

As with the previous figure comparing 50 and 120 MeV/Areactions, Figure 4.23 compares 120 and 200 MeV/Areactions. In this case the n/p double ratio for the 200 MeV/Areaction is even closer to the nonsensitivity limit and shows less sensitivity to γ. Upon close inspection it appears that the trend of a softer γ providing a larger double ratio has flipped, which might be expected at supersaturation densities. In those regions where $\rho/\rho_0 > 1$, values of $\gamma > 1$ would lead to larger forces ejecting neutrons from the
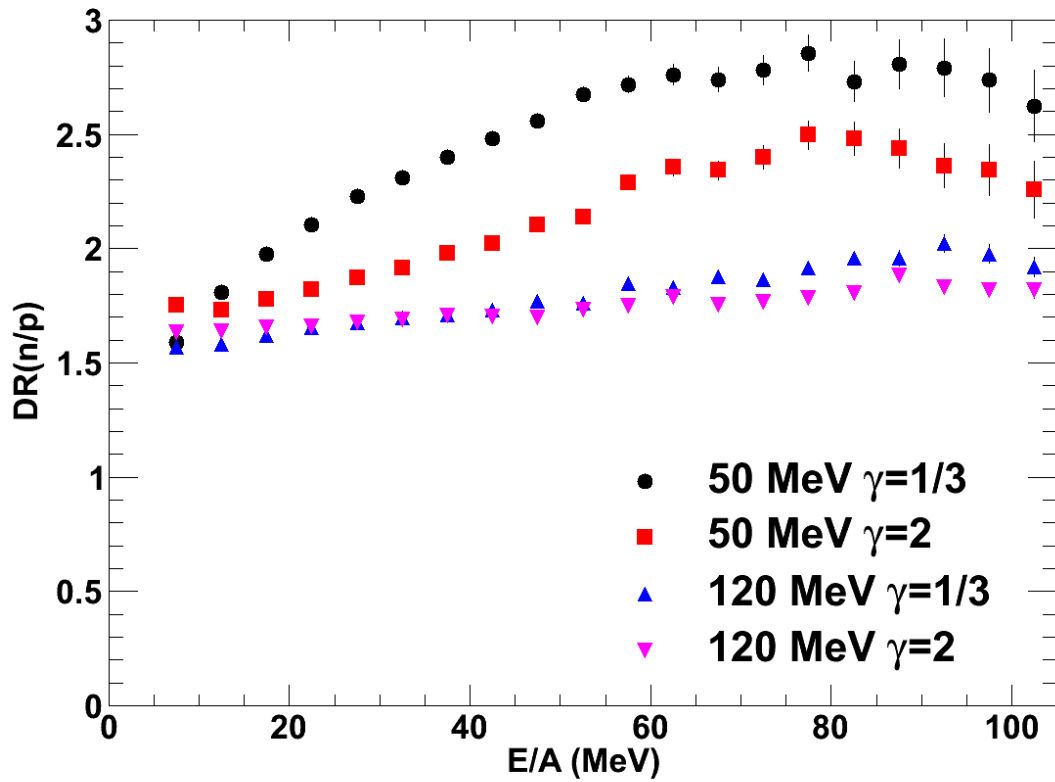
Figure 4.22: An example of the reduced sensitivity to both γ and the symmetry energy for 120 MeV/Areactions.
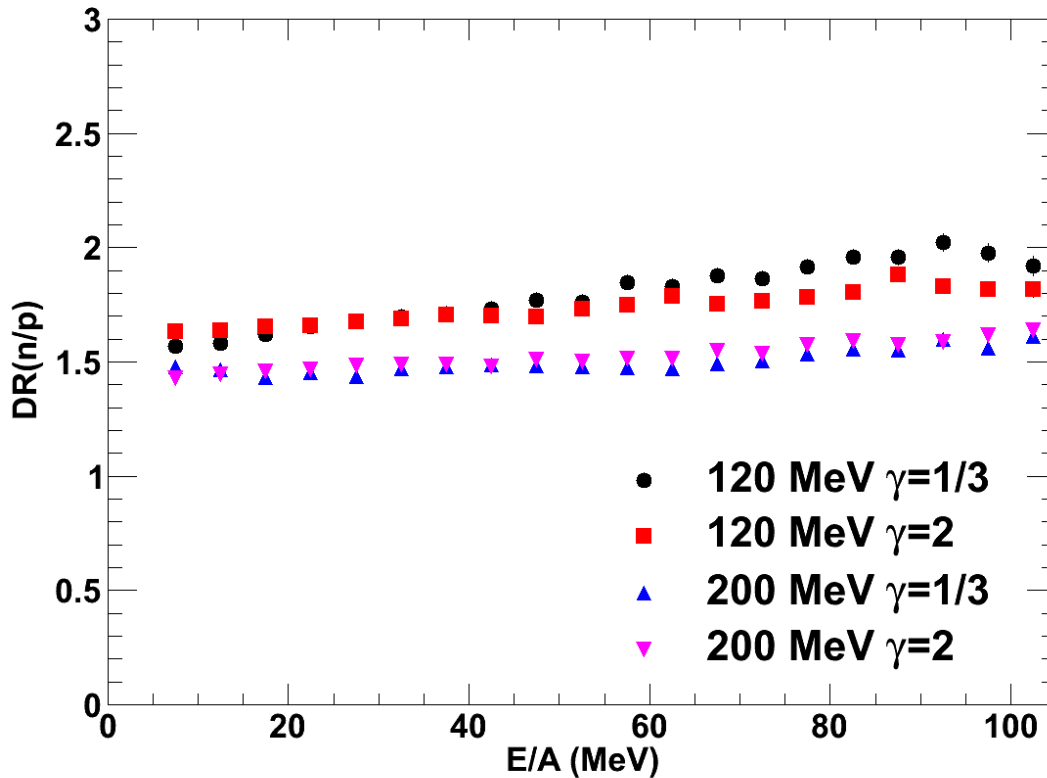
Figure 4.23: An example of the reduced sensitivity to the symmetry energy in 200 MeV/Areactions and possible reversal of trend in sensitivity to γ.

system instead of values of $\gamma < 1$ as in subsaturation densities. It is difficult to say this for certain as there is little sensitivity even at this energy. It is possible that a larger beam energy would enhance this trend. On the other hand, it is probable that the shortened interaction time at higher incident energies could be a more dominant effect and prevent an increase in sensitivity to γ. All of these trends are reproduced in the $t/^3$He double ratios as displayed in Figure 4.24. The only possible exception to this is the reversal of trend in the 200 MeV/Areaction between the two γ values, however they are nearly identical.

In general, one expects the role of clusters to decrease at higher energies. More specifically, if heavier clusters can be neglected, the calculations for nucleons and A<3
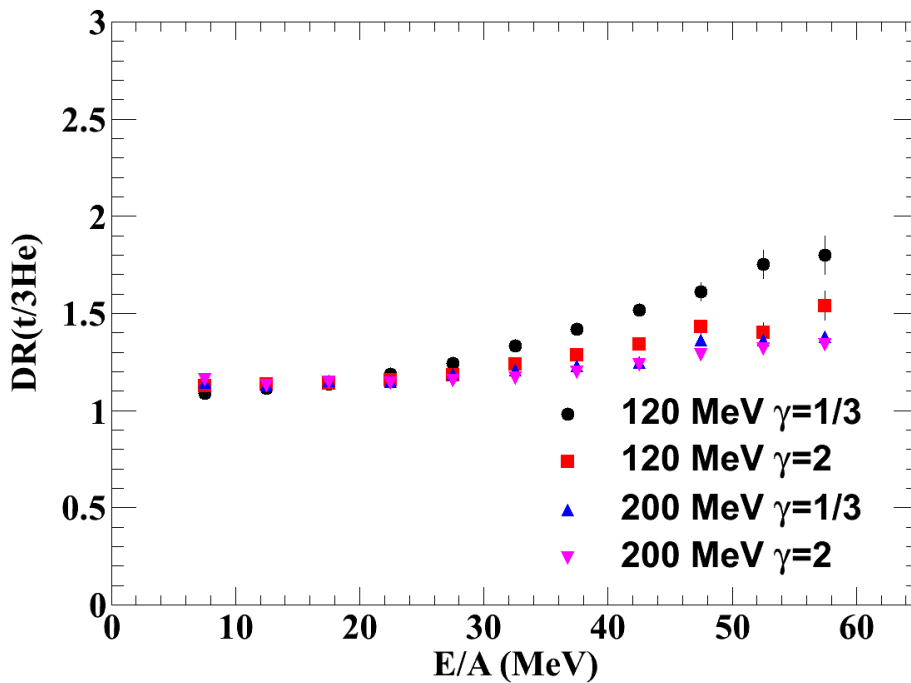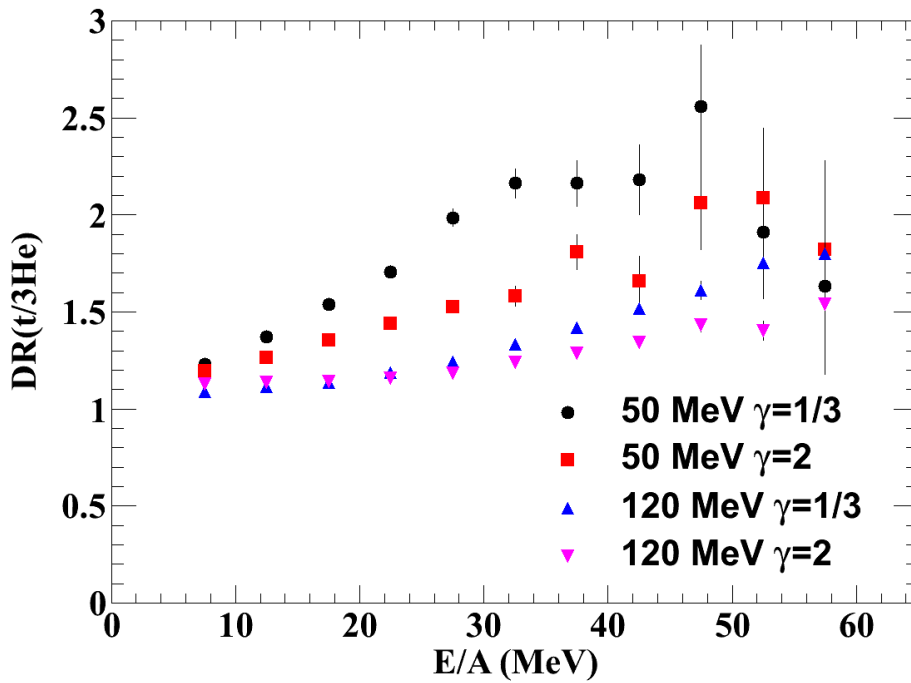
Figure 4.24: Comparison of the t/^{3}He double ratios at three different beam energies.

clusters should be more accurate. Consequently, the agreement between the neutron and triton independent particle ratios may improve as the beam energy is increased. Similarly, the agreement between the proton and ^{3}He independent particle ratio may also improve. Figure 4.25 displays these ratios for the 120 and 200 MeV/Areactions. In similar fashion to the 50 MeV/Areactions, the neutron and triton ratios (and similarly the proton and ^{3}He ratios) do not agree at low emission energy but do at higher energies. The discrepancy between the ratios at low energy does decrease as the beam energy is increased.

The intention behind this study was to see how different transport variables in pBUU influence observables that are sensitive to the symmetry energy, primarily n/p and t/^{3}He double ratios. We find that many of the variables, such as in-medium cross section or mean field compressibility have a smaller influence in the dynamics than the symmetry energy does. In Chapter 5, I will make direct comparisons between experimental data and specifically chosen simulated results. Details of those comparisons will be described there.
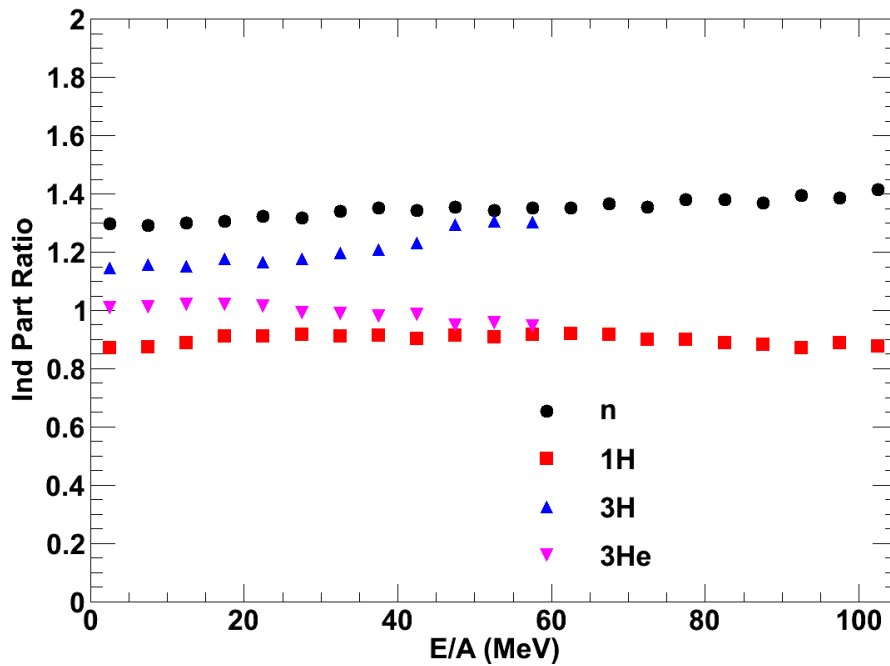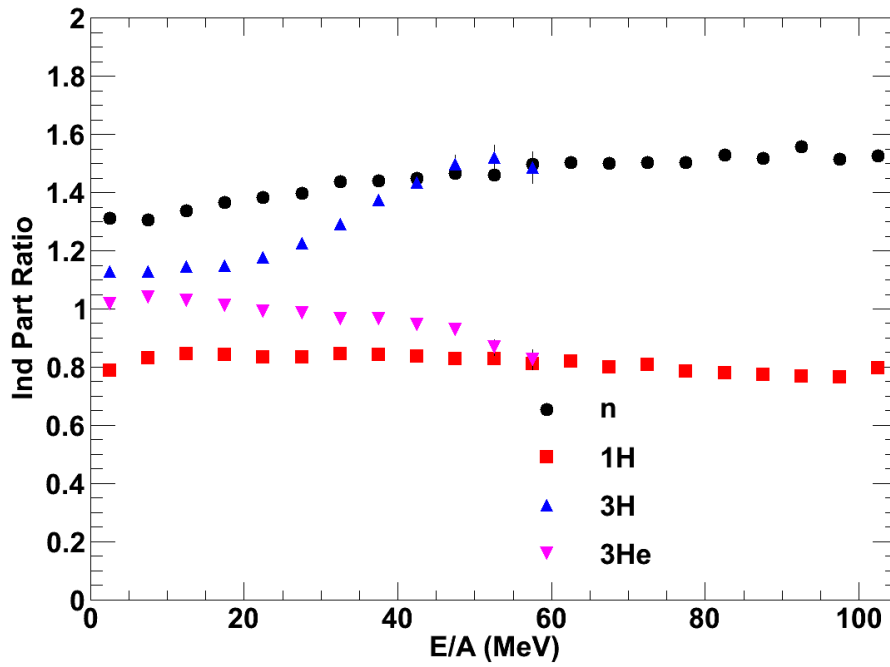
Figure 4.25: The independent particle ratios for 120 MeV/A(top) and 200 MeV/A(bottom) reactions. As the beam energy increases the coalescence agreement improves, noticeable at low energies.

Chapter 5

Experimental Results

Once the calibration of the Miniball and LASSA were completed, a select few observables were investigated. Before they could be investigated, several efficiency corrections must be addressed. We will begin with a discussion of efficiency corrections needed for spectra in the lab frame. There are several corrections that need to be made in order to produce reasonable spectra. Since LASSA is arranged only in six telescopes and not covering the full azimuthal range, a correction dubbed ε_{geo}, or geometric efficiency, is generated to compensate for the missing solid angle. This correction assumes azimuthally symmetric emission around the beam axis. Since we do not determine the reaction plane for these collisions, this is probably reasonable assumption. The next correction, the detector efficiency or ε_{det}, accounts for several additional effects that reduce the efficiency for the measurement of particles that hit the LASSA detectors.

5.1   Laboratory Frame

5.1.1   Azimuthal Efficiency Correction

In order to obtain a precise measurement of the effective multiplicity of charged particles from the reaction, the azimuthal coverage efficiency of LASSA was calculated and the data were corrected for the lack of azimuthal angular coverage in the lab frame. To calculate the geometric efficiency, we decided to bin the data every 1/2 degree in the lab which is on the same order as the size of one pixel. Each pixel has a solid angle of A/r^2 where A is the area of a pixel, 9 mm^2, and r is the distance from the target to the center of that pixel. This distance is measured to be around 21 cm for each pixel, for which this approximation of the solid angle is valid. To obtain a corrected number of counts we create an efficiency relative to full 2π coverage, $\varepsilon_{geo}(\theta)$. For a given angular bin, the solid angle is summed up for all pixels whose center is located in that angle bin. The formula for this is,

$$\varepsilon_{geo}(\theta_{Lab}) = \sum_{pixels} \frac{A}{r^2 2\pi \sin\theta_{Lab}\Delta\theta_{Lab}}, \tag{5.1}$$

where θ_{Lab} is the central value of the half degree wide bin in the lab frame and $\Delta\theta_{Lab}$ is 8.73 mradians (0.5 degrees) for the width of the bin. The geometric efficiency as a function of θ_{Lab} can be found in figure 5.1.

Figure 5.2 shows the locations in θ_{Lab} and ϕ_{Lab} active pixels that contribute to the geometric efficiency, in contrast with 2.5 which shows the optimum coverage if all strips and crystals and their respective electronics were working properly. Several different reasons arose for the removal of various pixels from the analysis. Certain strips of the

130
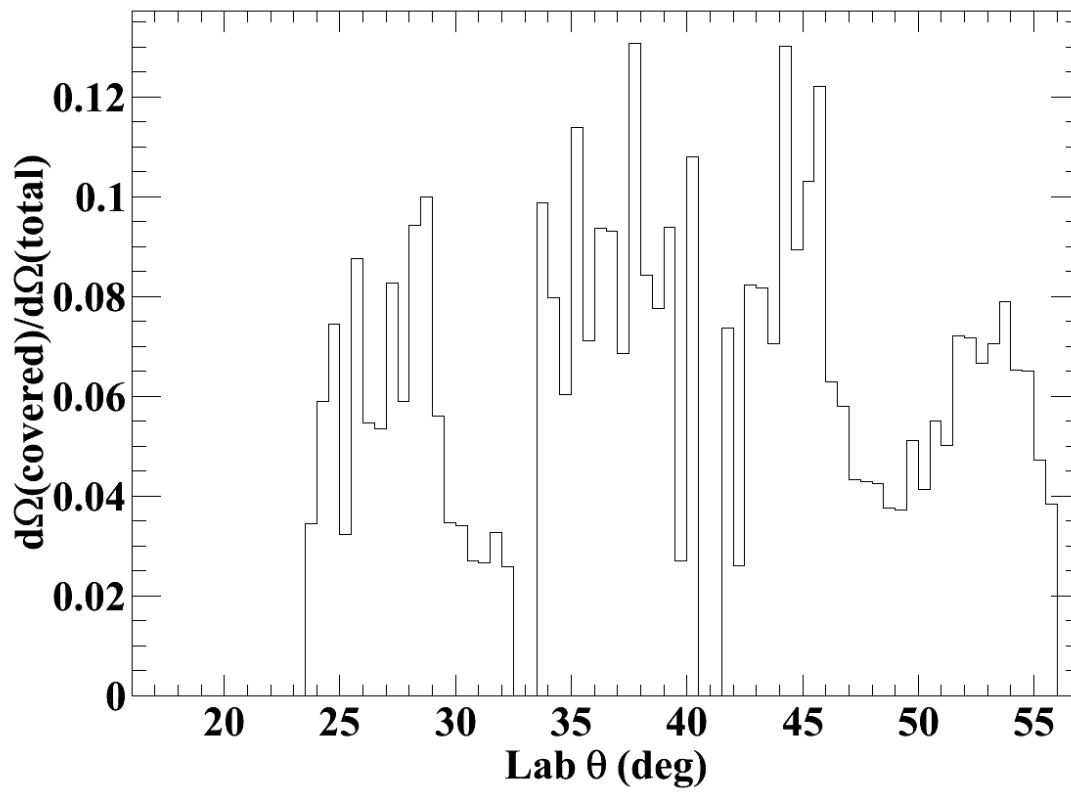
Figure 5.1: A plot of the geometric efficiency as it varies with θ_{Lab}
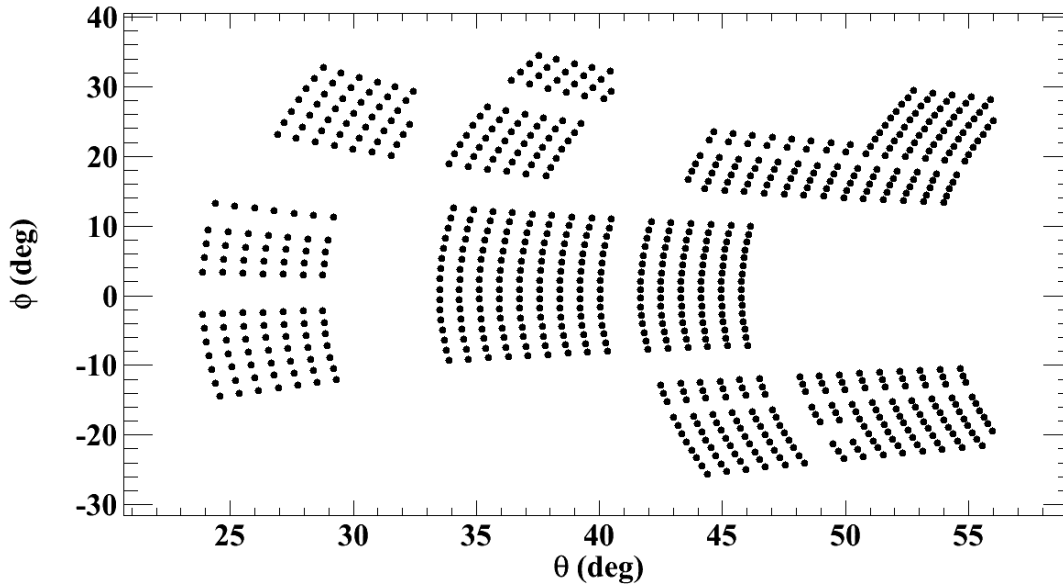
Figure 5.2: A plot of the angular coverage for what has been determined to be the working pixels in the experiment.

silicon had broken wirebonds inhibiting the ability to measure the energy of particles that passed through that strip. Several crystals and sets of strips were removed because they were partially or completely shadowed by either a Miniball element or an element of the Forward Array. In addition, the two most forward crystals were bombarded at a high enough rate that a particle identification technique was difficult to perform and since these two crystals provided very little coverage for the data of interest they were ignored. Finally, a small number of silicon preamplifiers stopped working part of the way through the experiment and so they too were identified and removed for the entire experiment.

5.1.2 Detector Efficiency

There are three types of detector efficiency that needed to be taken into account. The first of which is the multihit occupancy in the CsI crystals. This correction is required

because the CsI crystals have a limited granularity, i.e. if there were smaller crystals, this effect would be lessened. In general, it is only possible to properly identify particles when there is exactly one real particle in a CsI crystal. Multiple hits in a crystal typically cause the energy measured in the silicon or CsI to lie outside of a PID gate. This correction estimates the fraction of particles that cannot be properly identified because of this effect. Within general uncertainty, Poisson statistics imply that the probability for having exactly k number of particles in a crystal during a typical event is

$$P(k) = \frac{\lambda^k e^{-\lambda}}{k!}, \tag{5.2}$$

where λ is the average number of particles that hit that crystal per event. The hit fraction, r, or fraction of events in which that crystal measured at least one particle, is given as

$$r = P(k \geq 1) = \sum_{k=1}^{\infty} \frac{\lambda^k e^{-\lambda}}{k!}. \tag{5.3}$$

Using the relationship $P(k \geq 0) = 1$, one can quickly find that.

$$e^{-\lambda} = 1 - r. \tag{5.4}$$

Since λ is the average number of particles that should be detected in a given event and r is the fraction of events in which at least one particle is measured, then the efficiency is $\varepsilon_{\mathrm{CsI}} = P(k = 1)/\lambda = e^{-\lambda}$, which one can then derive that $\varepsilon_{\mathrm{CsI}} = 1 - r$.

The hit rate r is calculated independently for each crystal and each data run. More specifically, the hit rate is calculated for both central and peripheral collisions indepen-
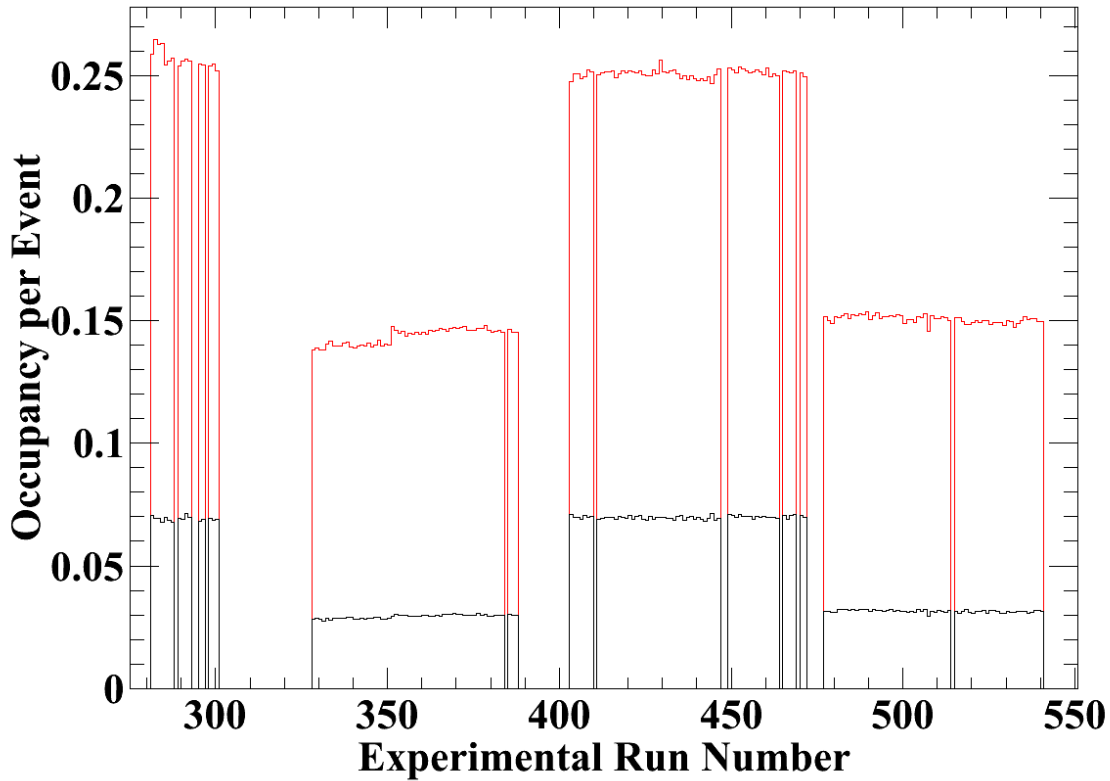
Figure 5.3: The fraction of events that a forward angle (red) and backward angle (black) crystal was hit by at least one particle.

dently and it is assumed to be the same value for all isotopes. Figure 5.3 displays the hit rate per event for a very forward (red) and very backward (black) crystal as a function of run number. This plot displays the extreme values for this correction. The efficiency for a given run would then be one minus the occupancy of that run.

There is another source of inefficiency in LASSA related to the effect of noise in the silicon readout. In particular, it is essential to set the discriminator on the ASIC readout to a low value in order to be able to trigger on energetic light particles. At such a low value it is possible for digital noise to trigger the ASIC electronics. When this happens the switch capacitor array stores the charge in the readout. If we don't supply a trigger the

134

charge is then cleared within about 2 μs. It is then possible that a later event comes along before the charge is cleared. Instead of reading out the event, the stale data is read as if it were part of the real event. Typically this does not occur often enough to be a problem resulting in the silicon electronics having a nearly 100% efficiency of collecting charge from the real signals instead of the stale data. In this particular experiment, however, there was a higher level of noise with the higher energy beam, possibly due to the high amount of particle bombardment into the detector. As a consequence, there was a slightly lower efficiency than was expected. We know this loss of efficiency stems from noise that is not correlated with an event. If a noise event occurs previous to when an actual event occurs, the noise would have already opened the switched capacitor array and stored the energy of the noise event instead of the real one. As seen in Figure 2.23, a 2 Hz pulser was run as an alternate trigger. The size of this pulse was designed to correspond to a hit well above the threshold of each channel. Every channel on the front and back of each telescope was pulsed during this process. By comparing the amount of pulses detected by each channel to the amount of pulses fired, we get an estimate of the efficiency of each front and back strip, ε_f and ε_b respectively. Figure 5.4 displays four examples of this efficiency. A front and back strip in telescope 5 (very forward angle) are shown in blue and black respectively, and a front and back strip in telescope 0 (very backward angle) are shown in green and red respectively. The back strips are generall quite efficient, however the fronts become increasingly less efficient the more foward in lab angle. The back strips are reasonably representative of the whole system. The front efficiencies in the figure show the range of efficiencies in the system.

Since the pulser was not put in place until a short while into the experiment the
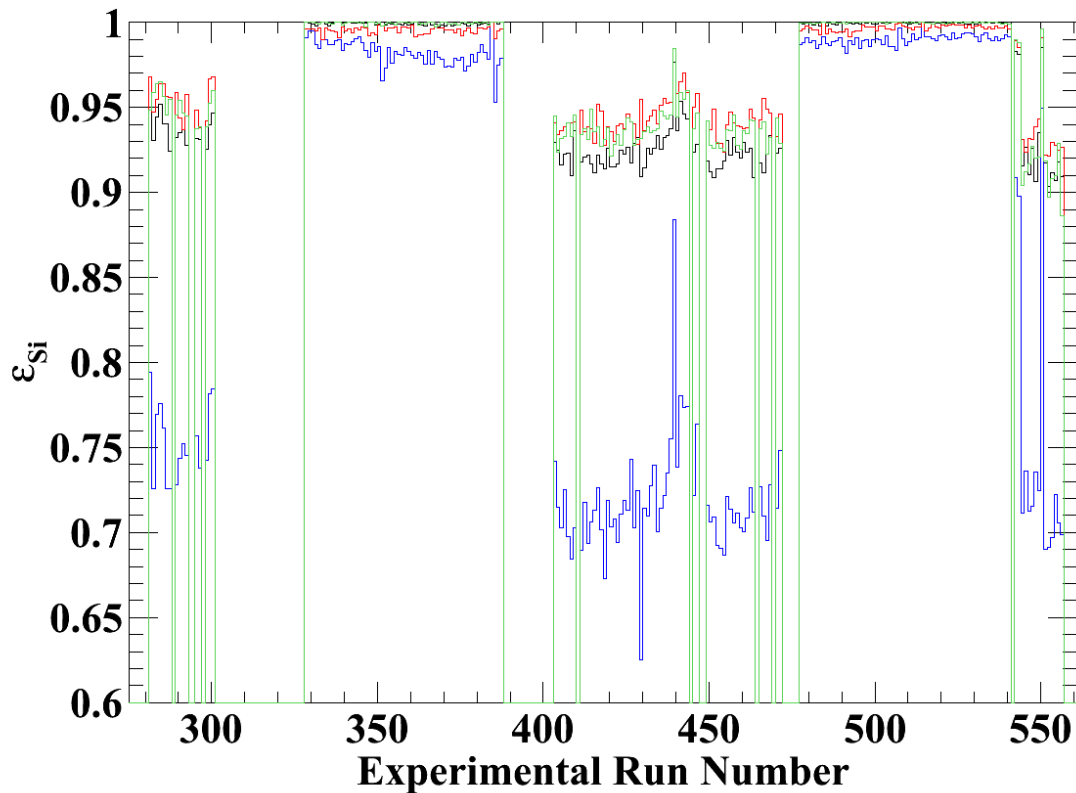
Figure 5.4: Example efficiencies for sample silicon strips. A front and back strip in telescope 5 (very forward angle) are shown in blue and black respectively, and a front and back strip in telescope 0 (very backward angle) are shown in green and red respectively. The back strips are generally quite efficient, however the fronts become increasingly less efficient the more foward in lab angle.

runs prior to run 281 cannot have efficiencies calculated this way. Since the efficiency is generally consistent over the course of an entire energy and target combination, an average efficiency for each strip was built using the runs from 281 to 300 and applied to the previous runs.

In general, it is assumed that detected events come from the center of the target, however, since the beam has a finite spread it is possible that events would take place slightly off from center. As such, it is possible that particles that would be detected in the center two strips (7 and 8) of either the front or back of the LASSA silicon might penetrate into the neighboring CsI instead of the one directly behind it. Similarly particles that hit in the edge strips (0 and 15) could hit the silicon and not hit a crystal. Neither of these effects are very likely due to the telescopic nature of the CsI crystals, however, since several of these strips are the only strip that cover a particular laboratory angle range, it is important to quantify the efficiency loss. To visualize this, it is simple to look at how the hits vary from strip to strip as in Figure 5.5. As seen with a linear fit line included, strip 8 is underdetecting particles. To correct for this, the number of counts in that strip is compared to the number of hits predicted by the fit line. The ratio of these two is included as an efficiency correction for these strips. Strip 9 of this detector was a bad strip as indicated by the lack of events.

Finally two corrections stemming from the course granularity of the telescopes are used. The first is a subtraction for the "blue haze", or randoms that can be seen in the PID spectrum in Figure 3.5. This blue background does have some slight energy dependence, that is as the CsI energy increases, the background decreases. Because there isn't a significant number of statistics in order to do a fine energy dependent calculation in
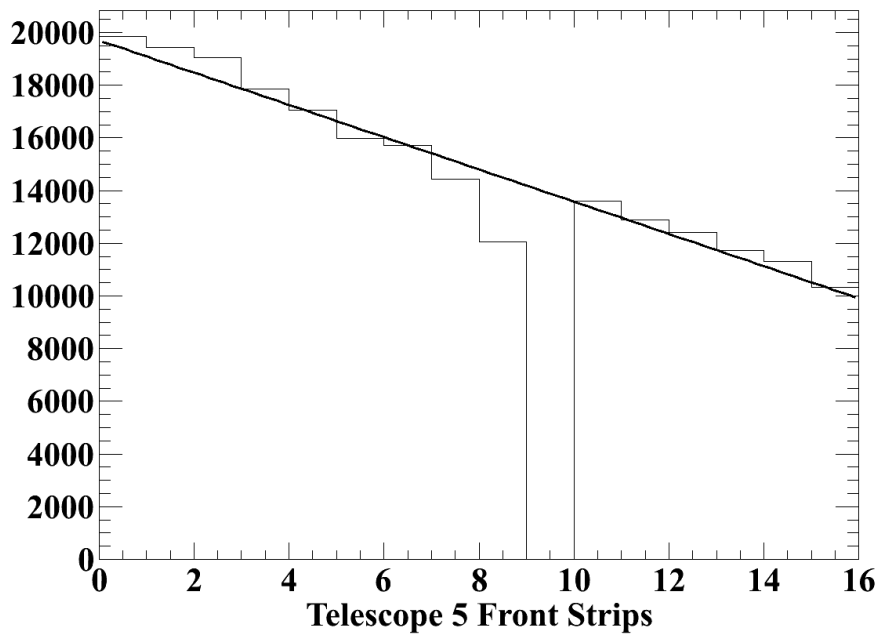
Figure 5.5: A plot showing the counts as a function of strip number in the front strips in Telescope 5. A line has been fit to the points showing the slight lack of production in strip 8. Strip 9 of this detector was a bad strip as indicated by the lack of events.

this treatment, we assume that the background is constant through the energy range from the energy of punch through of one particle to the next. More specifically, an efficiency reduction is created for the range of energies up to 150 MeV (protons), another from 150 to 195 MeV (deuterons), from 195 to 230 MeV (tritons) and a final for the high energy heliums above 230 MeV. Each crystal is treated independently and Figure 5.6 shows an example crystal at forward angles in a 50 MeV/Areaction for energies below 150 MeV. In this figure, we fit a flat background in the region that is known to be completely free from true charged particle lines. This fit is given by the red line. We then use this value to create an correction factor for the random background, C_{blue} using the formula,

$$C_{blue} = \frac{counts - background}{counts}. \tag{5.5}$$

The peaks in the figure reasonably correspond to the gates for different isotopes. The general contribution from this effect is less than 5%.

The final correction to laboratory spectra that must be made is a punch through correction. Particles that are energetic enough to punch through the CsI crystal will leave a distinctive ΔE-E signature. The particles will leave less energy in both the CsI and silicon than if it had stopped. This causes an extra line that, in the case of tritons, crosses the deuteron and proton lines, incorrectly increasing those particle multiplicities.

In order to compensate for this, a Monte Carlo simulation was written using data from LISE++ for each of the hydrogen isotopes. Helium isotopes do not reach high enough velocity to noticeably create a contamination in this experiment. The simulation assumes center of mass kinetic energy spectra similar to that of experimental data and calculates many events for a finely binned range of energies larger than that typically measured. In
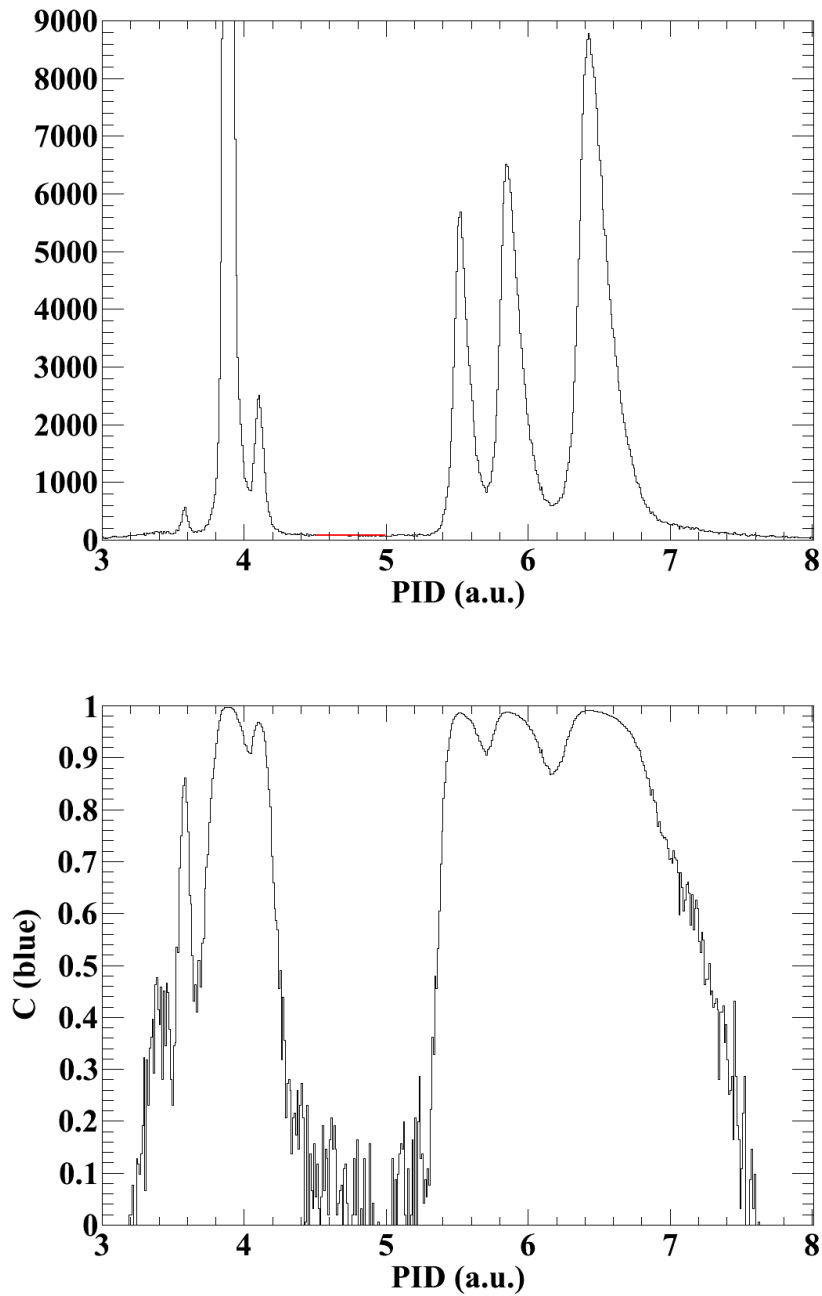
Figure 5.6: (top) The counts as a function of PID value for a 50 MeV/Areaction from a forward crystal. (bottom) For the same crystal, the ratio of real events to total events as a function of PID value providing the background correction factor.

each event the particle is assigned a random vector in the center of mass and is transformed back to the lab coordinate frame. If the lab vector corresponds to the lab angular region covered in our experiment the energy is then compared to the LISE energy deposition calculation for both the silicon and CsI. The silicon energy value is also given a randomly assigned Gaussian weighted variation to simulate the experimental resolution.

Since the simulation knows the lab energy of the particle, we fill two different plots of silicon energy versus CsI energy. If the particle is stopped by the CsI it fills the "*under*" plot and if not, it fills the "*over*" plot. We can then compare the number of particles in the two regions and create an estimate of the amount of stopped particles to total particles for a given silicon and CsI energy value using the equation,

$$C_{\text{punch}} = \frac{under}{over + under},$$ (5.6)

where C_{punch} is the correction factor that would be used to subtract events from the spectra. When referencing this equation for use with the data, we need to use the corrected CsI energy from 3.1.3 since the simulation does not have those ionization effects included.

We create an independent C_{punch} every five degrees in the lab in an attempt to follow the lab distribution trends. Figures 5.7 and 5.8 show the three plots used for the most forward laboratory angles. The top plot in the first Figure shows the ΔE-E curves for particles that are stopped by the CsI, with those that are not stopped by the CsI on the bottom. Figure 5.8 shows the ratio of stopped particles over total particles for those silicon and CsI energies.

As would be expected, the more forward angles in the lab have a higher concentration of particles that are not stopped by the crystals. It is particularly difficult to simulate all of
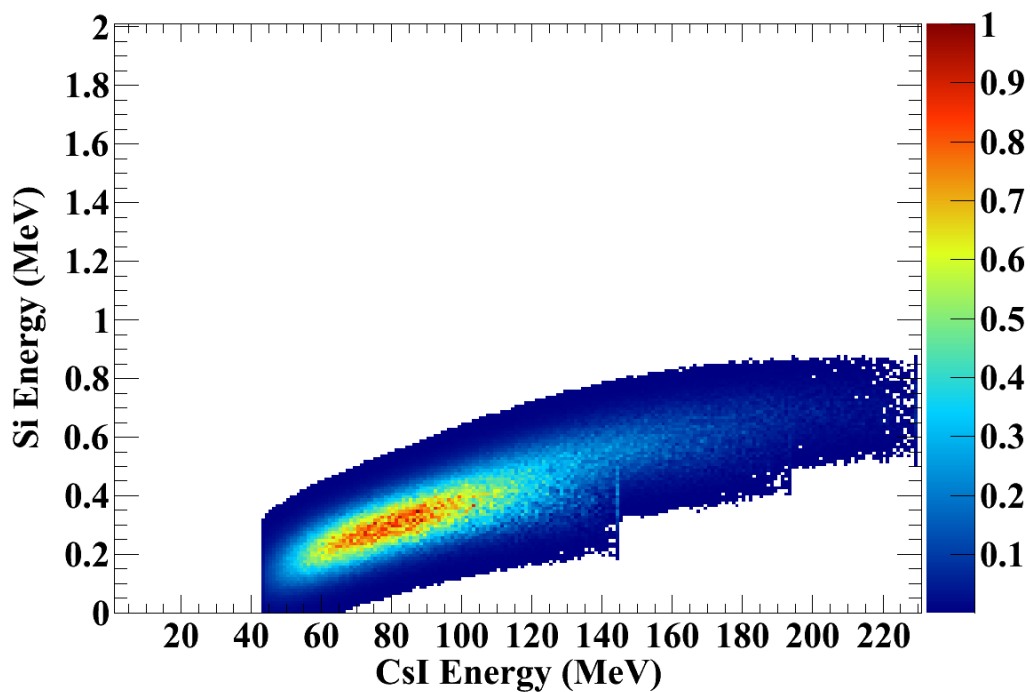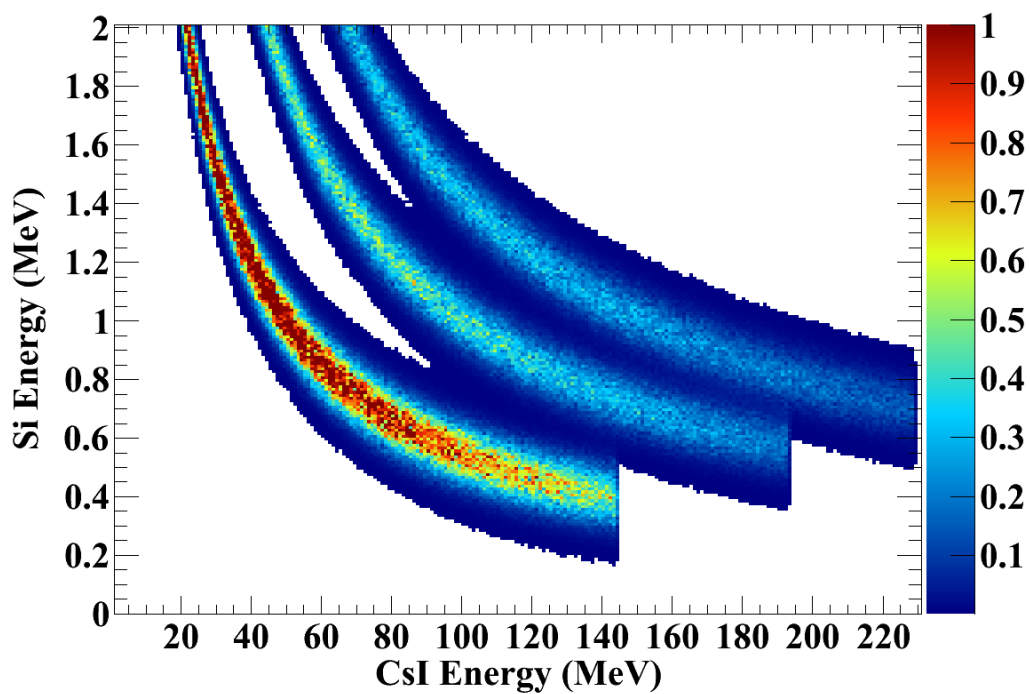
Figure 5.7: LISE simulation of the spectra that create the punch through correction factor. These plots represent the most forward angles in the lab frame. The top plot represents stopped simulated spectra. The bottom are spectra of particles that punch through the CsI.

142
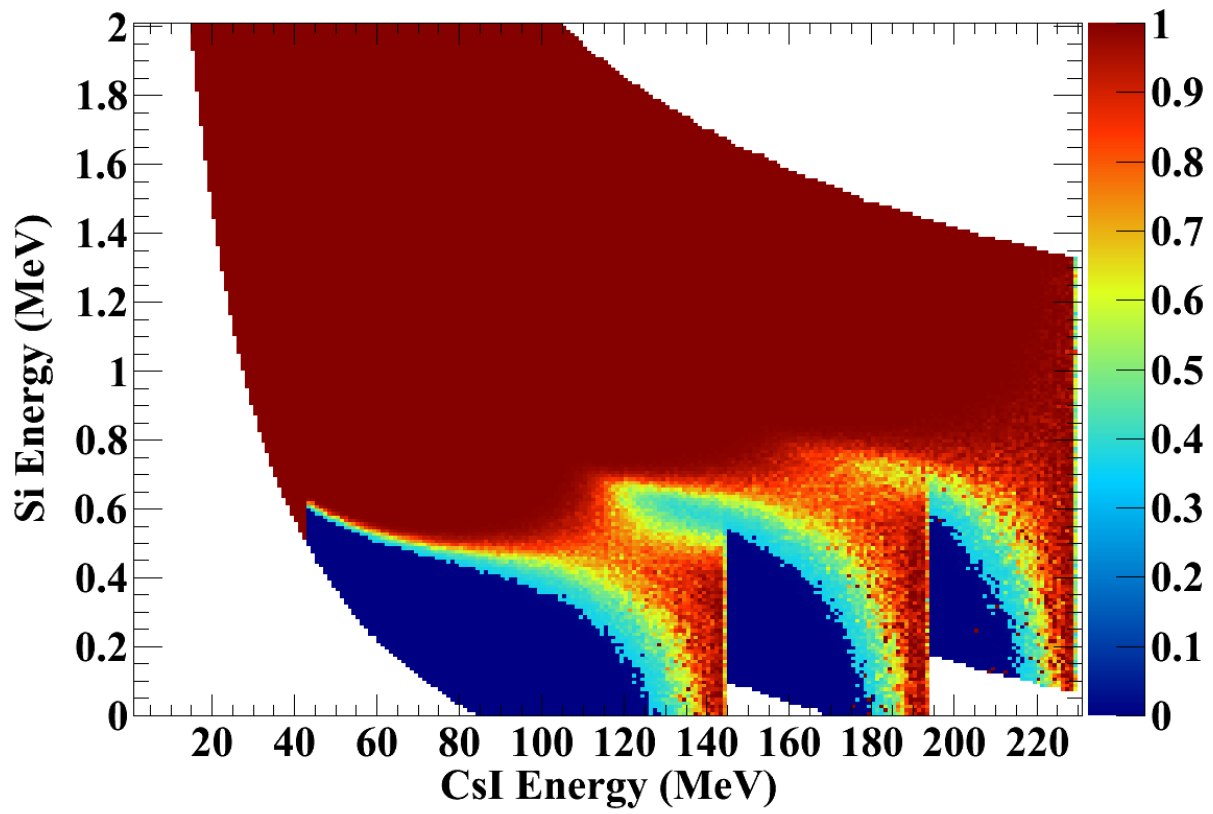
Figure 5.8: The correction factor due to the particles that punch through the CsI for a given pair of silicon and CsI energies.

the effects that go on in the ΔE-E curves, particularly the threshold effects and consistent resolution. This correction is one of the largest sources of systematic uncertainty in the whole analysis. Systematic errors will be discussed later this chapter. Figure 5.9 shows an example of the effect of the punch through correction for the ^{112}Sn system in the 120 MeV/Acollision at forward angles. The top part of the figure shows original uncorrected ΔE-E curves, with the bottom showing the corrected spectra. The dominant noticeable feature of this correction factor in the figures is the removal of the strong punch through line to the lower left of the proton line. Also, the continuation of this line between the protons and deuterons is reduced. There is an effect that the simulation does not correct for which is the increased spread across the silicon energy as the particles near the punch through point. This results in a small contamination of protons in the deuteron gate and an even smaller contamination of deuterons into the triton gate.

Lastly, due to the extreme forward angles of several of the detectors, Poisson statistics were insufficient to compensate for the inefficiency in the pixelation routine. Hydrogen isotopes, and in particular protons, were affected a great deal by multiple hits. As described in Chapter 3, the routine requires that each front strip has only one possible back strip that has a comparable energy. However, due to the behavior of the energy deposition and the physical resolution of the detector, two high energy particles (primarily protons) can deposit an energy within the tolerance of each other despite a significant difference in kinetic energy. If we were to take all possible combinations with comparable energy we would add 5-10% more pixels in the 50 MeV/Areactions varying over the angles covered in the lab, which at backward angles is reasonably comparable to the multi hit correction. In 120 MeV/Areactions, this effect can add between 10% and 35% more pixels. At backward
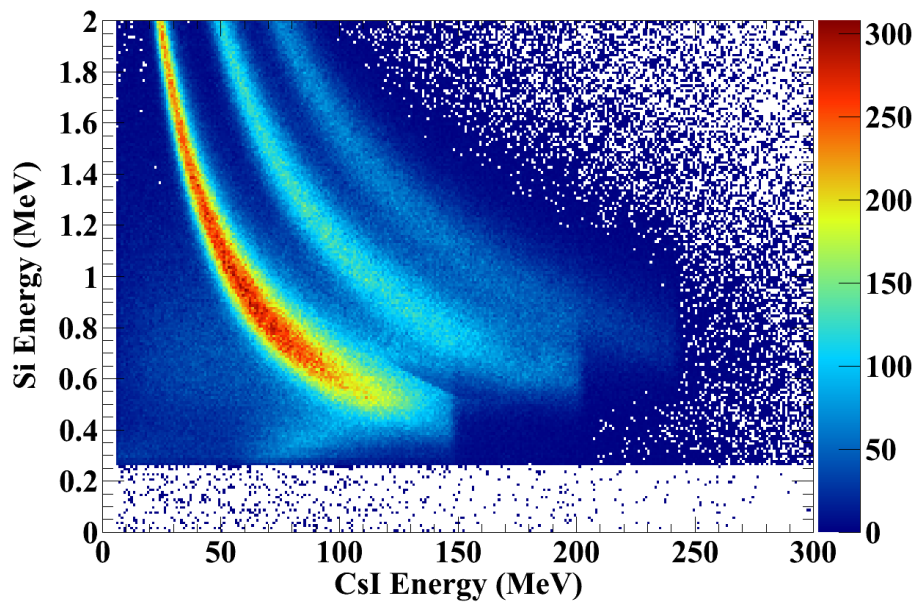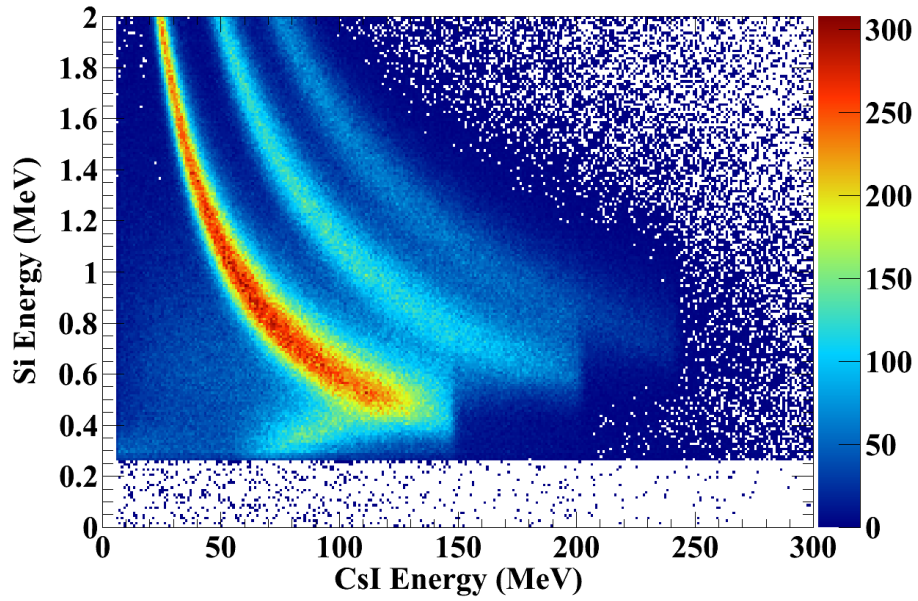
Figure 5.9: The effect of the punch through correction on data from the 120 MeV/A reactions on the ^{112}Sn system.

angles the Poisson statistics are still comparable to those of our multihit correction. At forward angles the effects are much larger than that predicted by the CsI multiple hit efficiency correction. The multiple hit correction assumes that double hits end up outside the particle identification gates for legitimate particles. With the extra number of matched pixels we need to evaluate whether we are correctly measuring the number of particles, if we are overcorrecting or if we are throwing away too many legitimate particles. If there were a defect in the process we would expect that a correction would be similar for all particles.

In an attempt to check the accuracy of the pixelation routine at forward angles, we visually investigated the two dimensional plots of transverse momentum versus center of mass rapidity, y_r, where the rapidity is defined as,

$$y = \frac{1}{2} \log \frac{E + p_z c}{E - p_z c},$$

(5.7)

and the transverse momentum is given by,

$$P_t = P_{\text{C.M.}} \sin \theta_{\text{C.M.}}.$$

(5.8)

Figure 5.10 shows an example of these plots. All plots in this figure represent protons from the ^{112}Sn reaction at 50 MeV/A. These plots include all corrections discussed through this point The bottom plot has interpolated the gaps where the is no coverage at that lab angle. The top plot in Figure 5.11 is a reflected and averaged version of the bottom plot in Figure 5.10. The bottom of Figure 5.11 shows the same data without a correction of 15% to increase the data in the most forward 2 crystals. Under the assumption that the

146

backwards crystals have a correct production (which is very likely because of the low multiple hit probability), we chose to increase the production for these crystals for all five isotopes reflecting the problem of correctly determining the proper number of pixels in this detector. In the 120 MeV/Areaction it was rather difficult to create a compensation for this effect and so we omitted the most forward three crystals for those energies. Since these crystals only contributed at low energy in the center of mass this is an acceptable loss of data. The top plots in this figure represent pure data, with the middle plots being the same with an interpolation routine used to fill the gaps. The solid black lines represent lines of constant center of mass angle and energy. For reference, the final P_t versus rapidity distributions can be found for all particles and both energies from the ^{112}Sn collisions in Figures 5.12 (protons), 5.13 (deuterons), 5.14 (tritons), 5.15 (^{3}He) and 5.16 (alphas).

5.1.3   Laboratory Spectra

Laboratory spectra have a number of uses, primarily as cross checks. In some very mass-asymmetric cases it can be useful to investigate spectra in the lab frame however, here the symmetric nature of this experiment allows for more natural comparison of spectra in the center of mass frame. Nonetheless, lab spectra are pivotal in confirming efficiency corrections and investigating trends. Figure 5.17 shows the lab protons in the 50 (top) and 120 (bottom) MeV/Areactions from ^{112}Sn+^{112}Sn. These plots are pure spectra with all the corrections made in the lab. Figure 5.18 shows the same data with the different angular regions scaled to separate them out.

If all corrections to the spectra are accurate and the angle bins evenly spaced one would expect to see a similar difference from angle to angle at high energy. The angle ranges
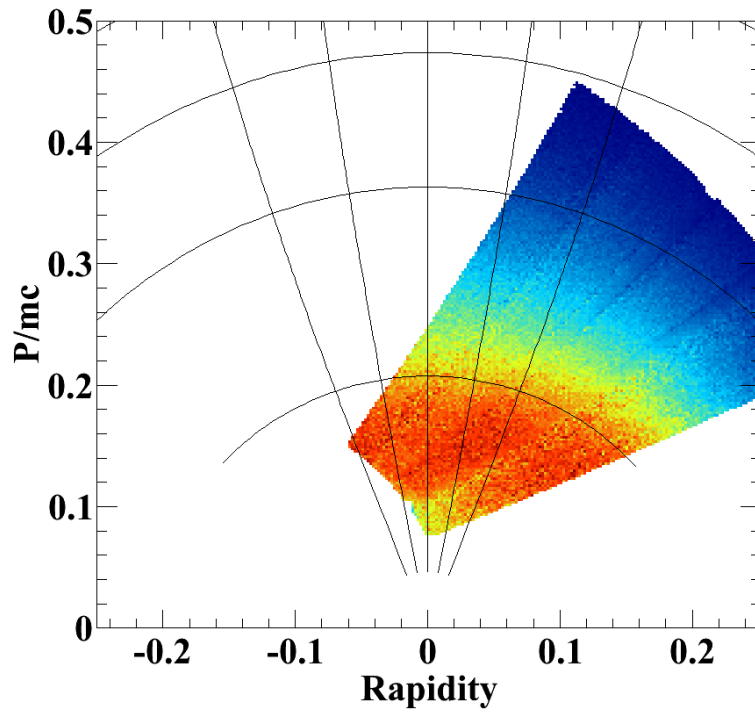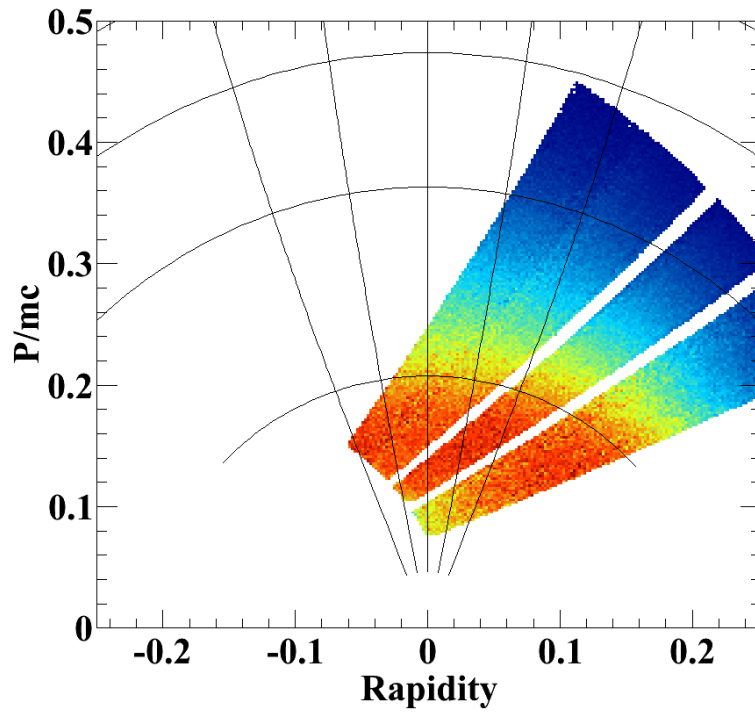
Figure 5.10: P_t versus rapidity plots for protons from the ^{112}Sn reactions at 50 MeV/A. The top plot is data with all lab corrections. The bottom row has interpolated the gaps in the coverage.
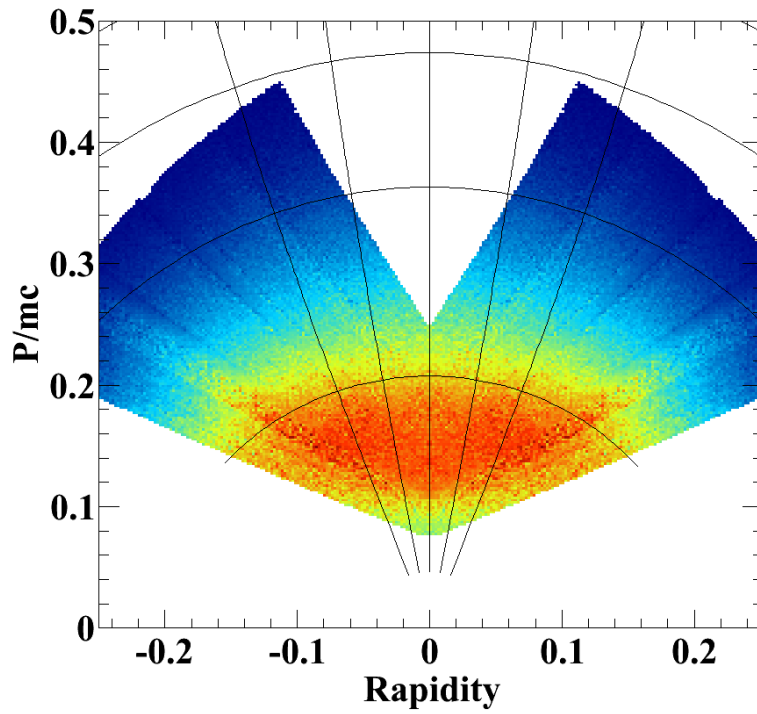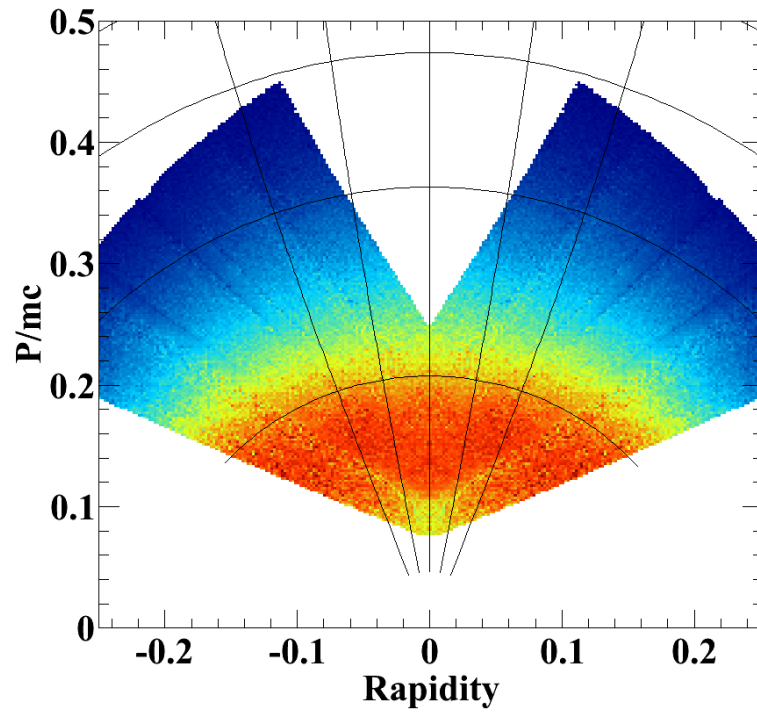
Figure 5.11: P_t versus rapidity plots for protons from the ^{112}Sn reactions at 50 MeV/A. The bottom plot is data before the 15% increase to the forward crystals while the top plot includes the scaling.
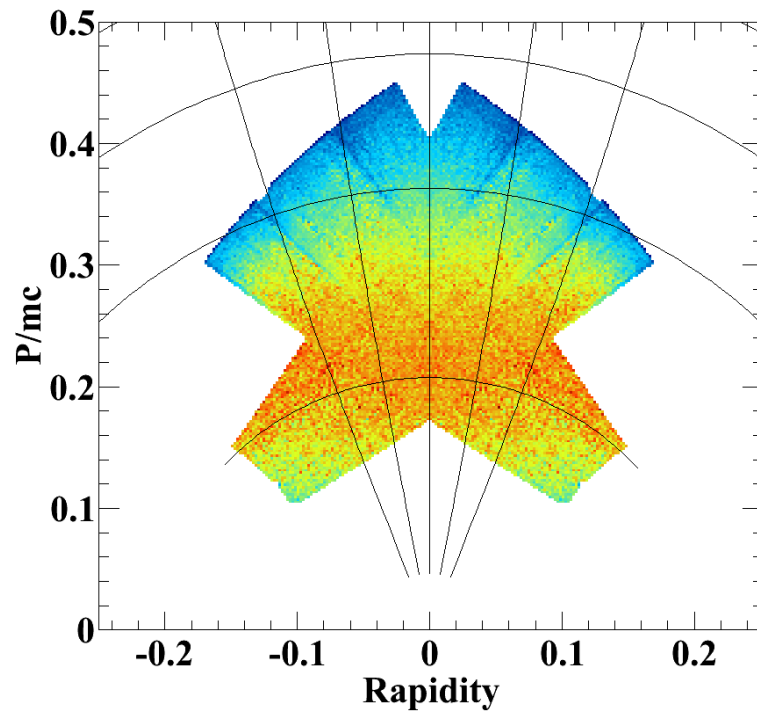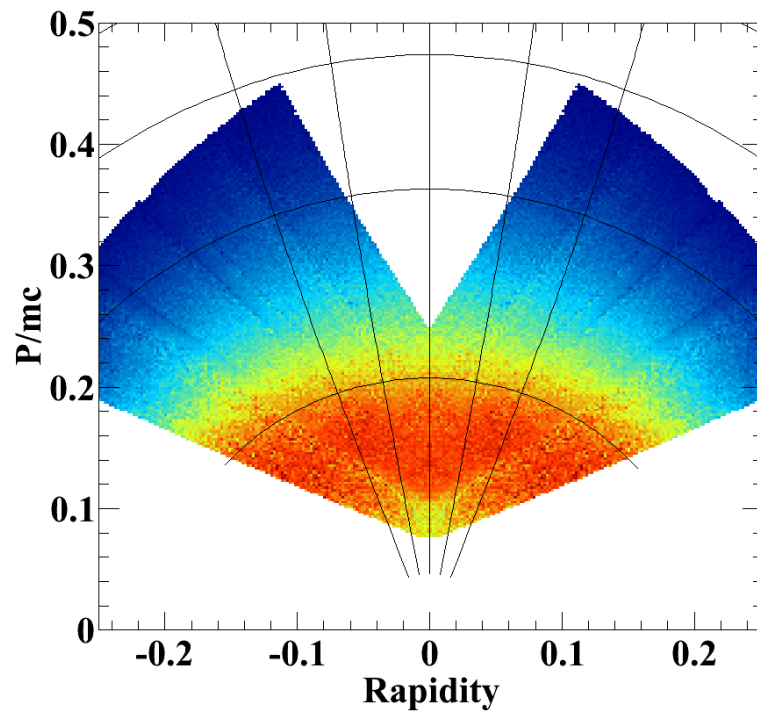
Figure 5.12: Final P_t versus rapidity plots for protons from ^{112}Sn at 50 (top) and 120 (bottom) MeV/Areactions.
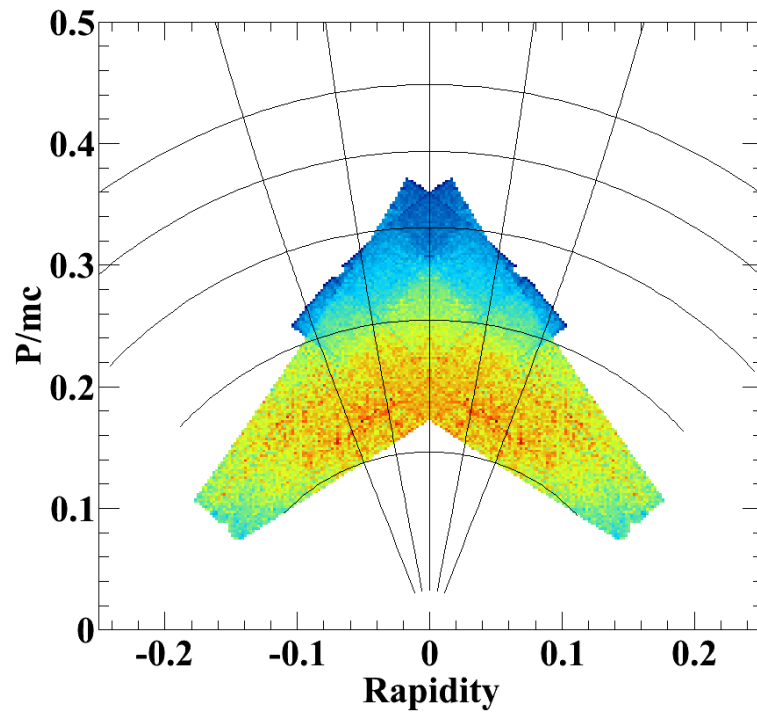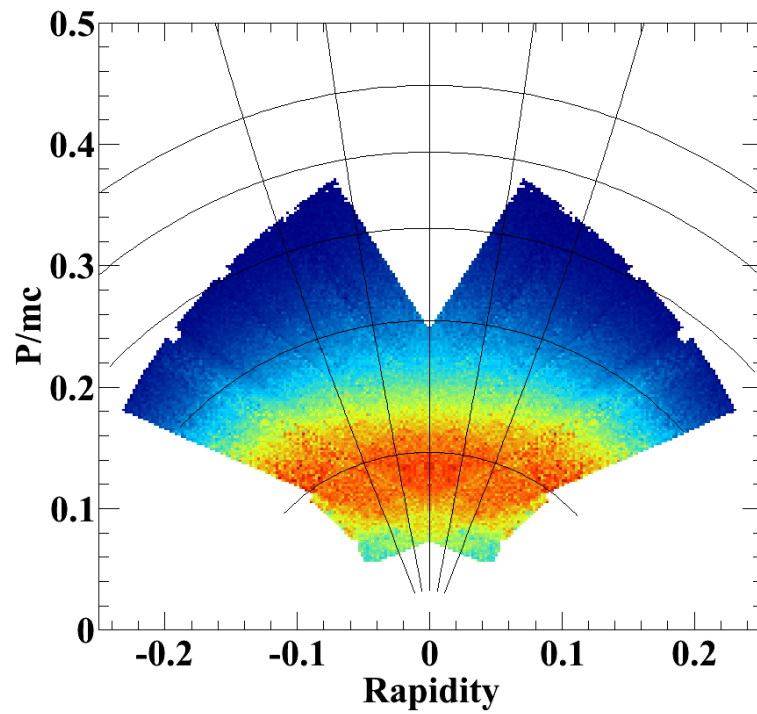
Figure 5.13: Final P_t versus rapidity plots for deuterons from ^{112}Sn at 50 (top) and 120 (bottom) MeV/Areactions.

151
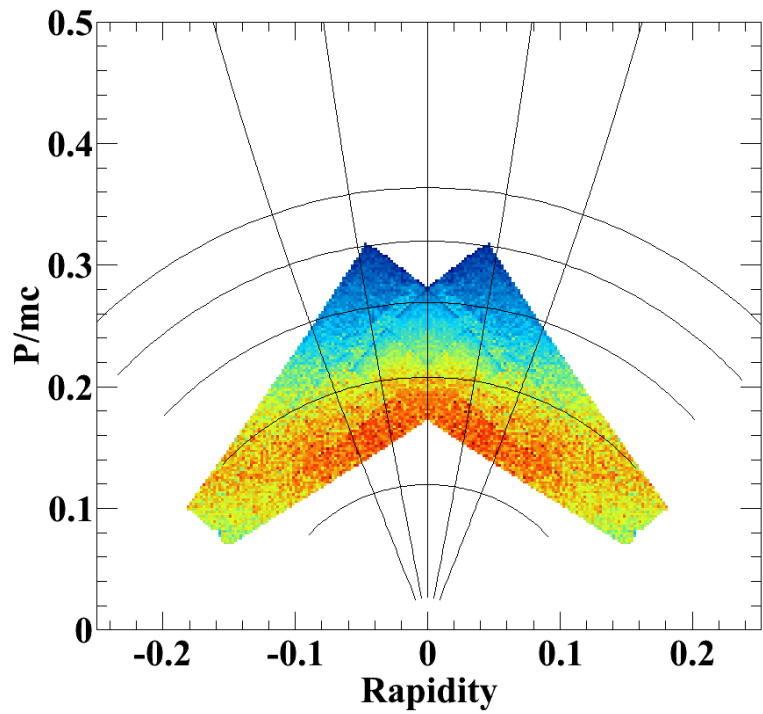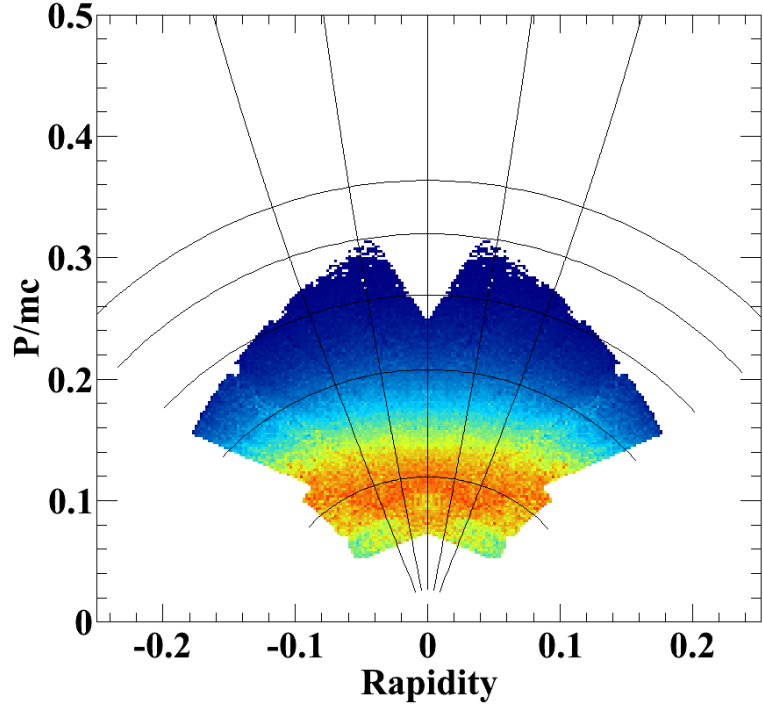
Figure 5.14: Final P_t versus rapidity plots for tritons from ^{112}Sn at 50 (top) and 120 (bottom) MeV/Areactions.
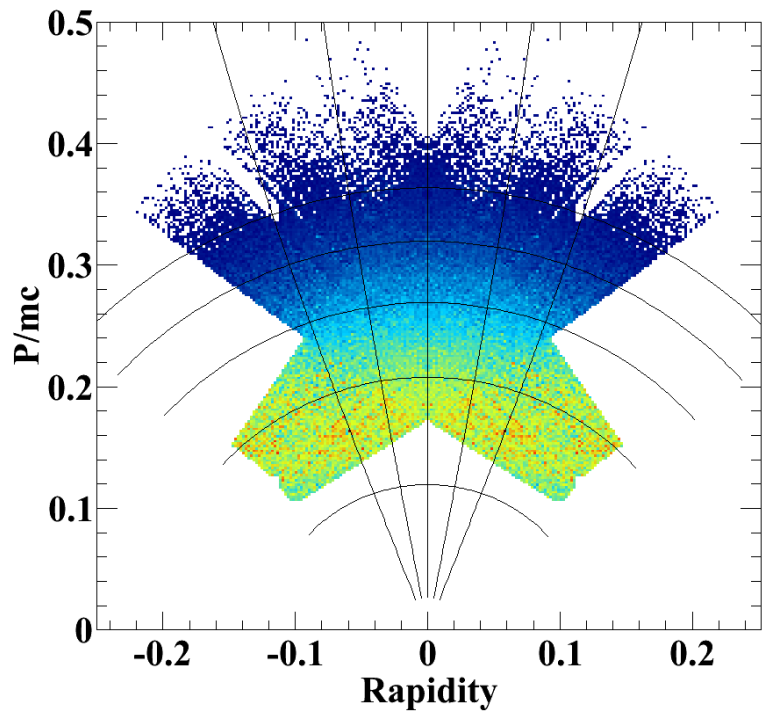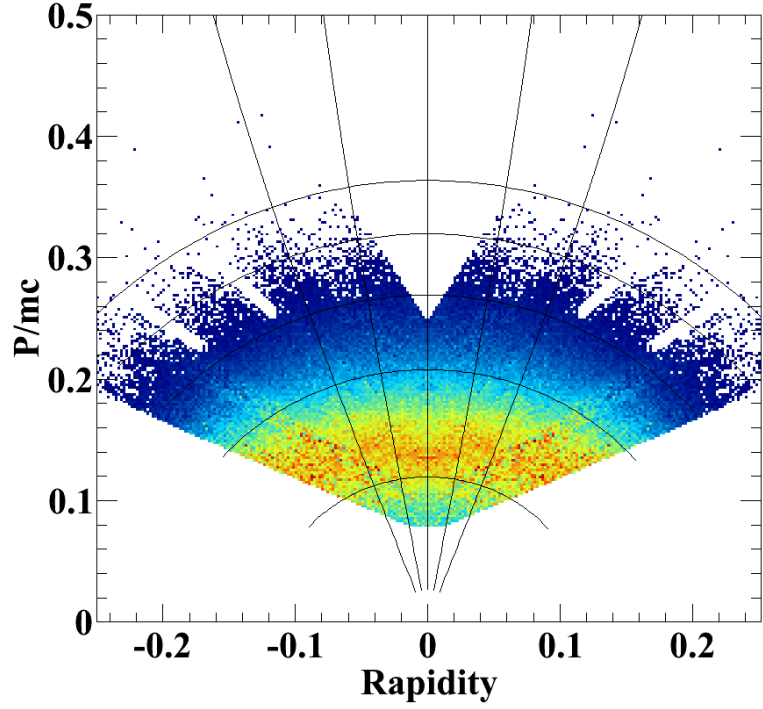
Figure 5.15: Final P_t versus rapidity plots for ^{3}He from ^{112}Sn at 50 (top) and 120 (bottom) MeV/Areactions.
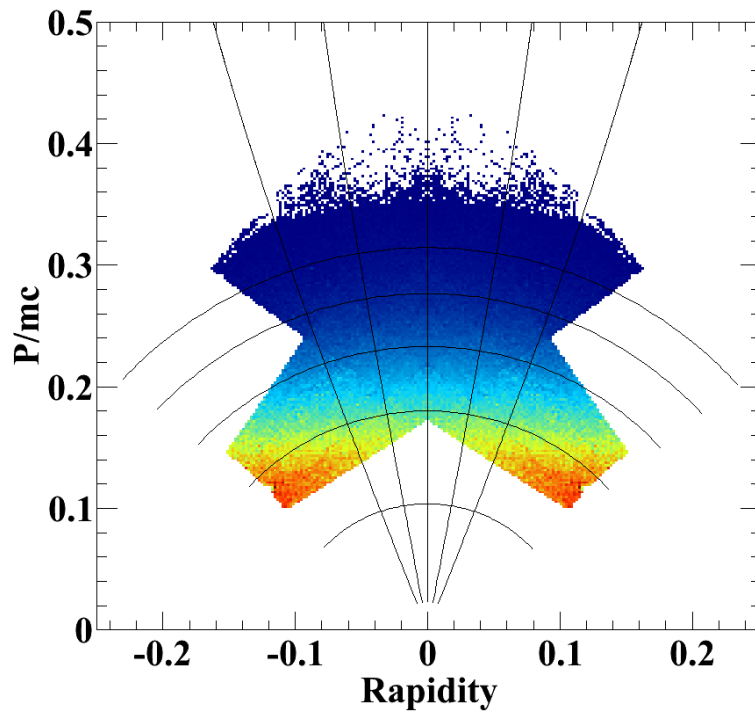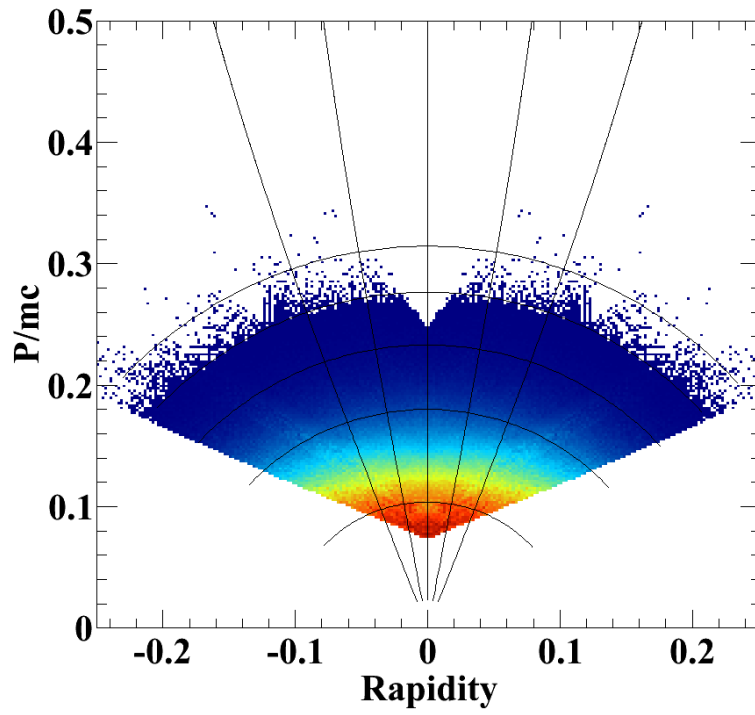
Figure 5.16: Final P_t versus rapidity plots for alphas from ^{112}Sn at 50 (top) and 120 (bottom) MeV/Areactions.

154
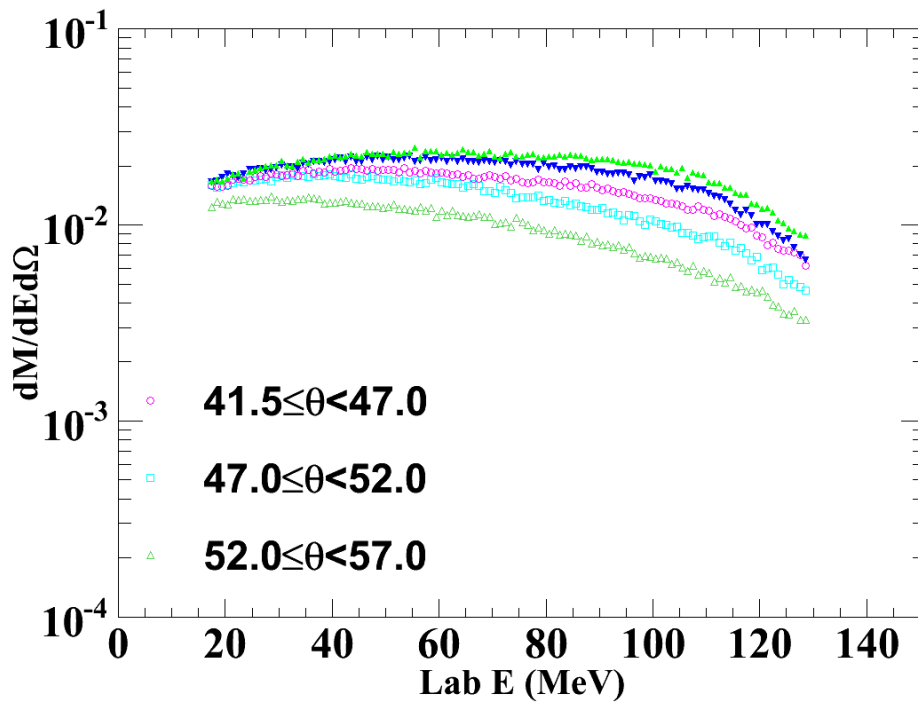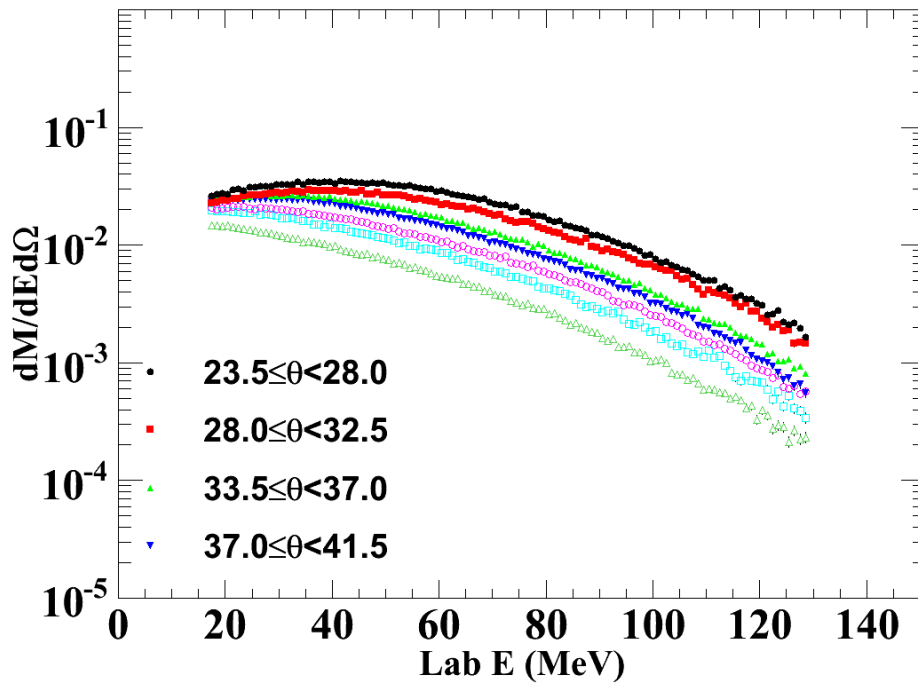
Figure 5.17: Lab spectra for protons from ^{112}Sn+^{112}Sn at 50 (top) and 120 (bottom) MeV/A.
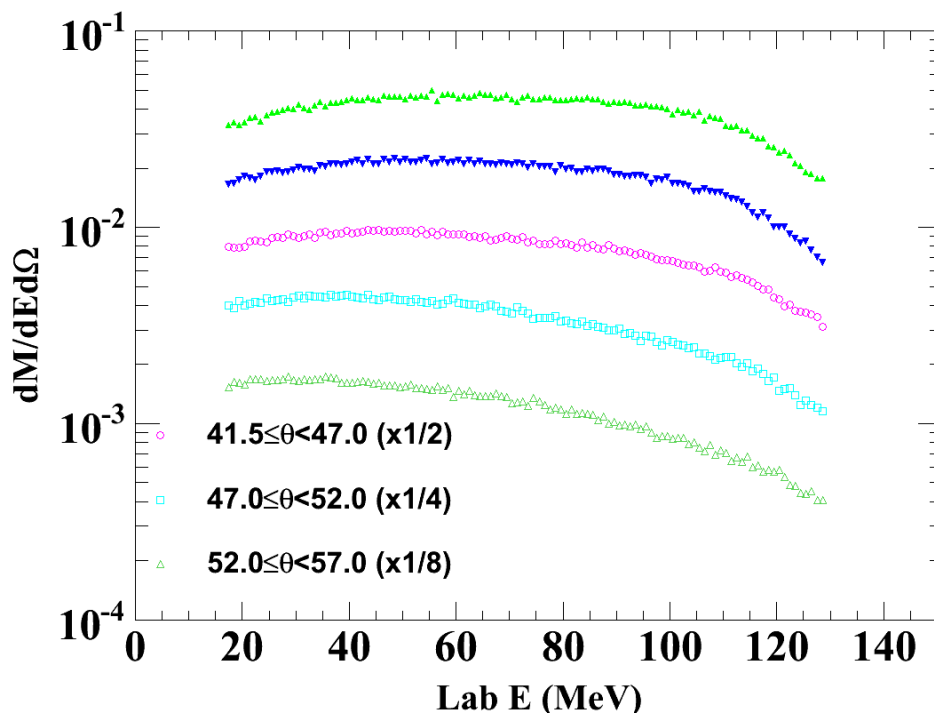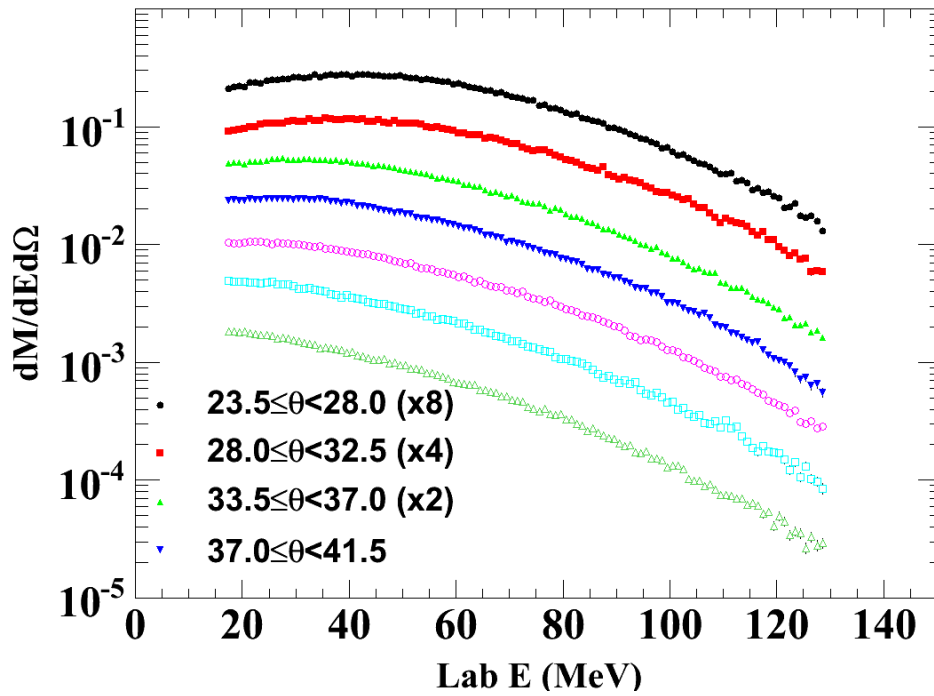
Figure 5.18: Lab spectra for protons from ^{112}Sn+^{112}Sn at 50 (top) and 120 (bottom) MeV/A. The different angular regions have been scaled to separate them out.

in the lab were chosen to avoid gaps in the coverage and maximize statistics in each bin. While the angles are not evenly spaced the trend of the data reasonably reproduces expectation. In the 120 MeV/Areaction, the expectation of a more isotropic set of spectra is reproduced until the most backward angles. Figures 5.19 (deuterons), 5.20 (tritons), 5.21 (^{3}He) and 5.22 (alphas) show unseparated data for the other measured particles for 50 MeV/Aon the top and 120 MeV/Aon the bottom. Only data from the ^{112}Sn reactions are shown. The ^{124}Sn systems are quite similar.

5.2 Center of Mass Frame

In the conversion from the laboratory frame to center of mass frame, several binning effects must be accounted for. In the case of infinitely fine binning, one lab energy and angle bin would correspond to one center of mass lab and angle bin. Since this can also cause statistical inconsistencies a certain bin width is chosen which means that multiple lab bins can contribute to the same center of mass bin. As will be shown later, the region from $70 \leq \theta \leq 110$ in the center of mass is rather isotropic. We decided in our analysis approach to assign each center of mass bin the same weight. This allows for an easier evaluation of data near the edges of the detectors. An efficiency, $\varepsilon_{\text{Edge}}$, for bins near the edge of the covered regions was created to address the fact that the edges of the detectors do not correspond to a fixed center of mass scattering angle. Similarly, at many center of mass energies we do not cover the full angular range from $70 \leq \theta \leq 110$. In order to correct for this, a coverage correction, ε_{Cov} is created to compensate for this lack of coverage.
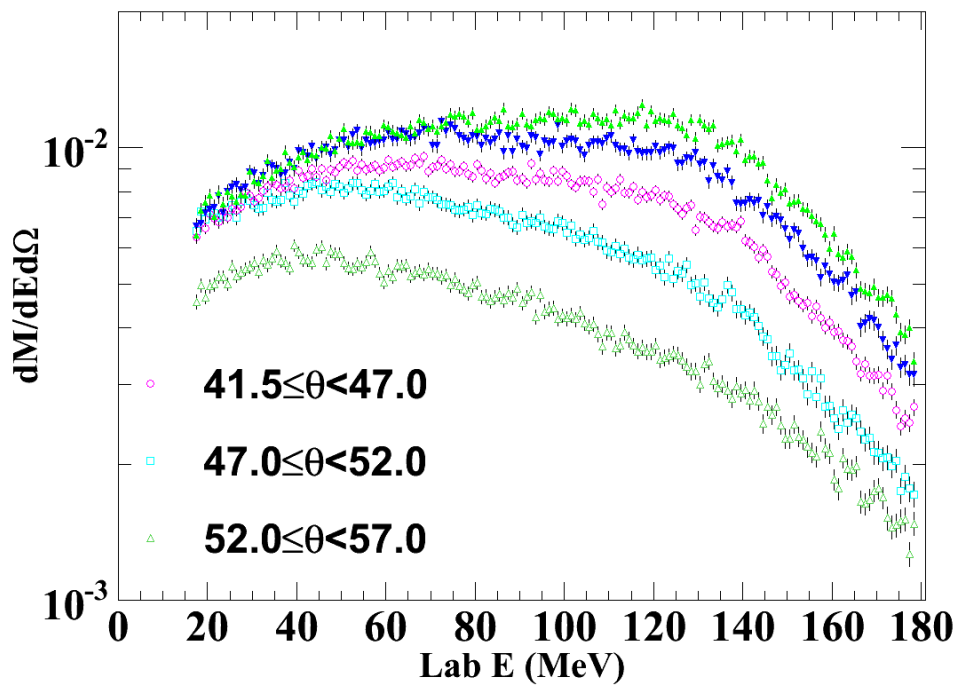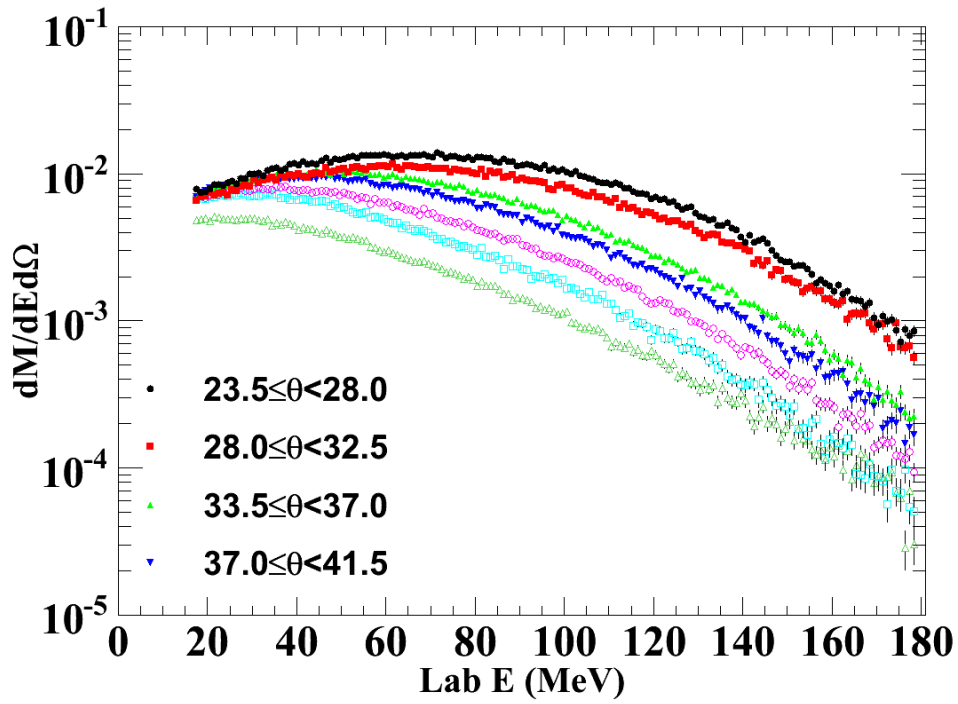
Figure 5.19: The lab angular distributions for deuterons. Data from 50 MeV/A is on the top and 120 MeV/A on the bottom. The different points represent the same angles as those in Figure 5.17.
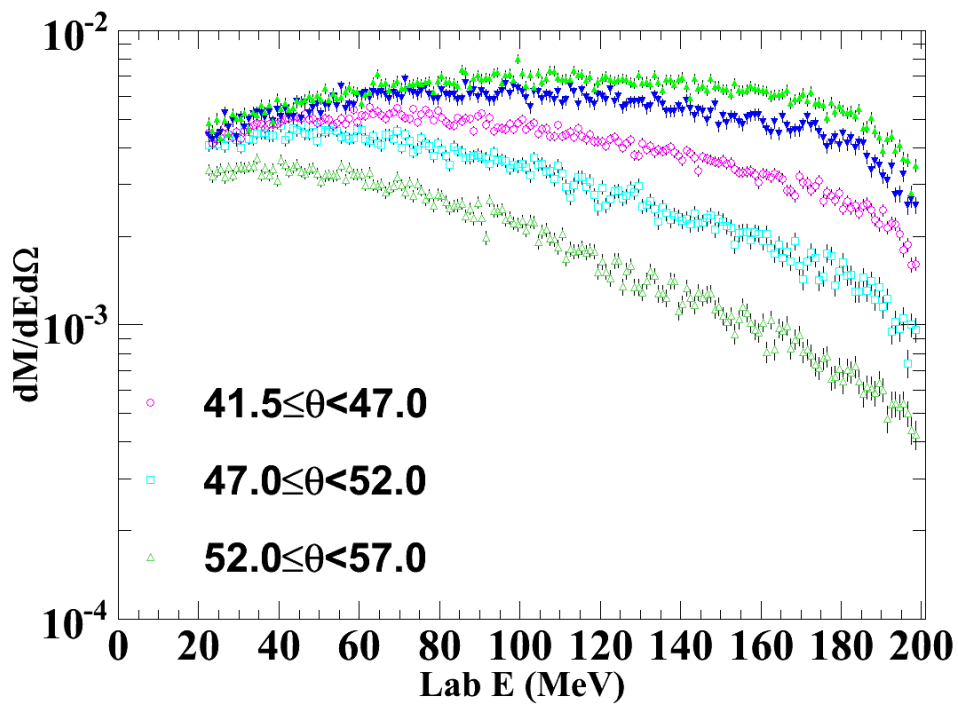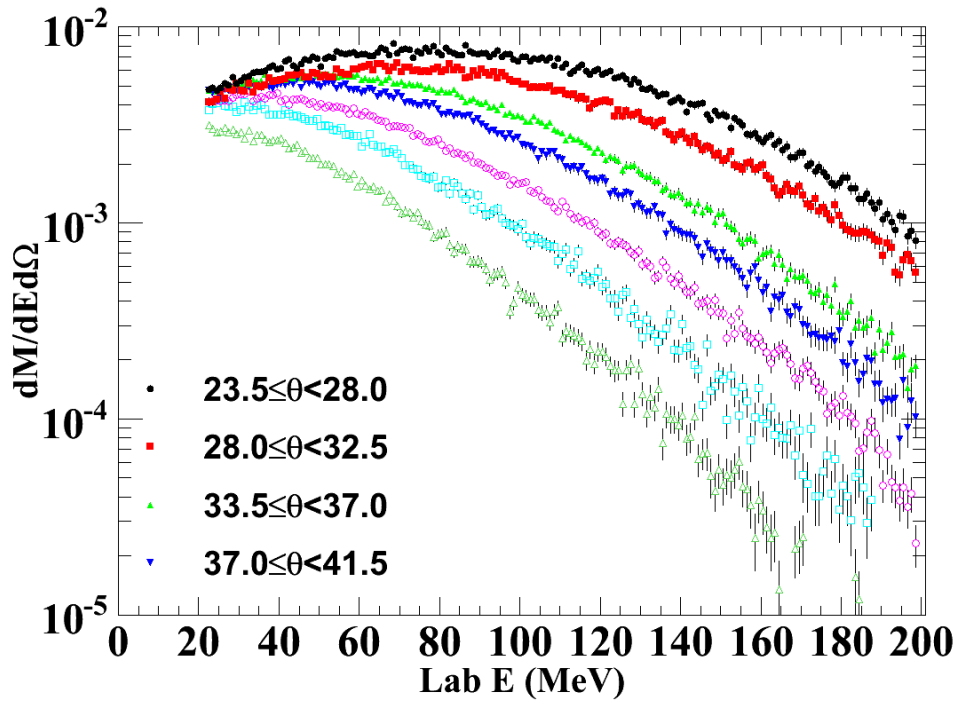
Figure 5.20: The lab angular distributions for tritons. Data from 50 MeV/Ais on the top and 120 MeV/Aon the bottom. The different points represent the same angles as those in Figure 5.17.
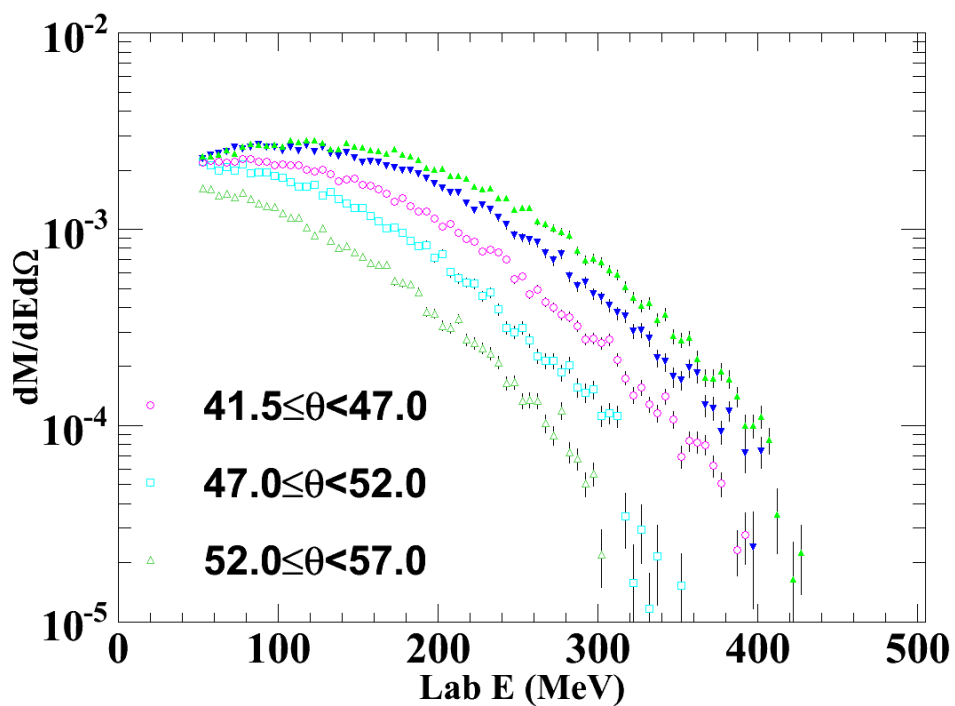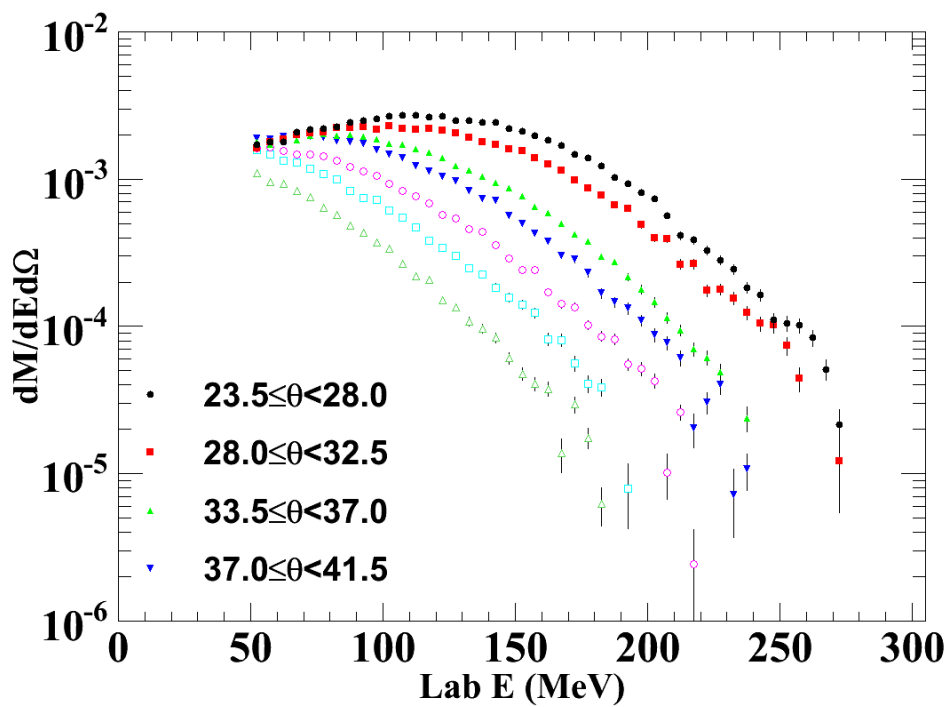
Figure 5.21: The lab angular distributions for ^{3}He. Data from 50 MeV/Ais on the top and 120 MeV/Aon the bottom. The different points represent the same angles as those in Figure 5.17.

160
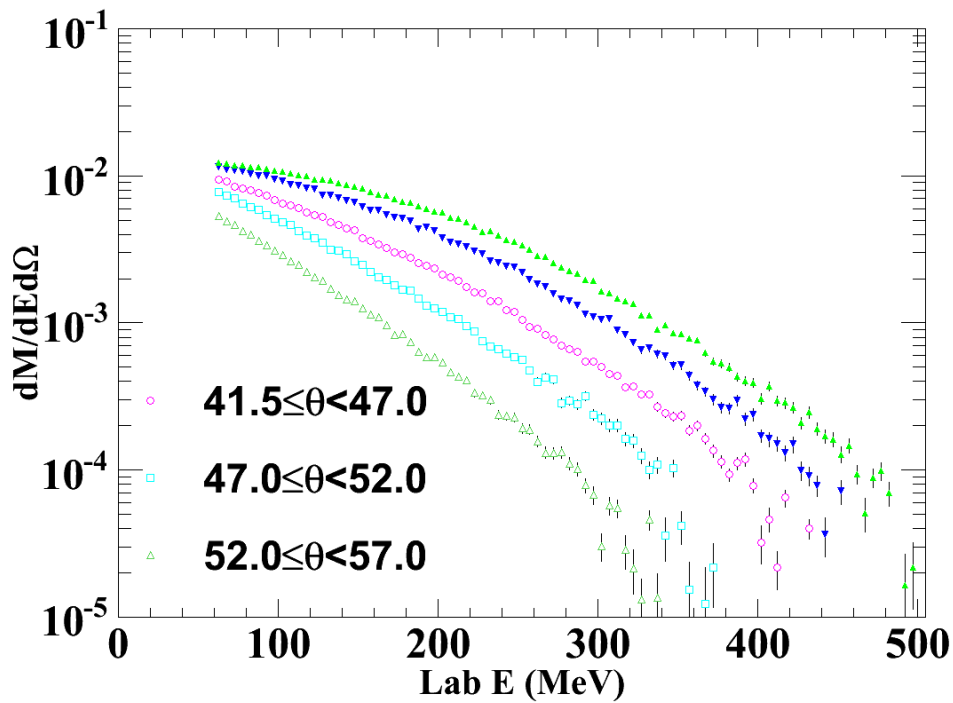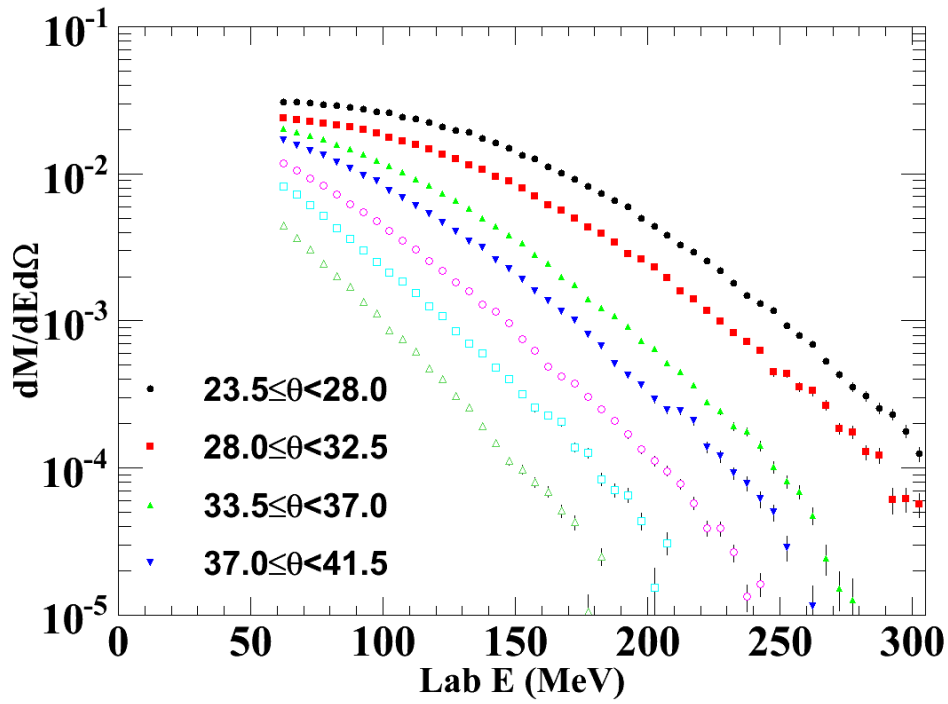
Figure 5.22: The lab angular distributions for alphas. Data from 50 MeV/A is on the top and 120 MeV/A on the bottom. The different points represent the same angles as those in Figure 5.17.

5.2.1 Edge Efficiency Correction

Due to the unfortunate issue with having gaps in the coverage in LASSA there are effects that need to be considered in the conversion from lab to center of mass angles and energy. Initially, every particle that is detected in LASSA is assigned a vector in the lab that points from the center of the target to the center of the pixel it was detected by. Of course this does not correspond to what would be the true distribution of particles. To account for a more true distribution, the vector is adjusted to maintain the same lab ϕ but be randomly distributed across the half degree θ bin that it lies in.

While this compensates for discrete effects, it does not fix the problem with edge effects. As the conversion from lab to center of mass vector occurs, bins in a plot of center of mass angle versus center of mass energy near these gaps in coverage are only partially filled compared to what would occur if there were no gap. Since the center of mass angle is important to constructing spectra it is important to compensate for this loss. In order to compensate for this a Monte Carlo simulation was completed for each isotope that is detected in LASSA. The simulation assigns 100 million particles a random lab vector varying θ from 15 to 60 degrees and ϕ from -50 to 50 degrees, which represents a physical space similar to that of our real system. The particles were then randomly given a lab energy in a range that was based on a threshold and maximum detectable energy specific to each isotope. For protons this energy range was from 15 to 130 MeV, the upper limit chosen to avoid contamination from deuterons and tritons that punch through the CsI. Figure 5.23 shows the coverage for θ and energy in the center of mass for protons in the Monte Carlo simulation on top. The plot on the bottom shows the same simulation that is selected only on particles that have a nonzero value for the geometric effeciency from

above, i.e. particles that are designated good data. The top of Figure 5.24 shows the ratio of the two. As expected, bins in the region where there is full coverage have an efficiency of exactly one and then it falls off as it nears the edge. The bottom plot of that Figure zooms in to better view the effects at the edge.

This process is necessary for each isotope, and to have it match experimental binning and energy ranges. Only data bins that have an edge efficiency of at least 30% are considered.

5.2.2 Coverage Correction

The last correction that must be made in the center of mass is to account for the lack of full solid angle coverage from 70 to 110 degrees. This correction assumes that the spectra in this region are reasonably isotropic. This was suggested to be true by pBUU simulations in Figure 4.8 and was experimentally confirmed. Since the experimentally binned data is sparsely filled at high energies, we use the Monte Carlo simulations from the edge efficiency calculation in the previous section to calculate the coverage correction. The calculation loops through all θ bins for a given energy and compares the solid angle for all bins with an edge efficiency of at least 30% to the full solid angle from 70 to 110 degrees. The formula for the coverage correction simplifies to,

$$\varepsilon_{\text{cov}}(E) = \frac{\sum\limits_{\theta(\varepsilon_{\text{edge}} \geq 0.3)} \sin(\theta)}{\sum\limits_{\theta} \sin(\theta)}, \tag{5.9}$$

where the summation is over the theta bins for a given energy. Figure 5.25 shows the correction for protons for the 50 MeV/Areaction as a function of energy as an example.

163
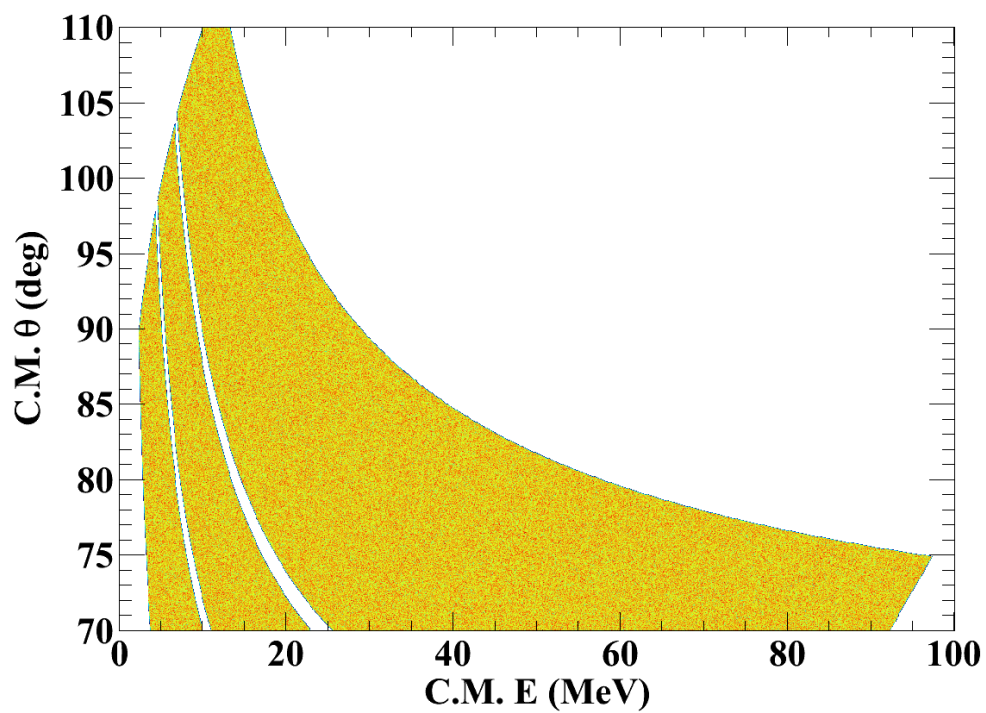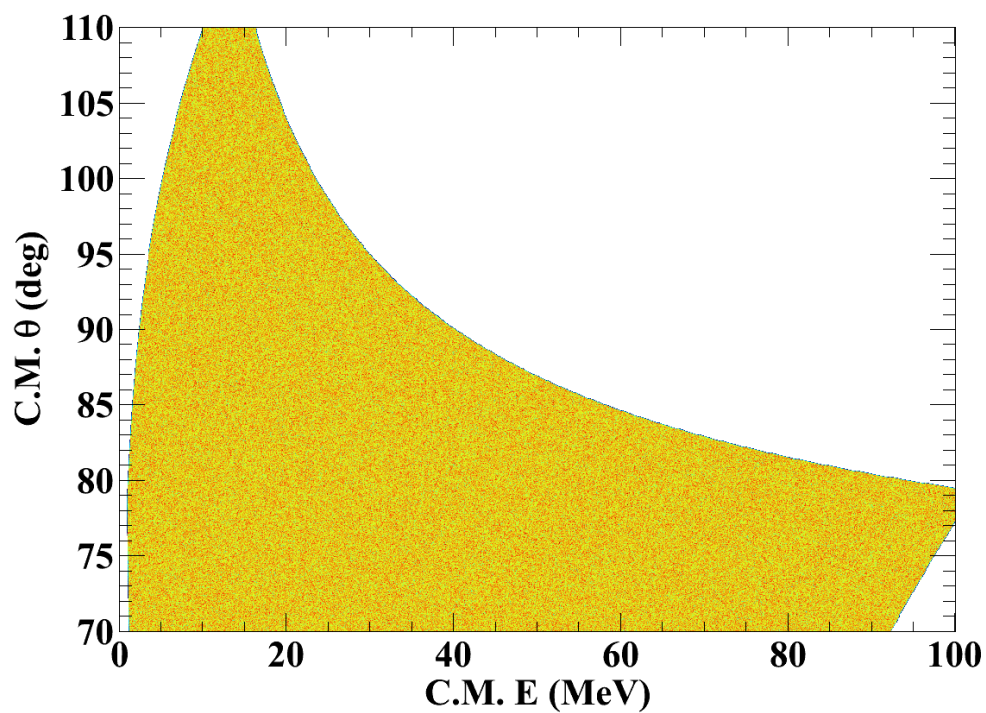
Figure 5.23: The plot on the top shows an example of the coverage in the center of mass from a monte carlo simulation for protons from a 50 MeV reaction. The bottom plot is the same with a geometric filter accounting only for θ coverage in the lab.

164
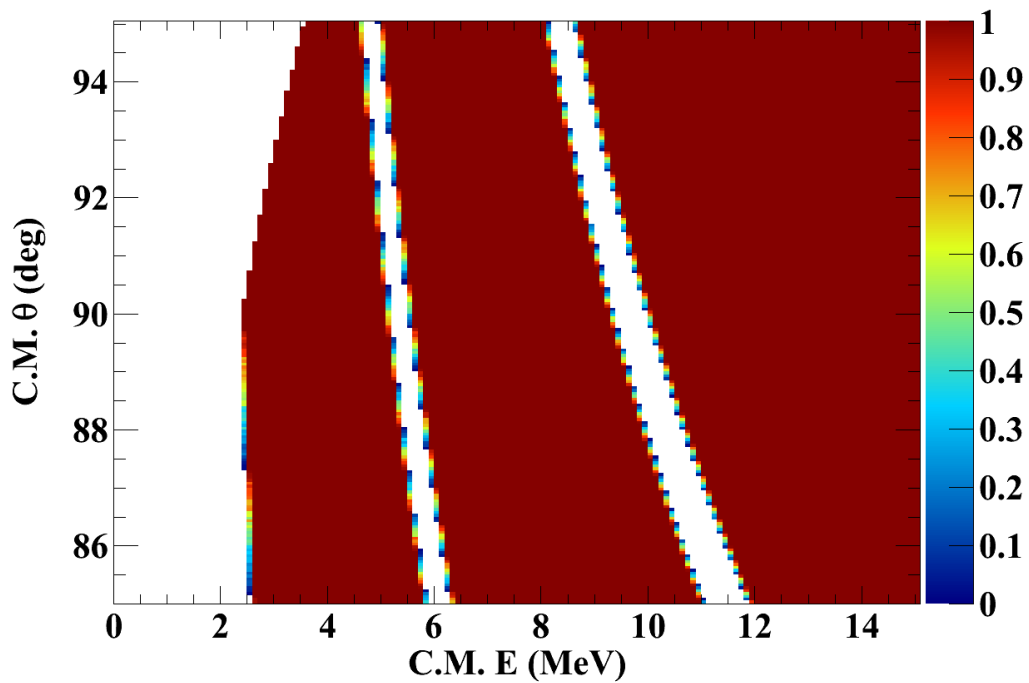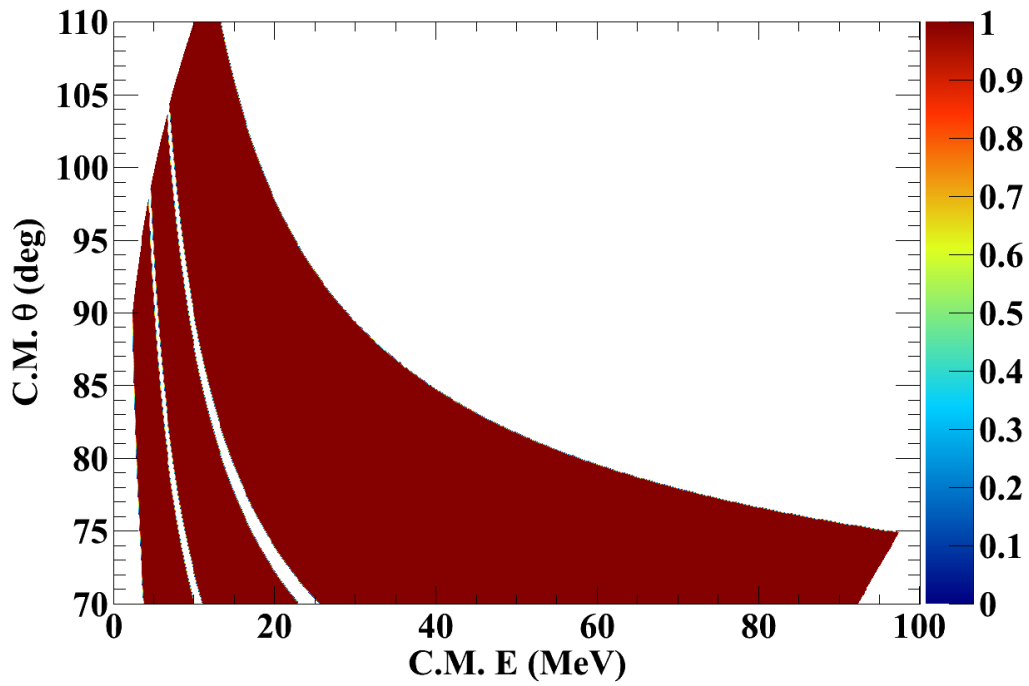
Figure 5.24: The top plot shows the ratio of the two plots of Figure 5.23 providing an edge efficiency correction for each bin. The bottom zooms in on a small region to better see the effects at the edge.
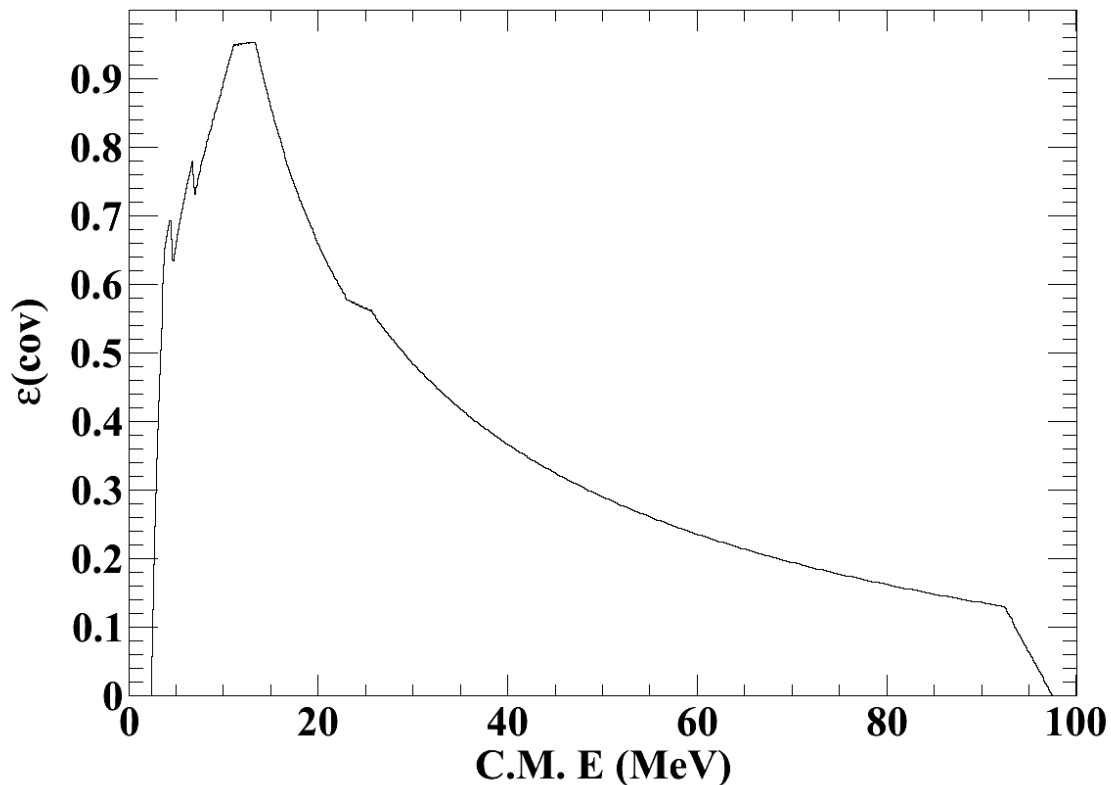
Figure 5.25: The correction for protons in a 50 MeV reaction for the lack of solid angle coverage in the center of mass.

Only data that has a coverage ratio of at least 3% is considered for final spectra.

5.2.3 Effects of Efficiency Corrections

Each efficiency correction has varying strengths of contribution. The lab azimuthal correction for example has the largest effect, roughly an order of magnitude, for the whole energy spectrum. Others such as the edge correction are much smaller, in this case a 1% correction. Figure 5.26 shows the effect that each correction has compared to the raw spectrum. Each of the nine plots in the figure represent the ratio of corrected data to raw data in the center of mass for protons from the 50 MeV/Acentral reactions gated in

the midrapidity region. Corrections for ^{112}Sn are in black and ^{124}Sn are in red. Moving from left to right across the top row, the plots are, (a) the ratio of fully corrected data to raw data, (b) the ratio of the azimuthal corrected data to the raw data and lastly, (c) the ratio of the silicon corrected data to the raw data. The middle row shows (d) the ratio of data corrected for double hits in the CsI, (e) the ratio of edge corrected data to raw data and finally (f) the data correceted for center of mass coverage over the raw data. The bottom row shows the effects of (g) the blue background correction, (h) the punch through correction and (i) the correction for inefficiency in the pixelation routine. Figure 5.27 shows the same set of corrections to the data for the 120 MeV/Acentral reactions.
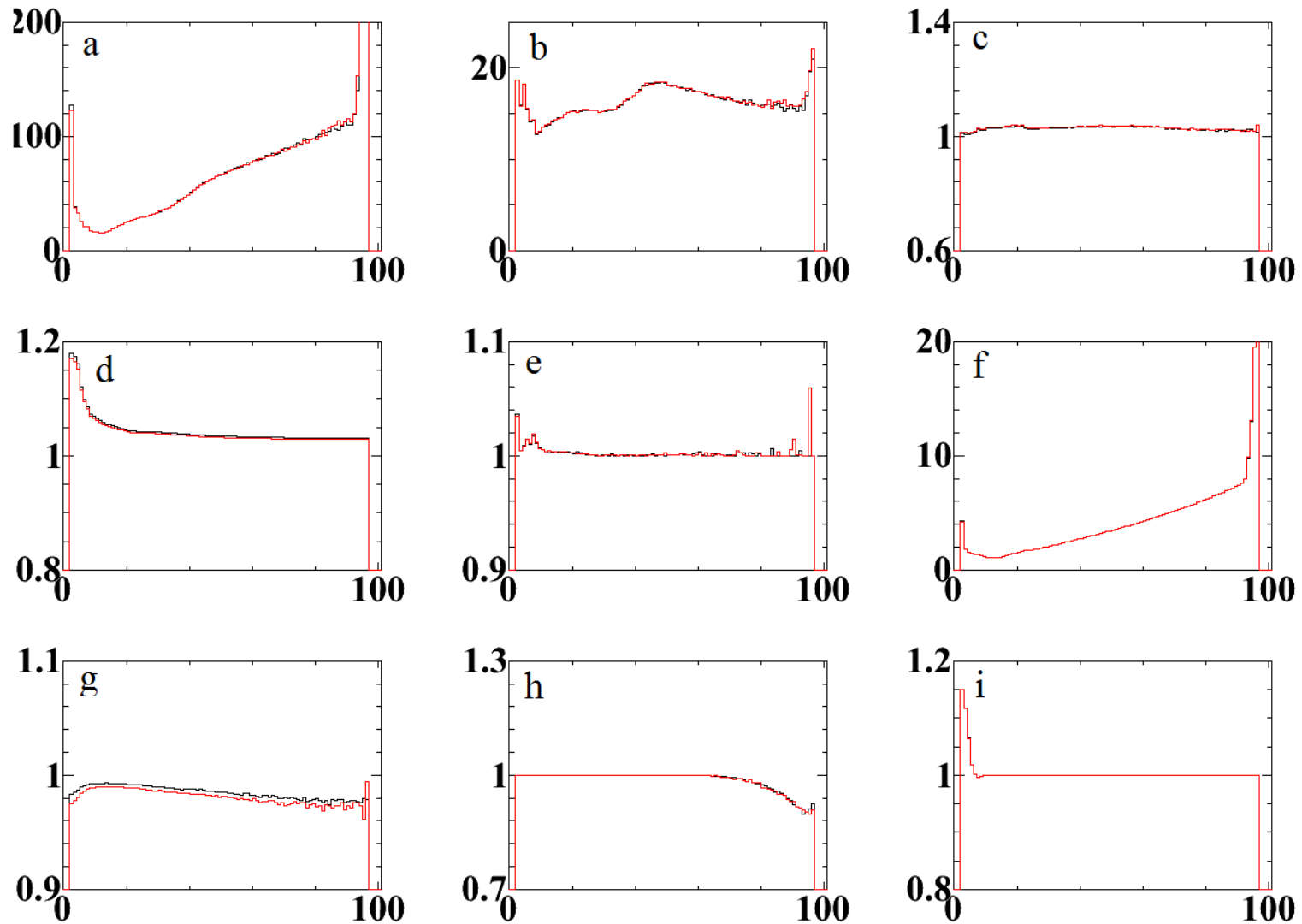
Figure 5.26: The effect of different efficiency corrections on protons in the 50 MeV/Areactions. Corrections for ^{112}Sn are in black and ^{124}Sn are in red. The corrections in order from left to right and then top to bottom are: (a) All corrections, (b) lab azimuthal, (c) silicon, (d) CsI, (e) edge, (f) center of mass coverage, (g) blue background, (h) punch through, and finally (i) pixelation routine inefficiency.
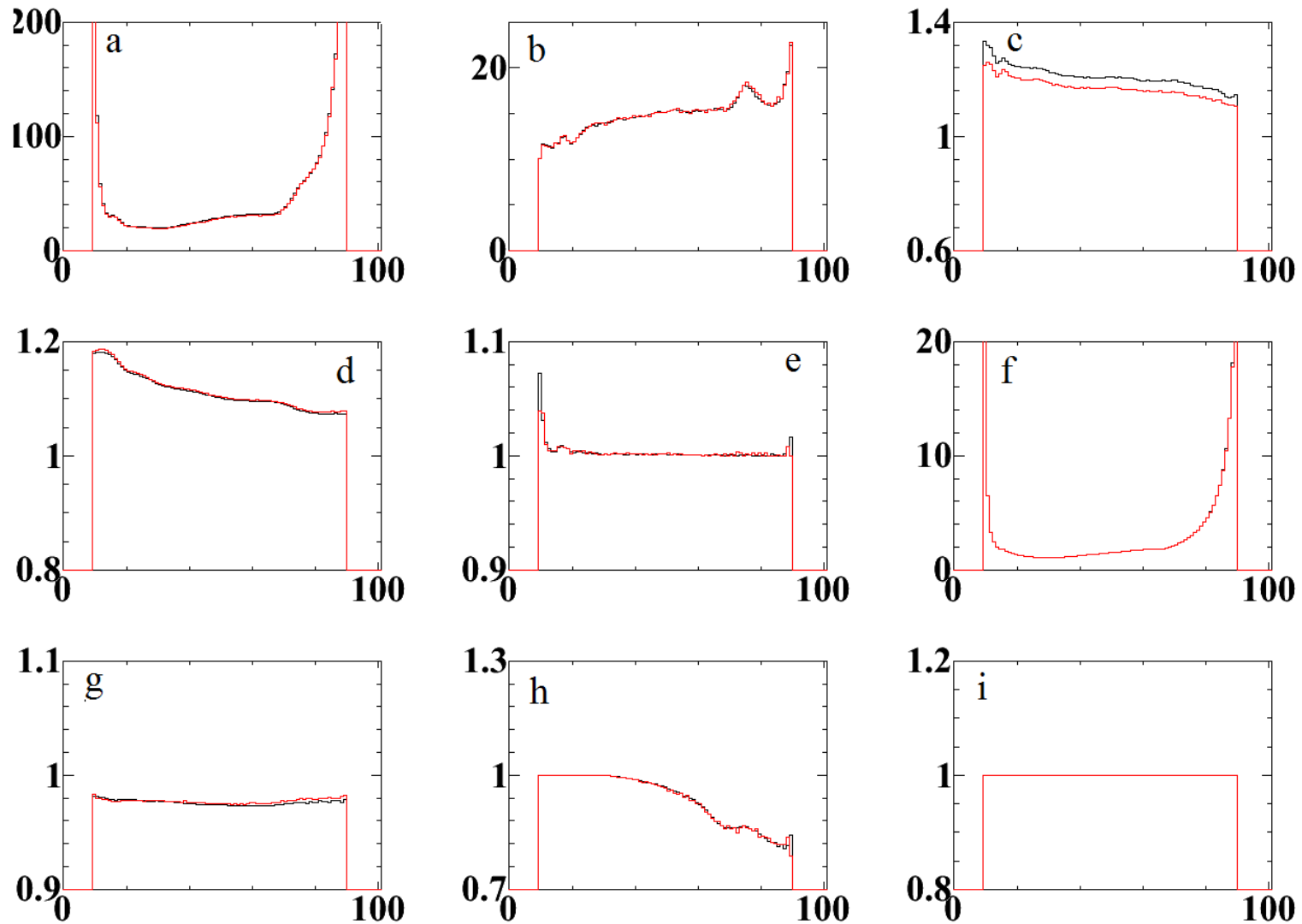
Figure 5.27: The effect of different efficiency corrections on protons in the 120 MeV/Areactions. Corrections for ^{112}Sn are in black and ^{124}Sn are in red. The corrections in order from left to right and then top to bottom are: (a) All corrections, (b) lab azimuthal, (c) silicon, (d) CsI, (e) edge, (f) center of mass coverage, (g) blue background, (h) punch through, and finally (i) pixelation routine inefficiency.

Correction	Predicted Systematic Uncertainty
Azimuthal	0.1%
Silicon	2%
CsI	0.5%
Edge	1%
Coverage	1%
Blue Background	2%
Punchthrough	15%
Pixelation Routine	10%

Table 5.1: Prediction for the systematic uncertainty stemming from each efficiency correction.

These represent the best estimation for these efficiencies and corrections. Table 5.1 shows an estimation of the uncertainties in these corrections. For instance, the locations of the pixels in comparison to the target were measured through a very precise method and so we believe that the azimuthal correction is accurate to within 0.1% of the displayed value. On the other hand, the correction for punch through have several avenues for discrepancy from the real data and so we believe that the correction is reasonable to within about 15%. We develop our systematic uncertainty in two ways. The worst case scenario is if all the corrections are correlated, which we do not inherently believe. Only the edge and center of mass corrections have a correlation. In order to develop a worst case systematic uncertainty for the spectra, we adjust all of the corrections in a direction to increase the value of the spectra. We also assume that the systematic uncertainty is symmetric. The more realistic situation is when the systematic uncertainties are uncorrelated which is where they are all added in quadrature. The magnitude of the systematic uncertainty will be shown later this chapter.

5.2.4   Center of Mass Spectra

Like the lab spectra, center of mass data is selected through the process of pixelation, all of the efficiency corrections, impact parameter cuts and the selection of particles that are emitted in the 70 to 110 degree range in the center of mass. Shown in Figures 5.28, 5.29, 5.30 and 5.31 are the spectra for each of the isotopes detected for hydrogen and helium in LASSA for the four target and energy combinations. The spectra in each of these plots is built the following way:

$$\frac{dM}{dEd\Omega} = \frac{N(C/\varepsilon)}{\Delta E \int_{70}^{110} 2\pi \sin\theta d\theta}. \tag{5.10}$$

Here ΔE is the width of the energy bins. This differential multiplicity is calculated event by event taking into account the efficiency, ε, and correction factor, C, that is unique to each particle in consideration. This efficiency is the product of all efficiencies discussed thus far. Similarly the correction factor is the product of all the correction factors previously discussed.

Figure 5.32 shows the evidence of the symmetry energy's effect on these collisions. In the top plot, only symmetric deuteron and alpha spectra are shown from the ^{112}Sn and ^{124}Sn reactions at 50 MeV/A. Since these particles are symmetric, the symmetry energy should have little effect, which is indeed the case with these particles. The bottom plot, however, shows protons, tritons and ^{3}He which are asymmetric. If the symmetry energy has an effect, we would expect the neutron rich tritons to have boosted production in the ^{124}Sn reaction and the neutron deficient protons and ^{3}He to have reduced production in the same reaction. Both of these expectations are confirmed in this data. In the 120 MeV/Areaction, these effects are smaller but still visible as seen Figure 5.33.
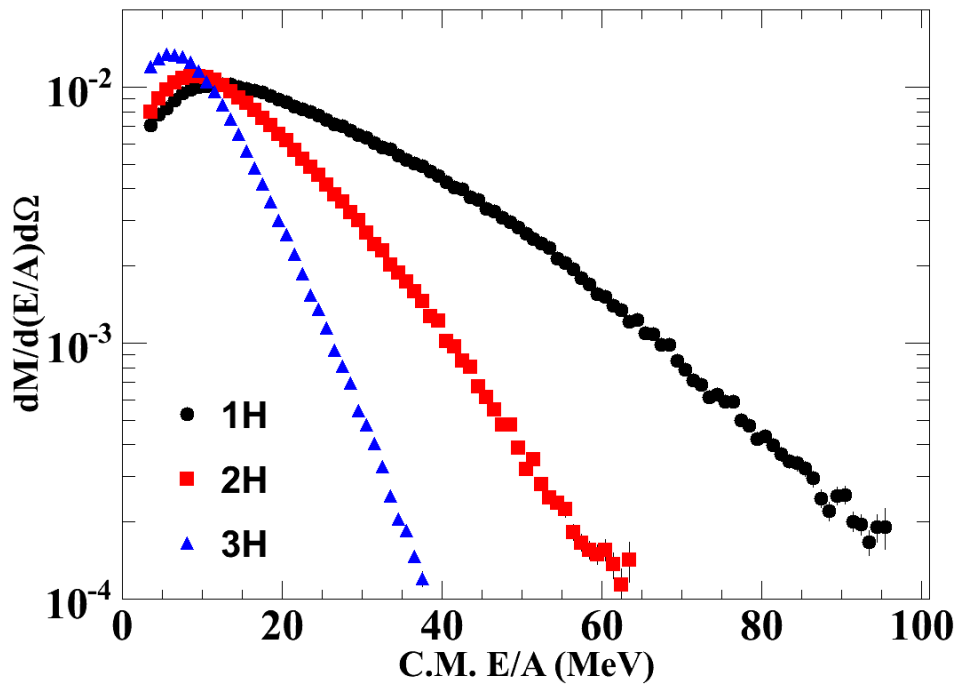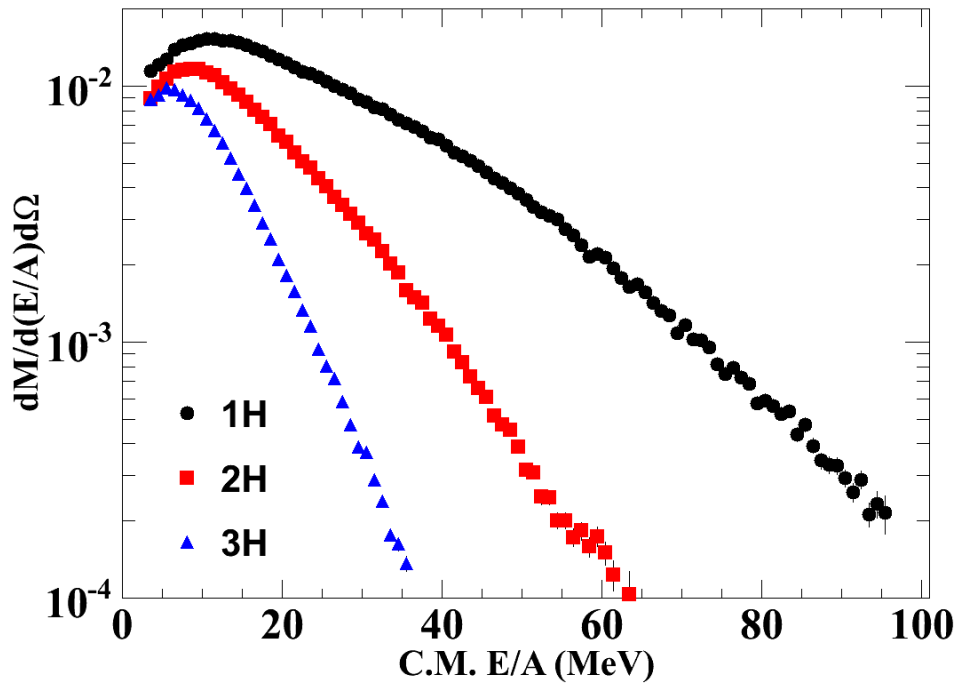
Figure 5.28: The spectra for the hydrogen isotopes measured in LASSA for the 50 MeV/Areactions. The top plots are from the ^{112}Sn reaction and the bottom are from the ^{124}Sn reaction.
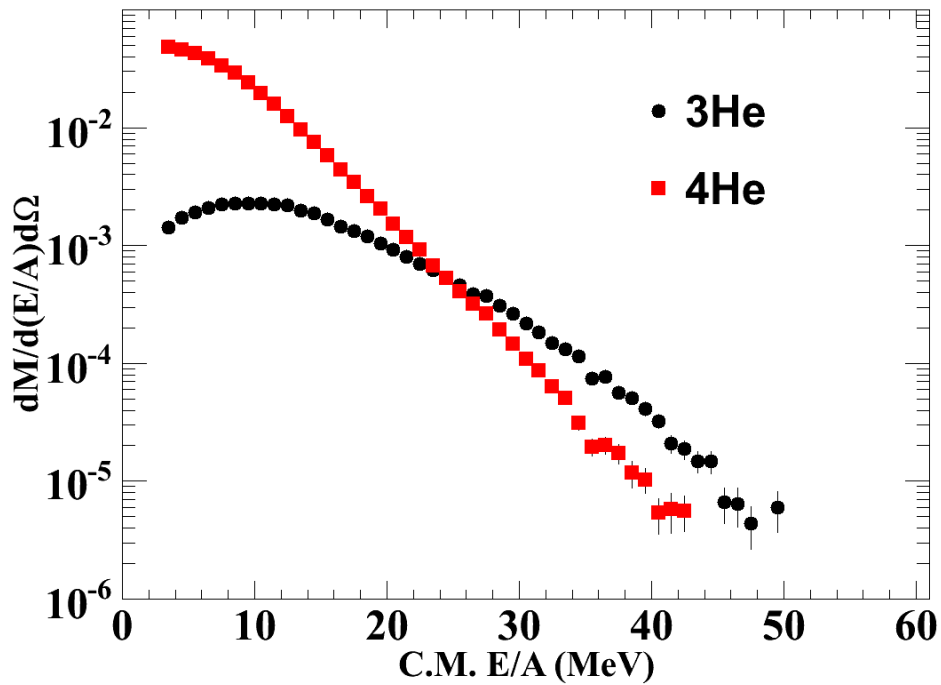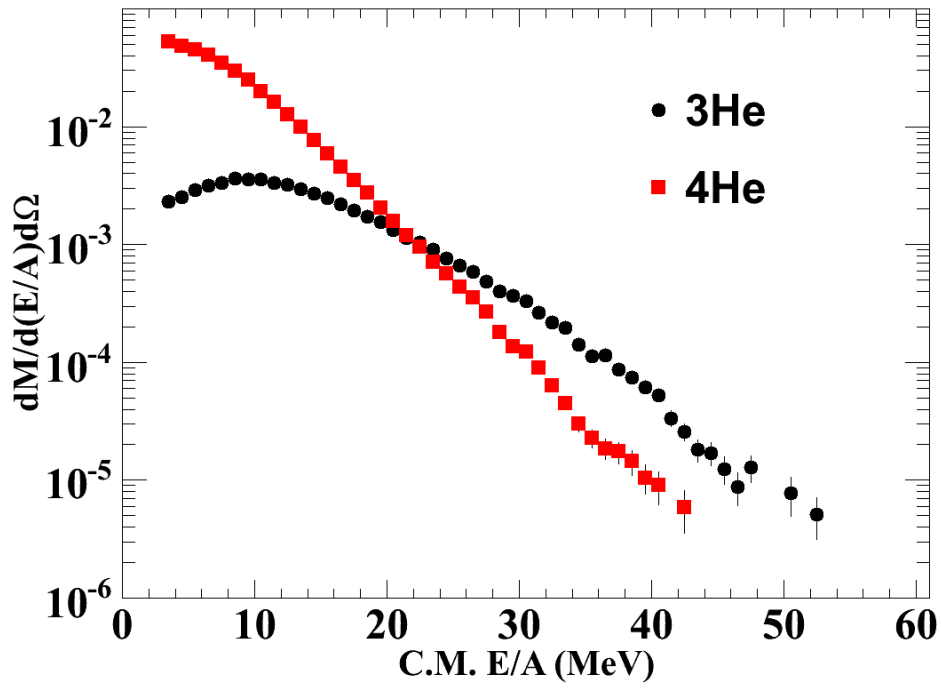
Figure 5.29: The spectra for the helium isotopes measured in LASSA for the 50 MeV/Areactions. The top plots are from the ^{112}Sn reaction and the bottom are from the ^{124}Sn reaction.
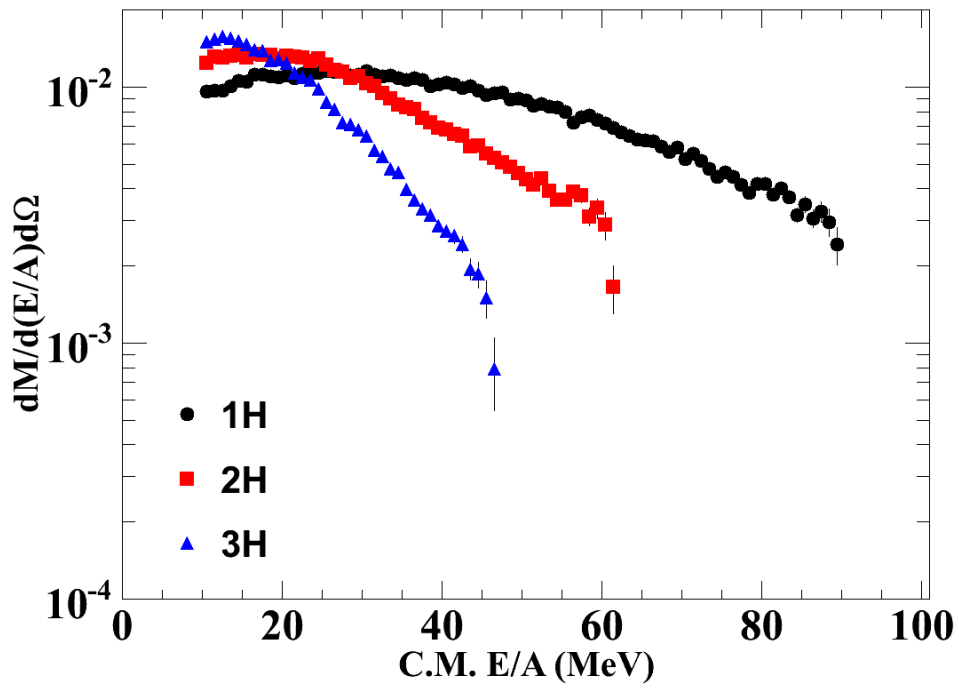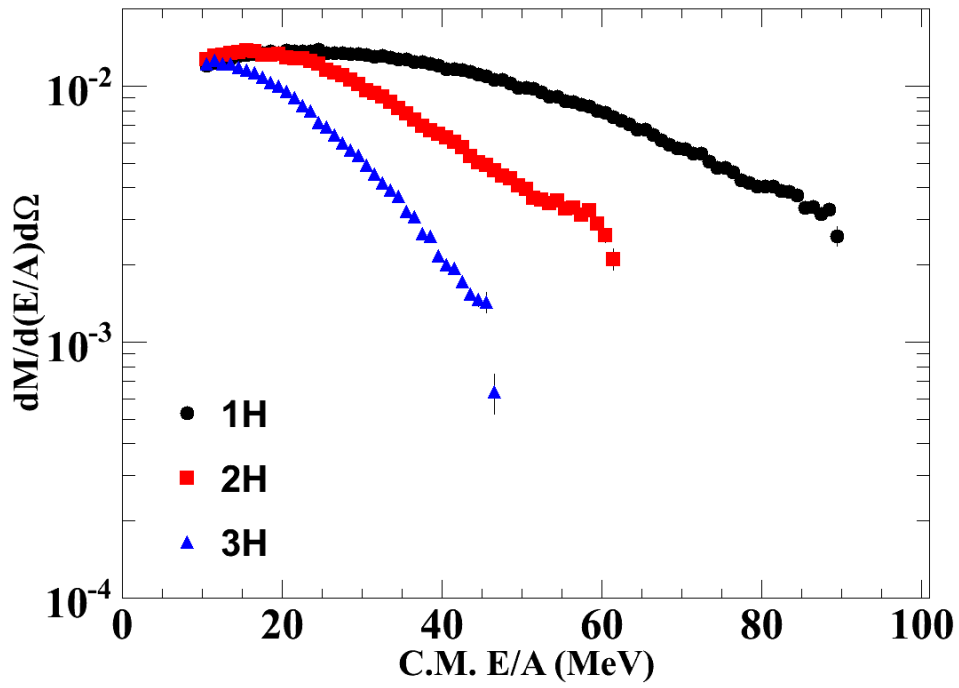
Figure 5.30: The spectra for the hydrogen isotopes measured in LASSA for the 120 MeV/Areactions. The top plots are from the ^{112}Sn reaction and the bottom are from the ^{124}Sn reaction.
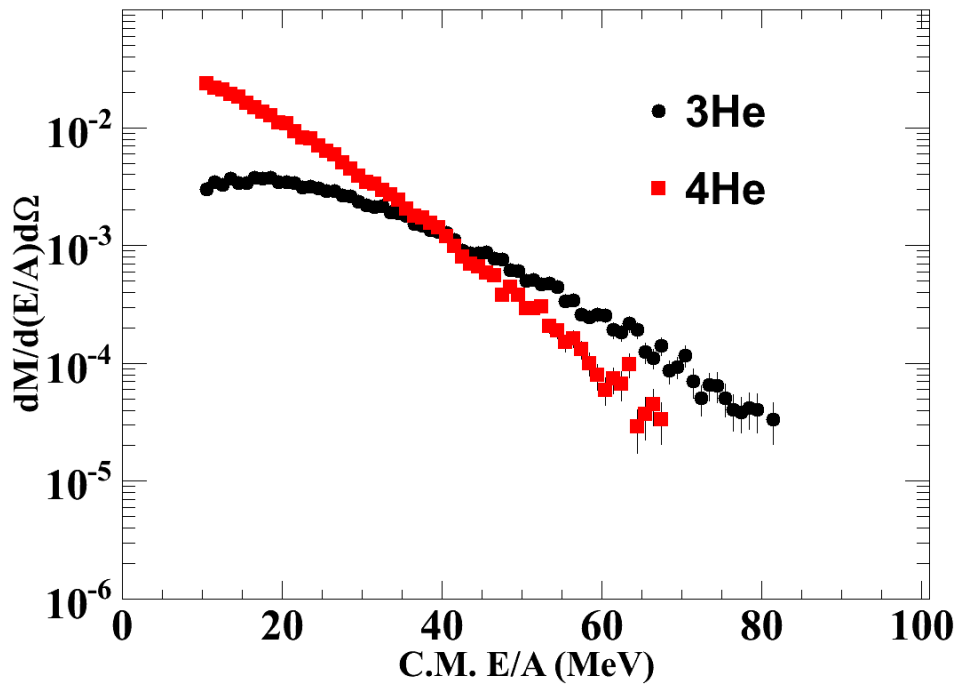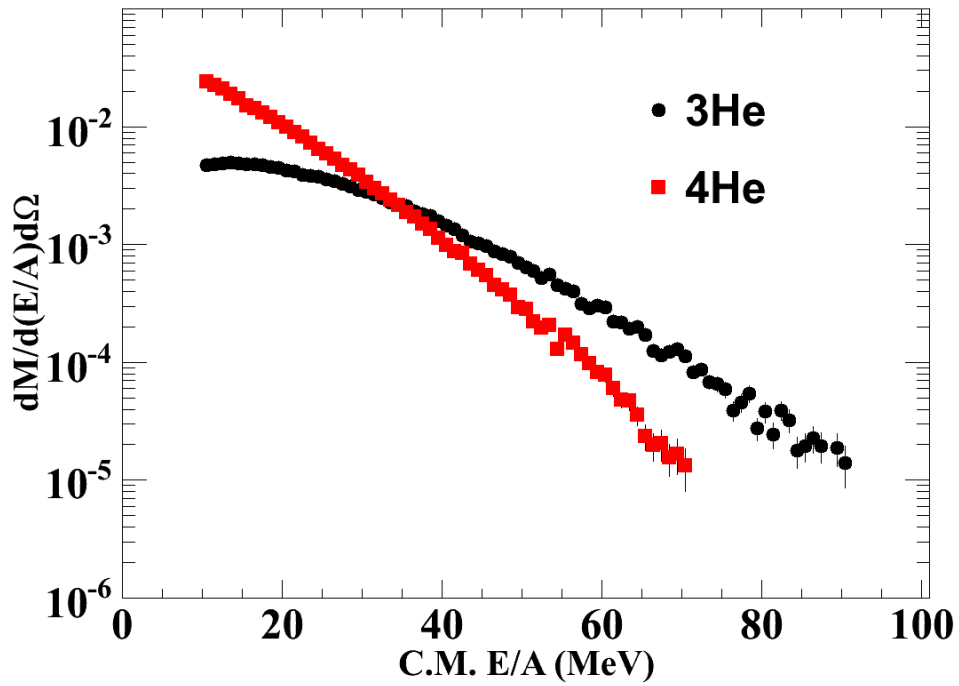
Figure 5.31: The spectra for the helium isotopes measured in LASSA for the 120 MeV/Areactions. The top plots are from the ^{112}Sn reaction and the bottom are from the ^{124}Sn reaction.
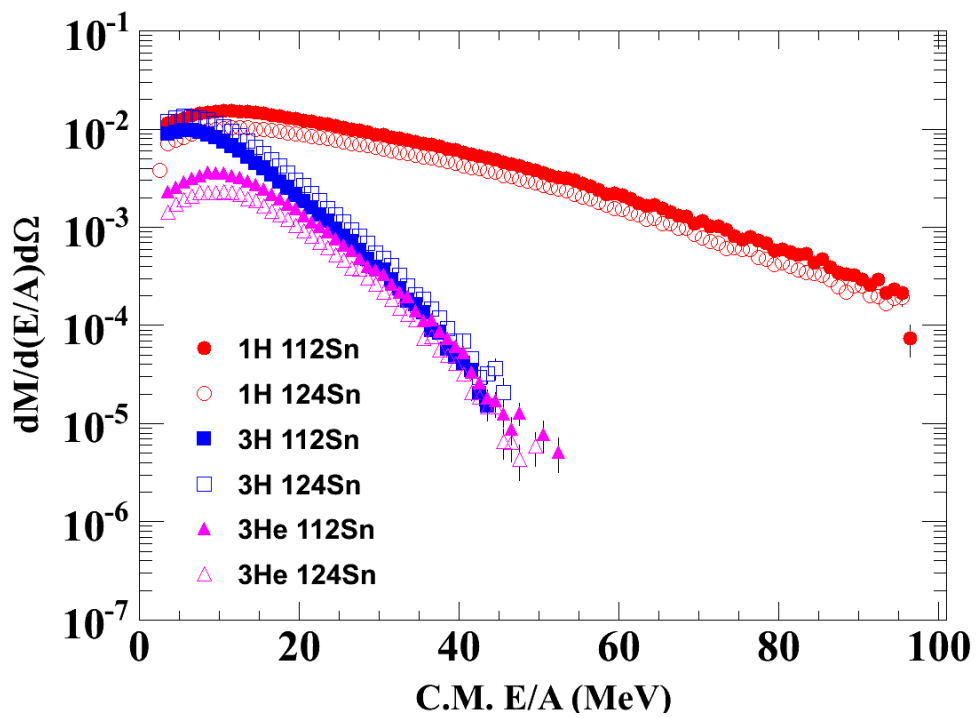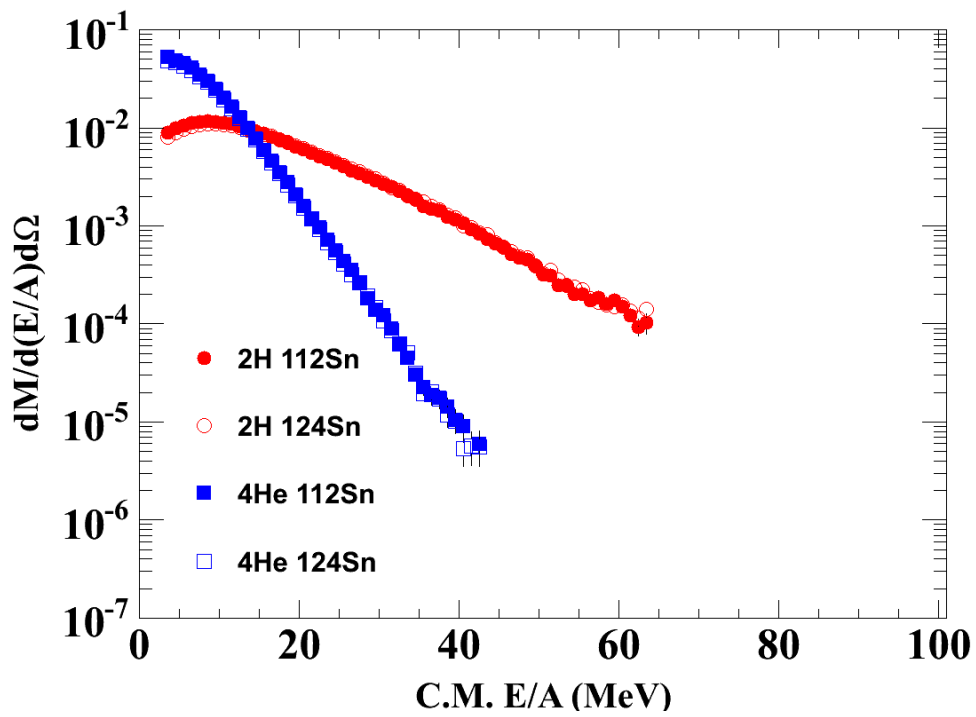
Figure 5.32: Spectra from 50 MeV/Areactions comparing the yields of symmetric (top) and asymmetric (bottom) particles.
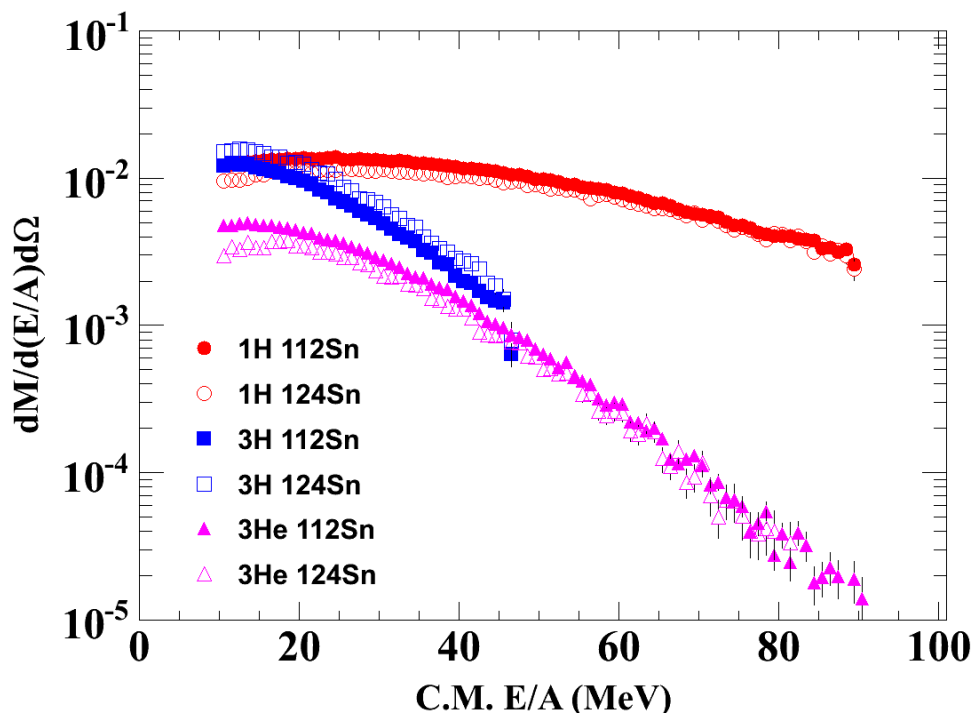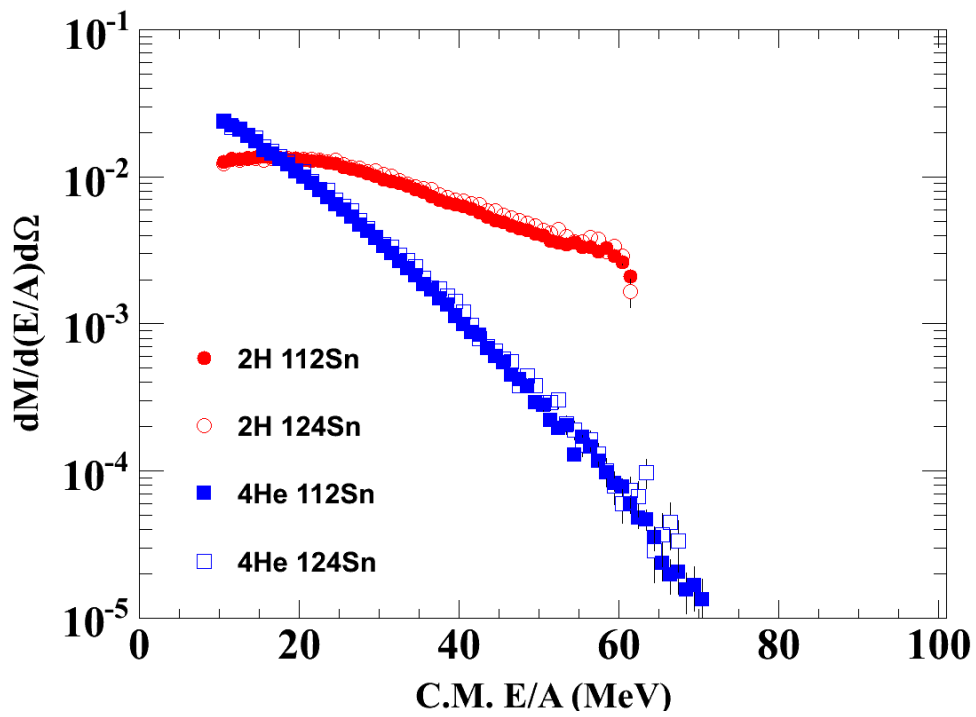
Figure 5.33: Spectra from 120 MeV/Areactions comparing the yields of symmetric (top) and asymmetric (bottom) particles.

As mentioned previously the systematic uncertainties are generally on the same order or less than the statistical uncertainties. Figure 5.34 shows the comparison between correlated (worst case scenario) and uncorrelated systematic uncertainty and statistical uncertainty. The figure shows the low energy (top) and high energy (bottom) range of protons from 50 MeV/A.

The coverage correction discussed earlier this section makes the assumption that the distribution of particles between 70 and 110 degrees in the center of mass is isotropic. In order to confirm this, we built different spectra for different angular regions, specifically five degree wide bins centered on 90 degrees and moving outward in both directions. Figure 5.35 shows this angular distribution for protons from the ^{112}Sn reactions at both energies. In this plot the solid black circles represent the 90 ± 2.5 degree region. The solid red squares represent the next five degree bin on either side of 90. For each step backward(forward) in angle, the spectra was scaled up(down) by an additional factor of two. The black line represents the data from the whole $70 \leq \theta \leq 110$ degree region. Evidenced primarily by the forward regions, since the backward has little coverage, it is easily seen that most spectra out through at least 70 degrees lines up almost exactly with the lines near 90. The only discrepancies occur at forward angles and high energies. If there was contribution from other sources, or a lack of isotropy in general, we would expect deviation from the black line for any of these regions. Farther away from 90 degrees, we do indeed see an increase in production as would be expected especially in the tritons and heliums. In the 120 MeV/Areactions we see a slight underproduction at the most forward angles in comparison to the average. In general the contribution from these regions is statistically small compared to the angular range of interest. This effect
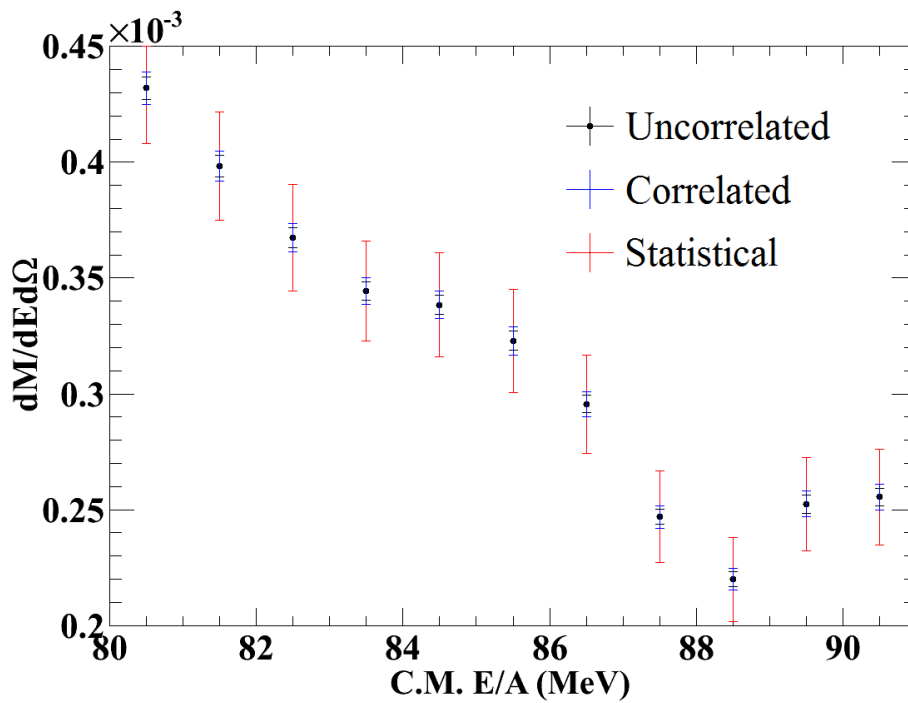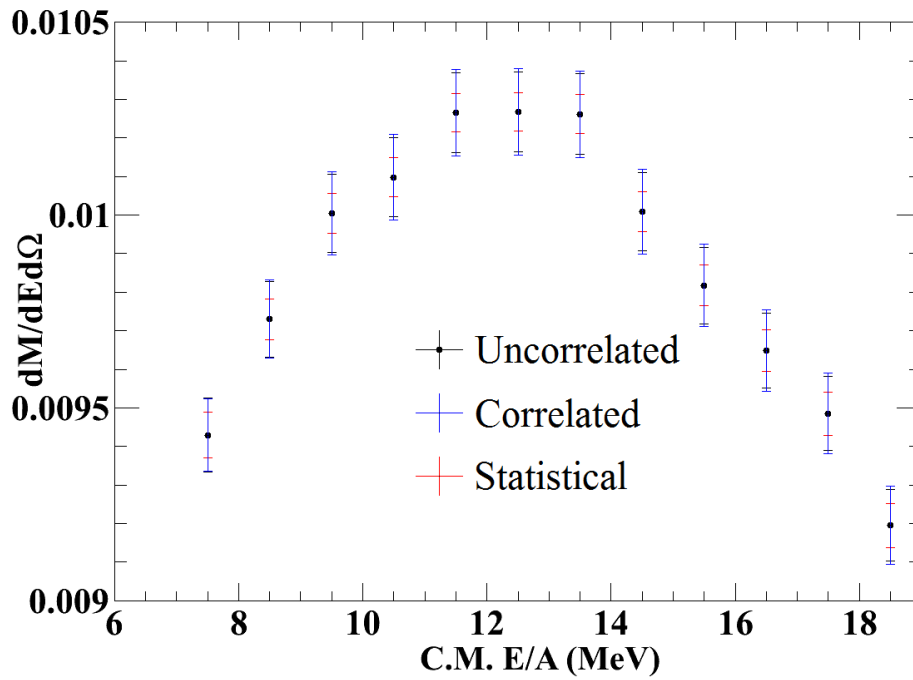
Figure 5.34: The comparison of statistical uncertainty to correlated and uncorrelated uncertainties. The top plot zooms in on spectra from Figure 5.28 for low energy protons in the ^{124}Sn reaction at 50 MeV/A. The bottom plot shows the high energy protons from the same reaction

may be caused by a lack of significant coverage in this angular region.

The full set of data for the ^{112}Sn for all particles and both energies can be found in Figures 5.36, 5.37, 5.38 and 5.39.

5.3   Coalescence

The idea of coalescence was initially brought up in Chapter 4. The coalescence model is a theory extensively studied in the past to describe the spectra of clusters of particles from those of neutrons and protons [43–55]. This model assumes that clusterization is a comparatively gentle process that occurs during the expansion stage of the reaction. It involves nucleons moving at nearly the same velocity and occupy the same volume. Collisions between the nucleons in the final cluster and nucleons outside the cluster nudge the particles into the same phase space to create the final cluster. These clusters can be anything from deuterons or tritons up through alphas or even larger clusters. Experimentally, we don't know the coordinate space density in the fragment production. Instead we can investigate the momentum space density. In this approximation the energy distribution of particles with N neutrons and Z protons can be described by a simple phase space volume. An experimental formula to describe this has been provided by Awes et. al. in Ref. [47] and has the form,

$$
\gamma \frac{d^3 M(Z,N)}{dk^3} = \frac{2s+1}{2^A} \frac{1}{N!Z!} \left(\frac{4\pi}{3} P_0^3 \right)^{A-1}
$$
$$
\times \left(\gamma \frac{d^3 M(1,0)}{dk^3} \right)^Z \left(\gamma \frac{d^3 M(0,1)}{dk^3} \right)^N ,
$$

(5.11)
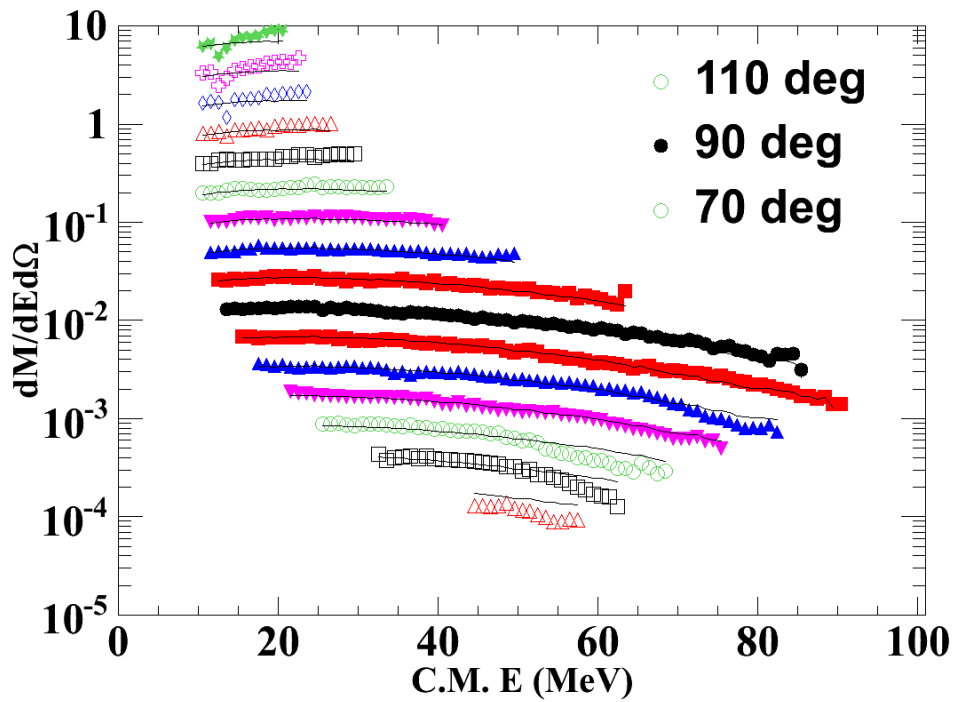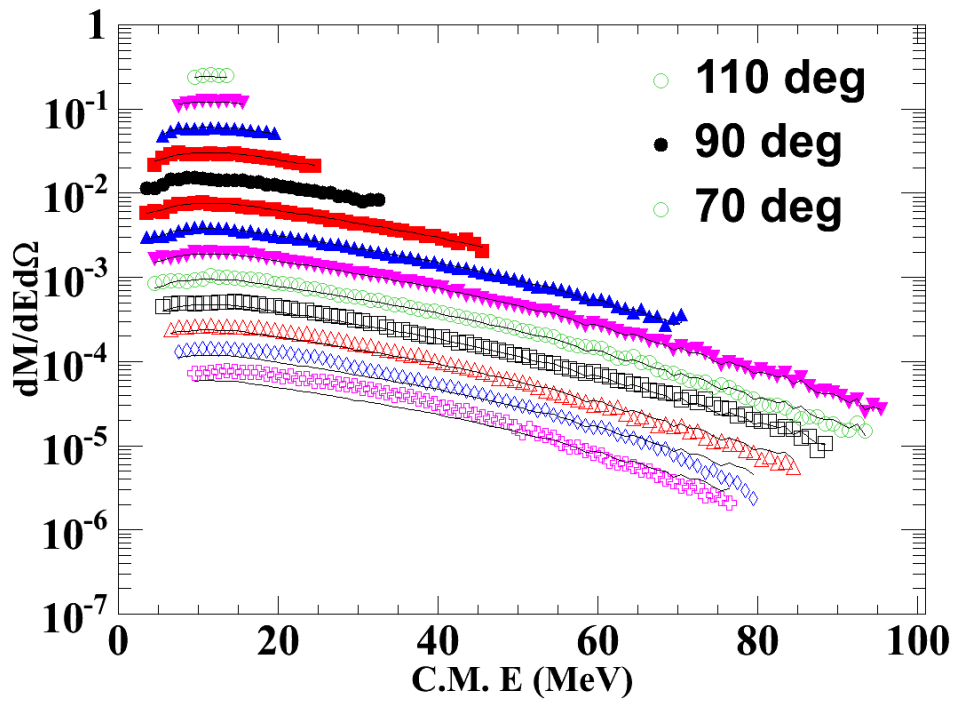
Figure 5.35: Angular distribution of protons from ^{112}Sn at 50 (top) and 120 (bottom) MeV/A. The solid black circles represent the 90 ± 2.5 degree region. Each step up(down) represents moving 5 degree backward(forward) in angle. The 90 degree region has not been scaled while each step away is scaled by an additional factor of two.

181
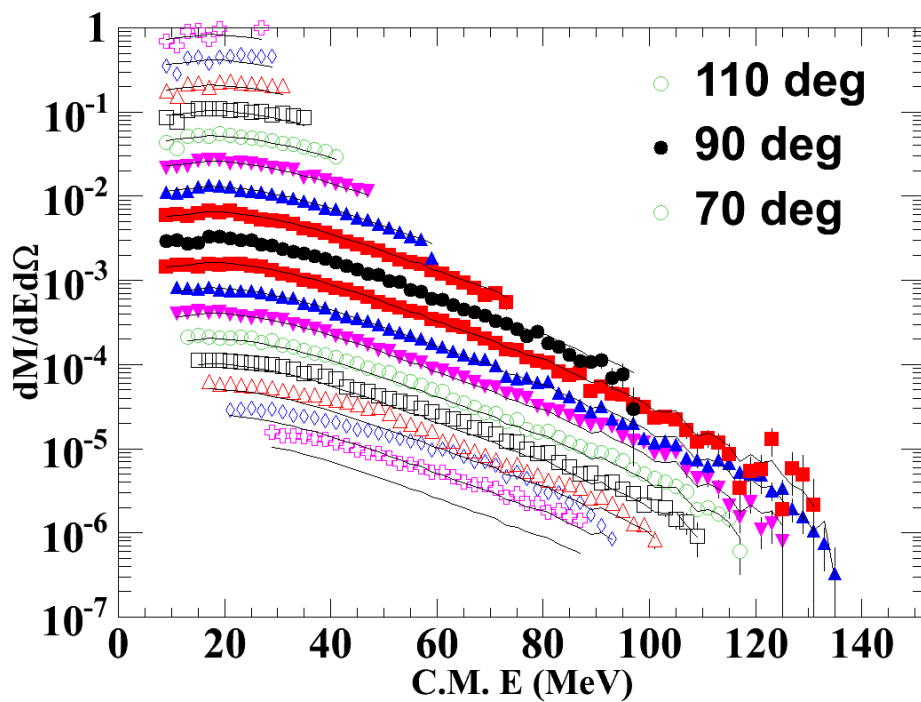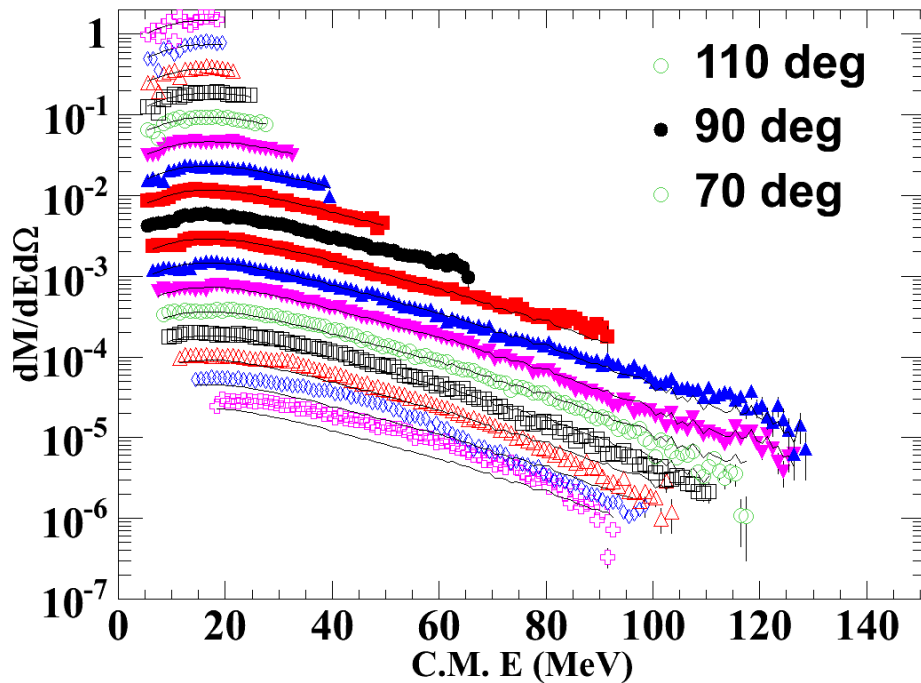
Figure 5.36: Angular distribution of deuterons (top) and tritons (bottom) from ^{112}Sn at 50 MeV/A. The solid black circles represent the 90 ± 2.5 degree region. Each step up(down) represents moving 5 degree backward(forward) in angle and is scaled up(down) by a factor of 2 for each step.
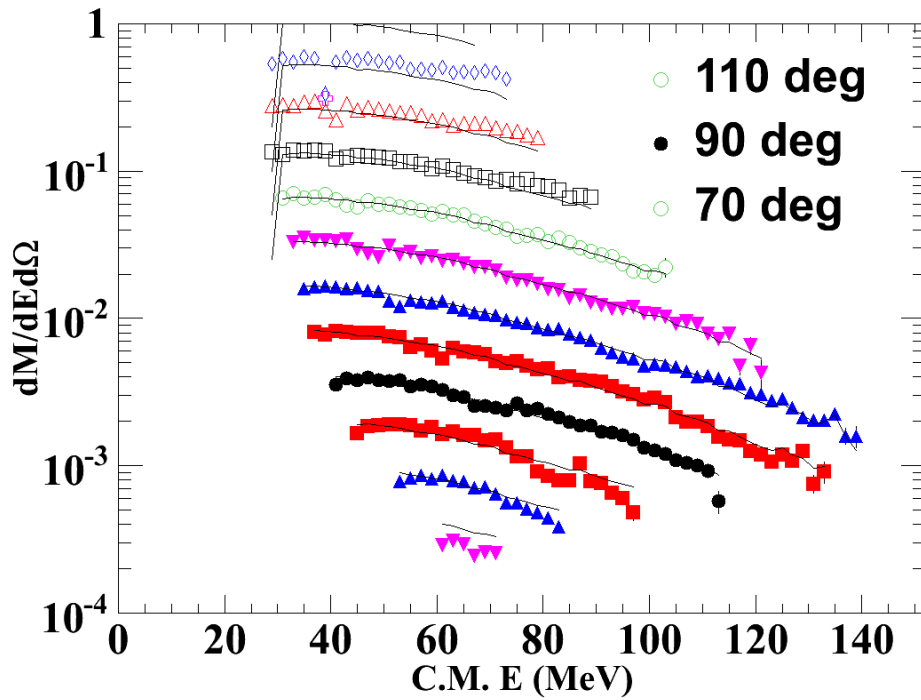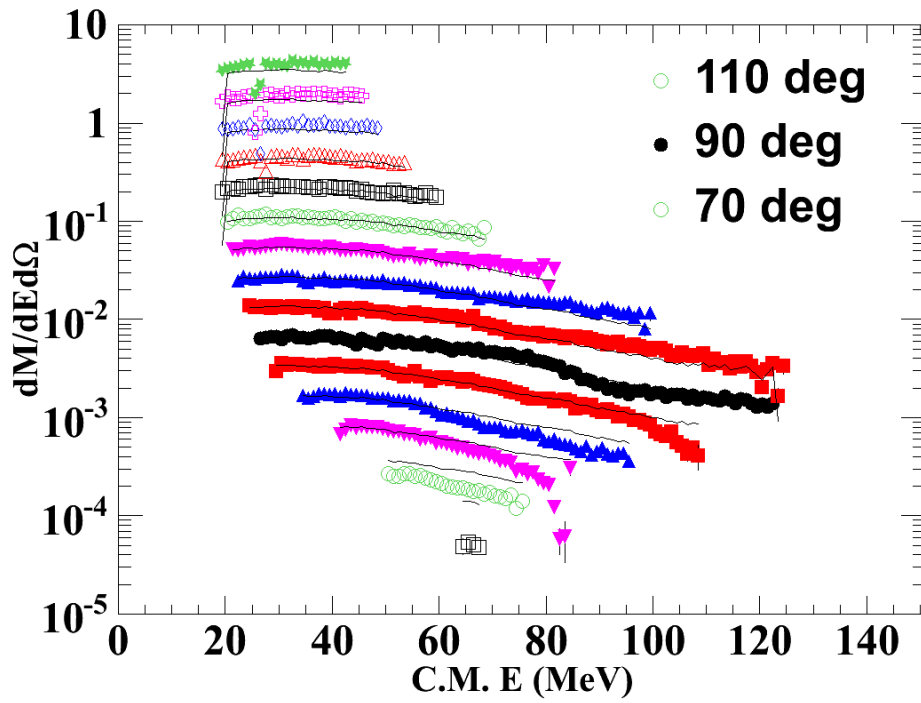
Figure 5.37: Angular distribution of deuterons (top) and tritons (bottom) from ^{112}Sn at 120 MeV/A. The solid black circles represent the 90 ± 2.5 degree region. Each step up(down) represents moving 5 degree backward(forward) in angle and is scaled up(down) by a factor of 2 for each step.
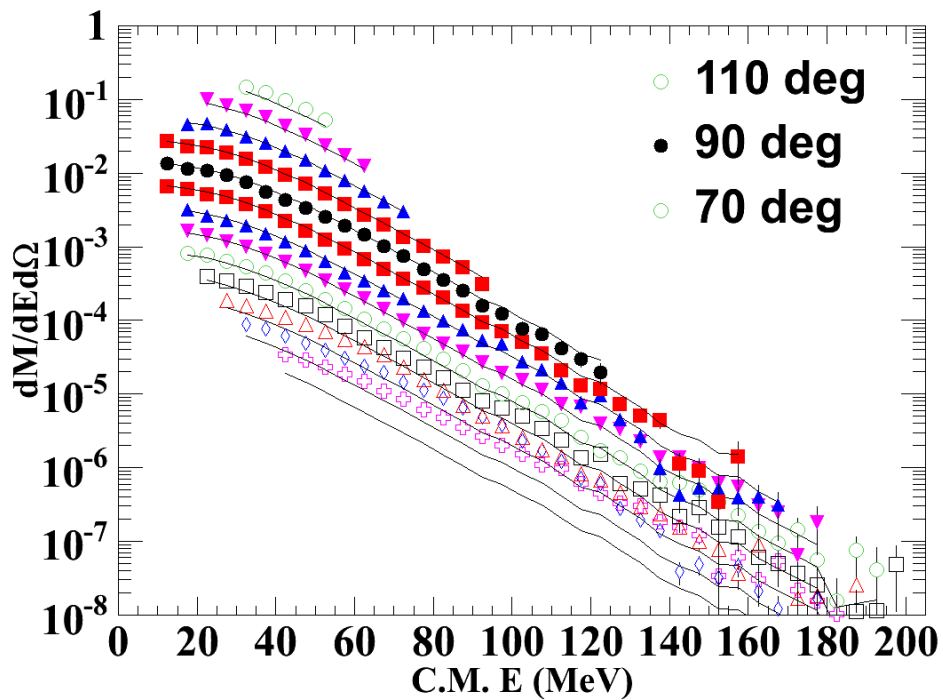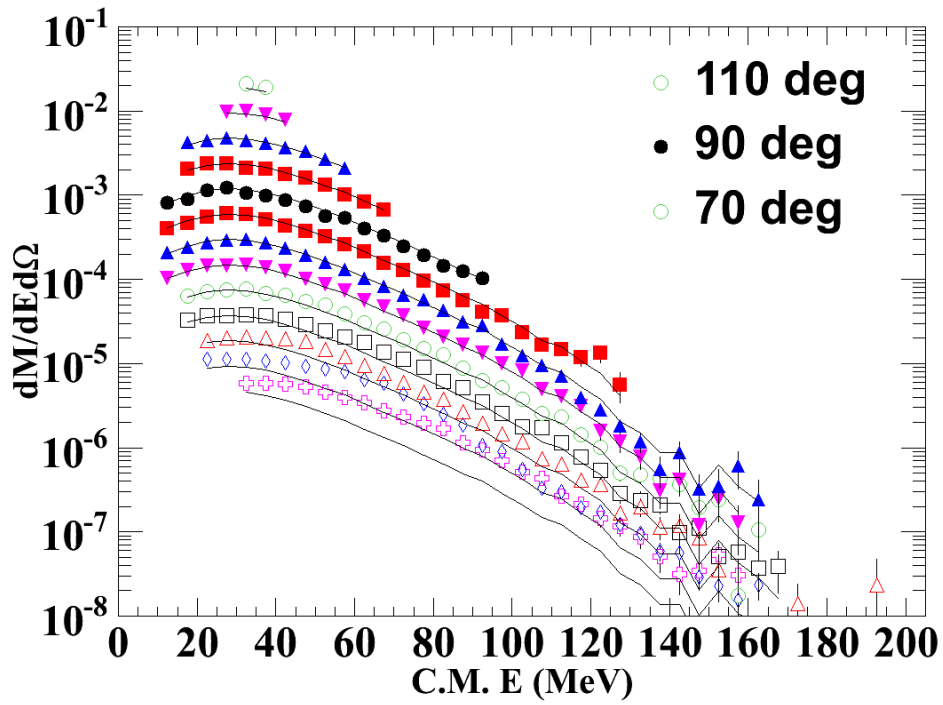
Figure 5.38: Angular distribution of ^{3}He (top) and ^{4}He (bottom) from ^{112}Sn at 50 MeV/A. The solid black circles represent the 90 ± 2.5 degree region. Each step up(down) represents moving 5 degree backward(forward) in angle and is scaled up(down) by a factor of 2 for each step.
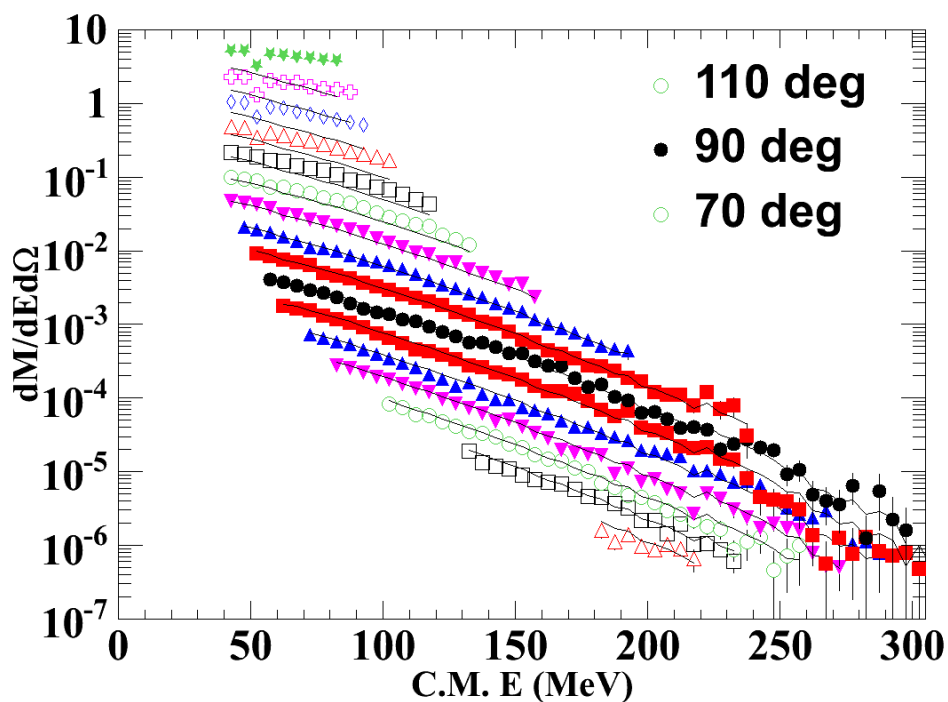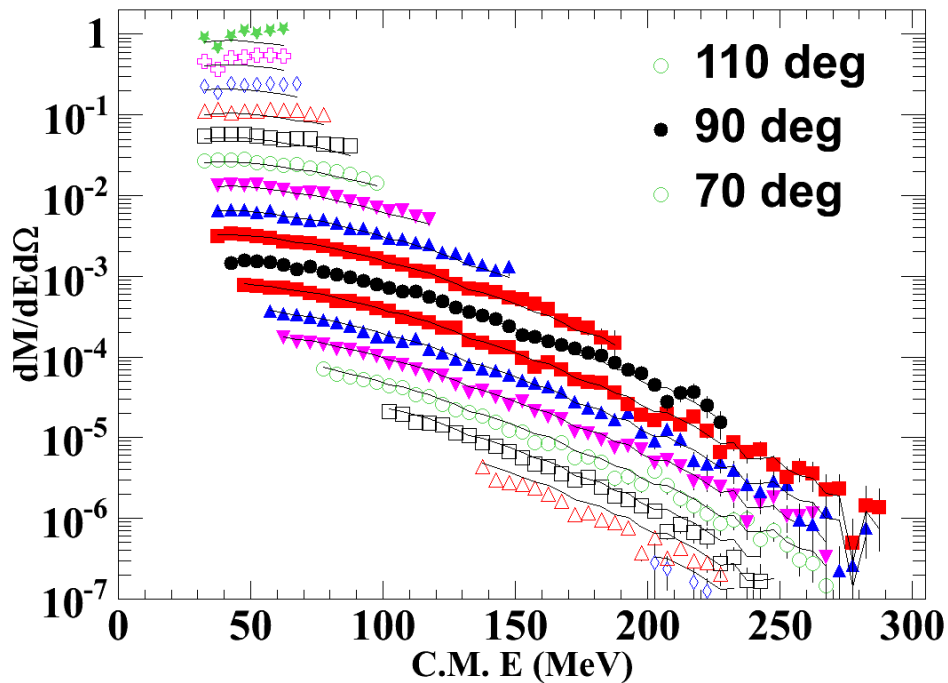
Figure 5.39: Angular distribution of ^{3}He (top) and ^{4}He (bottom) from ^{112}Sn at 50 MeV/A. The solid black circles represent the 90 ± 2.5 degree region. Each step up(down) represents moving 5 degree backward(forward) in angle and is scaled up(down) by a factor of 2 for each step.

where all k are given by the momentum per nucleon of the particles. There is only one parameter in this equation that can change the resulting spectra, P_0^3. All other quantities are fixed by the either the cluster of choice or the spectra of protons or neutrons. In theory, the volume $4\pi P_0^3/3$ represents the momentum space available for Z protons and N neutrons to create a cluster. However, the lack of relevant information about the configuration space volume of the cluster in this equation means that P_0^3 will also reflect the configuration space volume as well as the variation of the nucleon density within that configuration space volume which can be a function of the final cluster energy. In the seminal model of Butler and Pearson [56], the radius relevant to cluster formation is sensitive to the size of the final cluster and the range of the nucleon-nucleon force.

Instead of overtly interpretting the coalescence radius, we simply choose to measure it experimentally. This experiment actually has an added benefit of having measured free neutron spectra, where previous studies into this process did not. Instead, the previous studies chose to simulate neutron spectra by using Coulomb corrected proton spectra that were scaled by the neutron to proton ratio of the system, $(N_t + N_p)/(Z_t + Z_p)$. We can test the accuracy of this method and investigate its validity.

Because we have already built our spectra in terms of center of mass kinetic energy we can transform Equation 5.11 to,

$$\frac{dM_c}{d\Omega d(E/A)} = \frac{2s_c + 1}{N_c! Z_c!} \sqrt{2m_c^3 E} \left(\frac{4\pi P_0^3}{3}\right)^{X-1} \prod_{i=1}^{X} \frac{N_i! Z_i!}{2s_i + 1} \frac{1}{\sqrt{2m_i^3 E}} \frac{dM_i}{d\Omega d(E/A)}, \tag{5.12}$$

where all $dM/d\Omega d(E/A)$ have been Coulomb corrected by 10 MeV for each Z of the particle. The model assumes that a neutron and a proton moving at the same velocity can be approximated as a deuteron within a factor. Experimentally, the protons would have

extra energy due to the Coulomb boost from the barrier to the detector. This 10 MeV correction was chosen to be consistent with previous measurements on systems with similar total charge. In this equation, c represents the cluster being formed, s is the spin of the particle and E is still the energy per nucleon. There are several approaches to using Equation 5.12. One, used in [47], is to find a "best" value that describes the entire spectra of that cluster. Another is to adjust P_0 for each energy in order to exactly replicate the spectra of the cluster. As a first step, we adopt the latter approach to find P_0 or more specifically, $\log P_0$. Figure 5.40 shows the calculated value of $\log P_0$ as a function of center of mass energy per nucleon from the constituent protons and neutrons.

It is immediately obvious that there is indeed a strong energy dependence to the calculated P_0, however the spectra does seem to plateau at high energies. In addition we see that P_0 is dependent on the particle type. This figure showed the clusters if they were made from neutrons and protons. If we instead use the method of previous investigations and use scaled protons instead of neutrons we get the difference displayed in Figures 5.41 for hydrogen isotopes and 5.42 for helium isotopes.

While it is reasonable to assume a method such as scaling the proton spectra to replace the missing neutron spectra, this method shows that it is incomplete for asymmetric nuclei due to the symmetry energy. The ^{112}Sn system shows moderate agreement for P_0 as a function of energy if only at high energies, but the ^{124}Sn system shows vastly different results. It has been shown previously that coalescence models actually behave better at high energies. It is interesting to show that the while there is indeed better agreement in the 120 MeV/Asystem for P_0, the scaled proton method is still unable to reproduce the results using the actual neutron spectra as seen in Figures 5.43 for hydrogen isotopes and
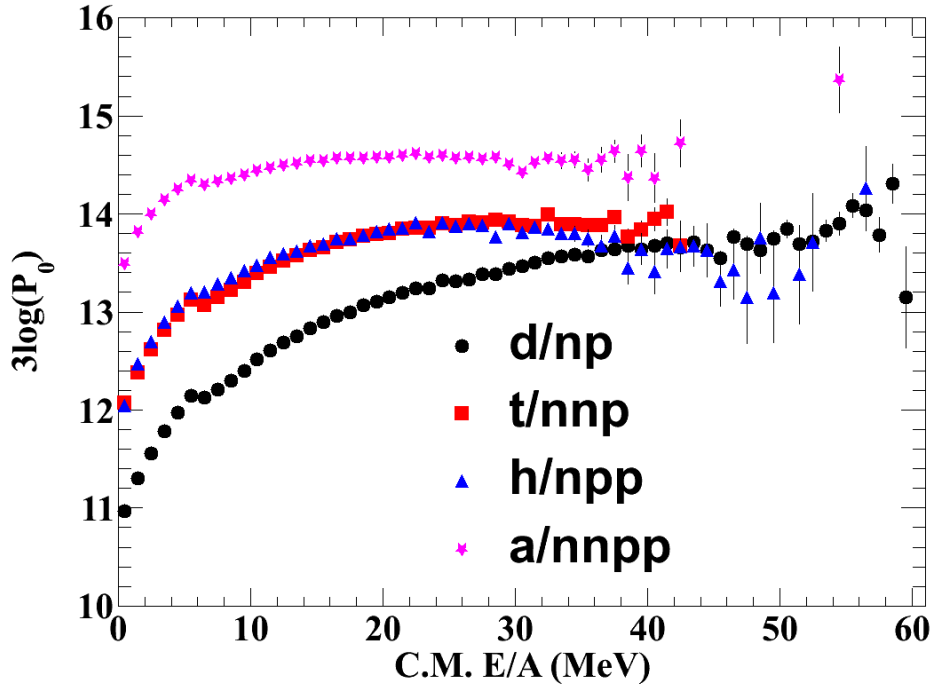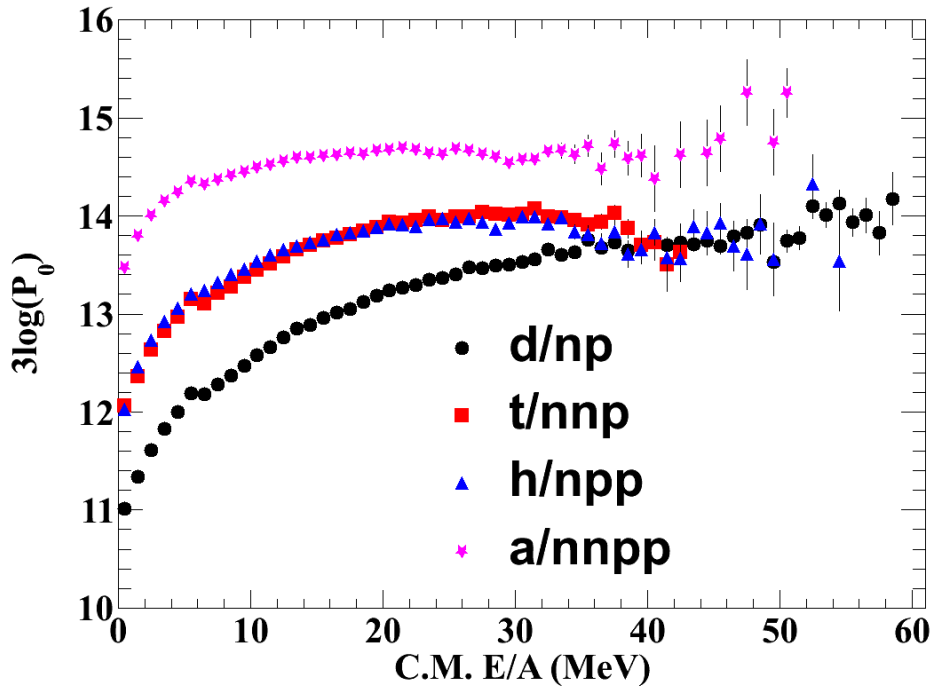
Figure 5.40: The dependence of $\log P_0$ on energy for different light clusters in the ^{112}Sn (top) and ^{124}Sn (bottom) systems at 50 MeV/A.
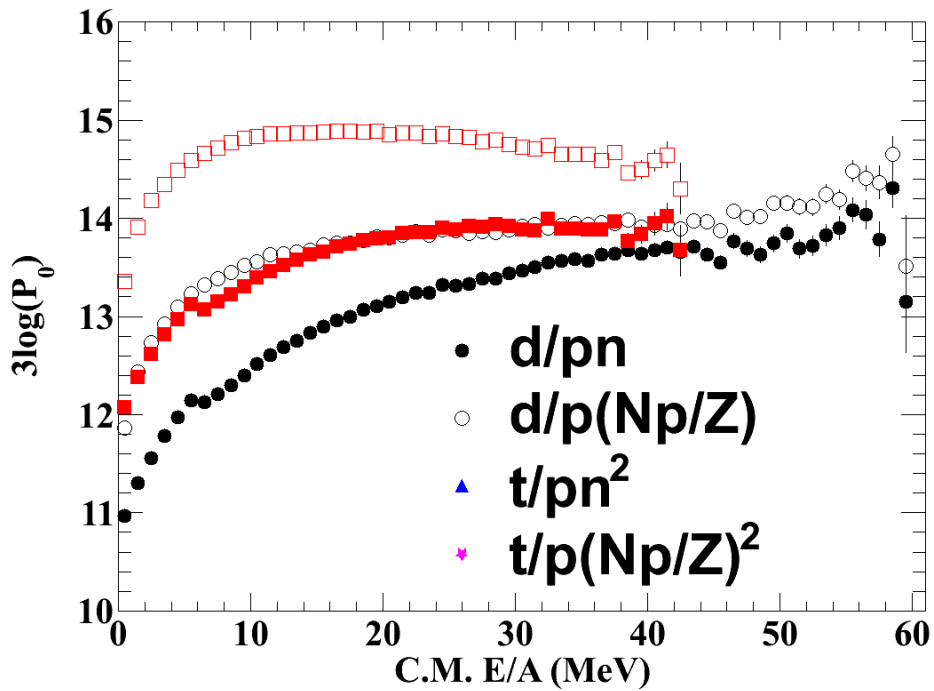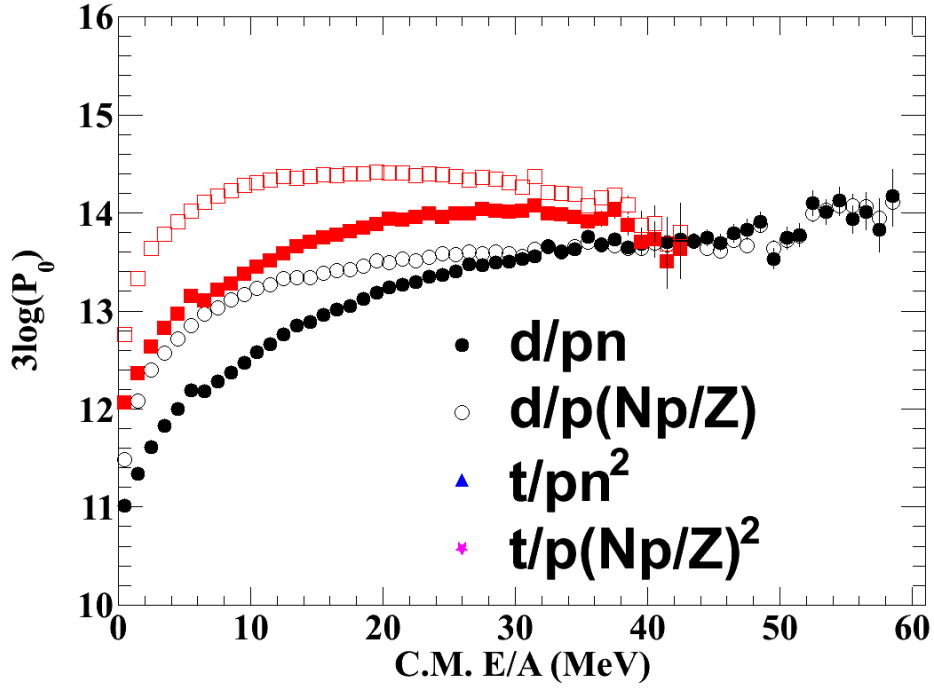
Figure 5.41: Creating hydrogen isotopes from neutrons and protons as given by the solid points. The open points are taken from protons and scaled protons as would have been performed in the past. ^{112}Sn is provided on top and ^{124}Sn on the bottom.
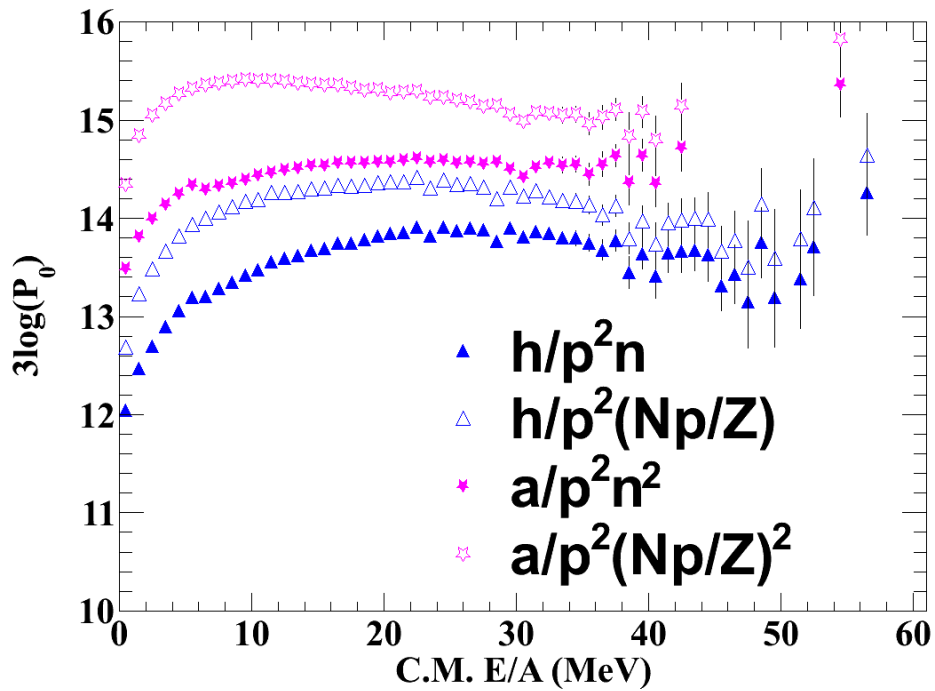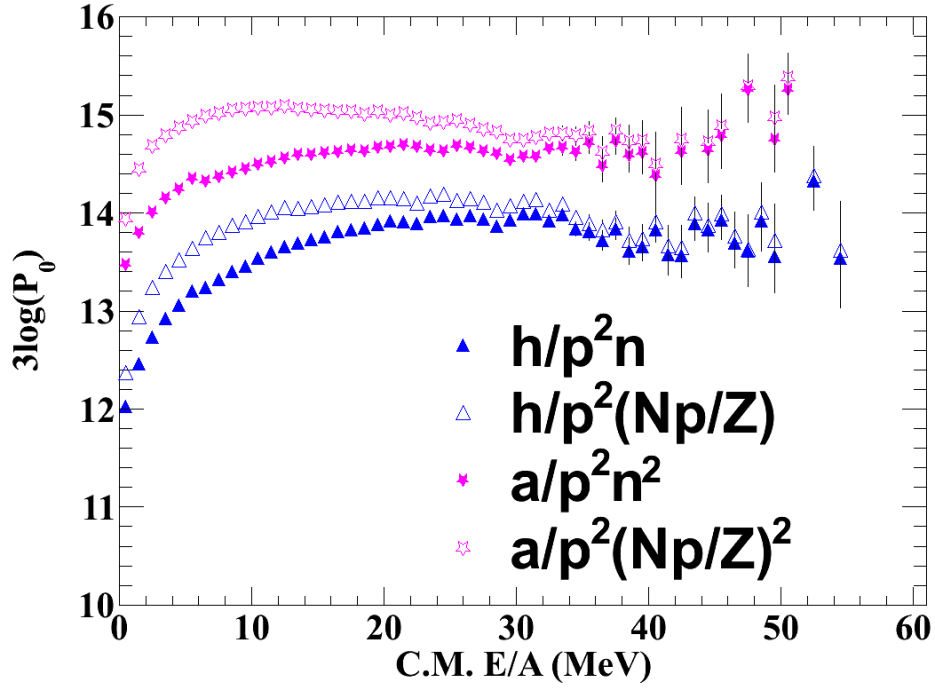
Figure 5.42: Creating helium isotopes from neutrons and protons as given by the solid points. The open points are taken from protons and scaled protons as would have been performed in the past. ^{112}Sn is provided on top and ^{124}Sn on the bottom.

5.44 for helium isotopes.

It is curious that the spectra of free particles were chosen to create the spectra of clusters. In principle, free protons and neutrons do not partake in coalescence and so a more accurate representation might to be use the coalescent invariant proton and neutron spectra. We build these spectra using the formula,

$$\frac{dM_{cip}}{d(E/A)d\Omega} = \sum_i \frac{dM_i}{d(E/A)d\Omega} \times Z_i, \tag{5.13}$$

for protons. Neutrons use the same equation replacing N_i for Z_i. By using these spectra, we are able to achieve much better agreement between the true method and scaled proton method as shown in Figures 5.45 for hydrogen isotopes and 5.46 for helium isotopes.

In principle since we have the coalescence radius and we have high energy protons and neutrons, we should be able to fit the energy dependence and extrapolate the triton spectra to higher energies. This is useful since we are only able to measure tritons to about 45 MeV/Adue to the punch through point in the CsI crystals and we can measure ^{3}He to much higher energies, especially in the 120 MeV/Areaction. In order to stay consistent, we use the P_0 from using free particles. Since the spectra flatten out we use a linear fit in the high energy regions. The fit and extended spectra can be found in Figure 5.47 for the 50 MeV/Areaction.

This dissertation will limit its treatment of this coalescence model to extend the spectra of tritons to higher energies in order to widen the range of comparison of tritons to ^{3}He.
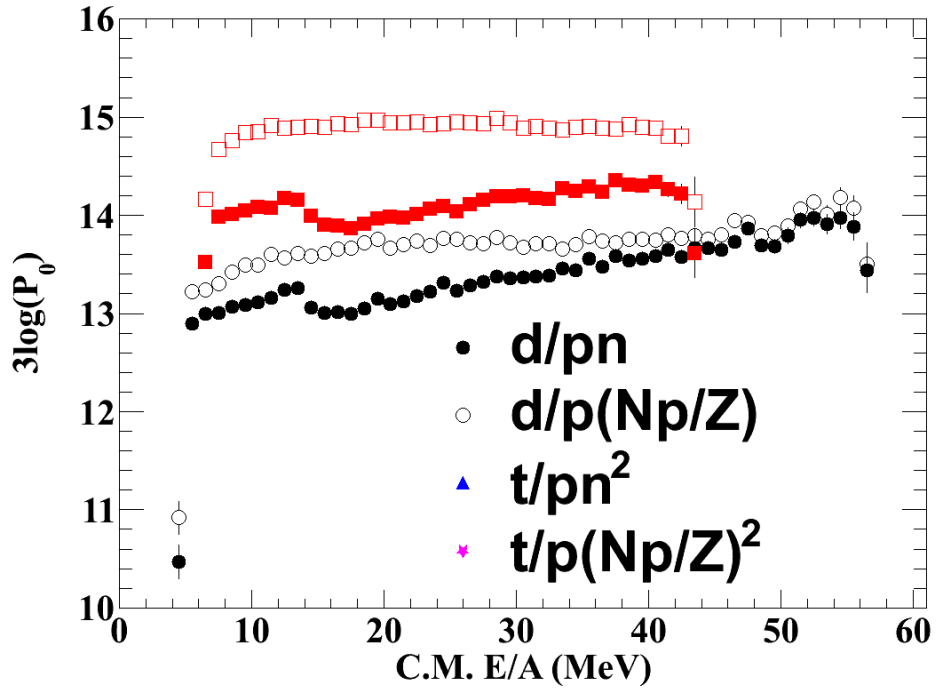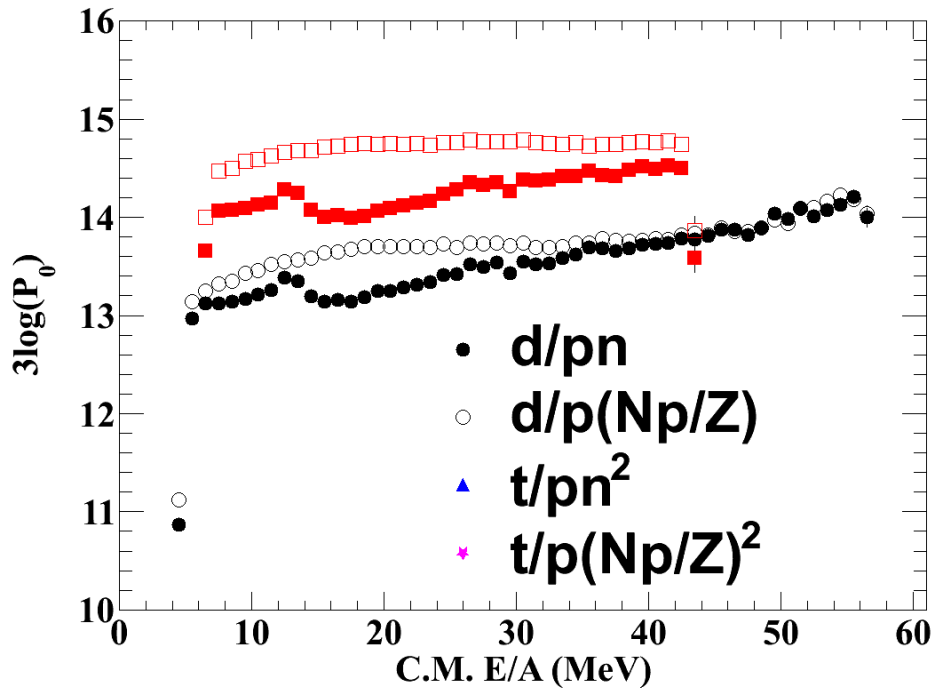
Figure 5.43: Creating coalescence radius for hydrogen isotopes in 120 MeV/Areactions. ^{112}Sn is provided on top and ^{124}Sn on the bottom.
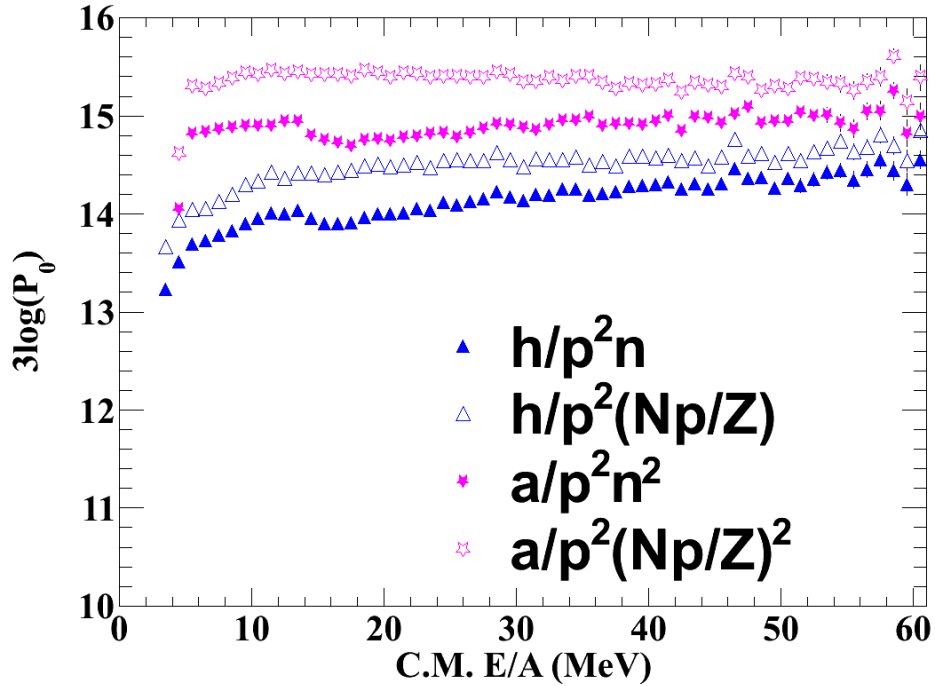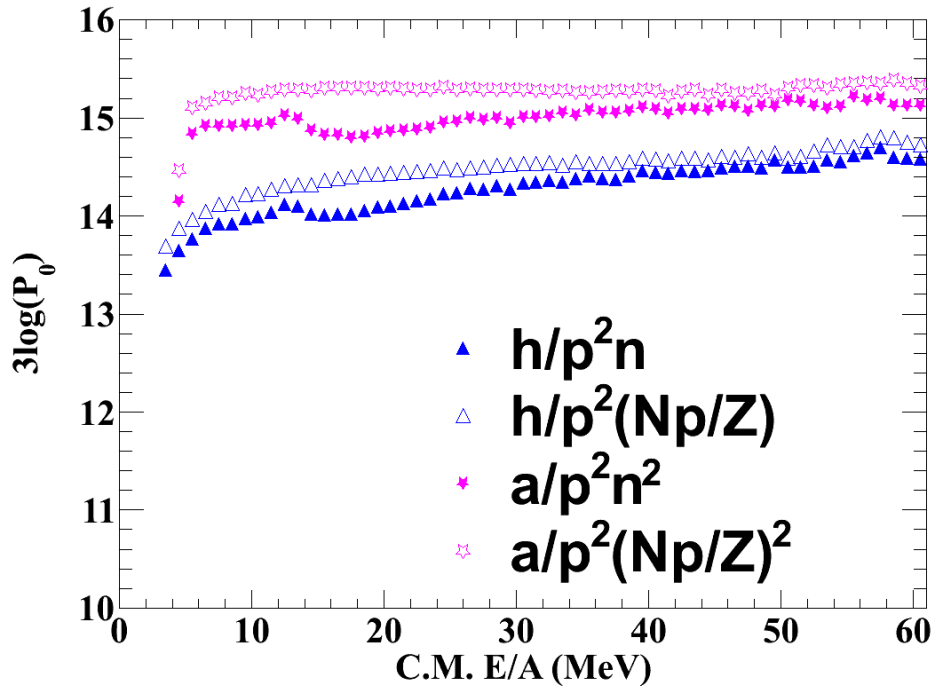
Figure 5.44: Creating coalescence radius for helium isotopes in 120 MeV/Areactions. [112]Sn is provided on top and [124]Sn on the bottom.
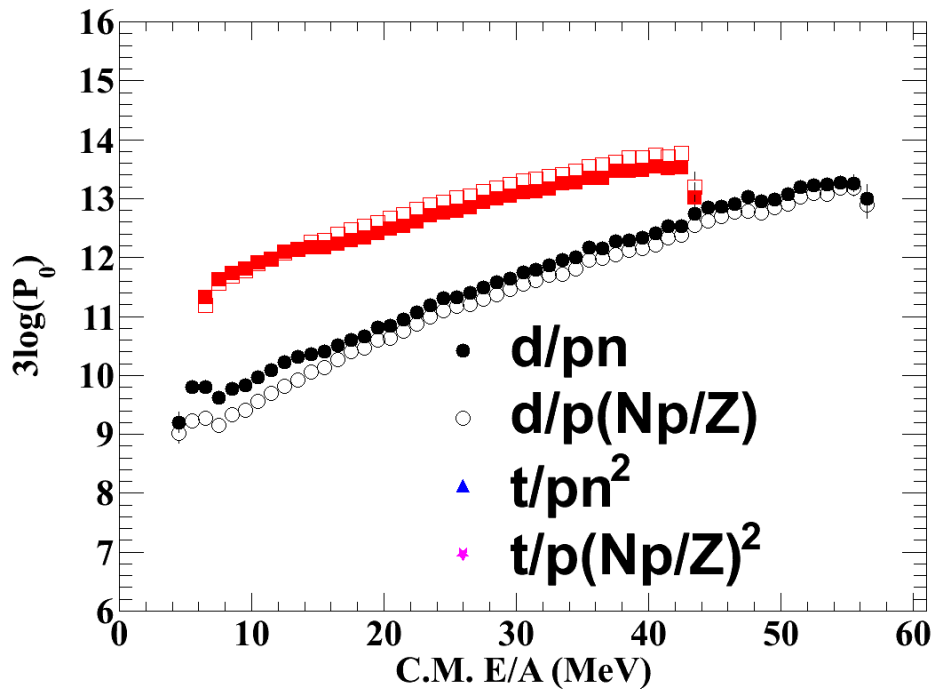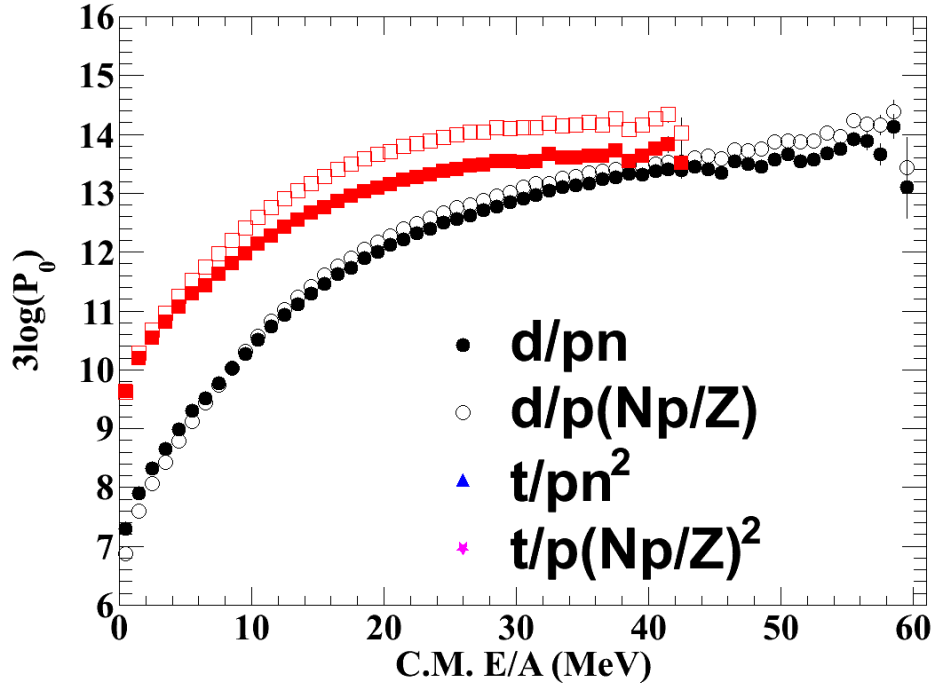
Figure 5.45: The coalescence radius for hydrogen isotopes in 50 MeV/A(top) and 120 MeV/A(bottom) for the ^{124}Sn system. The ^{112}Sn system shows a very similar trend with slightly better agreement.
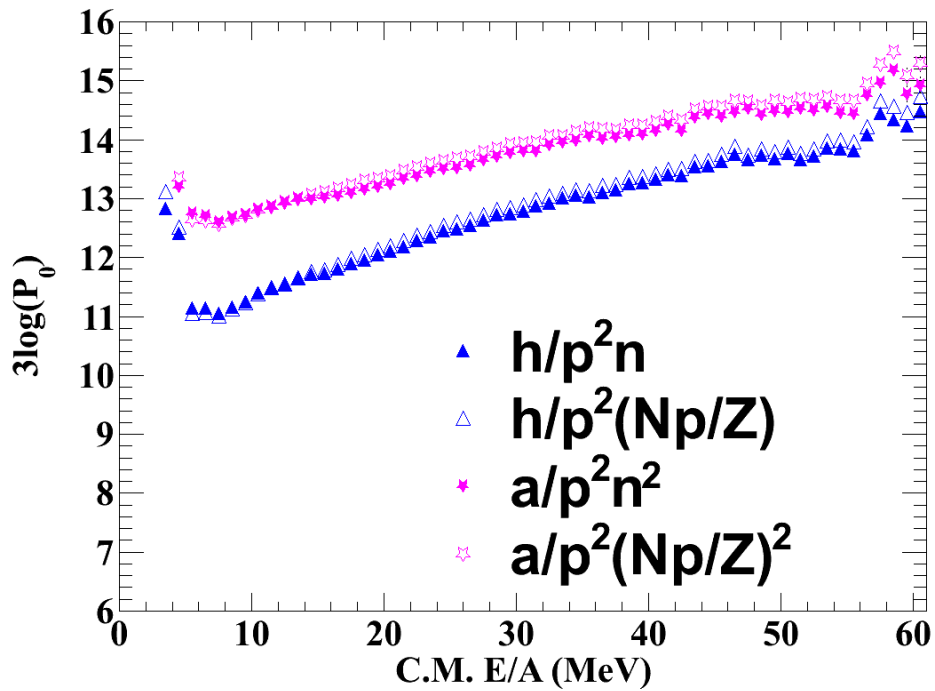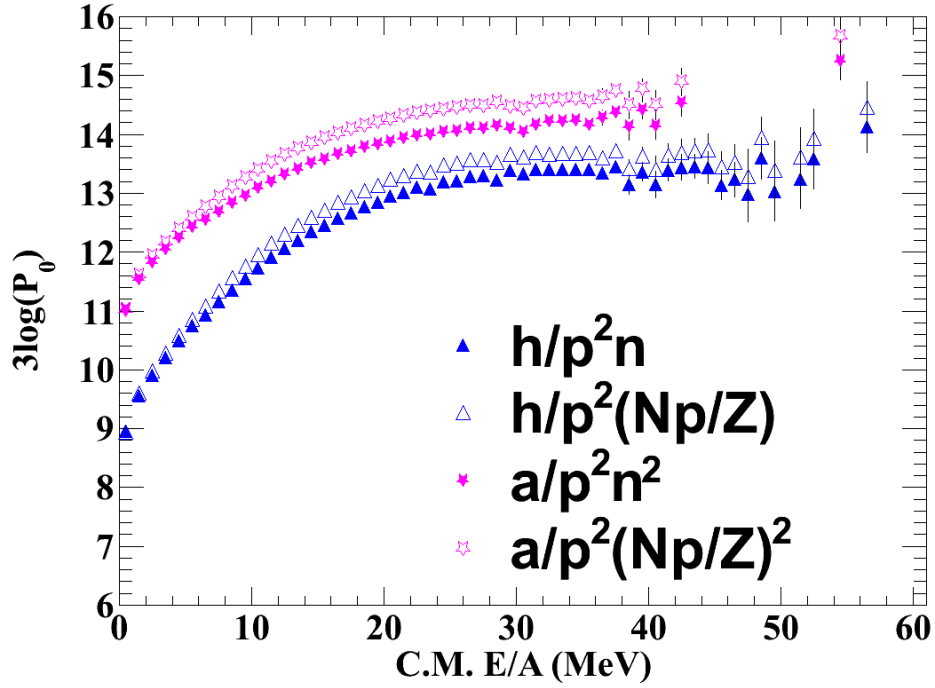
Figure 5.46: The coalescence radius for helium isotopes in 50 MeV/A(top) and 120 MeV/A(bottom) for the ^{124}Sn system. The ^{112}Sn system shows a very similar trend with slightly better agreement.
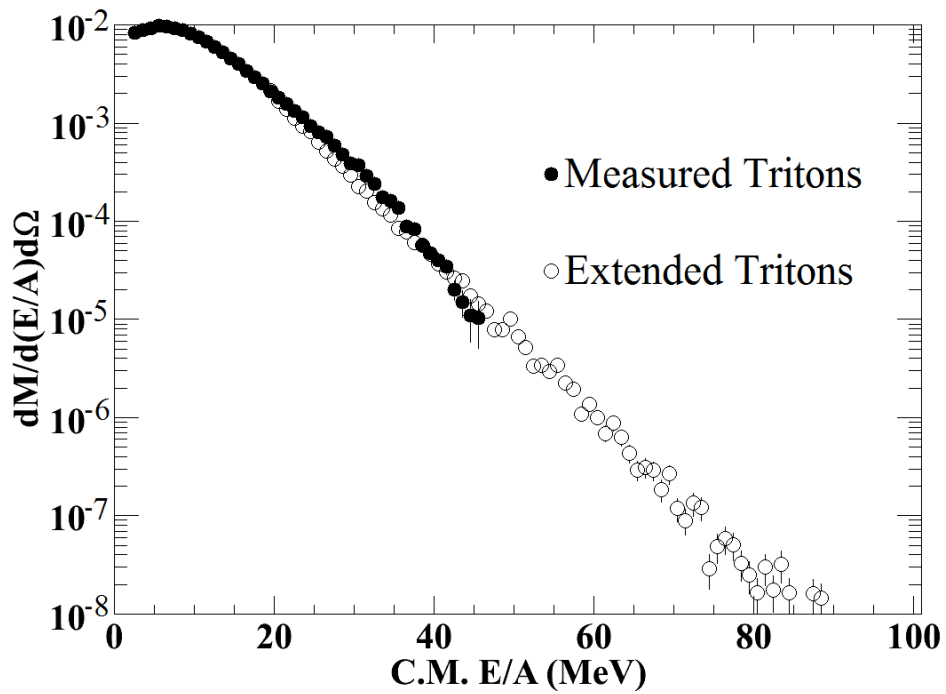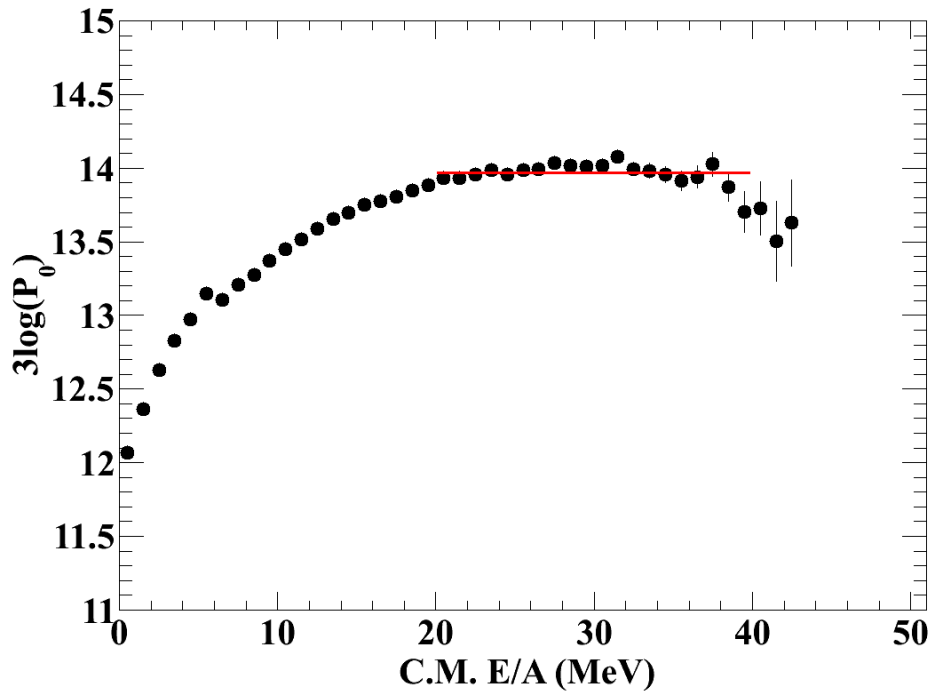
Figure 5.47: (Top) The $3 \log P_0$ for ^{112}Sn tritons. (Bottom) The extended triton spectra using the high energy neutrons and protons.

5.4 Independent Particle Ratios

Now we want to look at the dependence of the emission of various members of isospin multiplets with regard to the asymmetry of the system. We start by looking at the independent particle ratios similar to what was done in Chapter 4. Figure 5.48 shows the independent particle ratios, i.e. $Y_{124}(X)/Y_{112}(X)$ where X is a given isotope, for both energies. Details of the neutron analysis can be found in [1].

Several trends arise in this figure. Firstly, the symmetric deuteron and alpha particles show almost identical spectra between the two systems, i.e. their particle ratio is one. This may be expected since these particles would be unaffected by the symmetry energy. At high energies these ratios increase slightly, which may be due to the larger neutron number in the ^{124}Sn system and the fact that neutron emission removes excitation energy from the system and has been known to effect the spectra of charged fragments. We find that the proton and ^{3}He ratios are nearly identical. This seems to coincide with the prediction that the ^{3}He behaves similar to a proton reflecting that difference in the chemical potential of ^{3}He between the two systems is equal to that of protons. In the coalescence model from Section 5.3, this ratio would have been predicted to be,

$$\frac{^3\text{He}_{124}}{^3\text{He}_{112}} = \frac{n_{124}}{n_{112}}\frac{p_{124}}{p_{112}}\frac{p_{124}}{p_{112}} = \frac{d_{124}}{d_{112}}\frac{p_{124}}{p_{112}} = \frac{p_{124}}{p_{112}}, \tag{5.14}$$

assuming that the deuteron ratio was 1. The triton ratio is similar, though not equal, to that of the neutrons at either energy. The discrepancy is on the order of 15% which is comparable to the present uncertainties in the neutron efficiency. The fact that the triton and neutron (as well as ^{3}He and proton) ratios agree over the full energy range while the
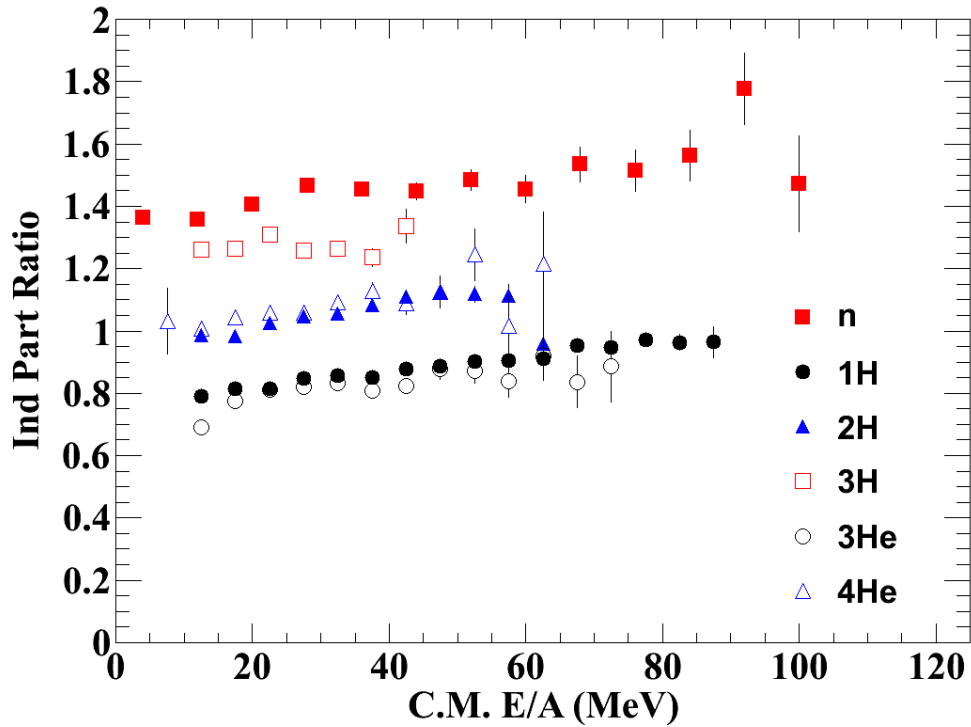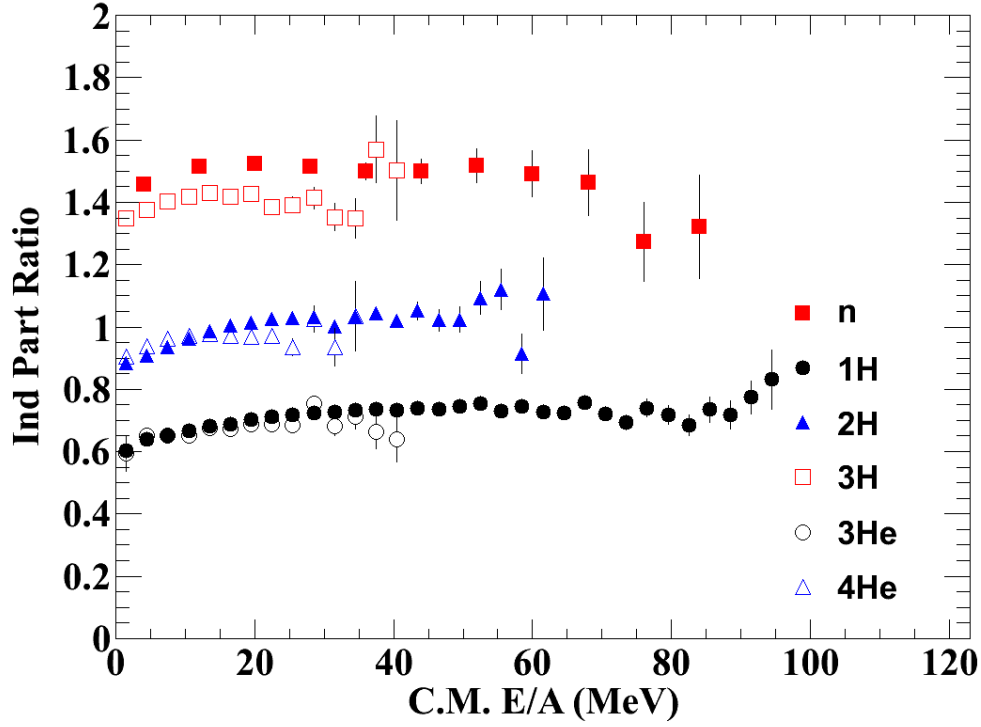
Figure 5.48: The independent particle ratios for 50 (top) and 120 (bottom) MeV/A for impact parameters less than 3 fm.

simulated results from Chapter 4 disagree at low energies is rather interesting. It appears that the chemical potentials of those particles not represented as equally in the theoretical prediction as they are in experiment.

The nearly identical values over the entire energy spectrum of the independent particle ratios for protons and ^{3}He as well as neutrons and tritons was not observed in the pBUU calculations in Chapter 4. Only at high energies did these ratios agree.

5.5   Spectral Ratios of Mirror Nuclei

Investigating ratios across systems provides some information about the symmetry energy but more sensitivity can be obtained from the ratios and yields involving the particles that have $t_3 \neq 0$ and are more strongly sensitive to the symmetry energy. For example, the neutron to proton ratios have such sensitivity and were studied in [1]. Here, we will examine complementary information from charged particle ratios. Information that is very complementary to the n/p ratios can be obtained by constructing ratios of the spectra of neutron-like tritons and proton-like ^{3}He. These t/^{3}He spectra can be seen in Figure 5.49 for both beam and energy combinations.

Instead of creating ratios of spectra for one particle type measured in two different systems, we examine the ratio of triton to ^{3}He yields in the same system. Figure 5.50 shows the t/^{3}He ratios for both the ^{112}Sn and ^{112}Sn systems for both beam energies. The top plot in the figure shows the ratios for these two systems at particle energies where we have measured tritons and heliums. Later we will construct coalescence invariant neutron to proton ratios. There we would like to explore the effect of extending the triton spectra to higher energy. For this purpose, we have used the asymptotic behavior of the
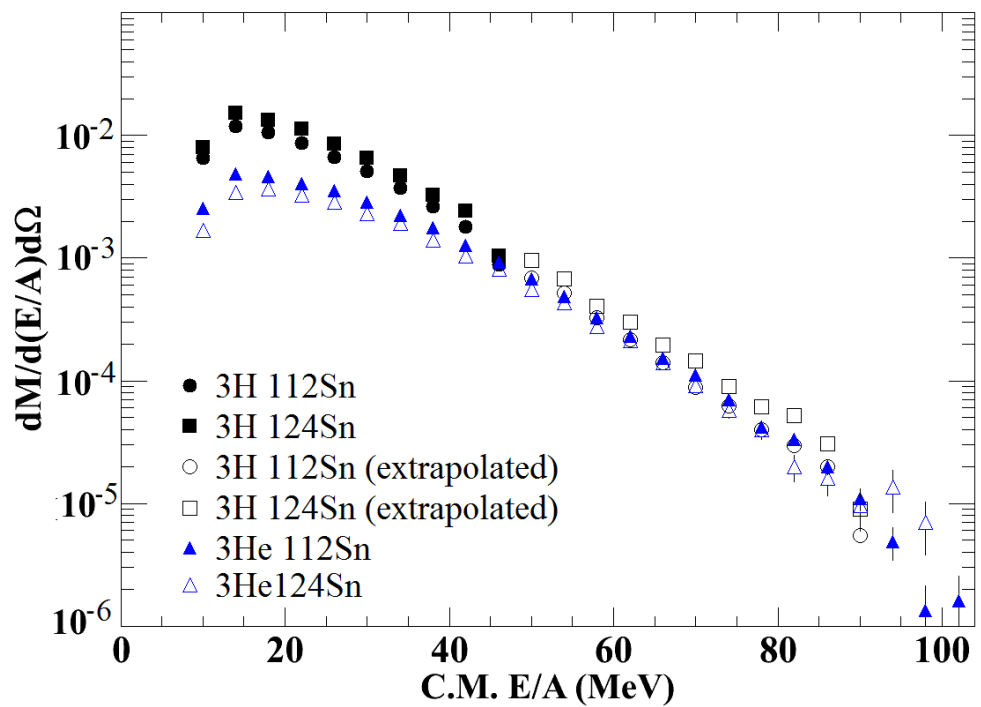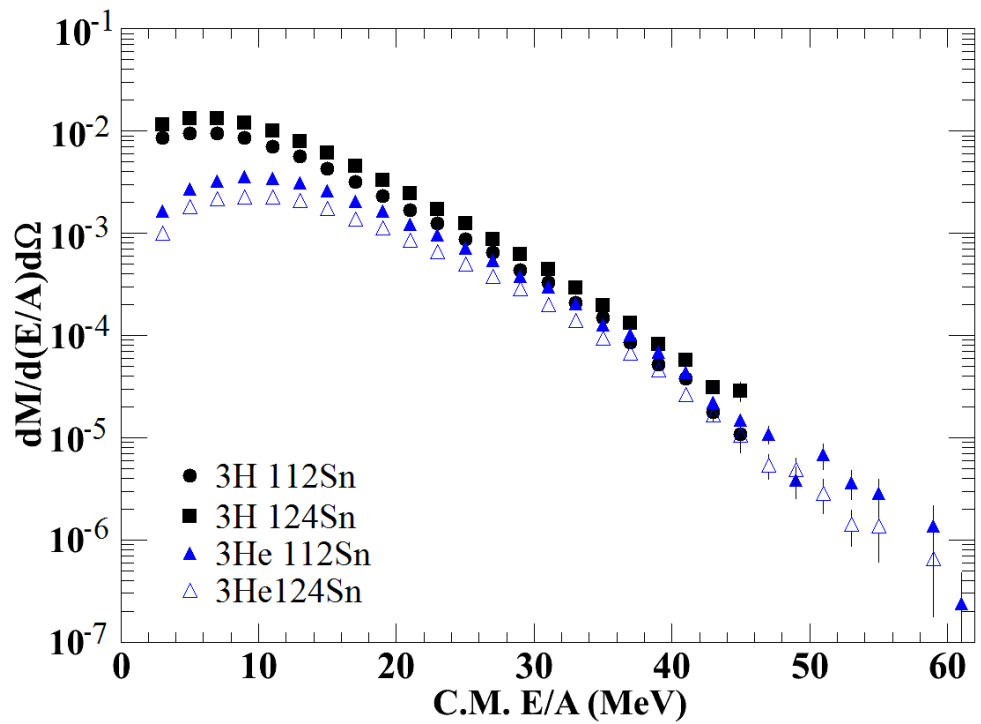
Figure 5.49: First step spectra for building the t/^{3}He ratios. 50 MeV/Areaction data is on top and 120 MeV/Adata on the bottom. Included in the 120 MeV/Aspectra are extrapolations using the coalescence model up through the region where there is reasonable ^{3}He as well.

coalescence radius to extend the tritons to energies comparable to the measured ^{3}He using the process described in Section 5.3. The bottom plot shows the ratios where we have extrapolated the tritons to higher energies.

As we discussed in the efficiency section, different particles have different efficiency corrections, primarily due to the influence of punch throughs, and from some effects that vary from system to system such as the "blue haze" correction or the silicon and CsI corrections. We find that magnitude of these effects are still quite similar between the two systems at the same energy. In this case, constructing double ratios ensures that the associated systematic corrections in these effects largely divide out in the ratio and its associated uncertainty is reduced. The t/^{3}He double ratio is shown in Figure 5.51. The top panel shows the ratios constructed from the measured tritons and heliums while the bottom plot shows the ratios with extrapolated tritons. At first glance we can see that the trend between the two systems is relatively similar to that between the neutrons and protons in [1]. Later in this chapter we will compare both these ratios to simulation from Chapter 4. In similar fashion to the results from pBUU and the n/p ratios the data from the 120 MeV/Asystem is lower in value, suggesting less of an effect from the symmetry energy than the 50 MeV/Areaction.

5.6   Effects of Impact Parameter Determination

All the results displayed so far have used events with an impact parameter of b<3 fm where the determination was selected using multiplicity in the Miniball. This was chosen to keep the protons consistent with those used in [1] for n/p ratios. We would like to test the effect of determining the impact parameter through transverse energy in the Miniball instead
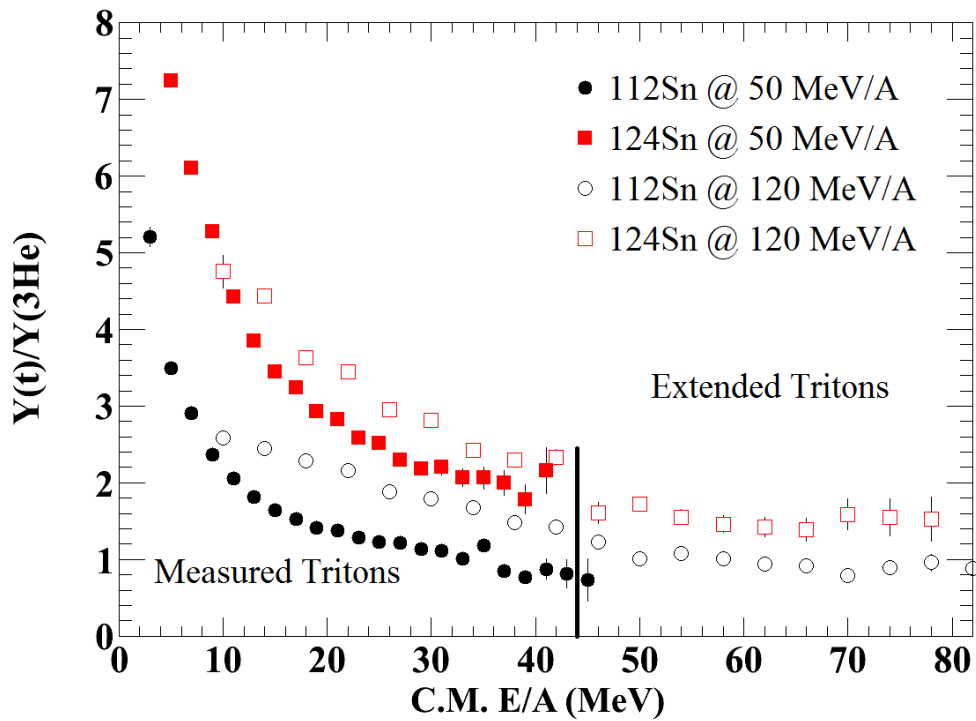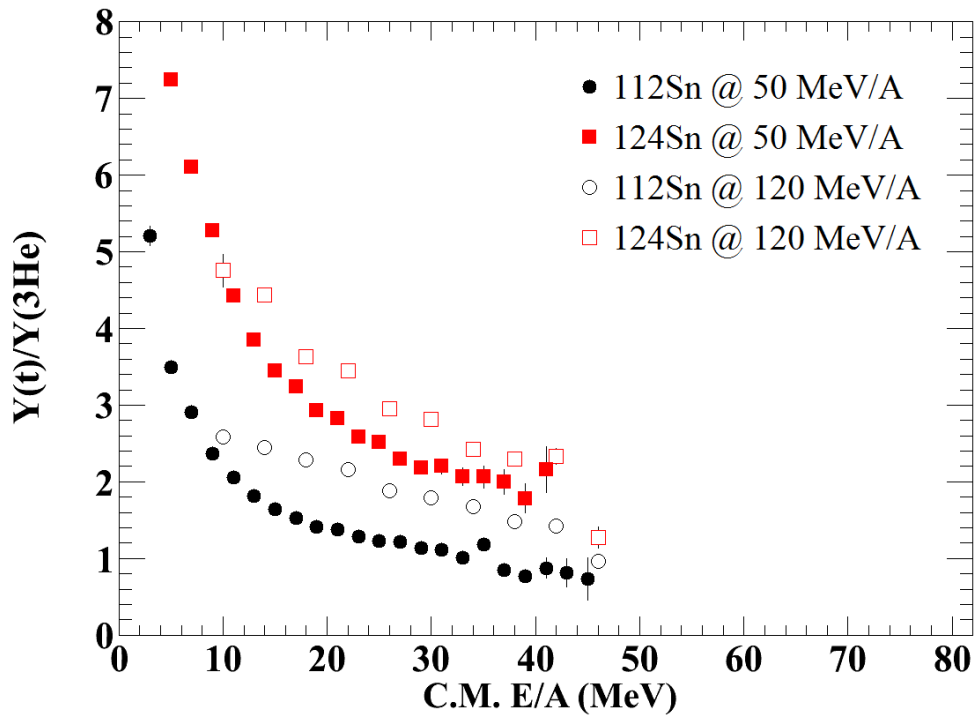
Figure 5.50: The single $t/^3\text{He}$ ratios for all four systems and energies. The top plot shows only measured tritons, whereas the bottom plot includes extrapolated tritons using a constant value for the coalescence radius at high energies as described in Section 5.3
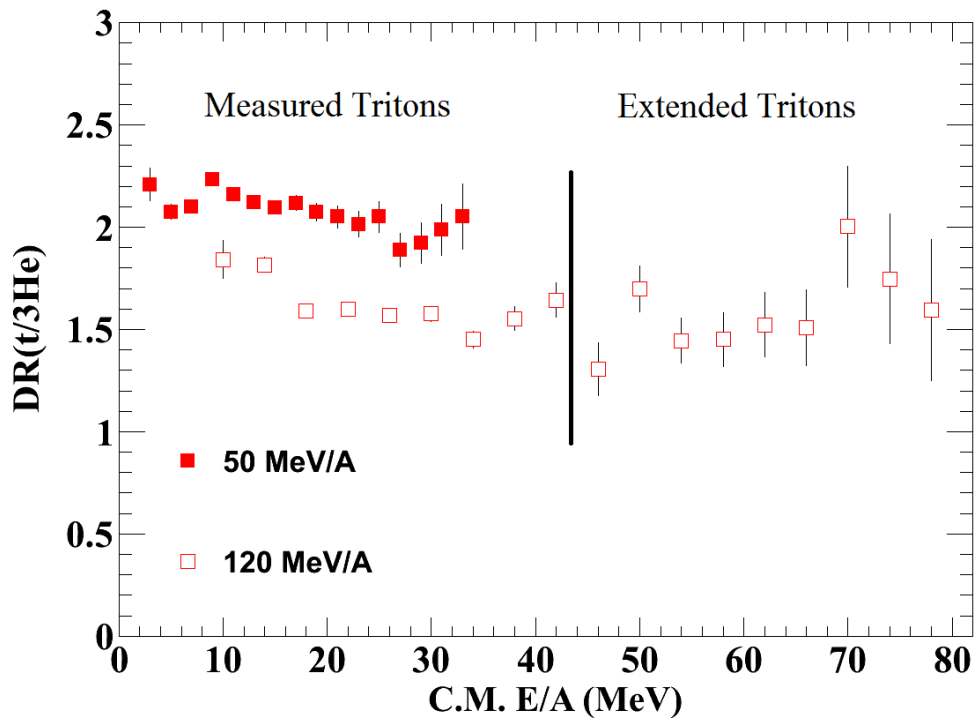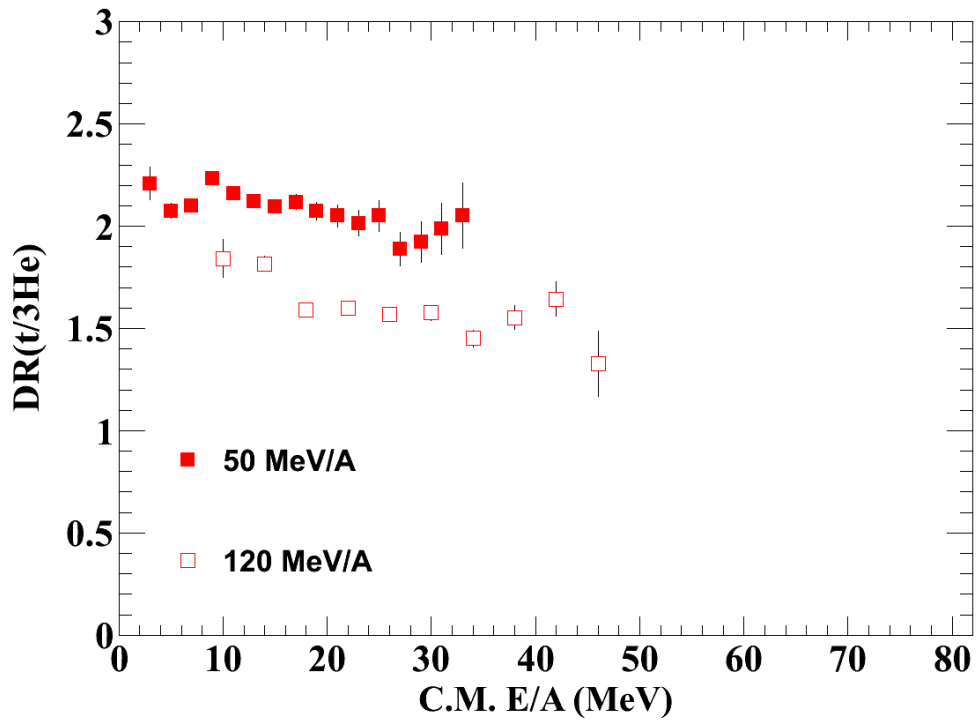
Figure 5.51: The double t/^{3}He ratios for both energies. The top plot includes only measured tritons, whereas the bottom plot includes extrapolated tritons using the coalescence model.

of multiplicity. The transverse energy determination allows us to more finely select the impact parameter. To make sure that we compare the same region, we select the minimum transverse energy to coincide with the same $\hat{b}$ as with charged particle multiplicity. As an added comparison, we also include data that are deemed central by both multiplicity and transverse energy. In this section we will investigate the differences between the spectra of both central and mid peripheral collisions as well as the differences between the different impact parameter selection procedures. Figure 5.52 shows the comparison of proton spectra from ^{112}Sn using different choices of centrality determination method. There is relatively little sensitivity (less than 10% effect) to this choice of centrality. The t/^{3}He single and double ratios show even less sensitivity as displayed in Figure 5.53. While the determination of centrality through transverse energy does seem to suggest a selection of events with larger transverse momenta and higher temperature, it has little influence over the ratios. In order to make comparisons to data in [1] we choose to use charge particle multiplicity for the rest of this treatment.

5.6.1 Mid Peripheral Spectra and Ratios

Our previous discussions have focused on data from central collisions, $b \leq 3$ fm. We also measured more peripheral events at impact parameters ranging from $3 < b \leq 6$ fm. Due to the restrictive nature of the trigger in the experiment which was chosen to maximize statistics of central events, low multiplicity events that would correspond to more peripheral events were not measured.

We recall that the results of spectra in the midrapidity region predicted by pBUU simulations in Chapter 4 did not display a strong sensitivity to impact parameter. We do
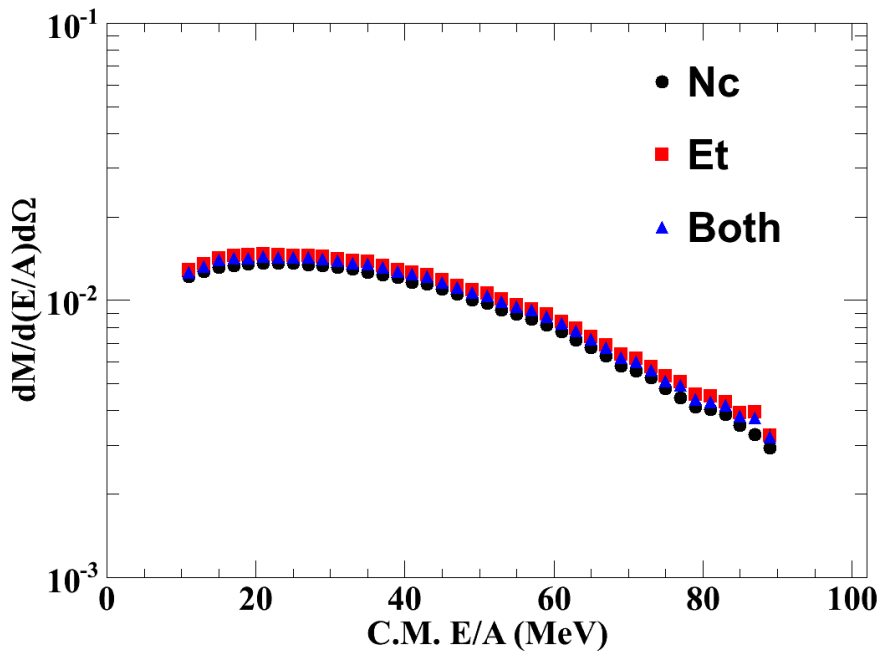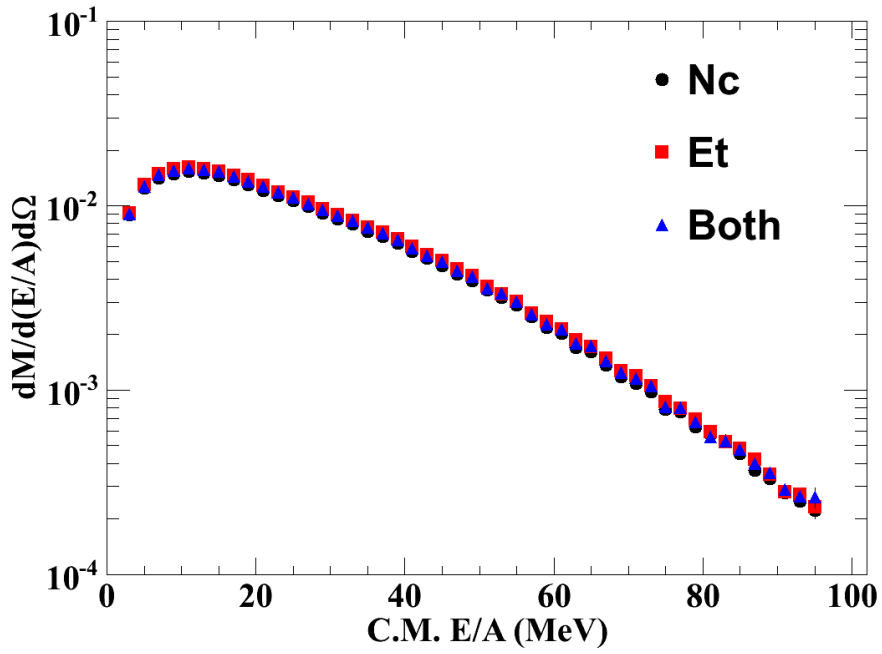
Figure 5.52: Effects of impact parameter determination. Spectra from 50 MeV/Aare on the top and 120 on the bottom. Proton spectra from [112]Sn are shown. The different particles provide a similar comparison.
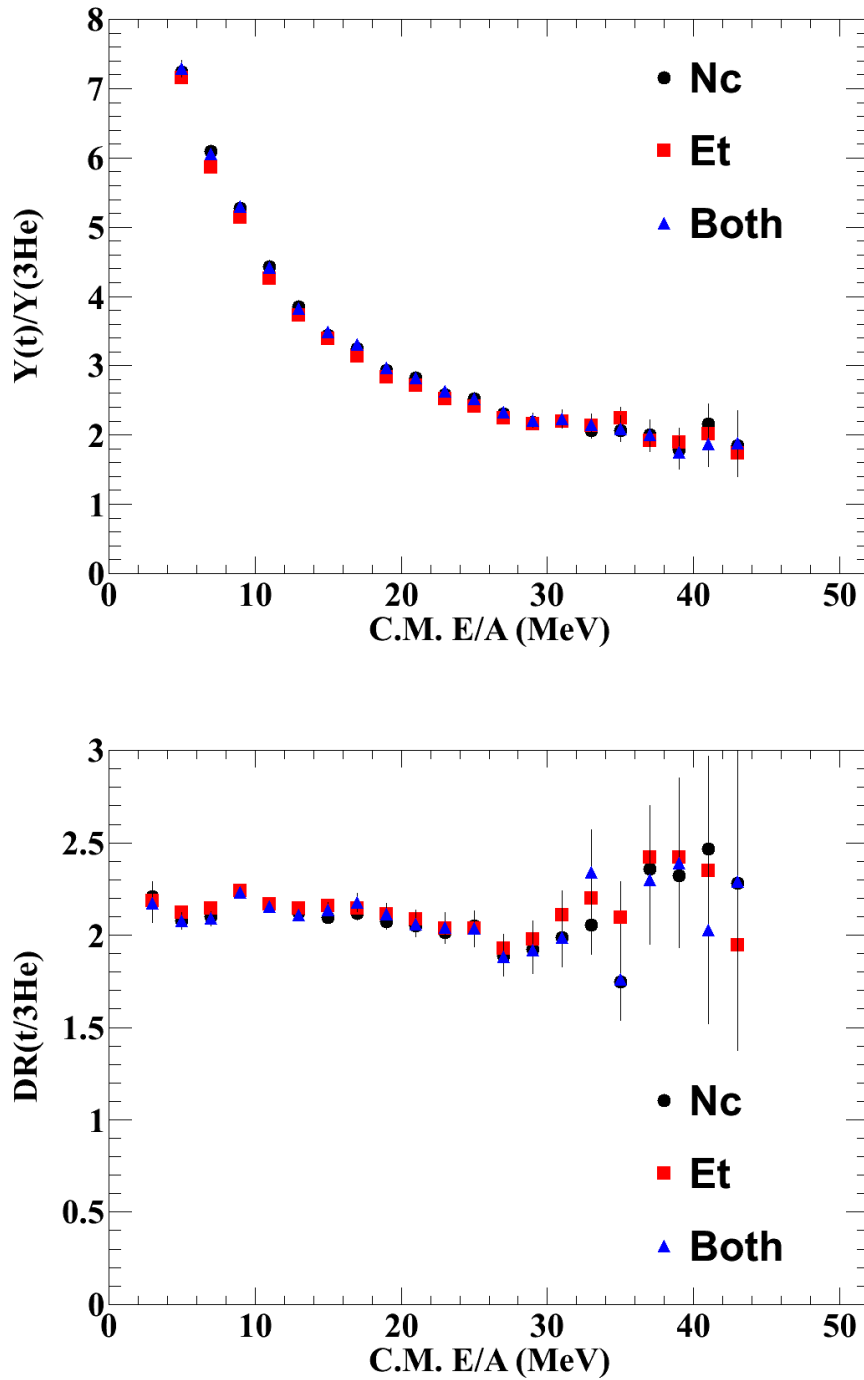
Figure 5.53: Effects of impact parameter determination. t/^{3}He single ratios from ^{124}Sn are shown on top with the t/^{3}He double ratios on the bottom. Both are from the 50 MeV/Areaction.

anticipate a decrease in the magnitude of the spectra with increasing impact parameter, but the shape to be quite similar. Figures 5.54 and 5.55 compare the measured spectra of protons and alpha particles from the central and peripheral collisions using charged particle multiplicity as the selected method of impact parameter determination. In the figures, protons are provided on the top with alphas on the bottom. The heavier particles are affected more by the centrality dependence than the lighter protons. Similarly, the centrality cut has a larger effect at the higher beam energy.

The t/^{3}He single and double ratios are also relatively unchanged by the determination of impact parameter. Figure 5.56 shows the single ratios from the ^{124}Sn reaction (top) and the double ratios (bottom) from the 50 MeV/Areaction. The 120 MeV/Areaction can be found in 5.57.

5.7   Comparison to Previous Data

The objective of this dissertation is of course to compare the data to simulation and attempt to constrain the symmetry energy. Before proceeding to that end, it is prudent to compare the current results to previous measurements. The 120 MeV/Areaction was chosen because it was a new energy regime for this measurement, however the 50 MeV/Areaction was measured at least twice previously in [24, 31]. Figure 5.58 shows the comparison of the single ratios between the three experiments while Figure 5.59 shows the double ratio comparison. The three experiments show good agreement in the double ratio with this experiment being able to achieve significantly better statistics than either of the previous measurements and even increase the energy range at which they were measured. It is curious that the single ratios between the Liu data (red squares) deviate from the other
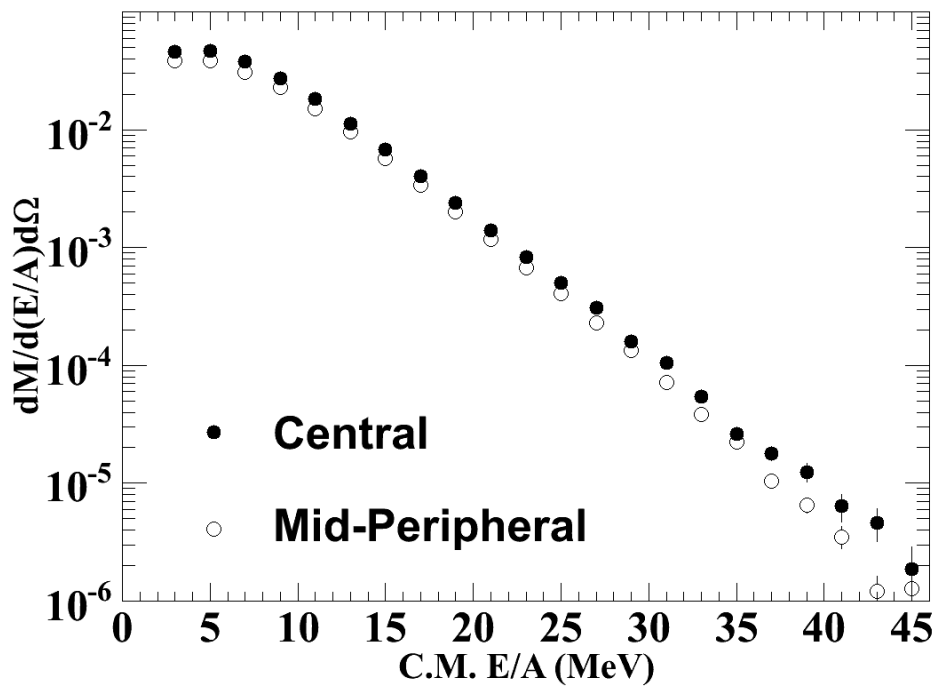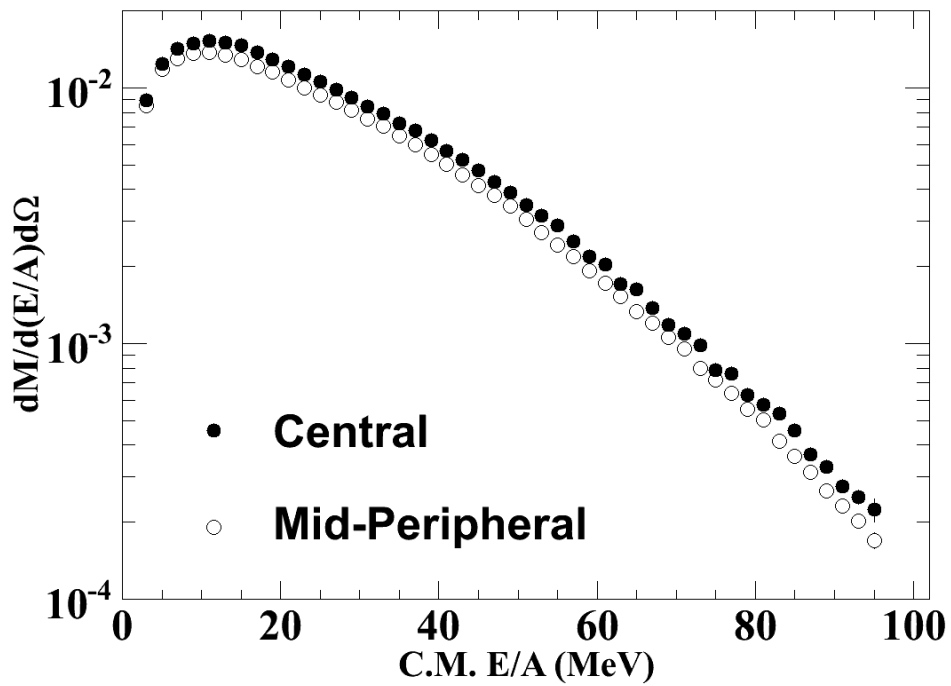
Figure 5.54: A comparison of the mid peripheral and central cuts for protons (top) and alphas (bottom) at 50 MeV/Ain the ^{112}Sn reaction. The other particles behave in a similar fashion.
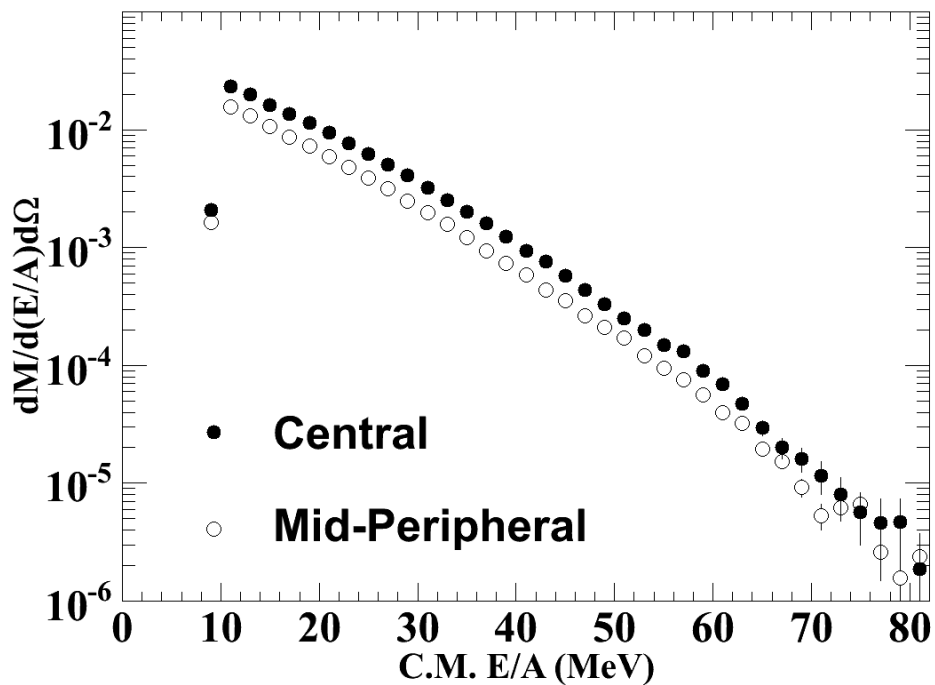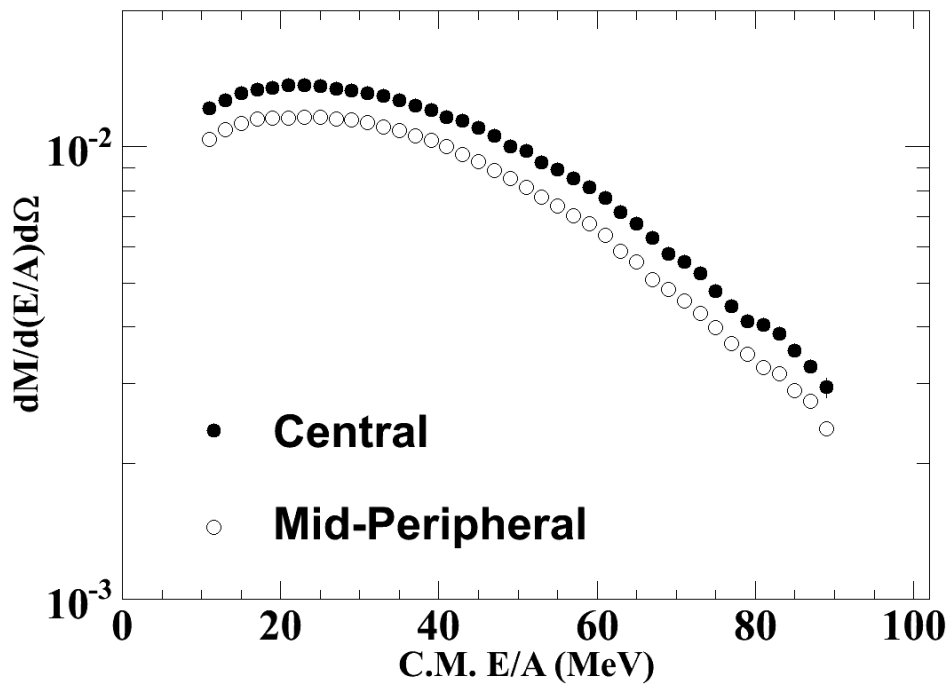
Figure 5.55: A comparison of the mid peripheral and central cuts for protons (top) and alphas (bottom) at 120 MeV/Ain the ^{112}Sn reaction. The other particles behave in a similar fashion.

209
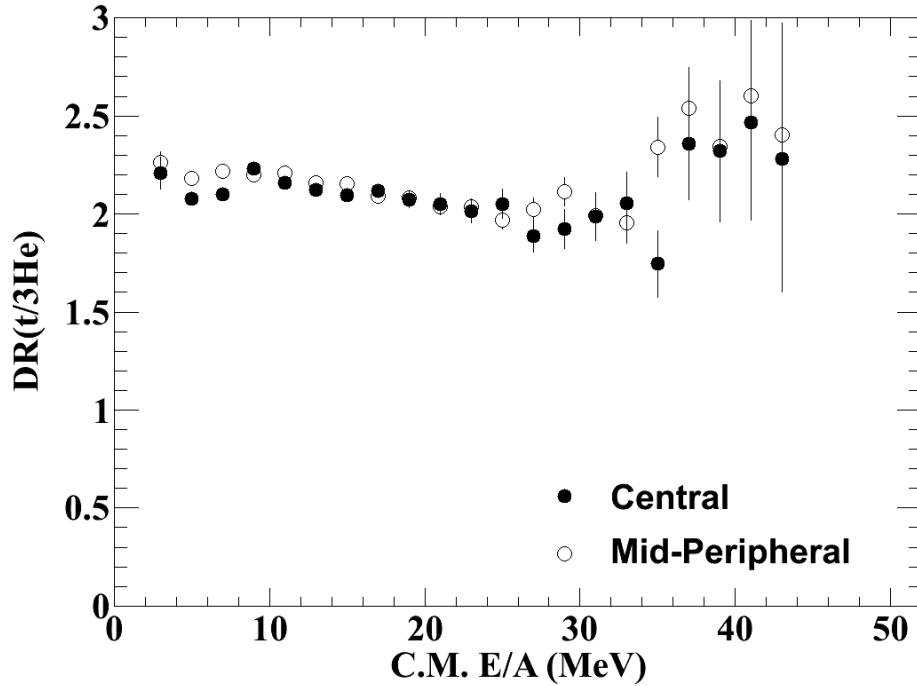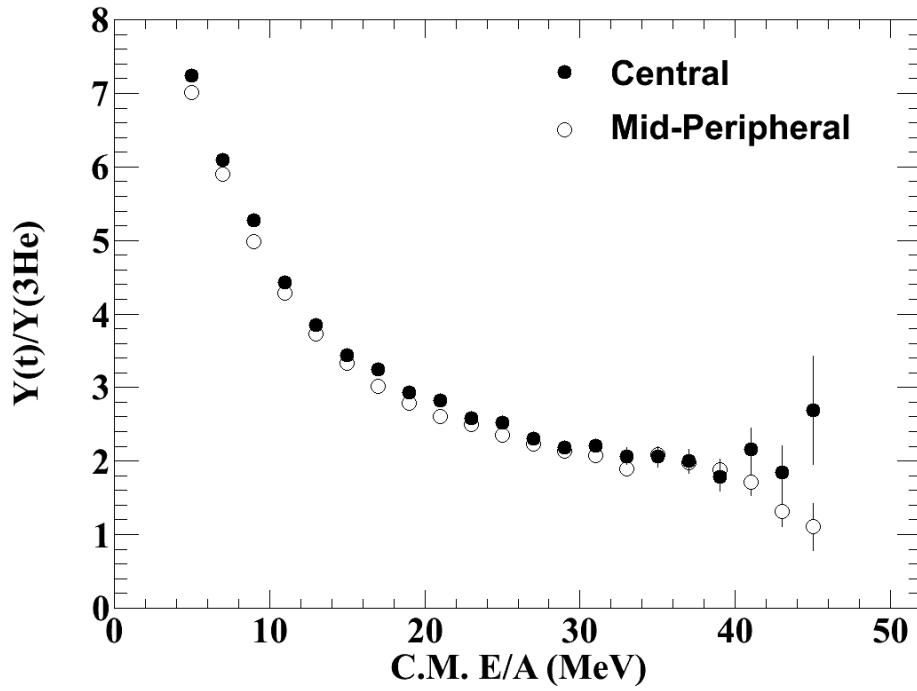
Figure 5.56: The single t/^{3}He (top) and double (bottom) from the 50 MeV/Areaction. The single ratios come from the ^{124}Sn reaction.
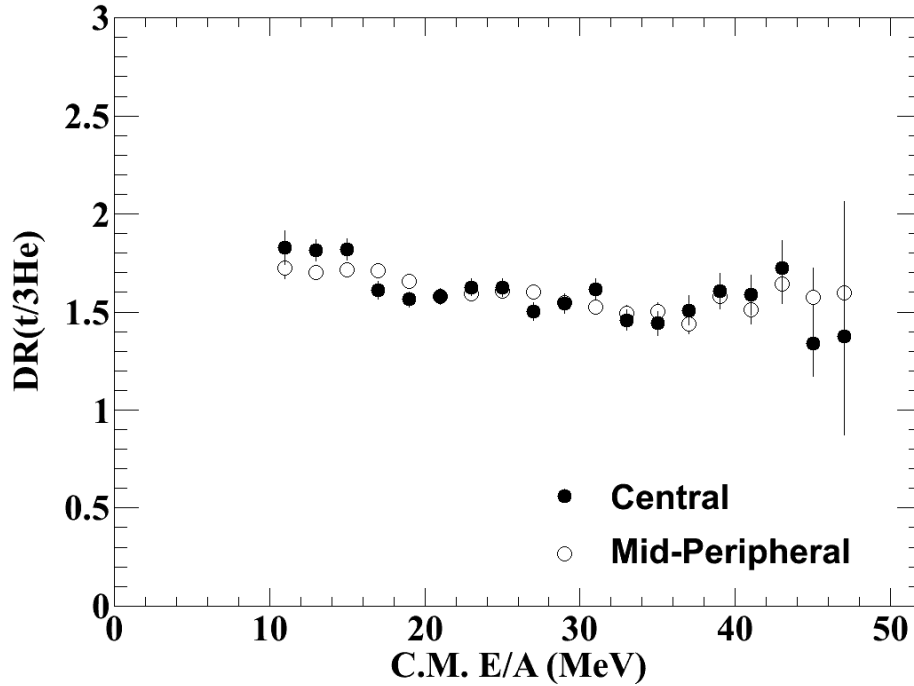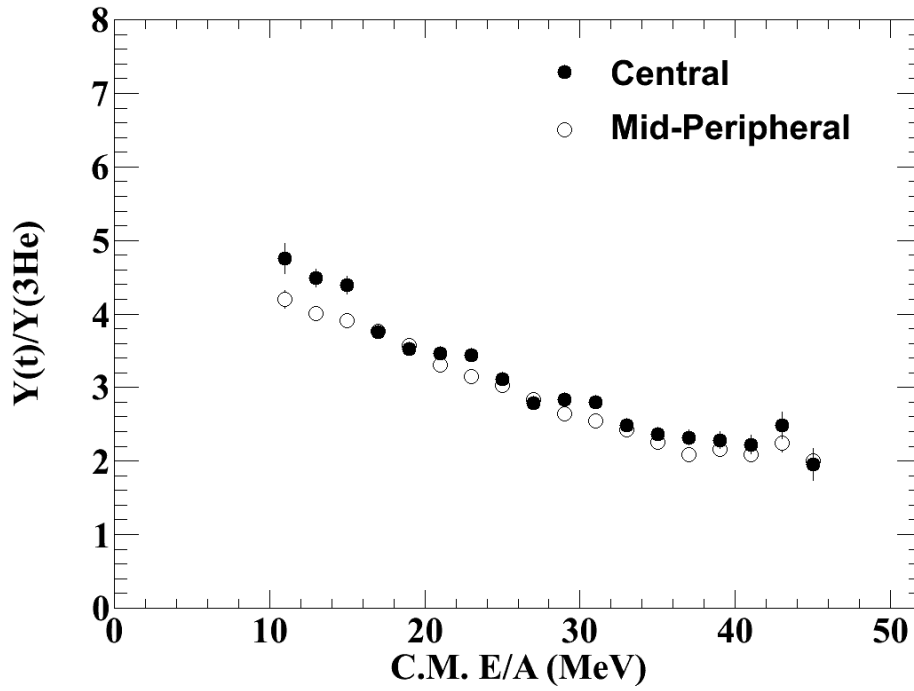
Figure 5.57: The single t/^{3}He (top) and double (bottom) from the 120 MeV/Areaction. The single ratios come from the ^{124}Sn reaction.

211

two while the double ratios show excellent agreement between all three measurements. Where available, we were also able to show good agreement between the independent particle ratios from the previous experiments and our current data as seen in Figure 5.60. So it appears that the only discrepancy is seen in the single t/^{3}He ratios.

In an attempt to understand the discrepancy in the single ratios between the Liu data and the new data, we investigated the original spectra for tritons and ^{3}He which can be found in Figure 5.61. The trend is that the previous data has a larger differential multiplicity at low energy and then falls off significantly faster than the new data. This is either due to a difference in the energy calibration or the efficiency between the two experiments.

At this point, a few comments regarding the previous experiment of Liu are prudent. That particular experiment was optimized for Intermediate Mass Fragments (IMF) in the range of $3 \leq Z \leq 10$ which required running the silicon electronics at relatively low gain resulting in efficiencies of hydrogen isotopes significantly less than one. Calibrations in that experiment used a cocktail beam which provided very good calibration for the IMFs. The calibration of the light particles were less extensive and the inefficiency in the silicon electronics are expected to produce too few hydrogen (and possibly helium) particles at high energy in the lab frame. The non-linear effects in the light output of the CsI crystals were parameterized in that experiment and were used previously in the energy calibration of the current experiment.

Assessments of the consistency of the energy calibrations should, in principle, be performed through comparisons in the lab frame. At present, only data in the center of mass frame is available from that experiment which renders interpretations of the

212
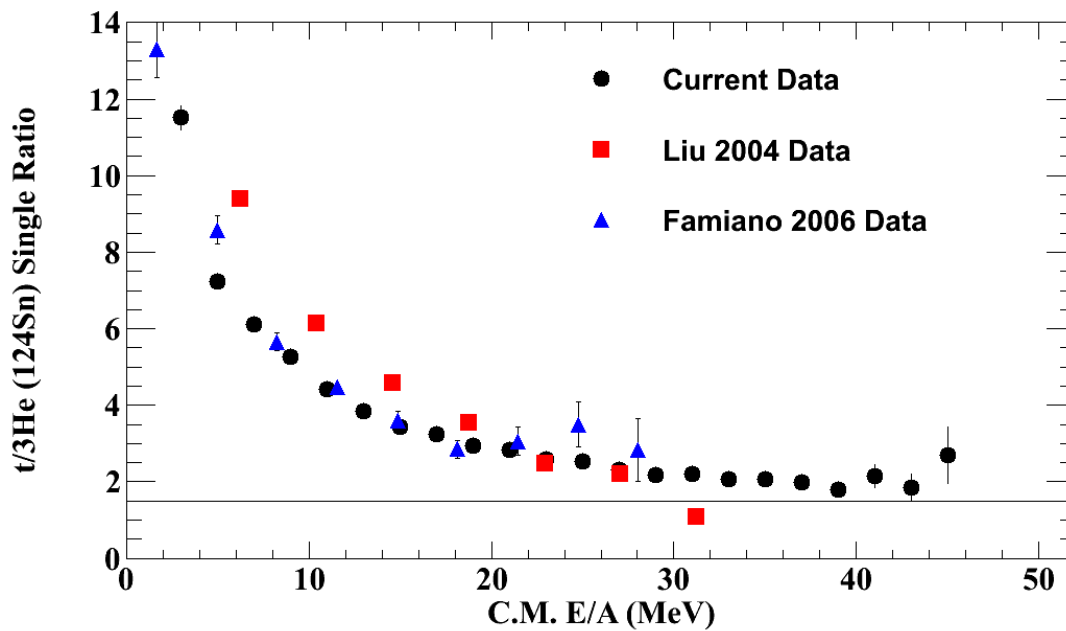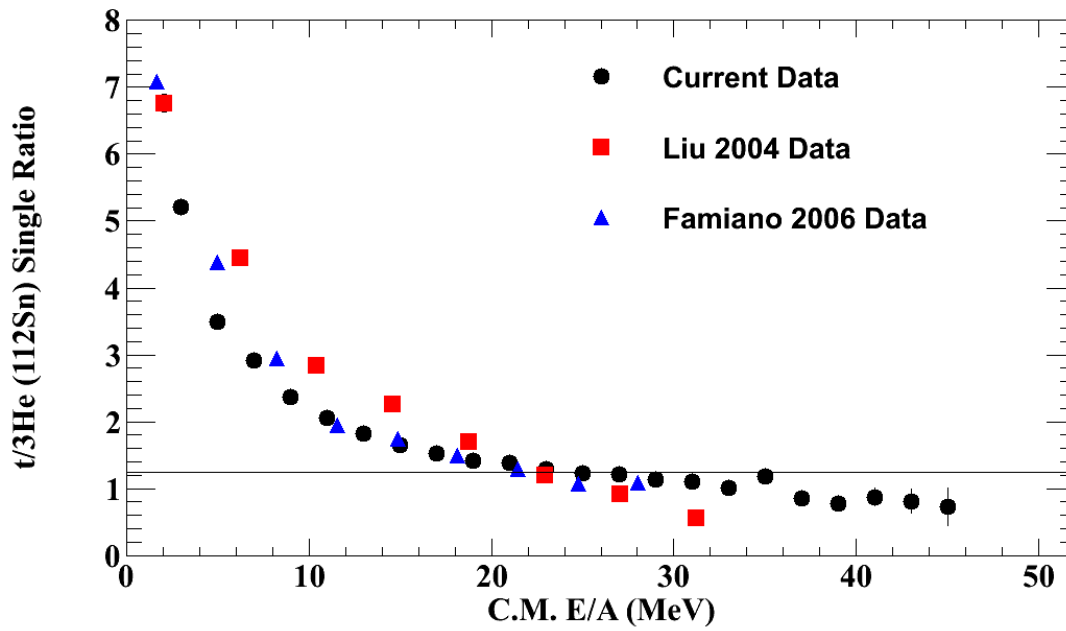
Figure 5.58: The single ratios for ^{112}Sn (top) and ^{124}Sn (bottom) of this experiment's data compared with two previous measurements.
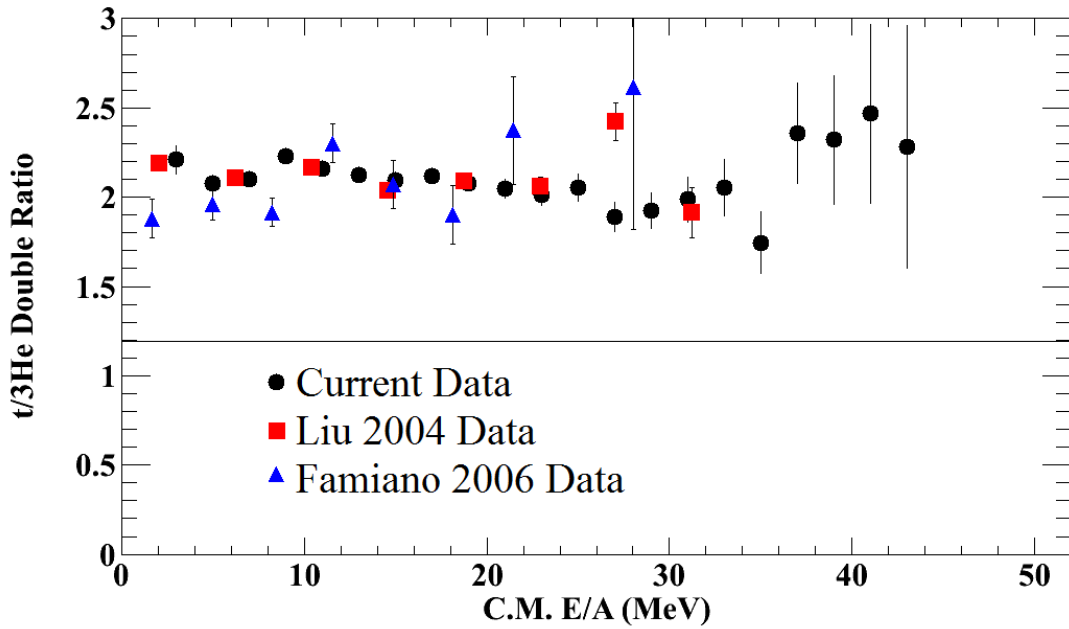
Figure 5.59: The double ratios of this experiment's data compared with two previous measurements.
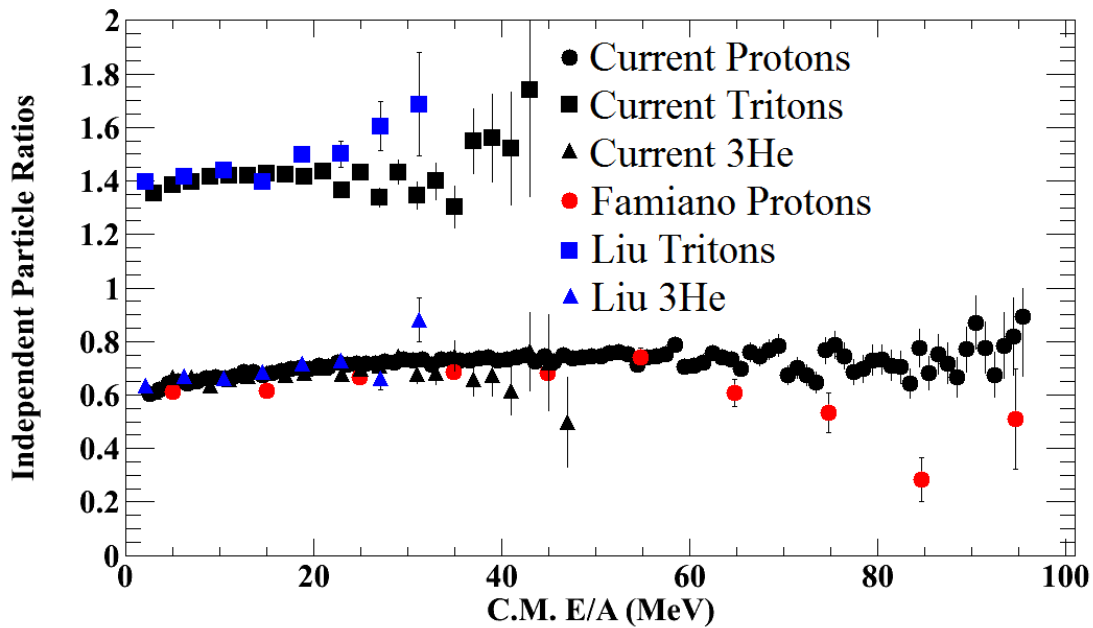
Figure 5.60: The independent particle ratios comparing current data to previous experiments where available.

214
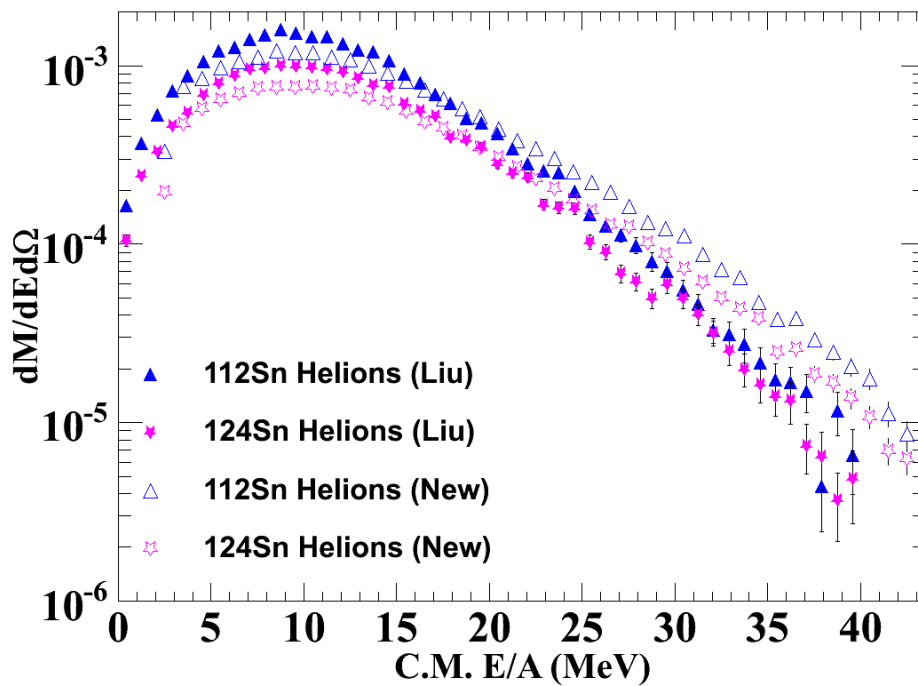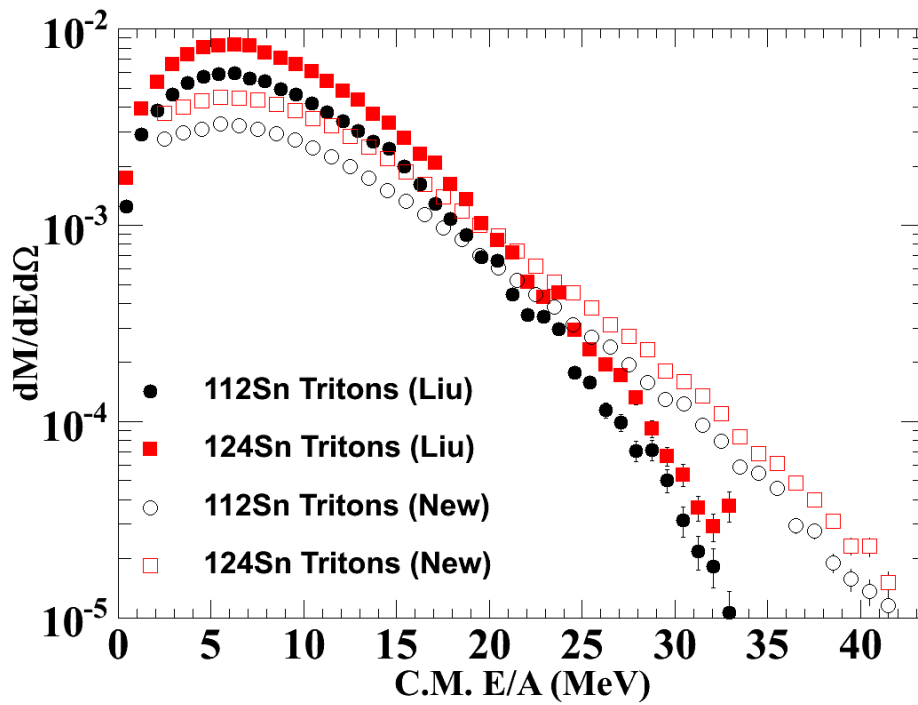
Figure 5.61: The comparison of the new tritons and ^{3}He with previous data. Tritons are represented in the top plot with ^{3}He in the bottom.

descrepancies somewhat tenuous. While some of the differences in the spectra could be partly related to a problem in the energy calibration of one or the other experiments, the large differences in the triton energy spectra at around E=8 AMeV probably originate in the efficiency calculations used for the data of Liu. We do not currently know how carefully the efficiency calculations were checked for light particles in this older data set. Due to the known inefficiencies in the proton spectra, Liu did not explore this ratio extensively in his thesis and thus a more complete checking may not have been completed. The efficiency for the IMFs on the other hand was extensively checked.

If there was an error in the efficiency calculation for the older data set it would influence both reactions. The independent particle ratios and double ratios would have this efficiency effect divide out and thus we would expect both of those results to match with the current data. The $t/^{3}$He results however would show this effect, and indeed this is where the difference between the two experiments is highlighted. On the other hand, we do see approximate agreement between the current experiment and the results of Famiano where the statistics of the latter experiment allows [24].

Several cross checks were completed in order to check the energy calibration of the current data. If the energy calibration were too high for example and we lowered the energy, we might expect an increase in low energy data. As a test, the lab energy was reduced by factors of 5, 10 and 15%. This did indeed change the spectra so that the shape was more similar to the old data. Unfortunately it was still unable to recreate the magnitude of the spectra, being consistently too low across the energy spectrum. Since we have no proof that our energy calibration is off we do not go through the process of trying to match the old data this way. Nevertheless, we will emphasize the double ratio

and independent particle ratios in the rest of this treatment since efficiency and calibration errors cancel out in these ratios to first order.

The other possible difference between the data could originate from differences in impact parameter. The previous data uses a reduced impact parameter of $\hat{b} < 0.2$, whereas the data quoted in this work uses a reduced impact parameter of something slightly larger. We have already shown that the magnitude of the spectra have little sensitivity to the impact parameter. There is also a negligible change in shape of the spectra as the method of selection or centrality changes. Given these results, we believe that the discrepancy between these data do not originate from the impact parameter selection.

5.8   Comparison to Simulation

One objective of this dissertation is to compare the data to simulations with the purpose of better constraining the symmetry energy. Chapter 4 showed the relatively low dependence of t/^{3}He ratios on momentum dependence and in-medium cross section. We choose momentum independent simulations with the Rostock in-medium cross section to compare to our data. The choice of momentum independence was chosen to maximize statistics without the expense of the time the momentum dependent calculations require. Since the momentum dependent calculations are more physically complete, a momentum dependent set of calculations would be used for a more realistic constraint, however, given the diminished sensitivity of the ratios to the choice of momentum dependence in comparison to the sensitivity of the symmetry energy, the momentum independent calculations will suffice for this treatment. Since we will be looking primarily at the clusters, obviously a cluster producing simulation is used. Comparing the spectra from experimental data

and pBUU simulations from Chapter 4 it is immediately obvious that the two do not match. Regardless, Figure 5.62 shows the comparison of spectra from 50 MeV/A reactions for tritons (top) and ^{3}He (bottom) from the ^{124}Sn system. The ^{112}Sn reactions provide similar comparisons. One sees that the calculated spectra greatly exceed the measured ones at E< 20 MeV/A yet the data at higher energies is not dissimilar.

Despite this difference at low energy, we proceed to inspect the various ratios in comparison between simulation and data. Figures 5.63 and 5.64 show independent particle ratios for the charged particles (up through mass A=3) in comparison to three different symmetry energy parameterizations. While the protons show a reasonably similar trend and value beginning around 20 MeV/A, the tritons and ^{3}He begin to agree around 25 and 30 MeV/A, respectively. It is at these energies that the data seemed to match better with the simulations from figure 5.62. We note that this low energy region is the region where alpha particles strongly produced as seen in Figure 5.29.

The t/^{3}He single and double ratios show discrepancies until around 35 MeV/A. Figures 5.65 and 5.66 show these ratios, again in comparison to different symmetry energy results from pBUU. The single ratios at least show a similar trend to the experimental data, just being much smaller in magnitude. Unfortunately, the experimental data is lacking above about 45 MeV. It appears that it is only above 30 MeV that the simulation's trend really matches that of the data as evidenced by the slight increase in the ^{124}Sn reaction and the flat nature of the ^{112}Sn reaction in these regions. This is the region in Figure 5.62 where the theoretical calculations do not significantly vary from the experimental data. It would be very interesting to have higher energy data in this energy region.

The single ratios displayed in 5.65 and the double ratios displayed in 5.66 present
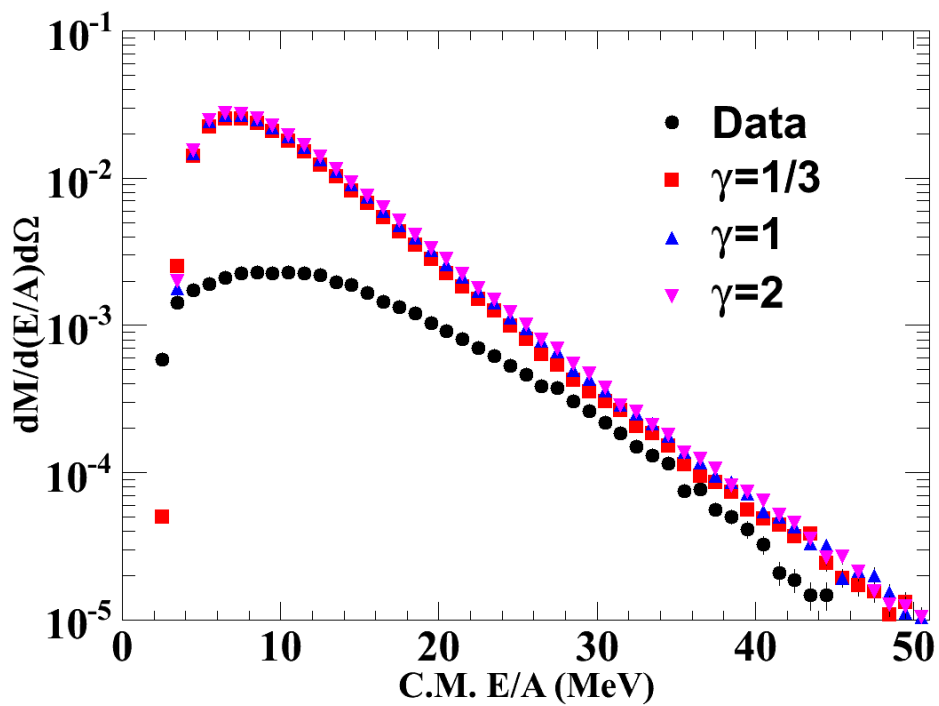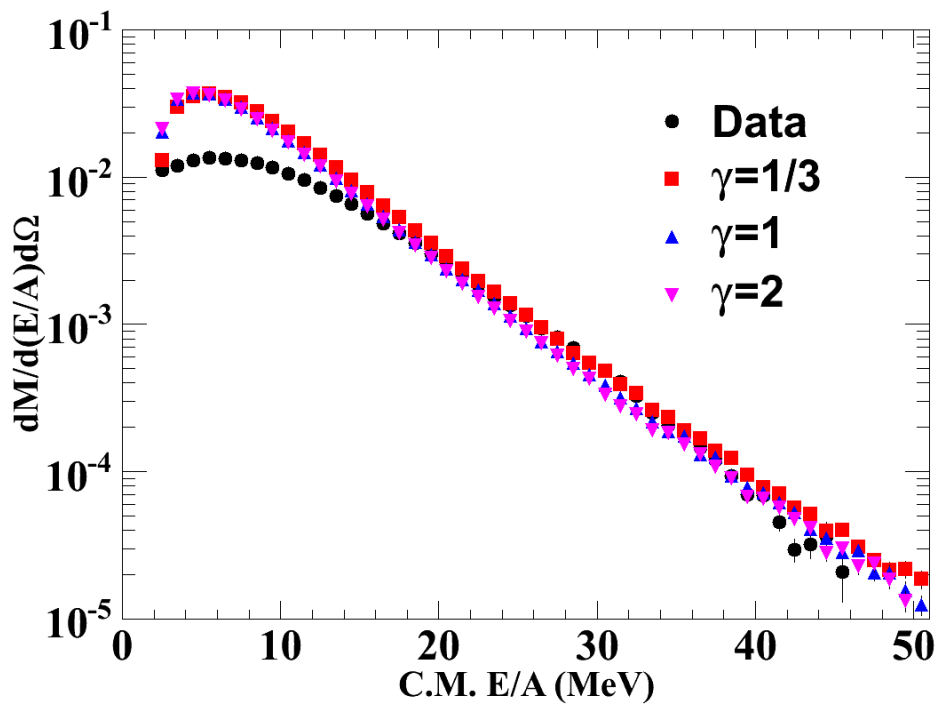
Figure 5.62: The spectra for tritons (top) and ^{3}He (bottom) from the ^{124}Sn system. All spectra come from 50 MeV/Areactions.
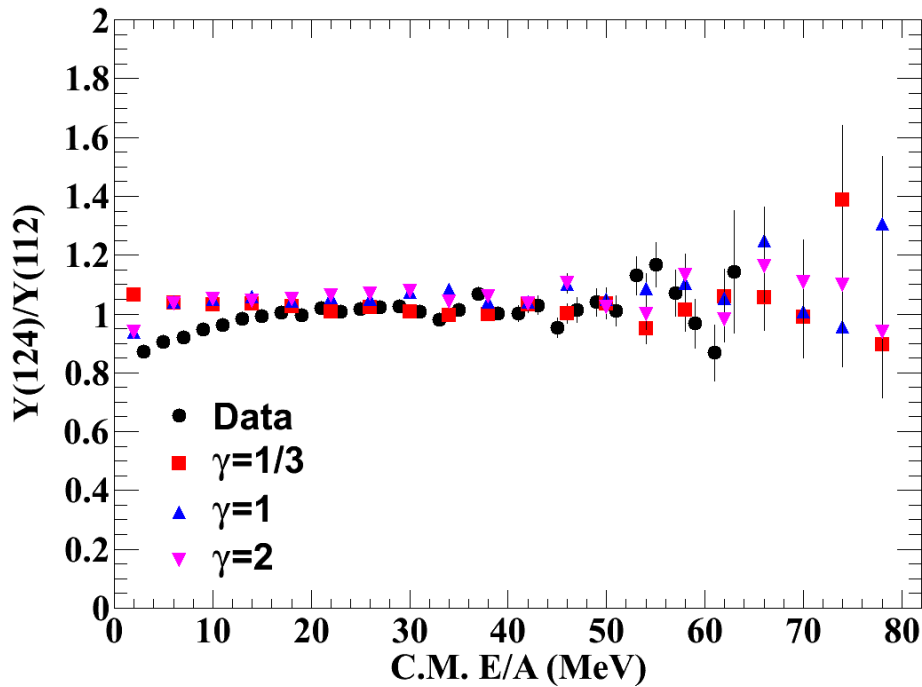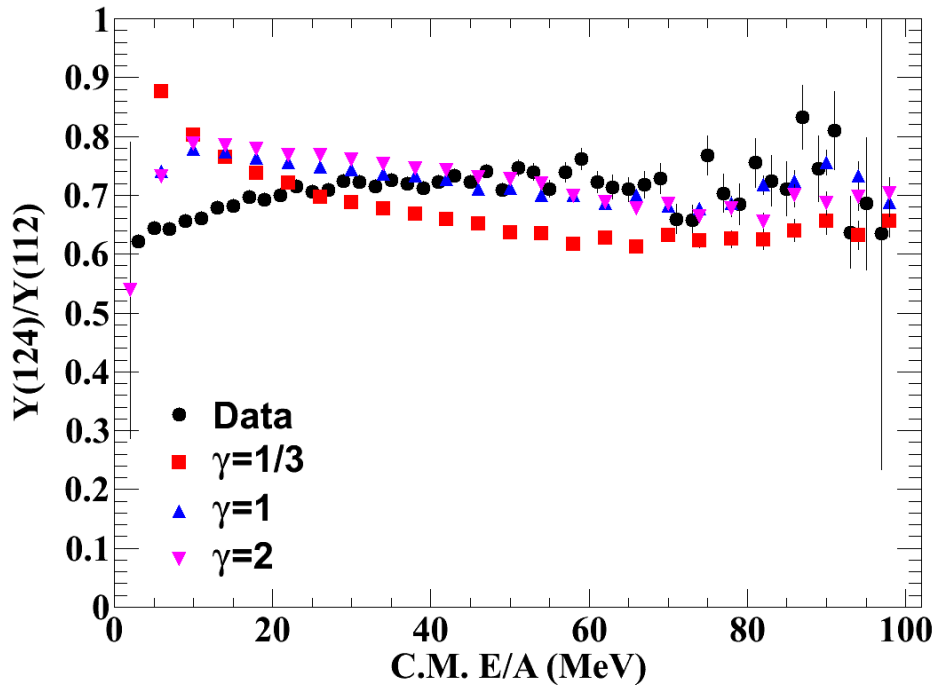
Figure 5.63: The independent particle ratios for protons (top) and deuterons (bottom) in comparison to pBUU results for three different parameterizations of the symmetry energy in 50 MeV/Areactions.
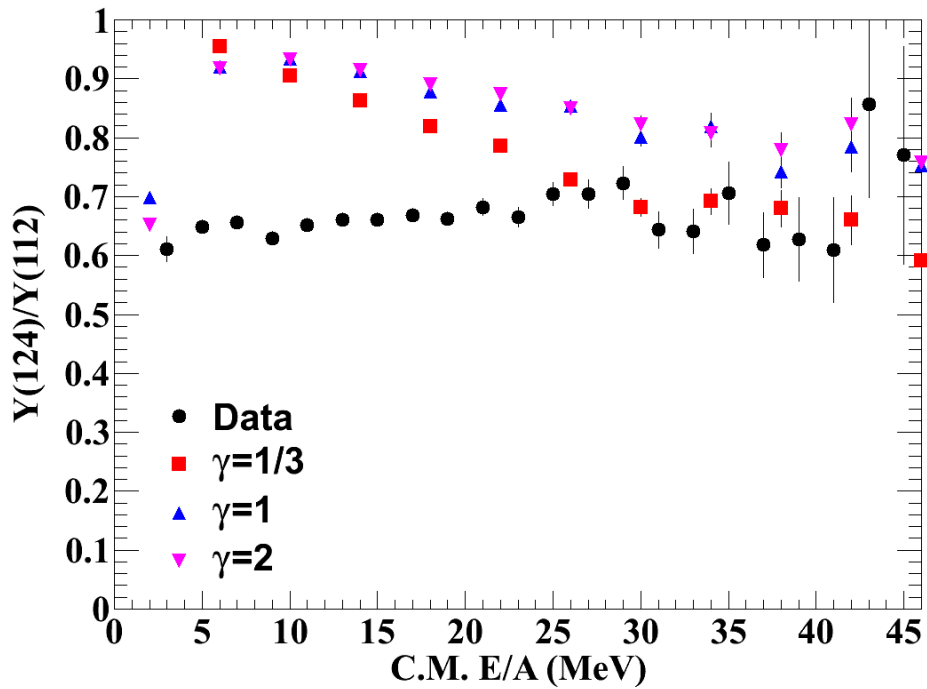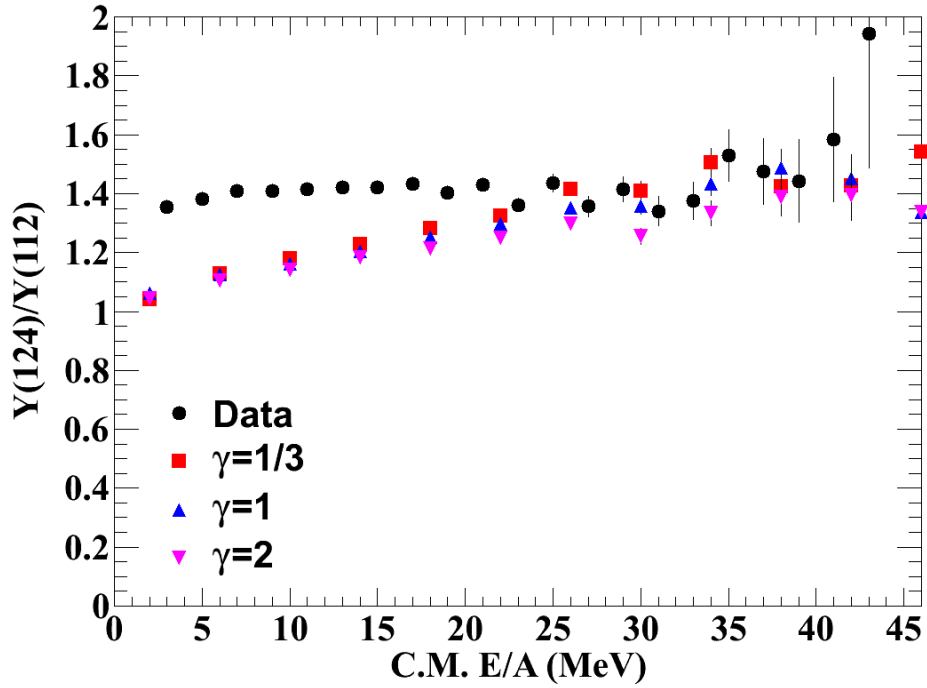
Figure 5.64: The independent particle ratios for tritons (top) and ^{3}He (bottom) in comparison to pBUU results for three different parameterizations of the symmetry energy in 50 MeV/Areactions.
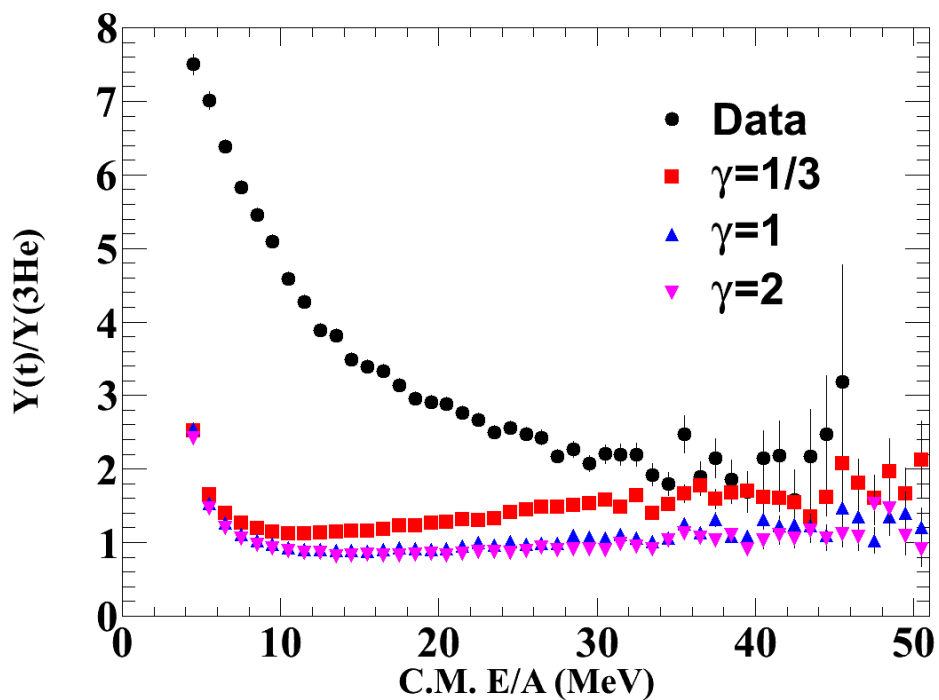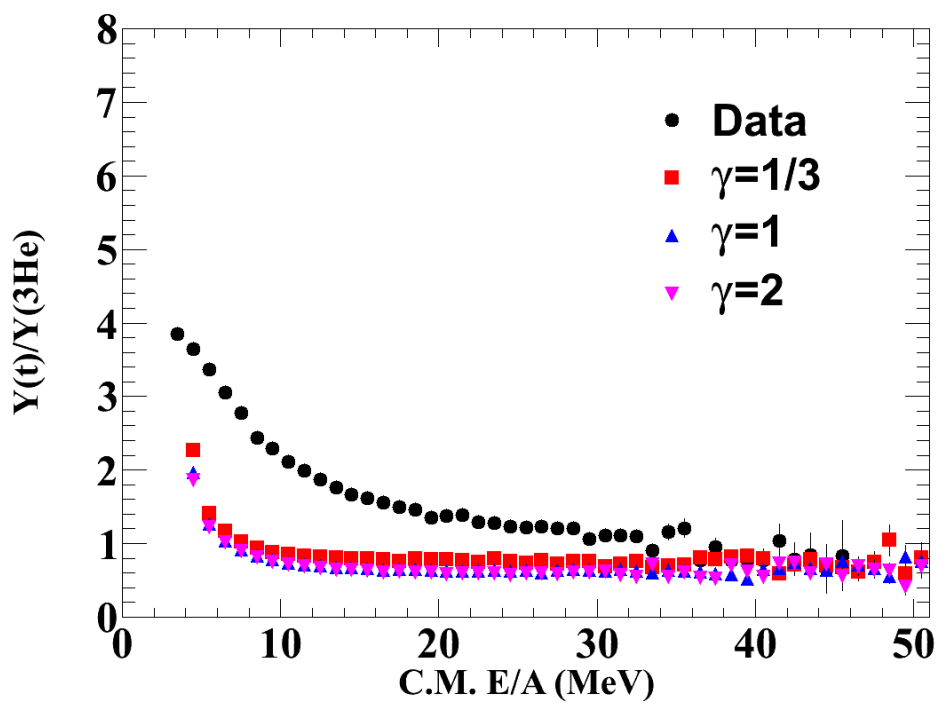
Figure 5.65: The single t/^{3}He ratios in comparison to pBUU simulations from 50 MeV/Areactions for ^{112}Sn on the top and ^{124}Sn in the middle.
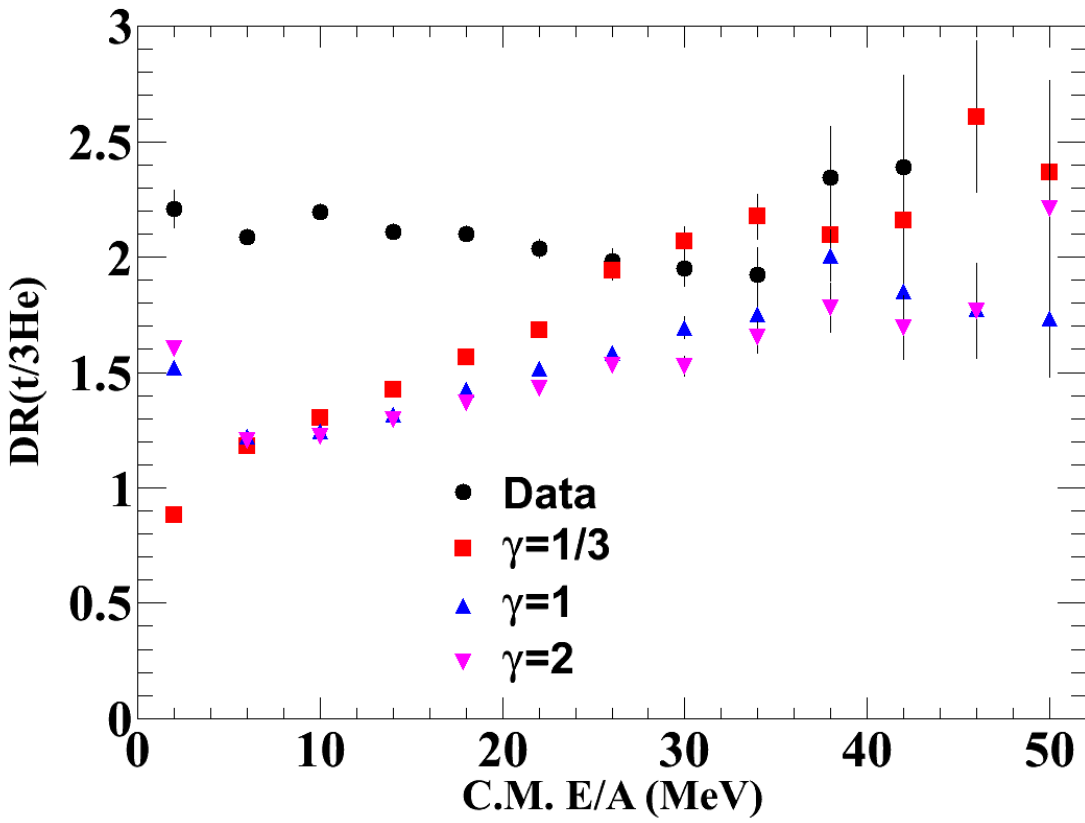
Figure 5.66: The double t/^{3}He ratios in comparison to pBUU simulations from 50 MeV/Areactions.
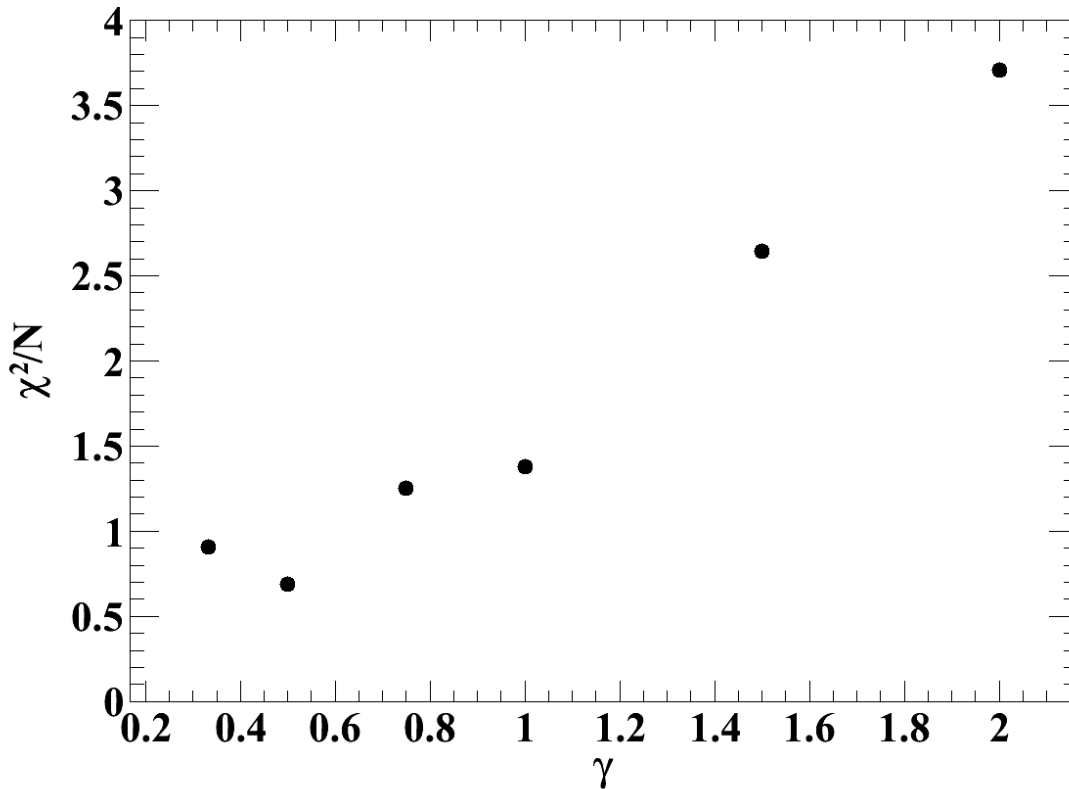
Figure 5.67: The χ^2 per degree of freedom for different simulation results of the t/^{3}He double ratio at 50 MeV/A.

a difficulty for the primary focus of this work. One of the primary purposes of this experiment was to measure precisely t/^{3}He double ratios and compare them to transport model simulations in order to constrain the symmtery energy. If we restrict the comparison to the regions where the cross sections for the data and the simulations do not greatly differ, the only appropriate region to make this constraint would be from 30 to 40 MeV/A. We have a large amount of simulated results to accrue better statistical uncertainty for six different values of γ: 1/3, 1/2, 3/4, 1, 3/2 and 2. We compare the experimental data to the results of these six calculations of the double ratio and provide a χ^2 comparison to data in Figure 5.67. Admittedly, the justification for this restricted comparison is relatively weak.

Let us return to the comparison of the spectra from the experiment and the simulations at low energies where there is a large discrepancy. One possible explanation that the extra yield is representative of emission from regimes with high density in phase space. Remembering that the calculation is only capable of creating clusters up through mass A=3 it is possible, even probable, that many of these particles at low energy would then have been a component of the production of alpha particles. If we reference the spectra in Figure 5.29 where alpha particles are the most dominantly produced particle at low energies (E/A<30 MeV) where the discrepancy mainly occurs. At higher energies, where the calculated and measured spectra are comparable, alpha production is nearly negligible. We would then like to propose a method to extend the comparison between calculated and measured yields to lower energies.

Let us consider how the calculation produces A=3 particles. It searches for two nucleons within close proximity and then calculate the probability that a third nucleon scatters off of another nucleon (not part of the A=3 cluster) and into the phase space of the initial two particles to form the final A=3 state. This occurs primarily within a region of high phase space density where it is possible that there is another nucleon close to the first two particles and would then create an A=4 cluster instead. However, the present calculation does not consider this as a possibility and so all potential A=4 clusters will pile up in the A=3 triton and ^{3}He. To better match the calculations to data, we therefore take half of our experimentally measured alpha particles and include them in our triton spectra. We do the same treatment to the ^{3}He data. The choice of splitting the alpha data equally between the two particles is naturally an approximation, however, in the case of having four particles scattered into the same phase space that would have created an alpha, there

225

is no physical reason for a significant bias towards creating one particle over the other. A comparison of this adjusted spectra is found in Figure 5.68.

Obviously this is not fully correct, but as initial proof of concept it is seems a reasonable path to continue forward. In order to correct for the Coulomb shift we assume that the particle gains 12 MeV (for computational ease) for each proton in the cluster as it travels from the barrier to the detector. If we want to then represent the energy spectra for alphas as if they were tritons or ^{3}He we use the following formulae,

$$E(^3He) = \frac{3(E(\alpha) - 2E_{Coul})}{4} + 2E_{Coul} \qquad (5.15)$$

and

$$E(t) = \frac{3(E(\alpha) - 2E_{Coul})}{4} + E_{Coul}, \qquad (5.16)$$

where $E(X)$ is the energy of a particle, and E_{Coul} is the Coulomb energy of 12 MeV. What this corresponds to is a 2 MeV/Ashift up for ^{3}He and down for tritons. The resulting spectra are in Figure 5.69. This provides a much better match of the data lending credence to the suggestion that many of the excess tritons and ^{3}He in the simulations are particles that would generally be used to form alphas if the alpha creation channel was included as an option in the simulation. As expected, not only do the spectra improve but so do the single and double ratios. The ^{124}Sn t/^{3}He ratios are shown in the top of Figure 5.70 with the double ratio on the bottom. Naturally a more complete treatment of the Coulomb effects along with proportionally adding the different spectra could be completed, however the true effects of what alphas would do to the simulated system are very hard to quantify without actually introducing it into the code which is outside of
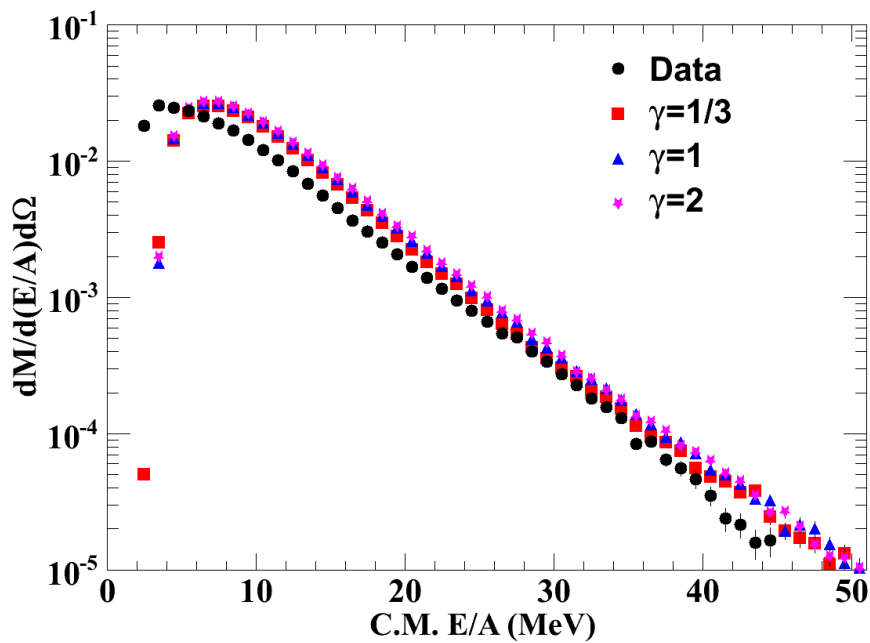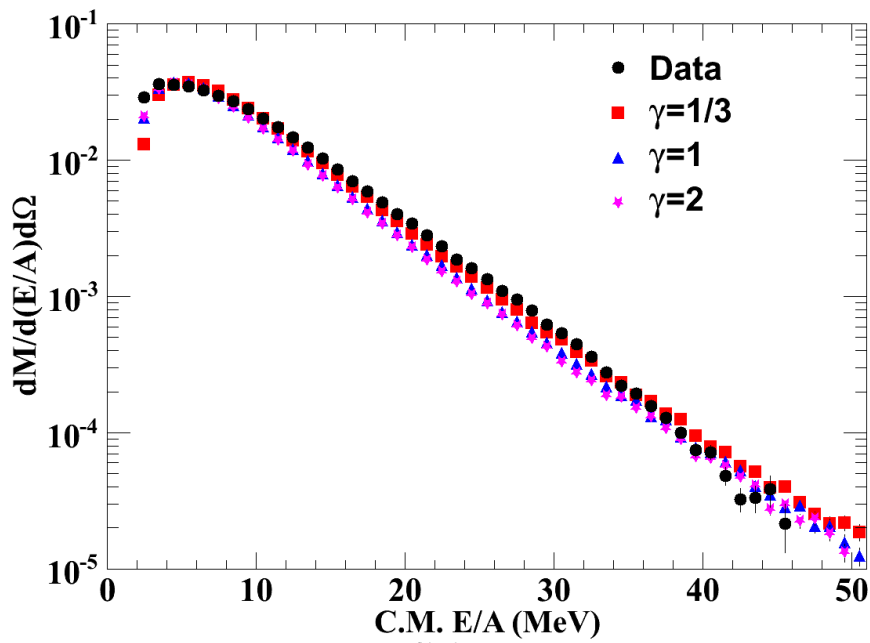
Figure 5.68: The adjusted spectra of tritons (top) and ^{3}He (bottom) at 50 MeV/A. Half of the experimental alpha spectra was added to each.

the scope of this dissertation. This is just one example of how important alpha particles are to simulating a true nuclear collision. Figure 5.71 shows the χ^2 comparison between simulation and experimental data. Even though there is good agreement at low energies for the soft symmetry energies, we are dominating that region by our alpha correction, which is significantly simplified over the true process. As such, we complete the χ^2 analysis for the same region as that of the free t/^{3}He analysis.

We have already discussed how the t/^{3}He ratios were believed to be similar to the n/p ratios which is part of what prompted the measurement in the first place. We have also just shown that alphas are important in the comparison between simulation to experiment. The next comparison will include a coalescence invariant n/p ratios. To accentuate the importance of alpha particles we will construct the spectra both with and without them. An example can be seen in Figure 5.72. Larger mass isotopes can contribute up to 15 or 20% more at energies below 15 MeV/Abut are negligible above that energy.

We would like to then compare the coalescence invariant n/p ratios to the free n/p and t/^{3}He ratios to identify any trends. The single ratios from both systems are shown in Figure 5.73. The double ratios are provided in Figure 5.74. In general the trend of the n/p and t/^{3}He ratios are quite similar. The neutron analysis has an efficiency value which is currently only known to with about 20%. The discrepancies between the n/p and t/^{3}He ratios are likely influenced by any error in the neutron efficiency. The present difference between n/p and t/^{3}He ratios could be due to an uncertainty in the neutron efficiency. Only statistical uncertainties have been included in these plots. The coalescence ratios have been strongly affected by the inclusion of the symmetric deuterons and alphas. At low energies the ratios that include clusters, and especially alpha particles, are systematically closer to
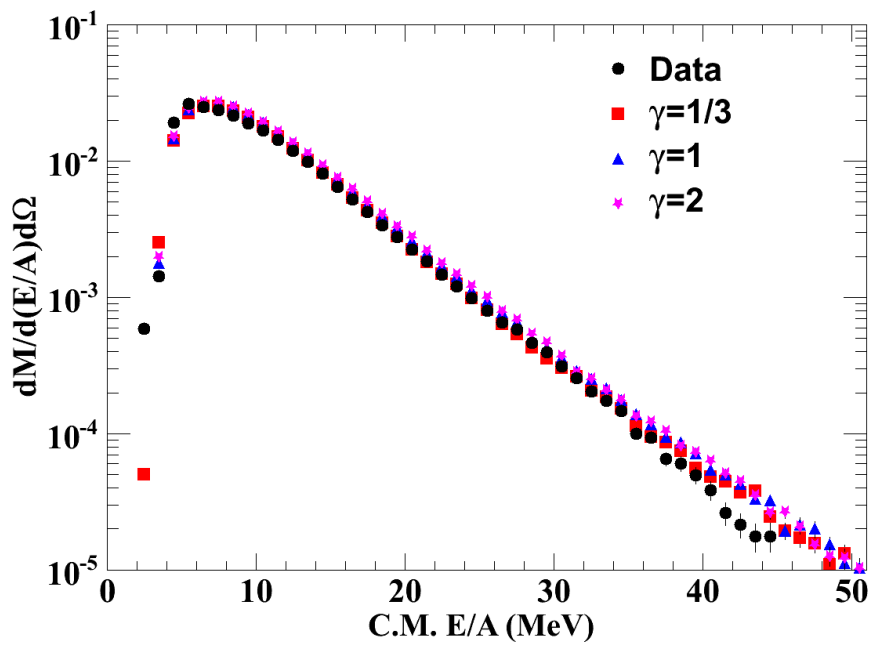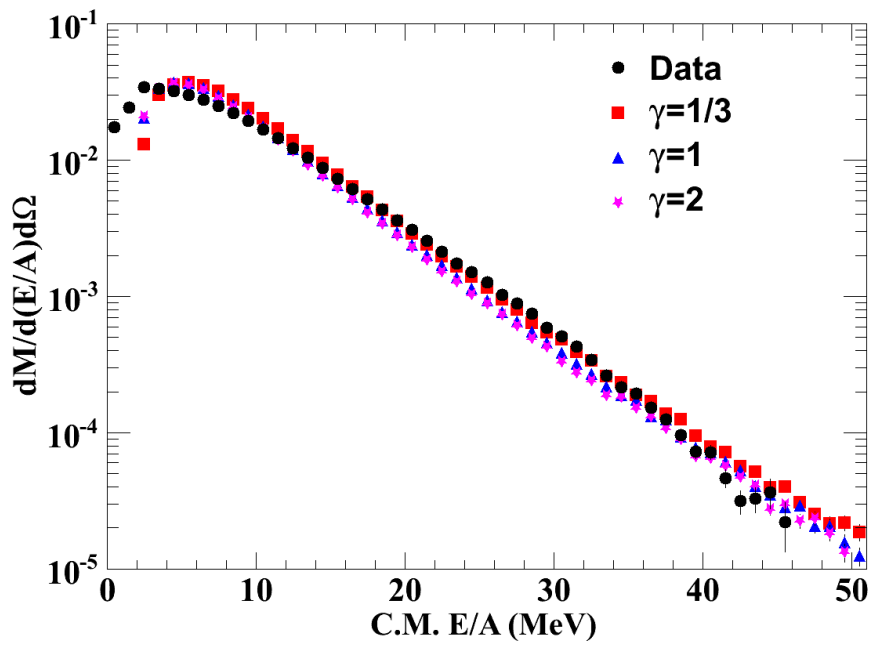
Figure 5.69: The adjusted spectra of tritons (top) and ^{3}He (bottom) at 50 MeV/A. Half of the experimental Coulomb corrected alpha spectra was added to each.
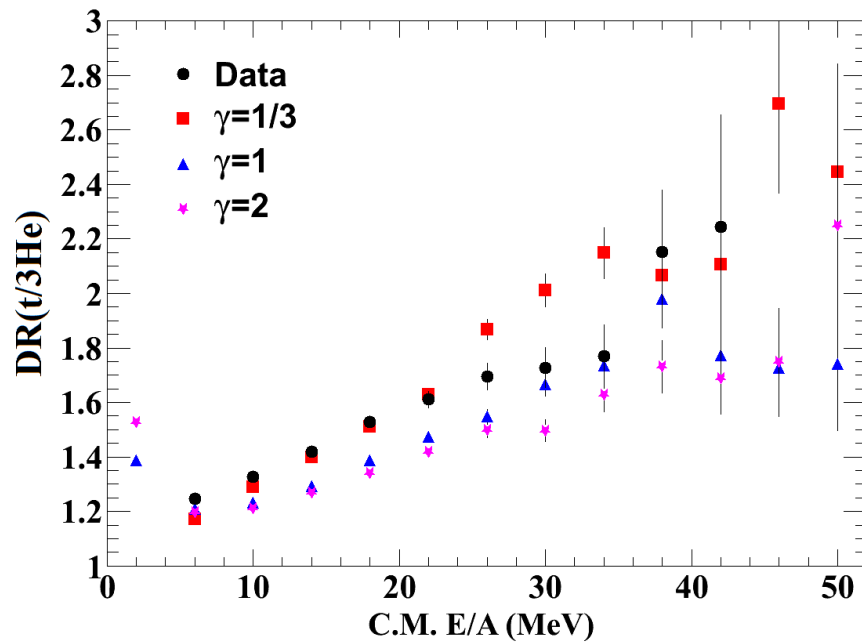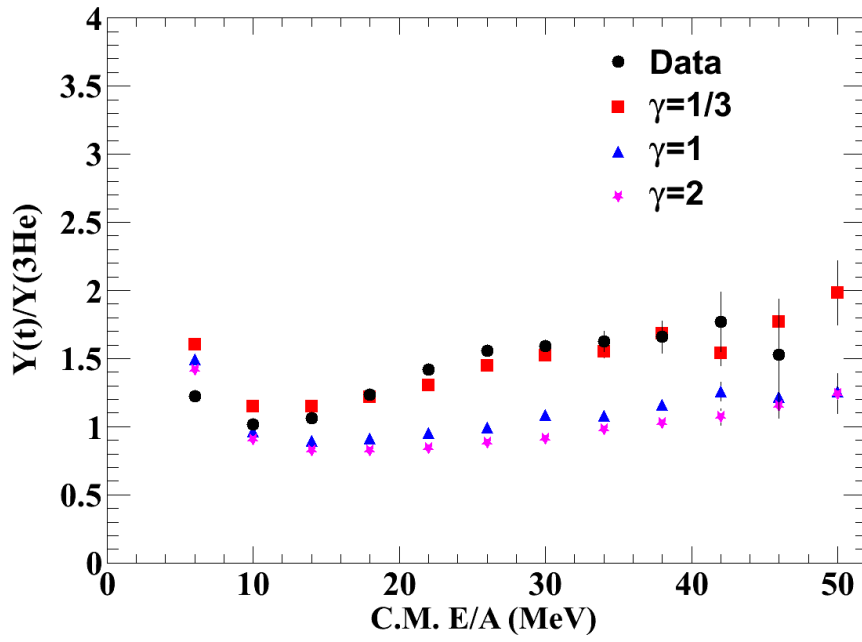
Figure 5.70: The t/^{3}He single ratio (top) from ^{124}Sn and double ratio (bottom) having included alpha data into the triton and ^{3}He data accounting for Coulomb effects.
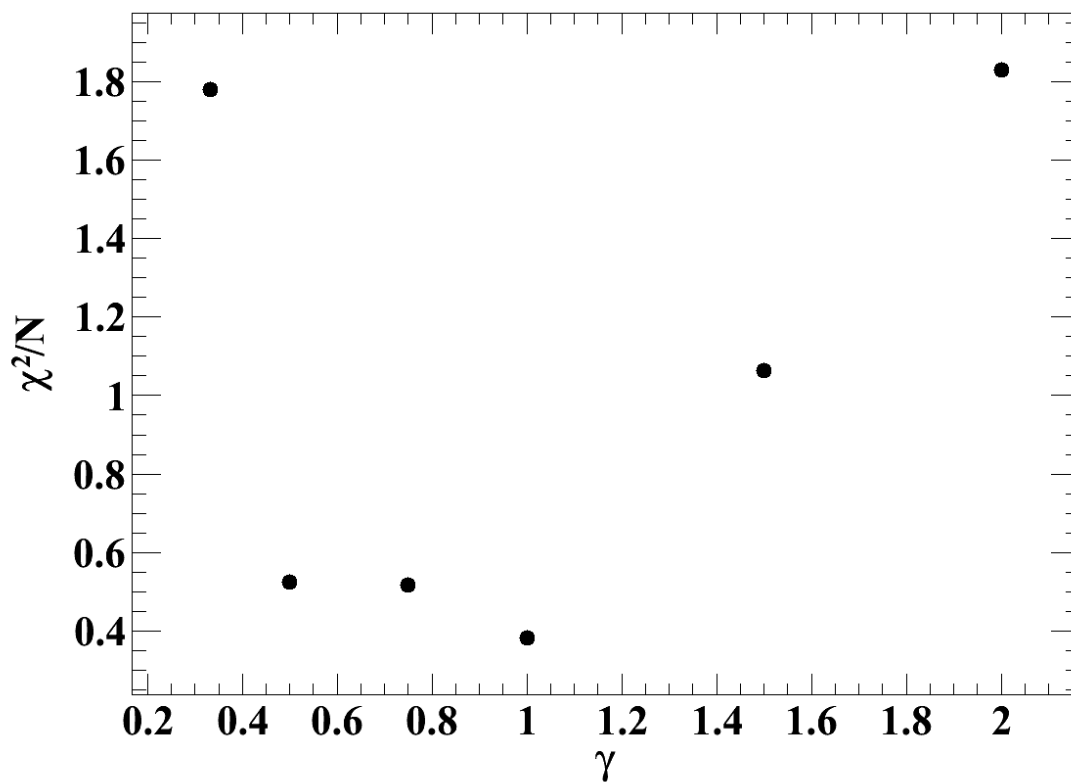
Figure 5.71: The χ^2 per degree of freedom for different simulation results of the t/^{3}He double ratio at 50 MeV/Awhen Coulomb corrected alphas were included as tritons and ^{3}He.
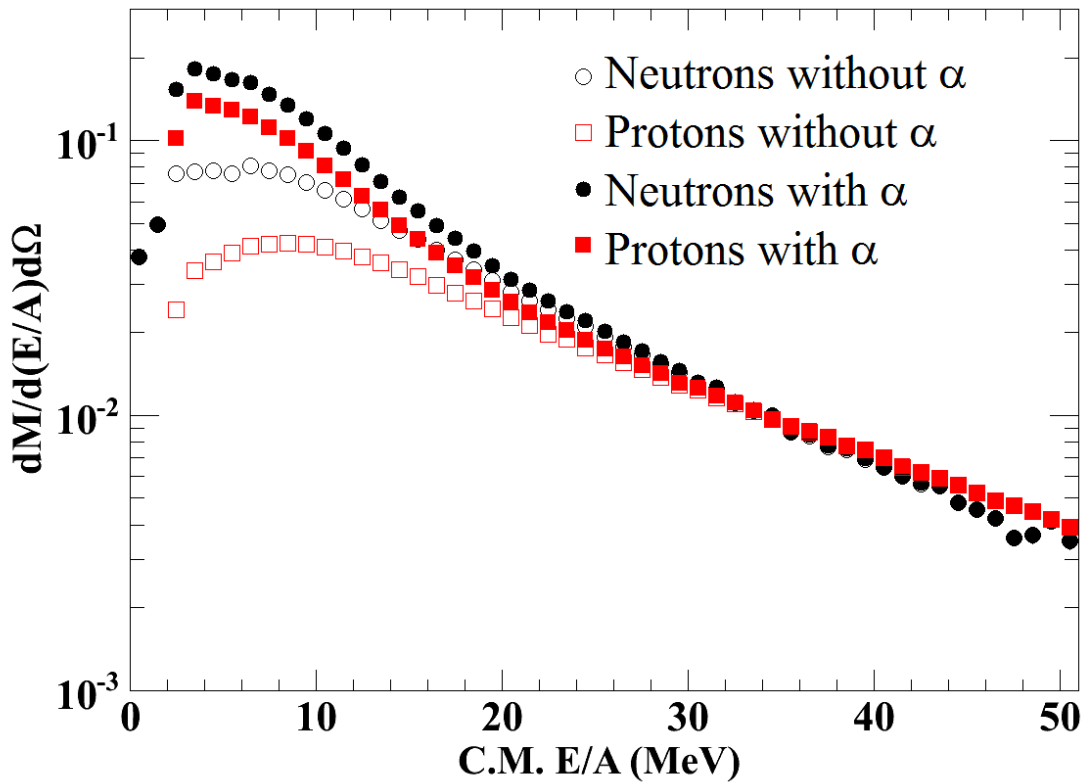
Figure 5.72: The coalescence invariant spectra for neutrons and protons from the ^{112}Sn reaction at 50 MeV/Awhen alpha particles are omitted (open point) or included (solid points) in the spectra. The alpha particles represent a significant portion of the spectra below 30 MeV/A.

1 as one should expect given the previous results so far.

The dissertation work completed by Coupland in [1] compares his n/p ratios, which included protons analyzed in this dissertation, to ImQMD simulations. Here we use the pBUU simulations to compare to the experimental double ratios. These calculations differ in many ways. We would point out that the ImQMD simulation includes cluster production but probably underpredicts alpha particle emission in part because it does not have correct alpha particle binding energies. Also, the ImQMD calculations consider the influence of an isovector nucleon effective mass which makes a big difference at higher excitation energies. Figure 5.75 shows three different comparisons of the experimental double ratios to simulation. The top plot shows the free experimental n/p ratios to the simulated free ratios. The lower figure shows the coalescence invariant spectra that includes all clusters up through A=4.

Surprisingly, the coalescence invariant n/p ratios in the lower panel suggest a stiffer equation of state, one with a $\gamma > 2$. This is contrary to what the t/^{3}He ratios suggest which had better agreement for equations of state with γ near 1. The inclusion of alphas does provide an improved comparison to the theoretical calculations below about 35 MeV/A. This conclusion is contrary to that derived from comparisons to ImQMD calculations in the dissertation of Coupland [1]. However, that conclusion reflects the comparison to calculation that includes an isovector nucleon effective mass which the present pBUU calculations do not.

So far we have only compared experimental data to the simulations in the 50 MeV/A reactions. It was suggested in Chapter 4 that the 120 MeV/A reactions did not show much sensitivity to the symmetry energy. Nonetheless, we investigate the comparison to simulations at
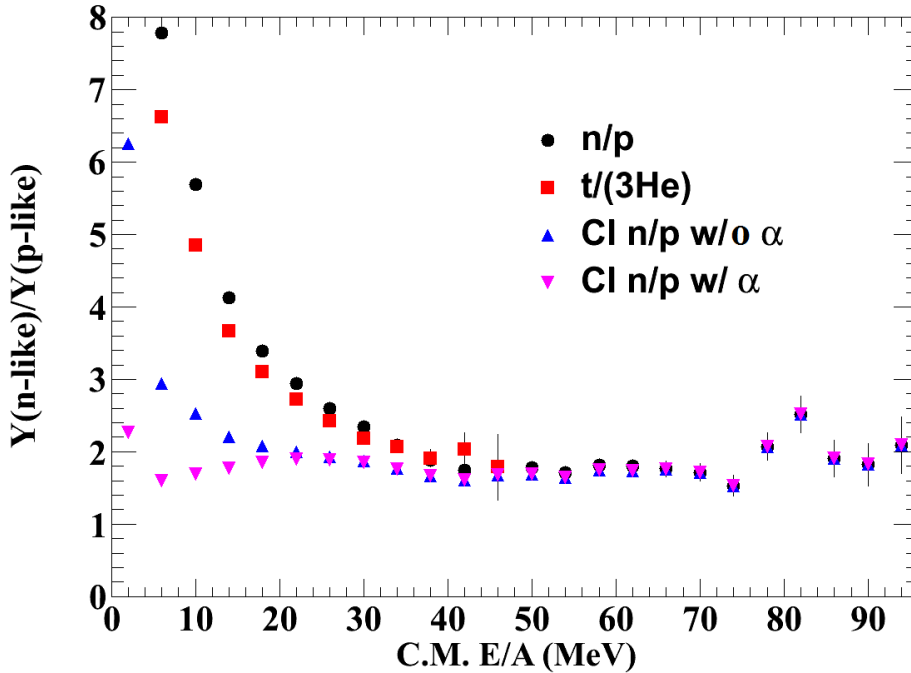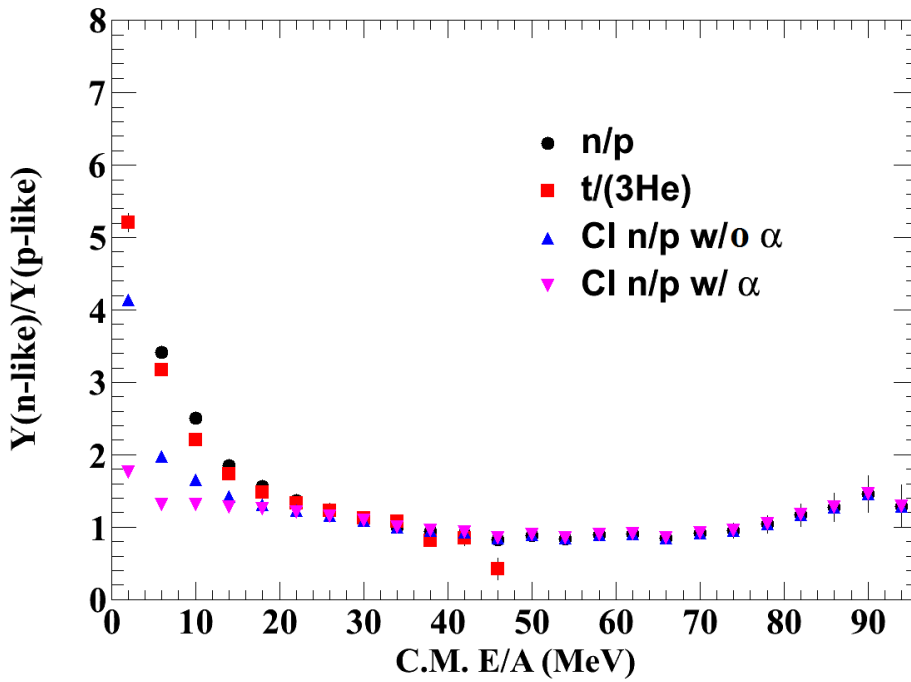
Figure 5.73: A comparison of the two different coalescence invariant n/p ratios with the free n/p and t/^{3}He ratios. Single ratios from ^{112}Sn are on top with ^{124}Sn on the bottom.
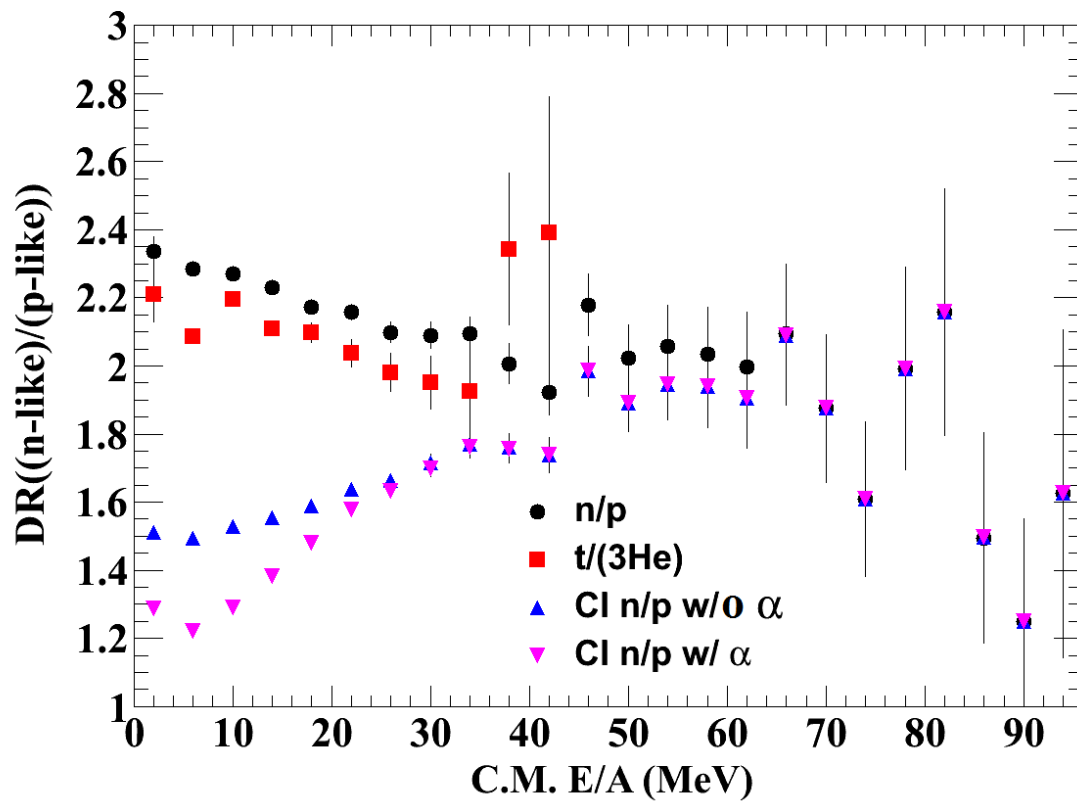
Figure 5.74: A comparison of the two different coalescence invariant n/p double ratios with the free n/p and t/^{3}He double ratios.
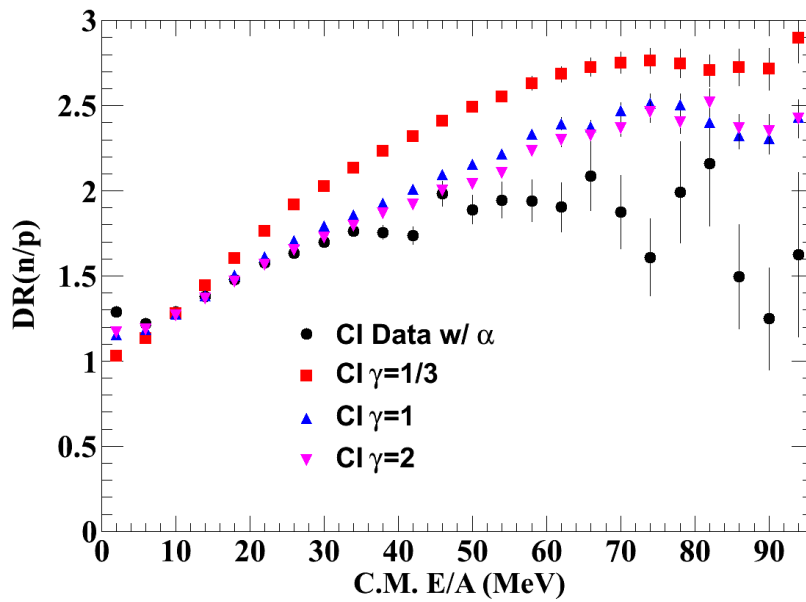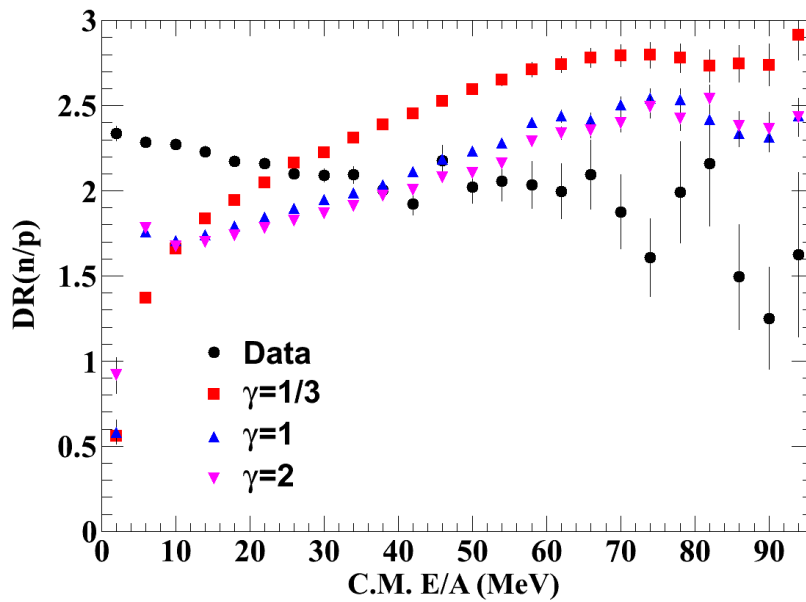
Figure 5.75: Three different comparisons of n/p double ratios to simulations. The top compares free experimental particles to free particles in the simulation. The middle shows coalescence invariant comparisons where the alphas have been omitted. The bottom shows the comparison for when alphas are included.

Skyrme	S_0 (MeV)	L (MeV)	m_n^*/m_n	m_p^*/m_p
SkM*	30	46	0.82	0.76
Sly4	32	46	0.68	0.71
pBUU $\gamma = 1/3$	31.5	44	0.7	0.7
pBUU $\gamma = 1$	31.5	82	0.7	0.7
pBUU $\gamma = 2$	31.5	139	0.7	0.7

Table 5.2: The top two rows of the table provide some of the properties of the mean field used in the ImQMD calculations. The lower three rows provide corresponding information about several pBUU calculations described in this dissertation. The significant difference in the two ImQMD calculations is the difference in nucleon effective mass splitting for the two Skyrme interactions. As a reference, pBUU values are included for three different values of γ.

this higher energy. We completed a similar study with the most extreme values of $\gamma = 1/3$ and 2. Figure 5.76 shows the comparison of simulation with t/^{3}He double ratios on top. The bottom portion of the figure includes half of the alpha spectra being treated like tritons and half like ^{3}He. The agreement is not as good as in the 50 MeV/Areaction but the effect is still significant. Figure 5.77 shows the free (top) and coalescence invariant (bottom) n/p double ratios in comparison to simulation results at 120 MeV/A.

By looking at the n/p ratios from this experiment, it is suggested in [1] that the nucleon effective mass splitting could be a larger contributing factor to the shape of the n/p ratio than the symmetry energy. As an exercise of investigating this effect in the t/^{3}He ratios, Figure 5.78 provides the double ratio from ImQMD-Sky [8] for two different Skyrme parameterizations from 50 MeV/Areactions. These two represent relatively soft symmetry energies with different effective mass splittings. Necessary information on the difference between the two Skyrme's can be found in Table 5.2. The double ratio from ImQMD shows a very similar behavior to pBUU, starting much lower than the experimental data and trending slightly upwards to meet the data around 30 MeV. The bottom portion of that figure also includes the comparison to data where the alpha particles have been included
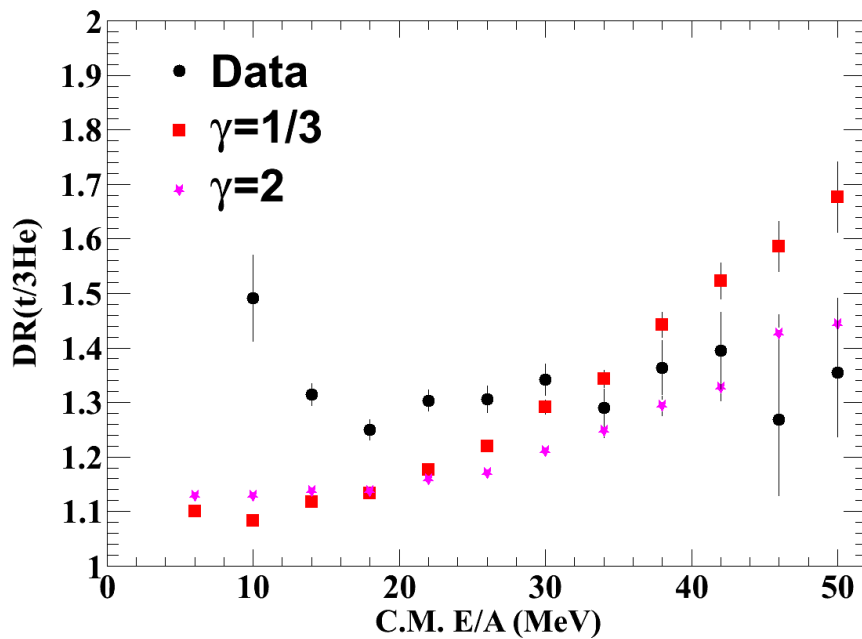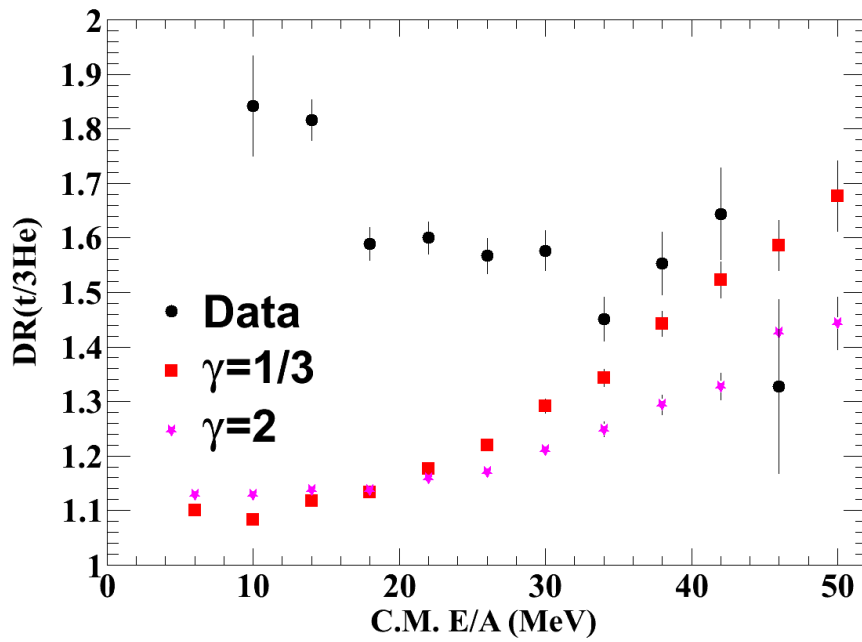
Figure 5.76: The t/^{3}He double ratios in comparison to simulations at 120 MeV/A. The top contains pure tritons and ^{3}He while the bottom includes half of the alpha spectra as part of each.
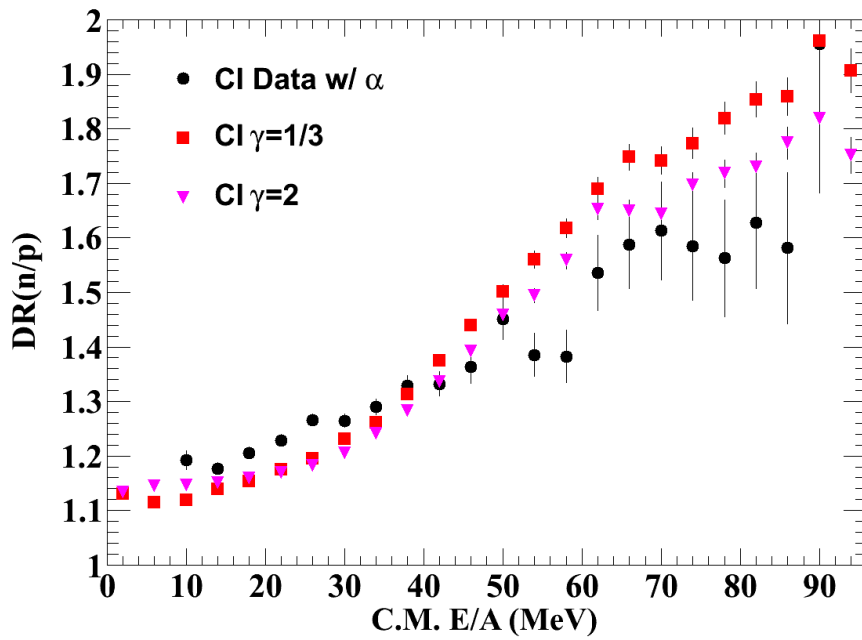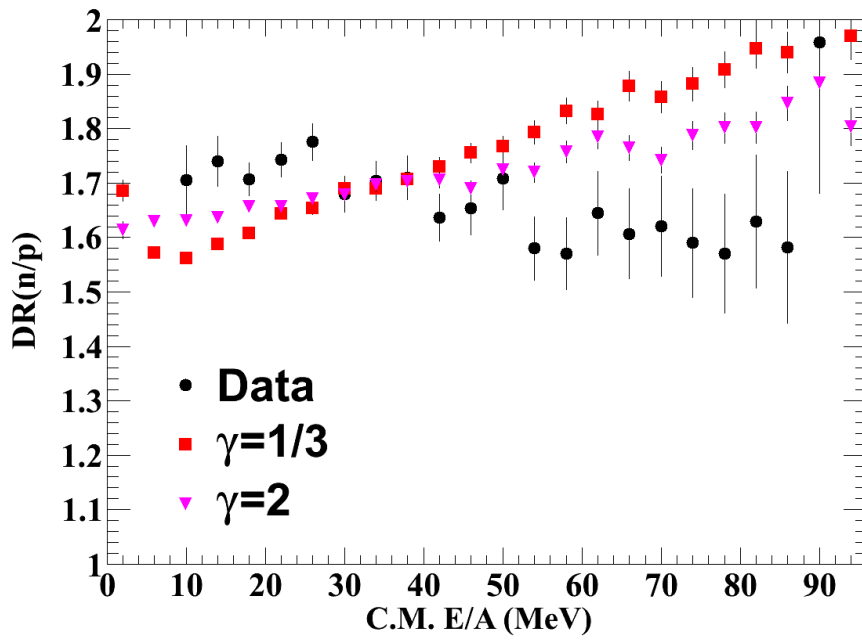
Figure 5.77: The free (top) and coalescence invariant (bottom) n/p double ratios in comparison to simulations at 120 MeV/A.

as part of the triton and ^{3}He spectra which shows much better agreement across the full energy spectra similar to the study before with pBUU.

There are several distinct reactions to take away from this. This simulation shows that the t/^{3}He double ratios show very little sensitivity to the effective mass splitting (unlike the single ratios displayed in Figure 5.79). Perhaps more importantly, ImQMD and pBUU are very different style transport simulation codes, yet both fail to adequately describe the emission of alpha particles and heavier clusters. pBUU simply does not include alphas but uses proper binding energies while ImQMD creates alphas albeit with an incorrect binding energy leading to an incorrect prediction of the alpha spectra.

Despite results of Chapter 4 suggesting that the ratios from 120 MeV/Areactions may be less sensitive to the symmetry energy than in the 50 MeV/Areaction, ImQMD provides evidence that they may be sensitive to the effective mass splitting at the higher incident energy. Comparisons of the data to pBUU shows a very similar result to that of the ImQMD results displayed in 5.80. pBUU shows a diminished sensitivity to the symmetry energy while ImQMD shows a complete lack of sensitivity to the nucleon effective mass splitting, at least up through the energies that we were capable of measuring in this experiment. This is true for the single ratios as well. Both pBUU and ImQMD do a better job of simulating these results than in the 50 MeV/Areactions, however both are still unable to recreate the experimental double ratios below 30 MeV unless the alpha particles are included as part of the triton and ^{3}He spectra as shown in the bottom part of the same Figure.

There are a number of reasons that investigation of the t/^{3}He double ratios might not match that of the ImQMD-sky results. One possible explanation is that the Binding Ener-
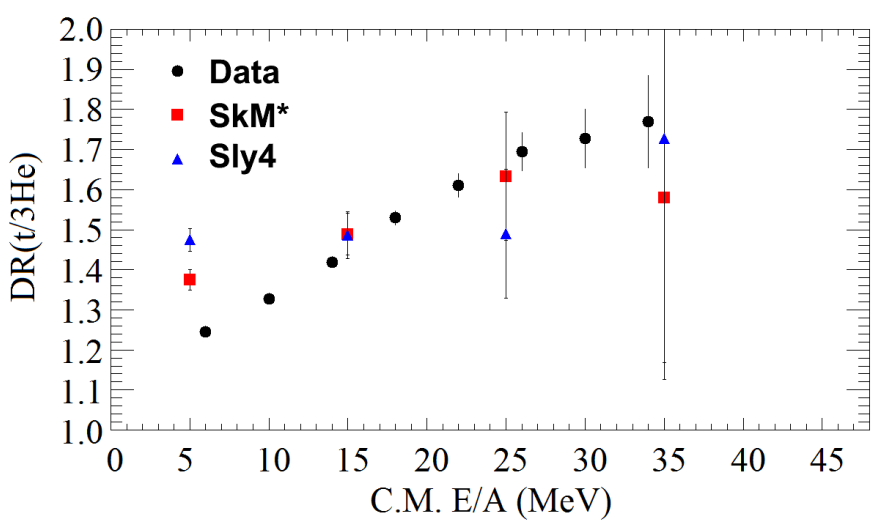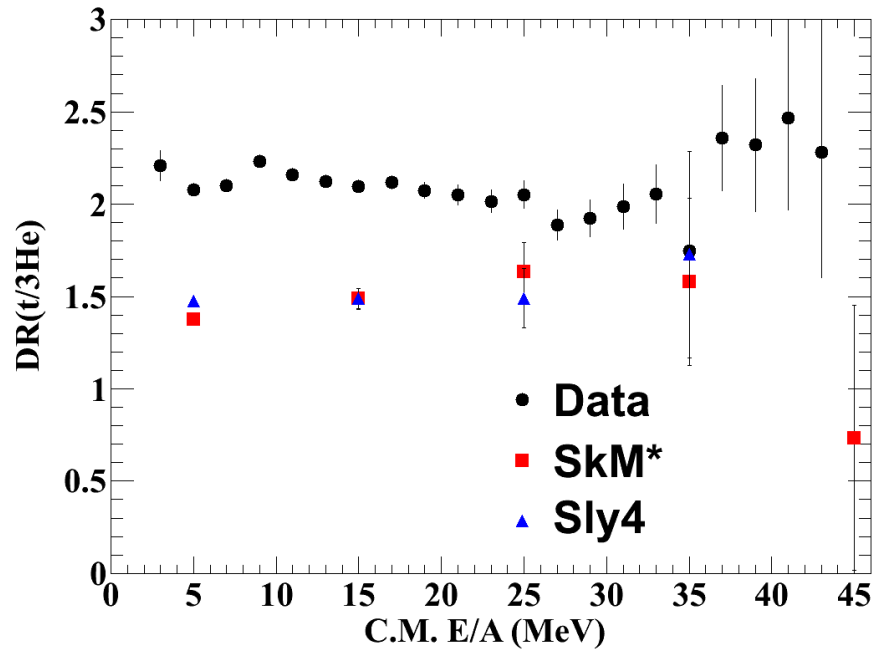
Figure 5.78: The t/^{3}He double ratio from 50 MeV/Areactions in ImQMD in comparison to this data. The top plot shows only tritons and ^{3}He while the bottom includes alpha particles as part of the triton and ^{3}He spectra.
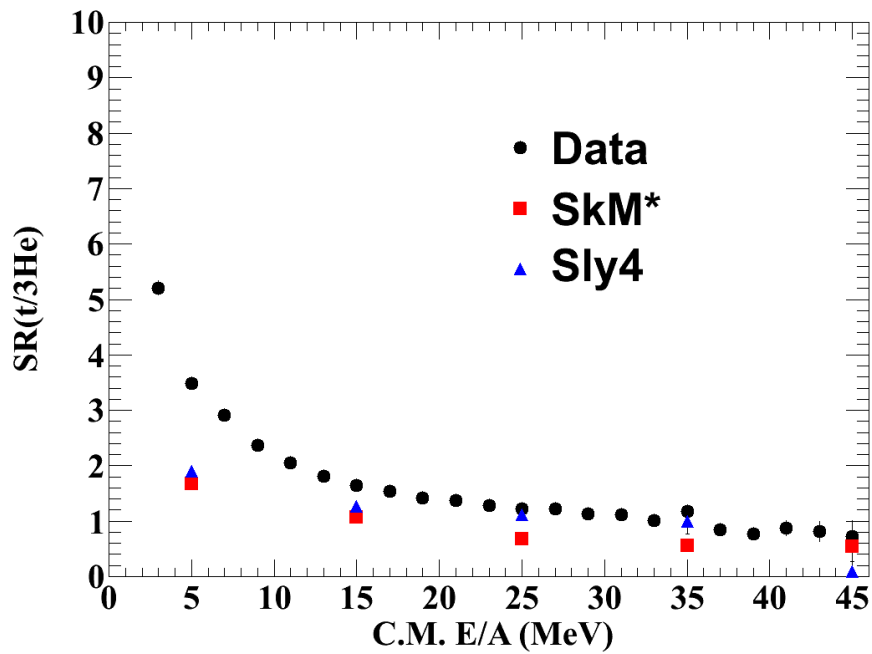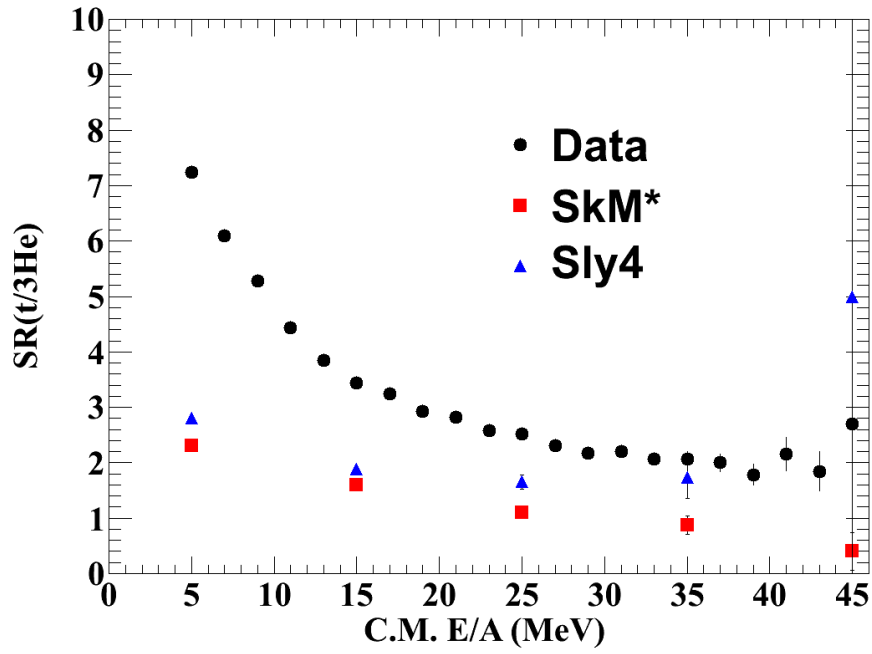
Figure 5.79: The t/^{3}He single ratios from ImQMD in comparison to this data. ^{124}Sn reactions are on top with ^{112}Sn reactions on the bottom.
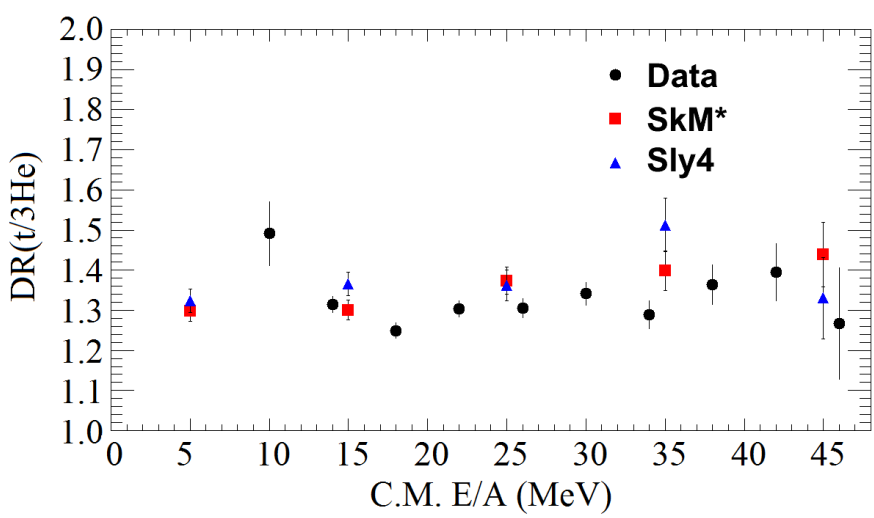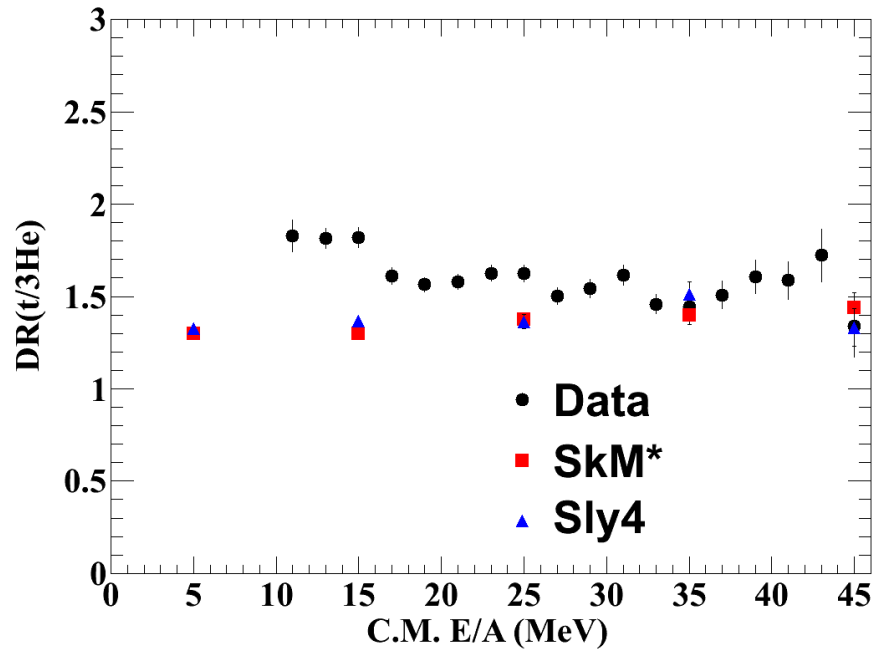
Figure 5.80: The t/^{3}He double ratio from ImQMD in comparison to this data for the 120 MeV/Areaction. The top plot shows only tritons and ^{3}He while the bottom includes alpha particles as part of the triton and ^{3}He spectra for both simulated and experimental results.

gies in this code are not properly treated. Coupland also sees these results in [1] for the n/p double ratio in comparison. However, if we investigate the coalescence invariant n/p double ratios for both the data and simulation we see much better agreement, similar to what is seen in pBUU. This can be seen in Figure 5.81. In this Figure, 50 MeV/Aexperimental data shows good agreement at low energies where there is little sensitivity to the nucleon effective mass, while at higher energies being somewhere in the middle of the two curves. In the 120 MeV/Acase, the data shows agreement at all energies with the Sly4 model which assumes a neutron effective mass less than that of protons.
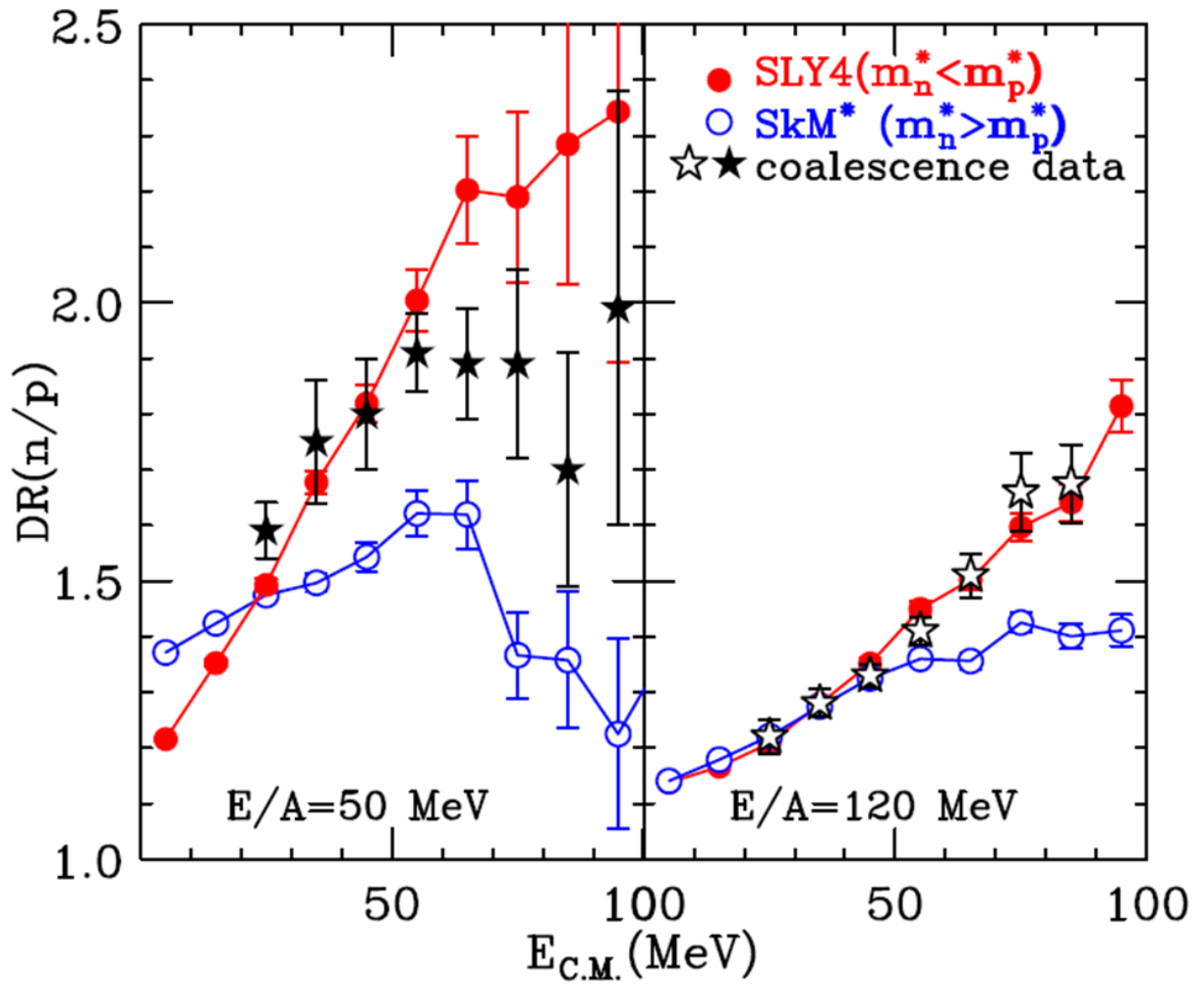
Figure 5.81: The coalescence invariant n/p double ratio from ImQMD in comparison to this data for the 50 (left) and 120 (right) MeV/Areactions. [1,8]

Chapter 6

Conclusions

6.1   Conclusions

The intention of this dissertation work was twofold. The first was to investigate the pBUU transport simulation code and determine how different transport variables effect light particle ratios, in particular n/p and t/3He single and double ratios from reactions of 112Sn+112Sn and 124Sn+124Sn at incident energies of 50 and 120 MeV/A. The second was to run and analyze an experiment for the same collisions and measure the t/3He ratios, and then constrain the density dependence of the symmetry energy in the Nuclear Equation of State by comparing these ratios to the corresponding pBUU simulations.

The studies of the pBUU simulations suggested that the t/3He ratios were less sensitive to many transport variables such as the momentum dependence of the mean field, impact parameter and in-medium cross section, than to the symmetry energy. It did however suggest a significant effect on the n/p ratio when cluster production is enabled. The pBUU calculations do not include momentum dependence in the symmetry potential so the important issue of relating the difference betwen neutron and proton effective masses was

thereby not explored. Upon comparison to the experimental data, however, there were many discrepancies between the two. The two sets of data trend quite differently, with comparable values only above 30 MeV/A, however below that energy the results are very different. We provide evidence that alpha particle production is a significant source of discrepancy between the data and simulation. Nevertheless, a comparison to simulation for t/^{3}He double ratios is made. This comparison implies a softer symmetry energy, in the range of $1/3 \leq \gamma \leq 1$.

We suggested a treatment that combines the alpha particle experimental results with that of tritons and ^{3}He in a rather simplistic fashion. It would be a large undertaking to properly do this, but it would be better if this could be fixed from the theory side by the inclusion of cluster production being capable of making alpha particles. Nevertheless, using this comparison, we find that through a χ^2 analysis, γ would be in the range of $\sim 0.4 < \gamma < \sim 1.2$.

Comparison with a different transport code, ImQMD-Sky, shows the lack of ability to recreate the ratios of free n/p and t/^{3}He. In addition, this code predicts little sensitivity to the difference in the effective mass of protons and neutrons in the energy range that we measured for t/^{3}He ratios. At higher emission energies this code predicts a larger sensitivity.

Both the ImQMD-Sky and pBUU calculations provide better agreement to the data when a coalescence invariant model is used for both. While at this time the pBUU is unable to provide a significant constraint on the symmetry energy, the ImQMD-Sky does suggest a sensitivity to the nucleon effective mass. This is amplified in the 120 MeV/Areaction where there is an improved agreement between the coalescence invariant experimental

data and the coalescence invariant simulated results when the proton effective mass is chosen to be larger than the neutron effective mass.

The t/3He single and double ratios have been measured previously for the 50 MeV/A reaction in at least two separate experiments. The double ratios for those experiments agree with this work, while this work improves upon those results with more statistics and the ability to reach higher emitted energies. The single ratios show quite reasonable agreement with one of those experiments but disagree with the other. The measurement at 120 MeV/A is new and supports the theory that at this density region the symmetry energy has a lessened effect on the system.

We briefly touch upon two different suggestions for coalescence, one suggesting that, in collisions such as those studied in this work, triton emission should, in many respects, resemble neutron emission. Similarly, ^{3}He emission should resemble proton emission. The independent particle ratios of protons and ^{3}He also suggest this to be true however, there are some discrepancies between the triton and neutron ratios which may be influenced by the current uncertainties in the neutron efficiency.

We briefly explore the coalescence model which suggests that in the presence of neutron and proton spectra, one can create spectra of clusters. By using the combination of tritons, neutrons and protons we are able to constrain the coalescence volume parameter of this model which does indeed let us extend triton spectra out to higher center of mass energies that are beyond the range of the LASSA detectors.

6.2   Outlook

There are many experimental and theoretical results that suggest that the t/^{3}He ratios are sensitive to the density dependence of the symmetry energy and a good candidate for constraining that dependence. This work provides more evidence for that. It also shows that while the theoretical and experimental sides agree that it is a good candidate, there is a significant source of discrepancy between the experimental data and simulated results. Proper treatment of alpha particles in these simulations is necessary for the future of these studies. pBUU can be improved if the alpha particle were included as another potentially created cluster. ImQMD-Sky would benefit from a more proper treatment of the Binding Energy which could help correct the single particle spectra and provide better agreement with experimental results.

This experiment was a rather complicated experiment to both execute and analyze due to the neutron detection. For t/^{3}He measurements, a different experiment could be designed and executed reasonably easily. Assuming these ratios are just as good a candidate of constraining the symmetry energy as n/p ratios, one might choose to complete more experiments specifically targeting clusters. There are three primary suggestions for this situation should those experiments actually be completed. If similar detectors are used for this experiment, moving the LASSA-like detector backwards in the lab, or using more of the detectors, to more fully cover the angular region of interest in the center of mass would be helpful. Since neutron detectors would not be needed, the inclusion of detectors used for impact parameter dependence at forward lab angles would also be prudent. Since the ImQMD suggest a dependence to the effective mass splitting at energies above the ones capable of being measured in this work, it would also be recommended to

be capable of measuring higher energy tritons and ^{3}He. Finally, a measurement of these ratios at an energy in supersaturation density regions could provide an interesting third set of data for testing the reversal of trend from a soft to stiff symmetry energy.

REFERENCES

REFERENCES

[1] Dan Coupland. *Probing the Symmetry Energy Using Heavy Ion Collisions*. PhD thesis, Michigan State University, 2013.

[2] Lijun Shi. *Transport Phenomena in Heavy-Ion Reactions*. PhD thesis, Michigan State University, 2003.

[3] M. B. Tsang, J. R. Stone, F. Camera, P. Danielewicz, S. Gandolfi, K. Hebeler, C. J. Horowitz, Jenny Lee, W. G. Lynch, Z. Kohley, R. Lemmon, P. Möller, T. Murakami, S. Riordan, X. Roca-Maza, F. Sammarruca, A. W. Steiner, I. Vidaña, and S. J. Yennello. Constraints on the symmetry energy and neutron skins from experiments and theory. *Phys. Rev. C*, 86:015803, Jul 2012. doi:10.1103/PhysRevC.86.015803.

[4] B. A. Brown. Neutron radii in nuclei and the neutron equation of state. *Phys. Rev. Lett.*, **85**:5296, 2000. doi:10.1103/PhysRevLett.85.5296.

[5] R.T. De Souza, N. Carlin, Y.D. Kim, J. Ottarson, L. Phair, D.R. Bowman, C.K. Gelbke, W.G. Gong, W.G. Lynch, R.A. Pelak, T. Peterson, G. Poggi, M.B. Tsang, and H.M. Xu. The msu miniball 4 fragment detection array. *Nuclear Instruments and Methods in Physics Research Section A: Accelerators, Spectrometers, Detectors and Associated Equipment*, 295(12):109 – 122, 1990. doi:10.1016/0168-9002(90)90429-A.

[6] P. Zecher. *Design Construction, and Use of the Neutron Wall Array in Measuring the ^8Li (n, gamma) ^9Li Astrophysics Reaction*. PhD thesis, Michigan State University, 1996.

[7] M. S. Wallace, M. A. Famiano, M. J. van Goethem, A. M. Rogers, W. G. Lynch, J. Clifford, F. Delaunay, J. Lee, S. Labostov, M. Mocko, , L. Morris, A. Moroni, B. E. Nett, D. J. Oostdyk, R. Krishnasamy, M. B. Tsang, R. T. de Souza, S. Hudan, L. G. Sobotka, R. J. Charity, J. Elson, and G. L. Engel. The high resolution array (HiRA) for rare isotope beam experiments. *Nucl. Instr. and Meth. A*, **583**:302–311, 2007. `http://dx.doi.org/10.1016/j.nima.2007.08.248`.

[8] Yingxun Zhang, 2013. Private Communication.

[9] R. B. Wiringa, V. Fiks, and A. Fabrocini. Equation of state for dense nucleon matter. *Phys. Rev. C*, 38:1010–1037, Aug 1988. doi:10.1103/PhysRevC.38.1010.

[10] Andrew W. Steiner. High-density symmetry energy and direct urca process. *Phys. Rev. C*, 74:045808, Oct 2006. doi:10.1103/PhysRevC.74.045808.

[11] Pawel Danielewicz and Jenny Lee. Symmetry energy i: Semi-infinite matter. *Nuclear Physics A*, 818(1 - 2):36 – 96, 2009. doi:10.1016/j.nuclphysa.2008.11.007.

[12] U. Garg, T. Li, S. Okumura, H. Akimune, M. Fujiwara, M.N. Harakeh, H. Hashimoto, M. Itoh, Y. Iwao, T. Kawabata, K. Kawase, Y. Liu, R. Marks, T. Murakami, K. Nakanishi, B.K. Nayak, P.V. Madhusudhana Rao, H. Sakaguchi, Y. Terashima, M. Uchida, Y. Yasuda, M. Yosoi, and J. Zenihiro. The giant monopole resonance in the sn isotopes: Why is tin so 'fluffy'? *Nuclear Physics A*, 788(1 - 4):36 – 43, 2007. Proceedings of the 2nd International Conference on Collective Motion in Nuclei under Extreme Conditions COMEX 2 doi:10.1016/j.nuclphysa.2007.01.046.

[13] A. Klimkiewicz, N. Paar, P. Adrich, M. Fallot, K. Boretzky, T. Aumann, D. Cortina-Gil, U. Datta Pramanik, Th. W. Elze, H. Emling, H. Geissel, M. Hellström, K. L. Jones, J. V. Kratz, R. Kulessa, C. Nociforo, R. Palit, H. Simon, G. Surówka, K. Sümmerer, D. Vretenar, and W. Waluś. Nuclear symmetry energy and neutron skins derived from pygmy dipole resonances. *Phys. Rev. C*, 76:051603, Nov 2007. doi:10.1103/PhysRevC.76.051603.

[14] Andrea Carbone, Gianluca Colò, Angela Bracco, Li-Gang Cao, Pier Francesco Bortignon, Franco Camera, and Oliver Wieland. Constraints on the symmetry energy and neutron skins from pygmy resonances in ^{68}Ni and ^{132}Sn. *Phys. Rev. C*, 81:041301, Apr 2010. doi:10.1103/PhysRevC.81.041301.

[15] I. Daoutidis and S. Goriely. Impact of the nuclear symmetry energy on the pygmy dipole resonance. *Phys. Rev. C*, 84:027301, Aug 2011. doi:10.1103/PhysRevC.84.027301.

[16] M. Prakash, T. L. Ainsworth, and J. M. Lattimer. Equation of state and the maximum mass of neutron stars. *Phys. Rev. Lett.*, 61:2518–2521, Nov 1988. doi:10.1103/PhysRevLett.61.2518.

[17] J. M. Lattimer and M. Prakash. Neutron star structure and the equation of state. *The Astrophysical Journal*, 550(1):426, 2001. doi:10.1086/319702.

[18] J. M. Lattimer and M. Prakash. The physics of neutron stars. *Science*, 304(5670):536 – 542, 2004. doi:10.1126/science.1090720.

[19] Anna L. Watts and Tod E. Strohmayer. Detection with rhessi of high-frequency x-ray oscillations in the tail of the 2004 hyperflare from sgr 1806-20. *The Astrophysical Journal Letters*, 637(2):L117, 2006. doi:10.1086/500735.

[20] M. B. Tsang, W. A. Friedman, C. K. Gelbke, W. G. Lynch, G. Verde, and H. S. Xu. Isotopic scaling in nuclear reactions. *Phys. Rev. Lett.*, 86:5023–5026, May 2001. `10.1103/PhysRevLett.86.5023`.

[21] D. V. Shetty, S. J. Yennello, A. S. Botvina, G. A. Souliotis, M. Jandel, E. Bell, A. Keksis, S. Soisson, B. Stein, and J. Iglio. Symmetry energy and the isospin dependent equation of state. *Phys. Rev. C*, 70:011601, Jul 2004. doi:10.1103/PhysRevC.70.011601.

[22] M. B. Tsang, T. X. Liu, L. Shi, P. Danielewicz, C. K. Gelbke, X. D. Liu, W. G. Lynch, W. P. Tan, G. Verde, A. Wagner, H. S. Xu, W. A. Friedman, L. Beaulieu, B. Davin, R. T. de Souza, Y. Larochelle, T. Lefort, R. Yanez, V. E. Viola, R. J. Charity, and L. G. Sobotka. Isospin diffusion and the nuclear symmetry energy in heavy ion reactions. *Phys. Rev. Lett.*, 92:062701, Feb 2004. doi:10.1103/PhysRevLett.92.062701.

[23] D. D. S. Coupland, W. G. Lynch, M. B. Tsang, P. Danielewicz, and Yingxun Zhang. Influence of transport variables on isospin transport ratios. *Phys. Rev. C*, 84:054603, Nov 2011. doi:10.1103/PhysRevC.84.054603.

[24] M. A. Famiano, T. Liu, W. G. Lynch, M. Mocko, A. M. Rogers, M. B. Tsang, M. S. Wallace, R. J. Charity, S. Komarov, D. G. Sarantites, L. G. Sobotka, and G. Verde. Neutron and proton transverse emission ratio measurements and the density dependence of the asymmetry term of the nuclear equation of state. *Phys. Rev. Lett.*, 97:052701, Aug 2006. doi:10.1103/PhysRevLett.97.052701.

[25] Bao-An Li, C. M. Ko, and Zhongzhou Ren. Equation of state of asymmetric nuclear matter and collisions of neutron-rich nuclei. *Phys. Rev. Lett.*, 78:1644–1647, Mar 1997. doi:10.1103/PhysRevLett.78.1644.

[26] Gao-Chan Yong, Bao-An Li, Lie-Wen Chen, and Wei Zuo. Single and double π^-/π^+ ratios in heavy-ion reactions as probes of the high-density behavior of the nuclear symmetry energy. *Phys. Rev. C*, 73:034603, Mar 2006. doi:10.1103/PhysRevC.73.034603.

[27] Gao-Chan Yong, Bao-An Li, and Lie-Wen Chen. Double neutron-proton differential transverse flow as a probe for the high density behavior of the nuclear symmetry energy. *Phys. Rev. C*, 74:064617, Dec 2006. doi:10.1103/PhysRevC.74.064617.

[28] H. S. Xu, M. B. Tsang, T. X. Liu, X. D. Liu, W. G. Lynch, W. P. Tan, A. Vander Molen, G. Verde, A. Wagner, H. F. Xi, C. K. Gelbke, L. Beaulieu, B. Davin, Y. Larochelle, T. Lefort, R. T. de Souza, R. Yanez, V. E. Viola, R. J. Charity, and L. G. Sobotka. Isospin fractionation in nuclear multifragmentation. *Phys. Rev. Lett.*, 85:716–719, Jul 2000. doi:10.1103/PhysRevLett.85.716.

[29] V. Baran, M. Colonna, M. Di Toro, V. Greco, M. Zielinska-Pfabe, and H.H. Wolter. Isospin effects in nuclear fragmentation. *Nuclear Physics A*, 703(34):603 – 632, 2002. doi:10.1016/S0375-9474(01)01671-2.

[30] E. Geraci, M. Bruno, M. D'Agostino, E. DeFilippo, A. Pagano, G. Vannini, M. Alderighi, A. Anzalone, L. Auditore, V. Baran, R. Barn, M. Bartolucci, I. Berceanu, J. Blicharska, A. Bonasera, B. Borderie, R. Bougault, J. Brzychczyk, G. Cardella, S. Cavallaro, A. Chbihi, J. Cibor, M. Colonna, D. DePasquale, M. DiToro, F. Giustolisi, A. Grzeszczuk, P. Guazzoni, D. Guinet, M. Iacono-Manno, A. Italiano, S. Kowalski, E. LaGuidara, G. Lanzalone, G. Lanzan, N. LeNeindre, S. Li, S. LoNigro, C. Maiolino, Z. Majka, G. Manfredi, T. Paduszynski, M. Papa, M. Petrovici, E. Piasecki, S. Pirrone, G. Politi, A. Pop, F. Porto, M.F. Rivet, E. Rosato, S. Russo, P. Russotto, G. Sechi, V. Simion, M.L. Sperduto, J.C. Steckmeyer, A. Trifir, M. Trimarchi, M. Vigilante, J.P. Wieleczko, J. Wilczynski, H. Wu, Z. Xiao, L. Zetta, and W. Zipper. Isoscaling in central 124sn+64ni, 112sn+58ni collisions at 35amev. *Nuclear Physics A*, 732(0):173 – 201, 2004. doi:10.1016/j.nuclphysa.2003.11.055.

[31] T. X. Liu, M. J. van Goethem, X. D. Liu, W. G. Lynch, R. Shomin, W. P. Tan, M. B. Tsang, G. Verde, A. Wagner, H. F. Xi, H. S. Xu, M. Colonna, M. Di Toro, M. Zielinska-Pfabe, H. H. Wolter, L. Beaulieu, B. Davin, Y. Larochelle, T. Lefort, R. T. de Souza, R. Yanez, V. E. Viola, R. J. Charity, and L. G. Sobotka. Isotope yields from central ^{112,124}Sn $+^{112,124}$ Sn collisions: Dynamical emission? *Phys. Rev. C*, 69:014603, Jan 2004. doi:10.1103/PhysRevC.69.014603.

[32] C.B. Das, S. Das Gupta, W.G. Lynch, A.Z. Mekjian, and M.B. Tsang. The thermodynamic model for nuclear multifragmentation. *Physics Reports*, 406(1):1 – 47, 2005. doi:10.1016/j.physrep.2004.10.002.

[33] G. F. Bertsch, H. Kruse, and S. Das Gupta. Boltzmann equation for heavy ion collisions. *Phys. Rev. C*, 29:673–675, Feb 1984. doi:10.1103/PhysRevC.29.673.

[34] P. Danielewicz and G.F. Bertsch. Production of deuterons and pions in a transport model of energetic heavy-ion reactions. *Nuclear Physics A*, 533(4):712 – 748, 1991. doi:10.1016/0375-9474(91)90541-D.

[35] P. Danielewicz. Formation of composites emitted at large angles in intermediate and high energy reactions. *Nuclear Physics A*, 545(1 - 2):21 – 34, 1992. doi:10.1016/0375-9474(92)90443-N.

[36] P. Danielewicz. Hadronic transport models. *Acta. Phys. Pol. B*, 33(45), 2002. `http://arXiv:nucl-th/0201032v1`.

[37] P. Danielewicz. Determination of the mean-field momentum-dependence using elliptic flow. *Nucl. Phys. A*, **673**:375, 2000. doi:10.1016/S0375-9474(00)00083-X.

[38] G.F. Bertsch and S. Das Gupta. A guide to microscopic models for intermediate energy heavy ion collisions. *Physics Reports*, 160(4):189 – 233, 1988. doi:10.1016/0370-1573(88)90170-6.

[39] B Davin, R.T de Souza, R Yanez, Y Larochelle, R Alfaro, H.S Xu, A Alexander, K Bastin, L Beaulieu, J Dorsett, G Fleener, L Gelovani, T Lefort, J Poehlman, R.J Charity, L.G Sobotka, J Elson, A Wagner, T.X Liu, X.D Liu, W.G Lynch, L Morris, R Shomin, W.P Tan, M.B Tsang, G Verde, and J Yurkon. Lassa: a large area silicon strip array for isotopic identification of charged particles. *Nuclear Instruments and Methods in Physics Research Section A: Accelerators, Spectrometers, Detectors and Associated Equipment*, 473(3):302 – 318, 2001. doi:10.1016/S0168-9002(01)00295-9.

[40] Tianxiao Liu. *Isospin Dynamics and the Isospin Dependent EOS*. PhD thesis, Michigan State University, 2005.

[41] `root.cern.ch`.

[42] Bao-An Li, Lie-Wen Chen, and Che Ming Ko. Recent progress and new challenges in isospin physics with heavy-ion reactions. *Physics Reports*, 464(46):113 – 281, 2008. doi:10.1016/j.physrep.2008.04.005.

[43] A. Mekjian. DIRECT INTERACTION, CLASSICAL THERMODYNAMIC AND QUANTUM STATISTICAL THEORIES OF HEAVY ION COLLISIONS. *Phys.Lett.*, B89:177–180, 1980.

[44] H. Sato and K. Yazaki. On the coalescence model for high-energy nuclear reactions. *Phys.Lett.*, B98:153–157, 1981.

[45] L.P. Csernai and Joseph I. Kapusta. ENTROPY AND CLUSTER PRODUCTION IN NUCLEAR COLLISIONS. *Phys.Rept.*, 131:223–318, 1986.

[46] A.Z. Mekjian. Explosive nucleosynthesis, equilibrium thermodynamics, and relativistic heavy-ion collisions. *Phys.Rev.*, C17:1051–1070, 1978.

[47] Terry C. Awes, G. Poggi, C.K. Gelbke, B.B. Back, B.G. Glagola, et al. Precompound emission of light particles in the reaction O-16+ U-238 at 20 MeV/nucleon. *Phys.Rev.*, C24:89–110, 1981.

[48] David H. Boal. COALESCENCE MODELS IN NUCLEON AND LIGHT ION INDUCED REACTIONS. *Phys.Rev.*, C25:3068–3077, 1982.

[49] I. Cervesato, E. Fabrici, E. Gadioli, E. Gadioli-Erba, and M. Galmarini. Light particle emission in Boltzmann master equation theory of pre-equilibrium reactions. *Phys.Rev.*, C45:2369–2378, 1992.

[50] J. Barrette et al. Production of light nuclei in relativistic heavy ion collisions. *Phys.Rev.*, C50:1077–1084, 1994.

[51] W.J. Llope, S.E. Pratt, N. Frazier, R. Pak, D. Craig, et al. The fragment coalescence model. *Phys.Rev.*, C52:2004–2012, 1995.

[52] Rudiger Scheibl and Ulrich W. Heinz. Coalescence and flow in ultrarelativistic heavy ion collisions. *Phys.Rev.*, C59:1585–1602, 1999.

[53] A. Mekjian. Thermodynamic Model for Composite Particle Emission in Relativistic Heavy Ion Collisions. *Phys.Rev.Lett.*, 38:640–643, 1977.

[54] K. Hagel, R. Wada, J. Cibor, M. Lunardon, N. Marie, et al. Light particle probes of expansion and temperature evolution: Coalescence model analyses of heavy ion collisions at 47-A-MeV. *Phys.Rev.*, C62:034607, 2000.

[55] R. Wada, K. Hagel, L. Qin, J.B. Natowitz, Y.G. Ma, et al. The Nuclear Matter Symmetry Energy at $0.03 \leq \rho/\rho_0 \leq 0.2$. *Phys.Rev.*, C85:064618, 2012.

[56] S. T. Butler and C. A. Pearson. Deuterons from high-energy proton bombardment of matter. *Phys. Rev.*, 129:836–842, Jan 1963.